



Improved Light Management and Photogenerated Carrier Collections Concepts for Third Generation Solar Cells

Koncepcje na poprawę zarządzania światłem oraz zbierania fotowzбудzonych
nośników ładunku w ogniwach słonecznych trzeciej generacji

Maciej Krajewski

Institute of Experimental Physics

Faculty of Physics

University of Warsaw

This dissertation is submitted for the degree of
Doctor of philosophy

Thesis supervised by
dr hab. Aneta Drabińska, prof. UW
with the assistance of
dr Piotr Wróbel

Warsaw

2024

Acknowledgements

As scientific research is almost always a team effort, the finishing of this thesis would not have been possible without the cooperation, devotion and kindness of the people with whom I had the pleasure to work. Herein, I would like to thank those who contributed to the research presented in this thesis:

Adrian Callies and Mario Hanser, thank you for your warm welcome and the introduction to the nanoimprint lithography technique and RCWA numerical methods. Our close cooperation was without a doubt a very fruitful and developing one.

Maryam Heydarian, Minasadat Heydarian, and Patricia Schulze, thank you for dedicating priceless time to the preparation and electrical characterization of the perovskite cells. Your kindness and expertise were undoubtedly crucial in finishing these investigations.

Benedikt Bläsi and Oliver Höhn, I appreciate the trust you put in me when you invited me to your facility. Thank you for your excellent supervision and guidance during my time at Fraunhofer ISE. The experience I gained was one of the most important in my career and personal life.

Mateusz Tokarczyk, thank you for conducting the XRD measurements, an introduction to the SEM imaging technique, along with countless hours of fascinating discussions and advice.

Karol Nogajewski, I am grateful for the solid fundamentals in photolithography and invaluable advice regarding other, various techniques.

Maria Kamińska, your help in every imaginable situation, dedication to the group's work, and never-ending trust and enthusiasm were invaluable. Without your engagement, I would not have had the opportunity to supervise and operate the ALD reactor. Thanks to your experience and optimistic outlook, the research effort became an extremely fascinating adventure and an opportunity for personal development.

Piotr Wróbel, thank you for conducting SEM and ellipsometry measurements and for many discussions regarding the science, especially the optical properties of the investigated materials. I appreciate your supervision during the most crucial moments of this thesis process.

Aneta Drabińska, thank you for giving me the opportunity to conduct research under your supervision and for your invaluable support in the initial steps of my scientific career.

I also would like to express my gratitude to all colleagues I have met at the Faculty of Physics. Your companion and hours of conversations not only helped me deepen my scientific knowledge but also developed my life beyond academia.

Finally, I would like to express my deepest thanks to my family: my parents for inspiring me with a love for science, my brother for his unwavering support and crossed fingers, and my wife and sons – the never-exhausting source of happiness and joy. Thank you for being with me.

Abstract

This thesis is dedicated to research aimed at the performance enhancement of solar cells by optimization of photon and electron management within the photovoltaic system. It particularly focuses on a crucial component of the solar cell, namely the transparent electrode, which is designed to let as much light as possible into the active layer, where free carriers are generated, and to efficiently collect these charges. Solar cells are currently a dynamically developing source of renewable energy, which in the future may account for the majority of generated electrical energy worldwide. Therefore, research to improve their efficiency is crucial for the development and widespread implementation of this technology.

The thesis introduces concepts aimed at improving the properties of the upper layer of the solar cell, both electrically and optically. The work consists of three main chapters covering various approaches to those materials and systems.

The thesis presents research on the deposition of atomic layers of co-doped zinc oxide, used as a planar conducting electrode. The obtained material exhibits excellent optoelectrical properties, surpassing the results achieved by the commonly used aluminium-doped zinc oxide. This section also focuses on the proposed composite electrode, composed of a multilayer structure of oxide-metal-oxide, as the promising approach towards the operation of transparent electrodes.

This work demonstrates also a structured anti-reflective layer placed on top of the solar cell, using the nanoimprint technique. This scalable solution, applicable in the current industrial production chain, visibly improves performance results, especially the generated current.

Another part of the thesis introduces a model of a structured electrode utilizing a submicron mesh embedded in a planar oxide electrode. The presented model illustrates trends to consider when choosing the mesh geometry and allows for its adaptation to the selected active layer. The impact on the optical properties of such a composite material is also determined, providing a basis for experimental verification of numerical studies in the future.

This doctoral thesis contains new information enabling the design and fabrication of solar cells incorporating the proposed concepts. The author hopes that the research presented herein will contribute to improving the efficiency of solar cells on a large scale and accelerate the implementation of the latest solutions and architectures. I believe that this thesis can be useful for young students and researchers looking for reliable information source about solar cells, the photovoltaic market and new concepts emerging in this field.

Streszczenie

Niniejsza praca poświęcona jest badaniom mającym na celu zwiększenie wydajności pracy ogniw słonecznych poprzez optymalizację zarządzania fotonami oraz elektronami wewnątrz ogniwa fotowoltaicznego. W szczególności skupia się na kluczowej części ogniwa, jaką stanowi przezroczysta elektroda mająca za zadanie przepuścić jak najwięcej światła do warstwy aktywnej, gdzie generowane są swobodne nośniki, a także efektywne zebranie tychże ładunków. Ogniwa słoneczne stanowią obecnie dynamicznie rozwijające się źródło energii, które w przyszłości może odpowiadać za większość wytworzonej energii elektrycznej na świecie. Stąd badania nad poprawą ich efektywności są kluczowe dla rozwoju tej technologii.

W pracy przedstawione są koncepty mające poprawić własności tej górnej warstwy ogniwa zarówno od strony elektrycznej jak i optycznej. Praca składa się z trzech głównych rozdziałów poruszających różne zastosowane materiały i układy.

Praca przedstawia badania techniką osadzania warstw atomowych kodymieszkowanego tlenku cynku mającego zastosowanie jako planarna przewodząca elektroda. Otrzymany materiał wykazuje bardzo dobre właściwości elektrooptyczne, niezbędne do tego zastosowania, przewyższając wyniki osiągnięte przez powszechnie stosowany tlenek cynku domieszkowany aluminium. Ta część skupia się także na zaproponowanej elektrodzie kompozytowej, złożonej jako struktura wielowarstwowa tlenek-metal-tlenek, jako kolejna generacja przezroczystych elektrod.

Badania przedstawione w tej pracy dotyczą również strukturyzowanej warstwy antyodbiciowej umieszczanej na górze ogniwa, stosując technikę nanoimprintingu. W ten sposób otrzymano skalowalne rozwiązanie możliwe do zastosowania w obecnym w przemyśle łańcuchu produkcji. Tak zmodyfikowane ogniwo znacząco poprawiło wyniki wydajności, w szczególności generowanego przez nie prądu.

Kolejna część pracy przedstawia model strukturyzowanej elektrody wykorzystującej nanometryczną siatkę umieszczoną w planarnej elektrodzie tlenkowej. Przedstawiony model pokazuje trendy, którymi należy się kierować przy wyborze geometrii takiej siatki, a także pozwala na jej dopasowanie do wybranej warstwy aktywnej. Określono także wpływ na właściwości optyczne takiej warstwy, co w przyszłości pozwoli na eksperymentalną weryfikację badań numerycznych.

Przedstawiana praca doktorska zawiera nowe informacje pozwalające na projektowanie i stworzenie ogniw słonecznych wykorzystujących zaproponowane w pracy koncepty. Autor niniejszej pracy ma nadzieję, że badania w niej przedstawione przyczynią się do poprawy wydajności ogniw oraz przyspieszą wdrożenie najnowszych rozwiązań. Ufam, że niniejsza praca doktorska może być użyteczna również dla studentów, pragnących znaleźć wiarygodne informacje nt. ogniw słonecznych, rynku fotowoltaiki oraz nowych konceptów obecnych w tej branży.

If I have seen further than others, it is by standing on the shoulders of giants.

~Isaac Newton

Table of Contents

Acknowledgements.....	i
Abstract.....	iii
Streszczenie.....	iv
Table of Contents	vii
Dissertation Outline.....	x
Abbreviations	xii
CHAPTER 1. Introduction to Photovoltaics	1
1.1. Research motivation.....	1
1.2. Solar cell working principles	4
1.2.1. P-N junction.....	4
1.3. Ideal and real solar cells.....	9
1.3.1. Effects of parasitic resistances	11
1.3.2. Solar spectrum mismatch	12
1.3.3. Optical losses.....	16
1.4. Generations of solar cells	17
1.4.1. First generation: silicon solar cells	18
1.4.2. Second generation: thin-films solar cells.....	19
1.4.3. Third Generation: emerging technologies.....	21
CHAPTER 2. Transparent Electrodes.....	24
2.1. Electrical and Optical Properties.....	24
2.1.1. Transmittance and reflection	24
2.1.2. Conductivity and Figure of Merit	26
2.2. Performance improvement strategies.....	29
2.2.1. Thin layer interference.....	29
2.2.2. Solutions beyond planar layers	32
CHAPTER 3. Methodology	35
3.1. Atomic layer deposition	35
3.1.1. ALD System Employed	37

3.1.2.	ALD growth dynamics and properties	38
3.1.3.	ALD Process Cycle and Reactions.....	42
3.2.	Nanoimprint lithography	46
3.2.1.	Nanoimprint method overview	46
3.2.2.	Roller nanoimprint system	50
3.3.	Characterization methods.....	51
3.3.1.	Scanning electron microscopy.....	51
3.3.2.	X-Ray Diffraction.....	54
3.3.3.	UV-Vis-NIR Spectroscopy.....	55
3.3.4.	Hall effect measurements	58
3.3.5.	J-V Characteristics and External Quantum Efficiency.....	60
3.4.	Numerical methods	62
3.4.1.	Transfer-Matrix Method.....	62
3.4.2.	Rigorous coupled wave analysis	64
3.5.	Summary	66
CHAPTER 4. ALD-grown ZnO as a Transparent Conductive Electrode		67
4.1.	Zinc oxide selected properties.....	67
4.2.	Aluminum doped zinc oxide ALD growth.....	69
4.2.1.	ZnO growth parameters optimization	70
4.2.2.	Structure and optical properties	75
4.3.	Co-doping of aluminium zinc oxide.....	79
4.3.1.	Samples and Morphology.....	80
4.3.2.	Electrical properties	85
4.3.3.	Optical properties	88
4.3.4.	Outlook and prospects for co-doped ZnO.....	93
4.4.	Performance optimization using multilayer TCE	94
4.4.1.	Numerical Findings – TMM Results	94
4.4.2.	Experimental Realization.....	98
4.5.	Summary	101

CHAPTER 5. Nanoimprinted Perovskite Solar Cell	102
5.1. Introduction	102
5.2. Proposed structures	103
5.2.1. Optical Studies of the Imprinted Structures.....	106
5.3. Perovskite Solar Cell Imprinting Process	108
5.3.1. Fabrication and Characterization of perovskite solar cell	108
5.4. Optical and Electrical Parameters	112
5.4.1. Effect of the ARC on the optical performance	112
5.4.2. Effect of the ARC on the EQE and J-V performance.....	116
5.5. Summary	119
5.6. Appendix to CHAPTER 5: RCWA calculations details.....	120
CHAPTER 6. Transparent Electrodes with Embedded Nanomeshes	122
6.1. Introduction	122
6.2. Proposed Model	123
6.3. Calculations examples and model predictions.....	126
6.4. Proposed Structures.....	129
6.5. Efficiency Results.....	132
6.5.1. Diffusion length influence	132
6.5.2. Efficiency applied for real cases of third generation photovoltaics .	136
6.6. Optical properties	140
6.6.1. Convergence analysis and RCWA simulation details.....	140
6.6.2. Reflectivity results	143
6.7. Summary	146
CHAPTER 7. Conclusions and Perspectives	147
Appendix: List of scientific articles.....	149
Figure List.....	151
References	156

Dissertation Outline

This thesis presents the concepts related to the performance of solar cells, in particular third generation photovoltaics. It focuses on the solar cell front surface which is a transparent electrode responsible for photogenerated carrier collection. The main goal of this thesis is to propose and evaluate the concepts for the enhanced operation of this part of the solar cell, taking an application-oriented approach. The thesis is structured as follows:

CHAPTER 1. presents an exhaustive introduction to the field of photovoltaic, encompassing both global climate change challenges, the current photovoltaic market situation, and the physics behind the operation of solar cells. Moreover, it showcases all the issues linked to enhancing the performance of the cell, which this thesis aims to comprehensively address.

CHAPTER 1. CHAPTER 2. focuses on the main topic of the thesis which is the transparent electrode used for photovoltaics. It emphasizes the importance of this component in the right operation of the cell and provides a throughout review of the current approaches to this part.

CHAPTER 3. contains a detailed description of the methods used in the thesis. It primarily focuses on the growth and structurization techniques employed in the thesis, namely atomic layer deposition and nanoimprint photolithography. Additionally, it introduces numerous characterization methods indispensable during the writing of this thesis, as well as provides a brief overview of numerical methods used to calculate the presented results.

CHAPTER 4. is devoted to atomic layer deposition grown ZnO thin films. It begins with the laborious process of finding the optimal growth parameters for singly doped, aluminium-doped zinc oxide. Subsequently, it focuses on the next step in transparent conductive oxide progress, which is doubly-doped material. The chapter discusses its structure and the reasons behind enhanced optoelectrical properties. Besides, it describes the numerical and experimental findings related to more advanced concepts, such as multilayer metal-oxide electrodes. While demonstrating the possibility of constructing such a material, it also explains the encountered difficulties along this path.

CHAPTER 5. demonstrates one of the first, perovskite solar cells with a directly texturized anti-reflective coating. This modification was made using a highly scalable and affordable roller nanoimprint technique. Such enhanced solar cell presents very

good antireflective properties, resulting in almost zero reflectance, thereby maximizing the current generated from the cell.

CHAPTER 6. in contrast to the previous chapters, presents entirely numerical results for the concept of a nanomesh embedded in the transparent conductive oxide electrode. This concept provides both exceptionally high conductivity and the high transparency needed for effective operation. Within this chapter, a new model is proposed to evaluate the best arrangement for embedded nanomesh electrodes. This search results in the optimization of the geometry, depending on the active layer beneath it, proposing a comprehensive view of the solar cell charge collection properties. These results are accompanied by optical simulations to assess the influence of the grid on the transmission of the electrode.

CHAPTER 7. is a brief summary of the thesis with the most significant results highlighted. Also, it provides an outlook for the next generation of photovoltaic devices.

Abbreviations

A list of the commonly used terminology in the thesis is provided. If applicable, the employed units are stated in square brackets.

ALD – atomic layer deposition

ARC – anti-reflective coating

AZO – aluminium-zinc oxide

FDTD – finite-difference time-domain

HAZO – hafnium-aluminium-zinc oxide

ITO – indium-tin oxide

PCS – perovskite solar cell

RCWA – rigorous coupled wave analysis

TCO – transparent conductive oxide

TCE – transparent conductive electrode

OSC – organic solar cell

E_G – bandgap energy [eV]

E_F – Fermi level [eV]

EQE – external quantum efficiency [%]

J_{sc} – short circuit current density [mA/cm²]

n – carrier concentration [1/cm³]

μ – carrier mobility [cm²/Vs]

γ – diffusion length [nm]

$\Phi_{AM1.5}$ – photon flux of the standard solar spectrum [# /m²s]

R_s – sheet resistance [Ω /sq]

R_w – reflectance weighted to the standard solar spectrum [%]

V_{oc} – open circuit voltage [V]

CHAPTER 1.

Introduction to Photovoltaics

1.1. Research motivation

Global climate change is one of the most urgent concerns of humankind that has been underscored in many scientific reports as a continuously growing issue that both current and upcoming generations will inevitably confront [1-4]. The industrial revolution, rapid population growth, and improved worldwide living standards, come at the expense of depleting planetary resources such as coal, crude oil, and natural gas. This, in turn, significantly contributes to the vast area of land impoverishment and pollution [5-7]. Given the continuous rise in electricity demand, the adoption of clean and affordable energy sources to meet global needs is now even of greater significance. It is estimated that the annual electrical energy consumption will surge to about 35 000 TWh in just 20 years, as depicted in **Figure 1**.

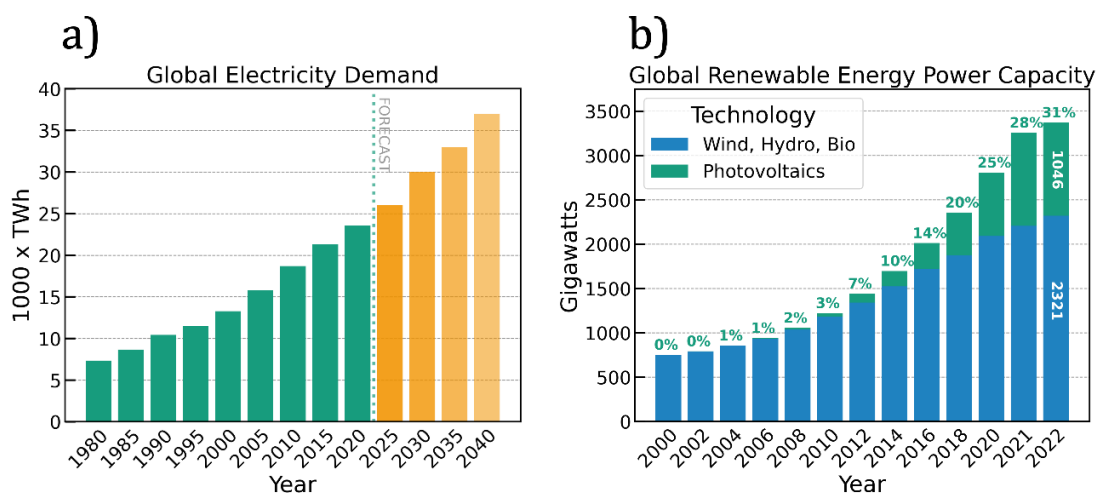


Figure 1. Global electricity market. a) Global electricity demand vs year with forecasting. The demand steadily continues to grow every 5 years. **b)** Share of the photovoltaics in renewable sources worldwide. A very dynamic growth can be observed after 2010, reaching currently almost $\frac{1}{3}$ of the global capacity. Data: IRENA [8,9]

Maintaining dependence on fossil fuels as a foundation for energy generation emerges as a risky and expensive decision, given the increasing depletion of natural resources and surging CO₂ concentration in the atmosphere[10-12]. The primary issue of global economic growth propelled by fossil fuels lies in the greenhouse gases emissions that accumulate in the atmosphere[13,14]. This accumulation causes increased temperatures, since CO₂ molecules very effectively absorb infrared wavelengths, storing more of its energy compared to unpolluted air. The observed correlation between CO₂ concentration and the observed global average temperature is profoundly manifested in **Figure 2**. The chart presents the consistent rise of documented CO₂ concentration in the atmosphere, which a decade ago exceeded the unsettling threshold of 400 ppm – a level never observed in the history of mankind [15-17]. **Figure 2b** presents the deviation from the 1901 – 2000 years average world temperature. Over the past two decades, there has been a swift and alarming ascent in the recorded temperature anomalies. Climatologists warn before the scenario where those deviations reach +1.5 °C [18-20]. Such an outcome would lead to the extinction of species and ecosystems that cannot thrive in such conditions, along with unpredictable and more frequent natural disasters such as floods, hurricanes, and wildfires [21-23].

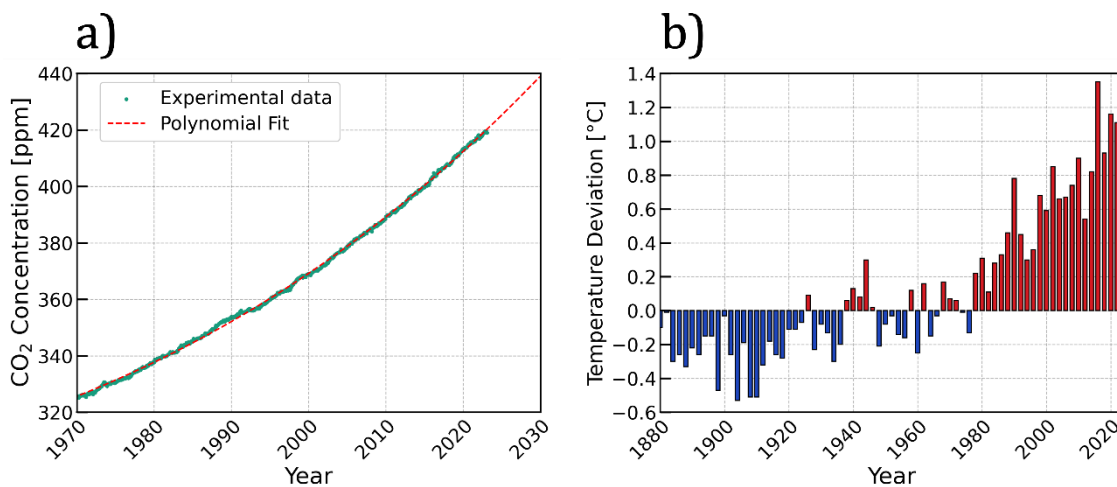


Figure 2. CO₂ concentration and temperature deviation. a) The chart shows the rise of CO₂ concentration levels in the atmosphere in recent decades, also known as the Keeling curve. **b)** Global Temperature deviation from the 1901 – 2000 average year temperature measured globally. The blue colour indicates temperature below the average, whereas the red colour indicates temperature above the average. Data: NOAA[24,25]

The solution to this widespread challenge, with repercussions extending beyond the one-generation lifespan, can be found in the rapid embracing of

renewable energy sources like wind, sun and hydropower [26-30]. These sources do not need constant fuel combustion to operate, thus their detrimental influence on the environment is significantly limited. The most promising among those alternative energy sources are photovoltaic cells, harvesting solar light energy and converting it into electricity.

For centuries, the Sun has been the primary source of energy on Earth. This massive thermonuclear reactor located 150 000 000 km away from our planet continuously delivers an enormous amount of electromagnetic energy, being the foremost cause of any life existence. While the efficient harvesting of such power has been an unfulfilled dream for many generations, recent decades have witnessed the realization of this concept, thanks to the discovery of the photovoltaic effect. This effect grants access to the free and most abundant energy source available. Initially, photovoltaics remained confined to academic circles, but soon after its recognition as a potentially disruptive technology in the industry, rapidly raised the attention of the wider public. The costs associated with photovoltaic cells made it not feasible for any commercial use for many years in the last century, as shown in **Figure 3**.

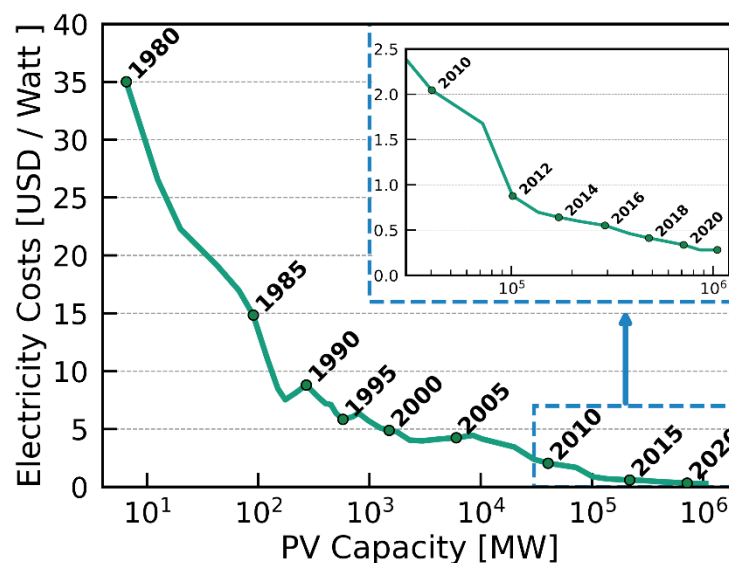


Figure 3. Electricity production costs vs. the photovoltaic capacity. After 2010 an average cost of 1 Watt PV production fell below 2 USD. Data by [31].

However, the ongoing advancements in the recent decades have led to a rapid decline in costs, photovoltaics has become one of the most cost-effective renewable energy sources available now. Besides the very competitive costs of energy production, the electricity obtained through photovoltaic cells is characterized by

its absence of harmful environmental impact arising from greenhouse gas emissions during the operation [32]. The ever-growing energy consumption, primarily driven by fossil fuel combustion has brought Earth's natural resources to a critical limit, making the energy transition towards more sustainable sources even more urgent.

The efficient, stable, and long-lasting solar cells provided by affordable techniques, scalable to terawatts scale worldwide are thus a fundamental condition for successful expansion of the solar energy. This thesis discusses the challenges related to this topic by considering the new concepts in photovoltaics to enhance the efficiency of their new-generation devices.

1.2. Solar cell working principles

A solar cell is a type of p-n junction that using the photovoltaic effect generates photocurrent during illumination. Despite different types depending on the expected system functioning, the p-n junctions share many common characteristics. The understanding of the phenomena inside the p-n junction is crucial for the investigation of any electronic devices, including solar cells.

1.2.1. P-N junction

There exists a plethora of p-n junction types, that fulfill very diverse roles in electronic systems such as voltage stabilizers, light-emitting elements, or AC-DC converters to name a few[33]. The following introductory discussion is based on a few classical handbooks regarding semiconductor physics [34-37].

A p-n junction is formed when two regions with different majority carrier types of either the same semiconducting material (*homojunction*) or two different (*heterojunction*) are brought together to create a contact. The region with more free electrons than holes is called an n-type semiconductor, whereas the region with an excess number of holes is a p-type semiconductor. A semiconductor material in the commonly applied model can be described by the valence and conduction band edge energies, the energy gap between them, carrier concentration, and the position of the Fermi level (E_F). The position of the Fermi level denotes the average energy of the electron inside the material and its uniformity throughout the system is the condition for attaining thermodynamic equilibrium. Doping of the material leads to the shift of the Fermi level, relative to its level in the intrinsic material. The shift's direction depends on the dopant charge type: p-type dopant shifts the Fermi

level towards lower energies, whereas n-type dopant, shifts the Fermi level towards higher energies. **Figure 4** schematically shows the difference between p- and n-type semiconductors regarding their Fermi level positions. In a p-type semiconductor Fermi level lies below the middle of the energy bandgap (E_i), due to a deficiency of electrons, bringing it closer to the valence band edge energy (E_v). In an n-type semiconductor Fermi level is situated above this value, closer to the conduction band edge (E_c).

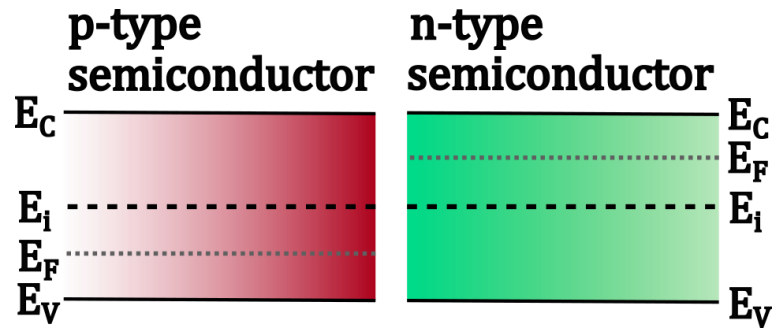


Figure 4. Two types of semiconducting material. The red one represents p-type semiconductors with holes as majority carriers. Green is a n-type semiconductor with an exceeding number of electrons. Fermi levels in the respective materials are shifted accordingly.

To derive the current-voltage (I-V) characteristic of the p-n junction, we employ the so-called abrupt p-n junction assumption that notably simplifies the discussion while retaining the fundamental attributes of the system.

First, we assume that both semiconducting materials exhibit comparable majority carrier concentrations which are uniformly distributed throughout the material with a step-like discontinuity at the junction. This distribution is depicted in **Figure 5a**. It is worth noting that the p-n system is not limited to this particular charge distribution, nevertheless, the abrupt p-n junction model reflects all the necessary dynamics inside the junction.

Upon contacting both materials, the free charges of both types present in the bulk crystals recombine with each other, leaving ionized atoms on both sides. These ions induce the emergence of an electric field (as illustrated in **Figure 5b**), effectively sweeping away any free charges in the region. That constitutes a depletion region with negligible free carrier concentration. The existence of this region opposes the motion of the charge in either direction, due to the in-built potential that repulses the carriers away from this zone (**Figure 5c**). The energy bands undergo bending to ensure that the Fermi level is common for both sides,

which establishes thermodynamic equilibrium. The energy diagram for electrons (depicted in **Figure 5d**) exhibits a potential barrier, equal to $q\psi_{bi}$, that electrons must overcome to move towards the p-type region. The barrier's height depends on the applied voltage and it is decisive for the current flow through the junction.

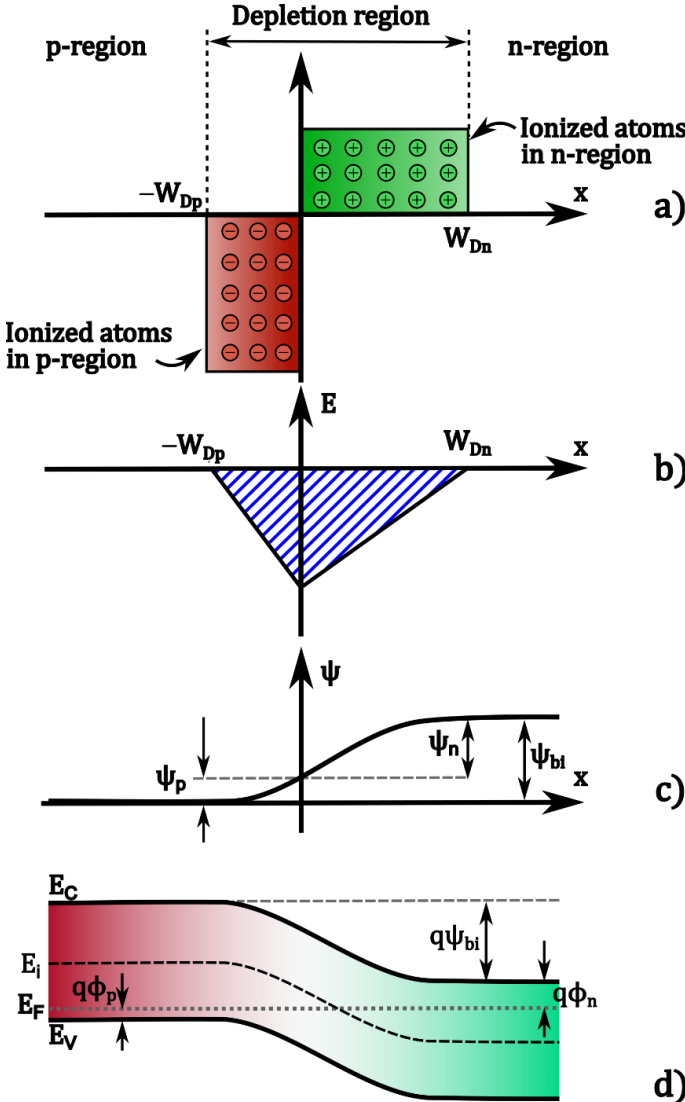


Figure 5. p-n junction diagrams in the thermodynamic equilibrium. a) Ionized atoms charge distribution in the junction showing step-like characteristics. b) Electric field built-up in the system due to the charge distribution c) Potential inside the junction d) Band diagram with conduction and valence band edges bending and built-in potential. Note the Fermi level is constant throughout the system. Graphically adapted from [37].

There are two main origins of the currents present in the junction:

- *Diffusion current* depends on inherent properties of the junction such as carrier concentration, its mobility, and diffusion coefficient, and it is

independent of the external bias. This current arises from the thermally generated minority carriers in the depletion region:

$$I_0 = qn_i^2 \left(\frac{D_p}{L_p N_D} + \frac{D_n}{L_n N_A} \right), \quad (1)$$

where n_i is intrinsic concentration, D_p and D_n – diffusion coefficients of holes and electrons respective, L_p and L_n – diffusion lengths and N_D , N_A – donors and acceptor concentrations. All terms in this equation are temperature-dependent themselves, therefore the I_0 value changes with temperature as well.

- *Drift current* depends on the applied electric field that pulls the carriers and lowers the potential barrier for carriers to overcome:

$$I_{drift} = I_0 \exp\left(\frac{qV}{k_B T}\right). \quad (2)$$

It depends on the barrier's height in the junction and comes from the drift carriers' movement generated by the external voltage. Combining **Equations (1)** and **(2)**, we therefore obtain the final formula governing the p-n junction current. This formula is called the Shockley equation and is widely used across the literature [38]:

$$I(V) = I_0 \left[\exp\left(\frac{qV}{k_B T}\right) - 1 \right]. \quad (3)$$

When a positive voltage is applied to the p-region, the potential barrier is lowered, effectively narrowing the depletion region. The carriers then have a chance to overcome this potential, consequently initiating a current flow through the junction with an exponential relationship.

A solar cell is a p-n junction designed to operate under light exposure, therefore it is crucial to explain the processes taking place inside the junction during illumination. **Figure 6** depicts the route that carriers must take to successfully contribute to the current generation inside the junction. First, the incident photon is absorbed within the active layer of the solar cell, creating an excessive amount of majority carriers of both types: holes and electrons. These excited carriers are bound together, forming an electron-hole pair, called an exciton. The injection of those carriers also disrupts the thermal equilibrium within the system, leading to the formation of the two distinct quasi Fermi levels (QFLS) – each for holes and electrons.

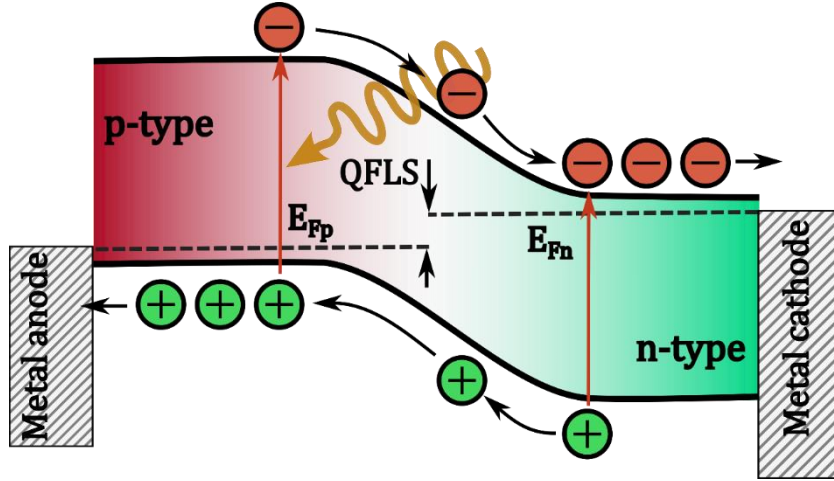


Figure 6. Solar cell under illumination operation scheme with photogenerated carriers route.

The splitting between the levels is closely related to the voltage subsequently generated from the cell. The electron-hole pair is an unstable quasiparticle that is prone to recombination, releasing back the absorbed energy in the form of heat or light, as a result not contributing to the current generation. In order to allow the current flow, this quasiparticle needs to be separated into a hole and an electron. The high recombination rate inside the cell shortens the carrier lifetime, significantly compromising the overall efficiency of the cell and therefore should be mitigated. There are a few relaxation channels through which the carrier can recombine, encompassing band-to-band radiative recombination, trap-assisted recombination (Shockley-Read-Hall) [39,40], surface recombination, and Auger recombination. The effective carrier lifetime is expressed in the following formula:

$$\frac{1}{\tau_{eff}} = \frac{1}{\tau_{rad}} + \frac{1}{\tau_{SRH}} + \frac{1}{\tau_{surface}} + \frac{1}{\tau_{Auger}}, \quad (4)$$

where each of the terms is proportional to the recombination rate of the respective mechanism.

The photogenerated carriers that did not recombine immediately, are then transported across the junction: the holes go to the p-type semiconductor area, whereas electrons travel to the n-type semiconductor area. To give rise to the observed current flow, they need to be collected at the respective electrodes: cathode and anode. Along this path, their recombination still remains possible, highlighting the need to minimize the distance a photogenerated carrier has to traverse to reach the collection point. This factor stands as a fundamental

determinant for ensuring the high efficiency of a solar cell. Shockley equation under illumination now holds:

$$I(V) = I_0 \left[\exp\left(\frac{qV}{k_B T}\right) - 1 \right] - I_L. \quad (5)$$

The collected carriers generate constant current flow (I_L), proportional to the incident light intensity, in the same direction as I_0 , depicted in **Figure 7**.

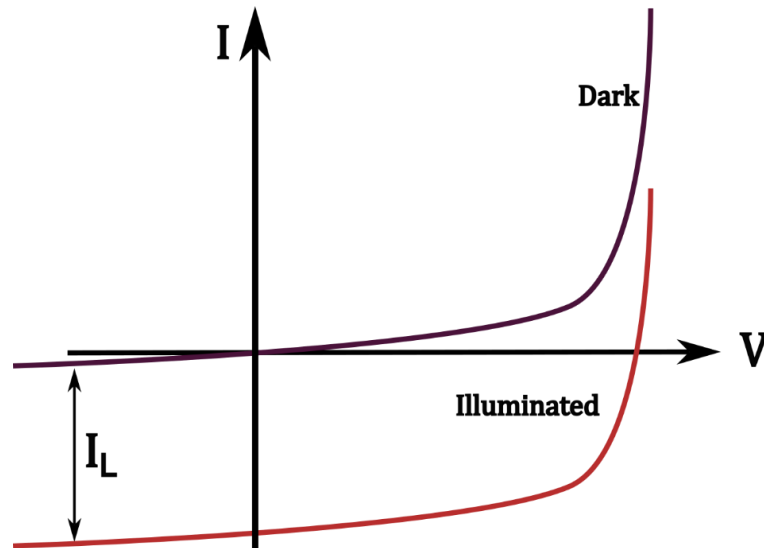


Figure 7. I-V characteristic of p-n junction in both conditions: dark and under illumination. The curve is an exponent shifted downwards by the I_L current value.

1.3. Ideal and real solar cells

After illumination of the cell, a shifting of the I-V curve downward is observed. However, the commonly adopted convention shows the I-V curve upside down to enhance the legibility of the specific electrical parameters. **Figure 8**. shows the typical solar cell I-V characteristic with significant points indicated. We define the following parameters that describe the behaviour and performance of the cell:

- V_{oc} – voltage at which there is no current flow in the junction, i.e. the intersection of the I - V curve and the voltage axis, so-called open-circuit voltage.
- I_{sc} – current generated by the cell with zero external bias, i.e. the intersection point of I - V and the current axis, so-called short circuit current.

- V_{MP} – external voltage at which the cell generates maximum power, i.e. the optimal working point of the cell. This value is used to calculate the final efficiency of the cell.
- I_{MP} – similar to V_{MP} , it is the current at which the cell generates the maximum power possible.

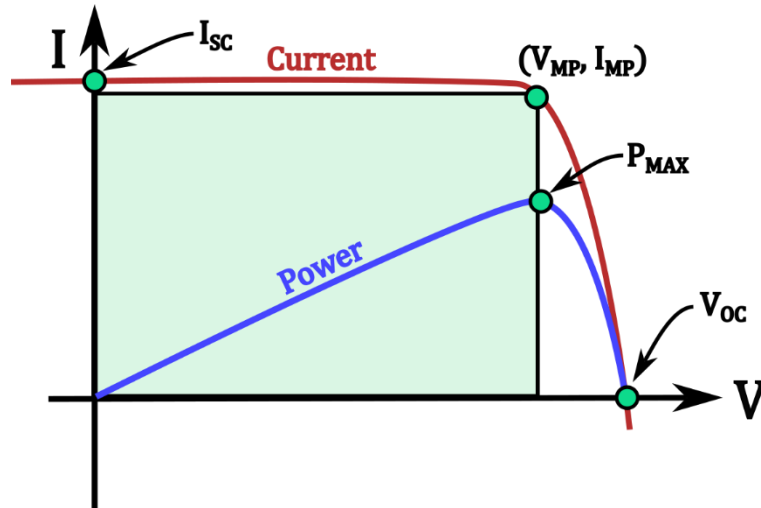


Figure 8. Solar cell I-V characteristic with commonly adopted convention. The red line represents the current generated from the cell, whereas the blue curve shows the power. The green rectangle depicts the maximum power generated from the cell.

As can be seen from **Figure 8.**, the values of V_{OC} and V_{MP} , as well as I_{SC} and I_{MP} are different. To estimate this deviation, the *fill factor* (FF) is defined, which describes the squareness of the I-V curve:

$$FF = \frac{I_{MP} V_{MP}}{I_{SC} V_{OC}}. \quad (6)$$

The closer to 1 FF is, the better performance the cell presents. However, this optimal value is always approached but never reached. Exceptional, state-of-the-art cells have FF above 0.8 [41], whereas values of 0.7 and below are presented by emerging technologies that suffer from unoptimized manufacturing processes [42]. Given the input power (P_{IN}) is known, we may now calculate the final efficiency of the cell which is defined as:

$$\eta = \frac{I_{SC} V_{OC}}{P_{IN}} \times FF. \quad (7)$$

The above-stated parameters are vastly used for every solar cell, regardless of the technology, providing all the essential information about the solar cell performance.

1.3.1. Effects of parasitic resistances

The fill factor highly influences the final efficiency of the cell. Its value depends on many factors, that are commonly related to the internal resistance of the cell [43].

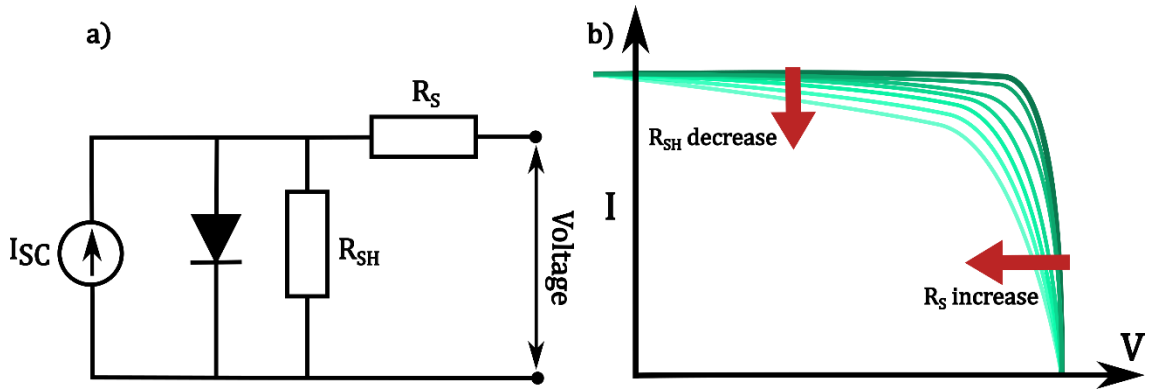


Figure 9. Real solar cell behaviour. a) equivalent circuit depicting series and parallel (shunt) resistances b) resistance influence on the I-V characteristic. Parasitic resistances cause a severe decrease in the fill factor of the cell and thus the maximum power generated.

Usually, one cell with a parallel and a series resistance model is employed to simulate the behaviour of the system. The equivalent circuit of the solar cell is presented in **Figure 9**. Applying Kirchhoff law to this circuit, we have the following equation for current:

$$I(V) = I_L - I_0 \exp\left(\frac{q(V + IR_S)}{k_B T}\right) - \frac{V + IR_S}{R_{SH}}, \quad (8)$$

where R_S and R_{SH} are series and shunt resistance respectively.

Note that the above expressions are helpful while estimating them having empirical data collected. **Equation (8)** is a transcendental one and can be solved only using either the Lambert W-function approach or some numerical approximation [44-47]. Resistive parameters can be estimated empirically by calculating the derivatives based on the measured I-V curve, using the following relations:

$$\begin{aligned}\frac{1}{R_S} &= -\left(\frac{\partial I}{\partial V}\right)_{V=V_{OC}} \\ \frac{1}{R_{SH}} &= -\left(\frac{\partial I}{\partial V}\right)_{V=0}\end{aligned}\quad (9)$$

Series resistance originates for example from the voltage drop outside the p-n junction, potentially arising from imperfect contacts between the interfaces of the involved layers both of semiconductor and metal. Also, it is associated with the intrinsic resistance of the materials in the junction. The series resistance within the solar cell is an unavoidable phenomenon and its excessive value causes a significant decrease in FF . Shunting resistance on the other hand comes from the manufacturing imperfections and defects that create alternative current pathways due to short-circuit sites within the cell. Those small short-circuit points reduce the current flow through the junction, inducing a decrease in generated voltage and the general distortion in the I-V curve that as a result shifts V_{MP} toward lower voltages. In the ideal diode model, the series resistance should be as low as possible, whereas the shunt resistance as high as possible.

1.3.2. Solar spectrum mismatch

The solar spectrum recorded in the space outside the Earth's atmosphere (AM0) very much resembles an ideal blackbody radiation at around 5800 K, shown in **Figure 10**. Due to the absorption and scattering in the atmosphere, we observe several downfalls in the spectrum, mostly in the near and middle IR range. Those decreases are associated with the vibrational energy spectrum of oxygen molecules (at 760 nm wavelength), H₂O vapour (1125 nm and 1800 nm), and CO₂ (at 2000 nm wavelength). In order to standardize the efficiency results obtained in laboratories around the world, the AM1.5G spectrum was introduced [48]. The spectrum is defined as a solar spectrum recorded at 48.2° of zenith angle which is associated with 1.5 value of the equatorial air mass that light has to travel through to reach the surface. The spectrum is used as the benchmark in the majority of the photovoltaic scientific literature, therefore this dissertation adopts this standard as well.

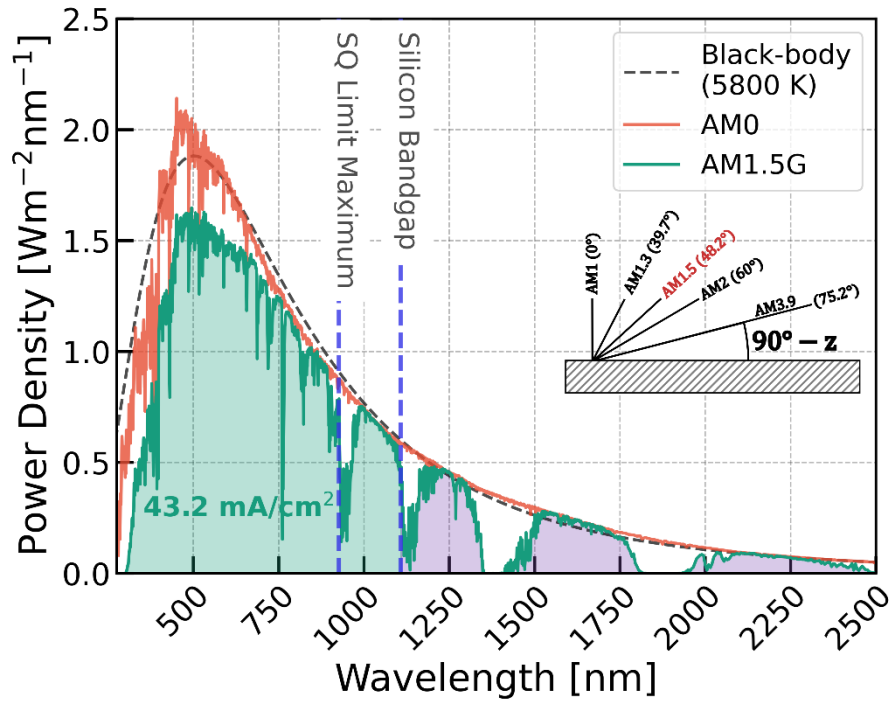


Figure 10 Solar spectrum power density measured at different atmospheric conditions. The inset shows the air mass vs. geographical latitude (z). The dotted curve represents the calculated black-body radiation, the red curve is the spectrum registered in the space, whereas the green curve is the AM1.5G standard spectrum commonly referenced in the literature. Two vertical lines represent wavelengths of the Shockley-Queisser limit for single junction solar cell and silicon bandgap with maximum current density available. Data provided by NREL [49]. The inset scheme represents the relationship between zenith angle and air mass.

The recorded solar spectrum intensity varies at different geographical latitudes and seasons, giving rise to a wide-ranging diversity in the yearly irradiation. As shown in **Figure 11**, the highest levels of irradiation are recorded in the subtropics zone, followed by the tropics and temperature zones. In Europe, the Sun on average irradiates the surface with an energy density equal to 4 kWh/m² each day. Solar cells are supposed to harvest as much solar energy as possible, which demands careful investigation of the cell operation under actual solar spectrum illumination.

As previously discussed, the photogeneration of the carrier takes place only when the incident photon has higher energy than the bandgap in the active layer. That means that the light with energies below the bandgap is going to be lost due to very little absorption of the cell. However, lowering the bandgap does not result in an endless increase in the current generation.

DIRECT NORMAL IRRADIATION

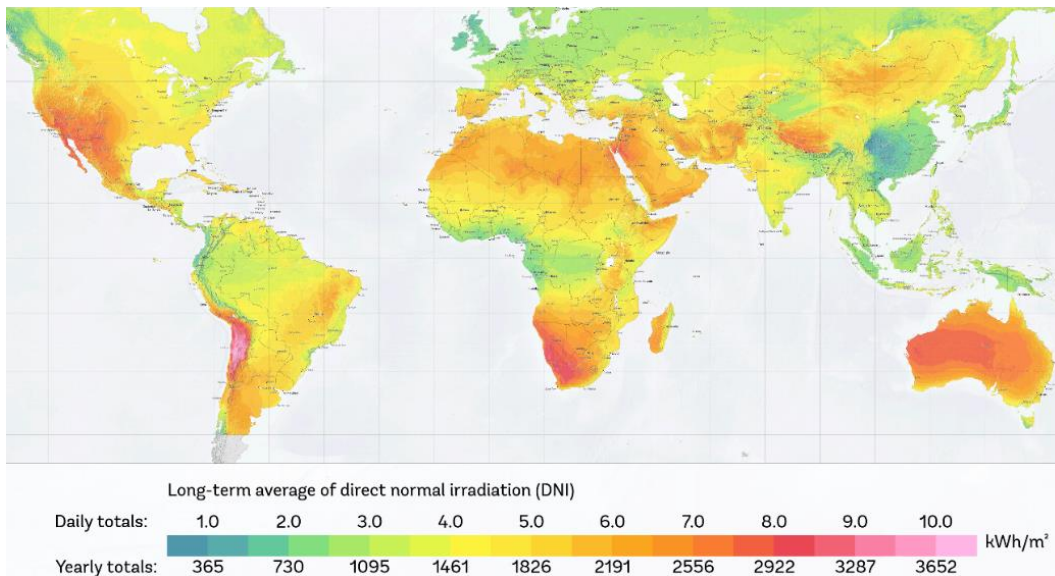


Figure 11. Solar irradiation world map. The scale shows differences in the yearly kWh/m² solar energy at different locations. Provided by [50] and further adapted.

This is due to the phenomenon whereby the photon energy above the bandgap is transformed into lattice vibrations, i.e. heating of the system. Therefore, a carefully investigated balance between those two effects must be established to find the best energy bandgap value. The maximum achievable efficiency within a single bandgap solar cell was calculated by Shockley and Queisser (so-called the Shockley-Queisser limit, or simply *SQ limit*) [51,52]. This limit is derived based on the black-body radiation spectrum and the statistics of photogenerated carriers in the p-n junction. According to it, the maximum efficiency that can be achieved for a single solar cell is around 31%. Later on, the model used in the calculations was expanded to include more parameters (such as reflection losses and the AM1.5G spectrum illumination), which currently holds an efficiency limit equal to 32.5% or 33.7% [53,54], depending on the model employed. **Figure 12** illustrates the correlation between solar cell bandgap and the highest achievable efficiency.

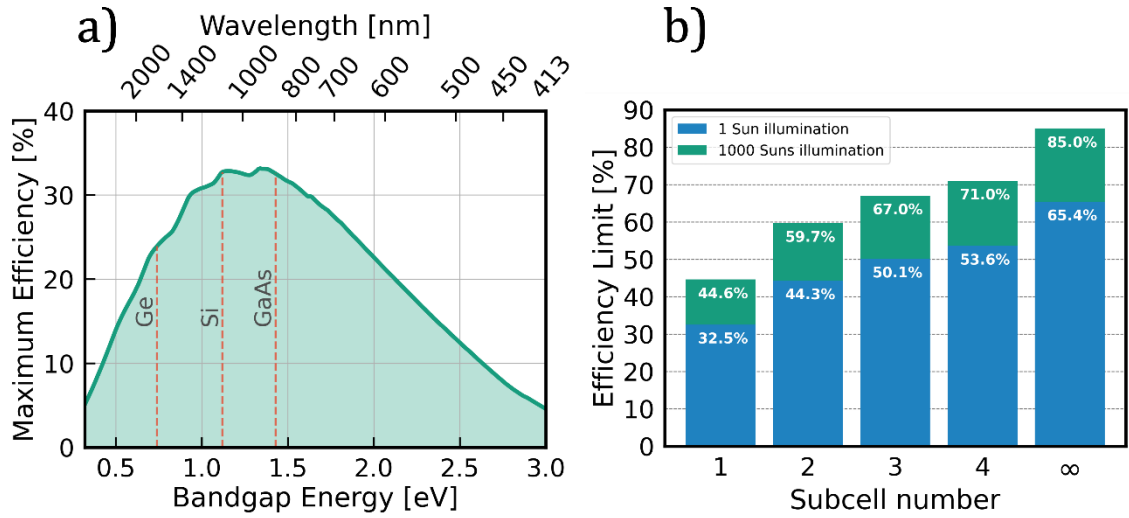


Figure 12. Efficiency limits for selected solar cells. a) Schockley-Queisser limit for single junction cell with a given bandgap energy. Vertical lines show some selected semiconductors bandgap used in the industry. **b)** Calculated efficiency limit for single and multijunction cells, up to the theoretical infinite material stack. The green bar represents the 1000 sun concentration condition which further lifts the limit. Data provided by [53,54]

This limit can be further extended for systems with two, three, or more subcells, up to a theoretical infinitely long stack of materials with varying bandgap [55]. Despite introducing additional subcells to the system, there still exists an unsurpassable efficiency value equal to 85% due to the thermodynamical limits (**Figure 12b**). Besides the final efficiency, we may also estimate the maximum current density (J_{sc}) generated from the cell that depends on the energy bandgap of the active layer. The exact formula for J_{sc} is given by:

$$J_{sc} = q \int_0^{\infty} A(\lambda) \Phi_{ph}^{AM1.5}(\lambda) d\lambda = q \int_0^{\lambda_{max}} \Phi_{ph}^{AM1.5}(\lambda) d\lambda, \quad (10)$$

where q is the elementary charge, $A(\lambda)$ is the absorbance of the cell stating which part of the light at the given wavelength is transformed to the current and $\Phi_{ph}^{AM1.5}(\lambda)$ is the photon flux of the standard AM1.5 solar spectrum. In the ideal solar cell scenario, $A(\lambda)$ is equal to 1 for every wavelength with energies above the bandgap of the solar cell absorber, which as a result gives the maximum current density generated from the cell with the given bandgap. For the silicon solar cell, the maximum current density is equal to 43.2 mA/cm².

1.3.3. Optical losses

Similarly to the resistance losses, all real cells suffer from optical losses related to two main effects:

- Non-ideal absorption characteristics result in ineffective photons harvesting inside the active layer and outcoupling of the light.
- Reflection losses occur at different parts in the cell: at the top of the cell, before reaching the absorber, at the bottom of the cell where the light is reflected outside the cell, or at any interface within the system.

The first effect is related to the absorption coefficient function of the used semiconducting material. Semiconductors exhibit very low absorption for energies below their bandgap energy, therefore the effective penetration depth of the light quickly gets orders of magnitude bigger than the active layer thickness, resulting in a low number of photogenerated carriers. Usually, the silicon cells have a thickness of around 300 μm , yet due to this effect, most photons with wavelengths above 1100 nm are lost. Exemplary materials and their penetration depths for a given wavelength are shown in **Figure 13**. The lower the bandgap of the semiconductor, the greater part of sunlight is absorbed, nevertheless, some energy is lost due to thermalization processes. Direct bandgap semiconductors exhibit very high absorption coefficients above the bandgap, thus they are perfect for forming efficient solar cells with the low thickness of the absorber at around 500 nm.

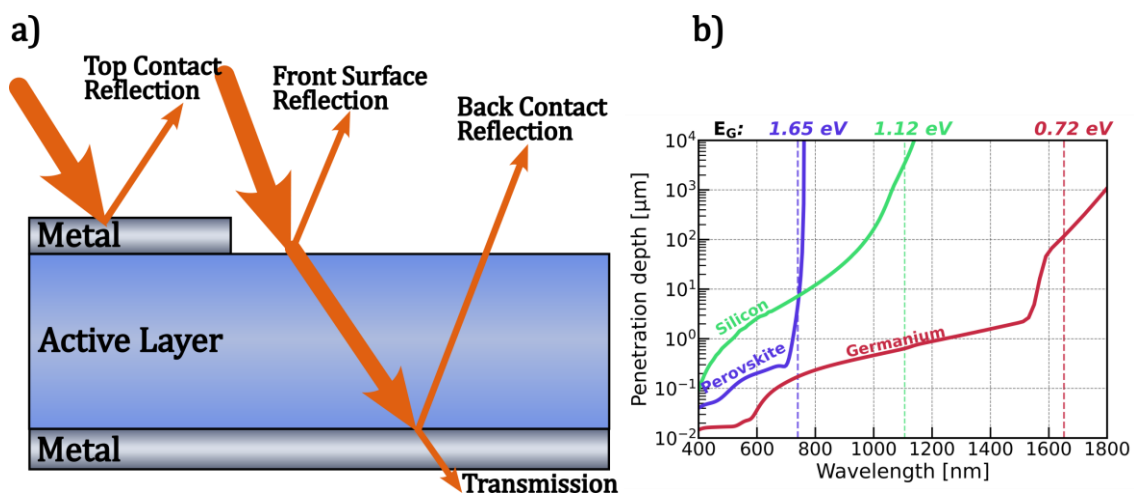


Figure 13. Sketch of optical losses inside the solar cell. a) Sources of the reflection loss at different parts of the cell. **b)** Penetration depth for selected semiconductors with varying bandgap values. n-k data provided by [56]

The second factor is related to reflection losses manifesting at the interfaces within the system, with the most pronounced reflections occurring at the top and the bottom surfaces of the cell. Those losses mainly stem from the unmatched refractive indices of the top layer and the absorber, as well as the metallic contact layers present in the cell. If not appropriately addressed, this issue may grow to the most significant loss factor. For instance, a bare, polished silicon wafer reflects around 30% of the sunlight.

All the aforementioned effects: parasitic resistance, spectral mismatch, and optical losses result in the inability to reach maximum efficiencies. Throughout the history of development in photovoltaics, there have been many attempts to mitigate those losses and propose diverse concepts for achieving optimal solar light harvesting. All these concepts collectively constitute the light management strategy for the photovoltaic system, which is one of the main focal points of this thesis.

1.4. Generations of solar cells

Solar cell technology has undergone an impressive evolution over the past few decades. The first solar cells were developed in 1940', and started with a conversion efficiency of around 1% - 2% with notable progress made in 1955 when an 11% efficiency solar cell was made [57]. Recent advances have improved the efficiency to a staggering value of 48%, achieved by small-scale solar cells [58]. The differences in their architectures led to a natural distinction into three main generations of the solar cells:

- First generation: mono- and poly-silicon solar cells
- Second generation: thin-films materials and multijunction III-V cells
- Third generation: concentrator cells, organic, dye-synthesized, and perovskite absorbers

Figure 14 presents the evolution of maximum efficiencies achieved by the selected technologies throughout the last two decades. The horizontal red line indicates the Auger-constrained limit as a practical maximum for single junction cell efficiency [59-61]. Efficiencies above 30% can be reached only using two or more junction architectures, that use multiple semiconductor absorbers to capture a wider range of the solar spectrum. Despite a rapid development regarding novel concepts, such as multijunction devices, thin-films, or perovskites; silicon solar cells continue to dominate the market with 95% shares in 2023, leaving just 5% for thin-

films technologies, specifically CdTe and CIGS [62]. This dominance is mainly due to the well-established production process, contrary to a very preliminary industrial ecosystem of the other technologies.

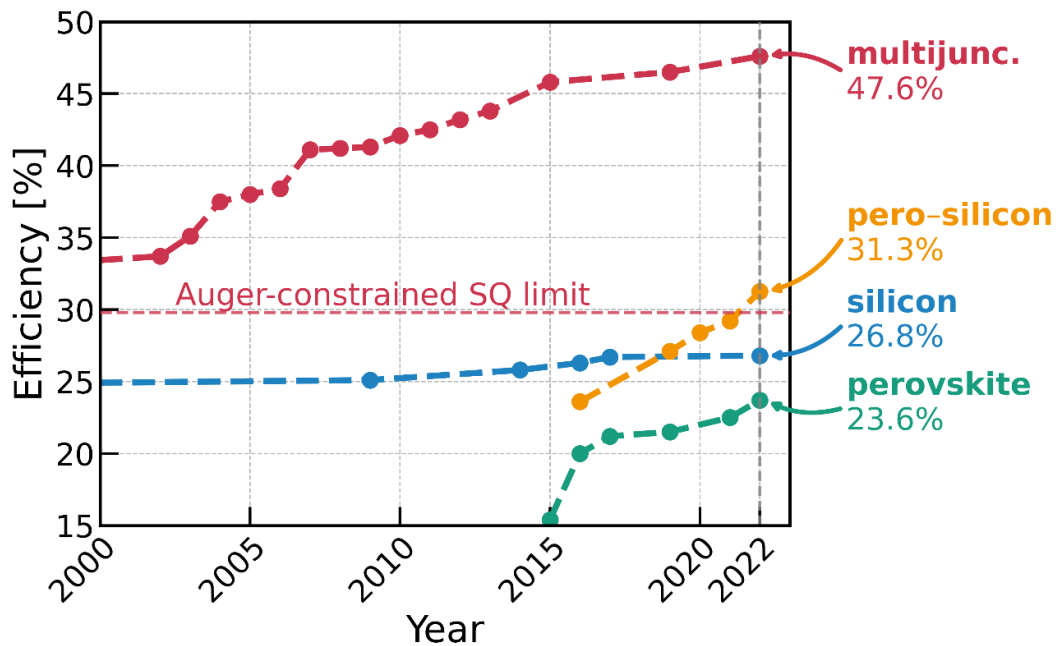


Figure 14. Current Maximum Efficiencies achieved by different photovoltaic technologies. The horizontal line depicts the Auger-constrained Schockley-Queisser limit for single junction cells under the 1.5 AM spectrum. Data provided by: NREL [63].

1.4.1. First generation: silicon solar cells

Silicon solar cells either mono or polycrystalline constitute the first generation of solar cells, being the most widespread technology so far. The silicon solar cell scheme is shown in **Figure 15**. It consists of a texturized silicon p-n homojunction and additional antireflective coating (ARC) sandwiched between metallic contact layers. Cells with this architecture were also the first to demonstrate a practically working device, around 70 years ago, therefore it is also the most mature technology. Despite its pioneering status, throughout the last 30 years of advancement, this architecture has gained only a modest 3% improvement: from 24% in 2000 to 26.8% in 2023. This efficiency enhancement relies mainly on advancements in cell doping and light management strategy optimization [64,65].

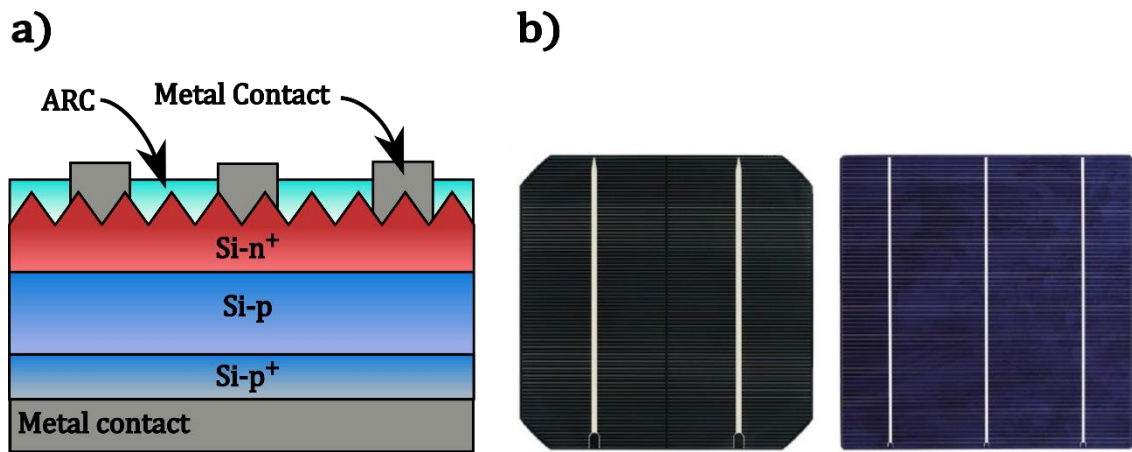


Figure 15. Silicon solar cell. a) Sketch of the cross-section with the anti-reflective, texturized coating indicated. b) Real image of two types of solar cells: left – monocrystalline module and right – polycrystalline module with flakes of crystals visible. Module image provided by [66].

As current silicon solar cells are approaching the Auger-constrained SQ limit, novel concepts are expected to be proposed and widespread. Also, another deficiency related to silicon cells lies in their indirect bandgap and low absorption coefficient, which involve a high thickness of the wafer of about 300 μm . Despite this limitation, the silicon cells are relatively affordable, and durable and utilize a well-established technology. Consequently, it has acquired dominance within the contemporary photovoltaic market.

1.4.2. Second generation: thin-films solar cells

To address the issue of the low absorption coefficient of silicon, thin-films solar cell technology was introduced. Materials used in thin-films solar cells are characterized by the direct bandgap, assuring excellent absorption abilities that enable layers as thin as 400 nm to effectively absorb all the light above the bandgap [67-69]. This approach helps to limit the material usage and in result immensely reduce the production costs. Second generation solar cells include materials such as cadmium telluride (CdTe), copper indium gallium selenide (CIGS), gallium arsenide (GaAs), and amorphous silicon (a-Si). Those materials can be grown by established deposition techniques such as chemical vapour deposition, sputtering, or spin-coating [70,71]. **Figure 16** presents a typical scheme of the thin film solar cell. The main difference is the presence of a transparent conductive oxide (TCO)

layer atop the cell. The TCO layer serves a dual purpose: allows for high transmission of light to the active layer and effective collection of photogenerated carriers.

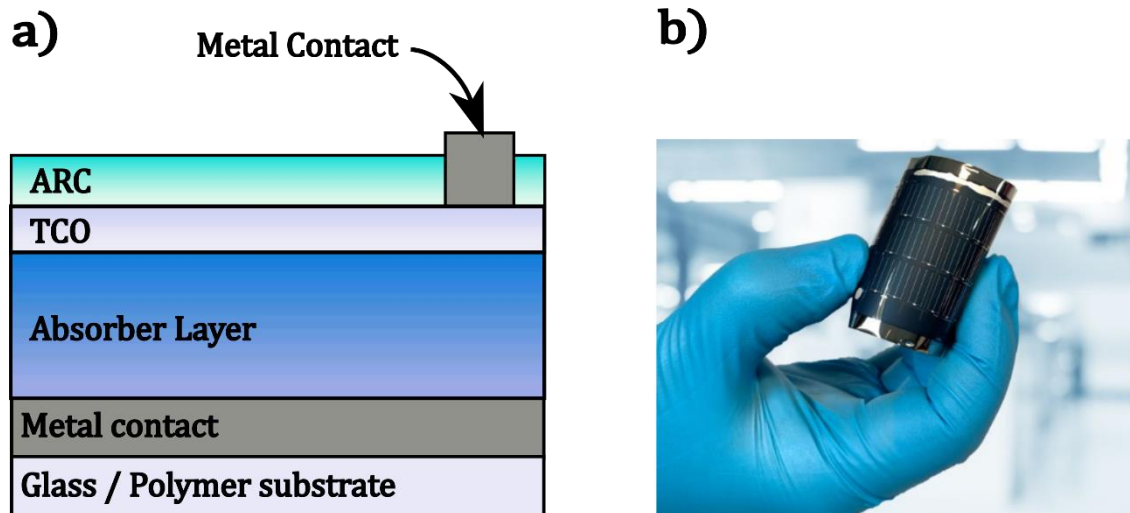


Figure 16. Thin film solar cell. a) Sketch of the cross-section. Note the presence of the transparent conductive oxide layer. **b)** A real photo of an exemplary thin film solar cell (CIGS) with the flexibility of the panel indicated. CIGS cell image provided by [72].

The manufacturing process for thin-film cells is similar to the widespread semiconductor production line for photodetectors, sensors, etc. Besides, two or more semiconducting materials can be joined together, creating a multijunction system with a detailedly tailored bandgap to assert maximum light harvest [73,74]. For instance, the epitaxial, 4-junction devices offer unraveled efficiencies, currently reaching 47.6% featuring four semiconducting materials with varying bandgap energies. However, the manufacture involves many step-processes which highly elevate the costs of the device. Therefore, those cells occupy a marginal share of the market, usually finding application in specific domains, where the high-efficiency demand outweighs the cost involved in the production (space, military, and aviation industries [75]). On the other hand, single junction thin-film solar cells such as CIGS or amorphous silicon still suffer from low efficiencies, prohibiting their global widespread.

1.4.3. Third Generation: emerging technologies

Third generation photovoltaics proposes new absorbers such as organic compounds (OSC) and perovskites (PSC), fabricated using very simple methods, such as spin coating or spray-coating. Those materials combine very good absorption properties with cost-effective manufacturing. Also, third generation photovoltaics delves into novel concepts regarding concentrating lenses [76,77], semitransparent materials, dye-sensitized cells [78,79] and up- or down-converting particles [80,81].

The third generation photovoltaic promises to surpass the SQ limit for single junction cells, while maintaining very competitive costs and systems. One of the foremost candidates for this purpose are the cells utilizing perovskite crystal structure as the absorber, commonly abbreviated to perovskite cells. The device scheme is shown in **Figure 17**, along with a typical elementary cell of the perovskite.

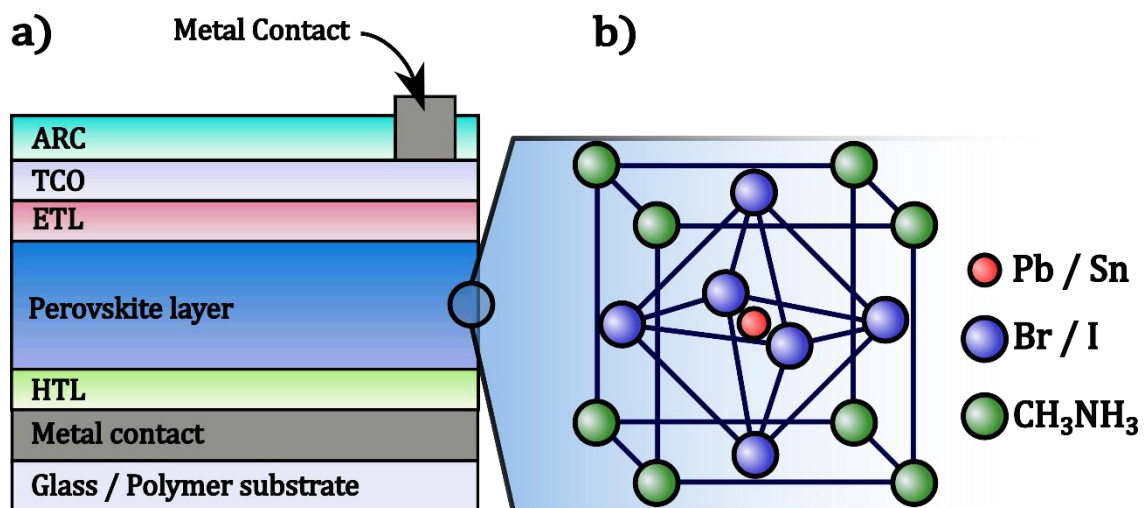


Figure 17. Perovskite solar cell scheme. a) Sketch of the cross-section. **b)** Typical perovskite crystal structure employed for photovoltaics applications.

Since their recognition for photovoltaic application, a very dynamic efficiency growth has been observed, currently equal to almost 24%, only 2% below the silicon cell record. Besides the competitive efficiency, perovskites exhibit an exceptional bandgap tunability, making them a perfect complement for silicon cells by forming tandem structures, currently surpassing Auger constrained SQ limit.

Figure 18 presents the standard energy level diagram of a perovskite cell, comprising the absorber layer with adjacent hole and electron transport layers

(HTL and ETL respectively). These layers enable the separation and transport of the photogenerated charges. Perovskite's general formula is described as ABX_3 with the structure of calcium titanate. Perovskites constitute a broad family of materials, however for the photovoltaic application, the most prominent subclass is the organic-inorganic hybrid material which consists of:

- A-site: methylammonium ($CH_3NH_3^+$ or abbreviated MA^+) or formamidinium ($CH_3(NH_2)_2^+$ or abbreviated FA^+),
- B-site: a divalent metal cation (Sn^{2+} or Pb^{2+}),
- X-site: monovalent halide anion (Cl^- , Br^- , I^-).

The cations inside the perovskite structure can be substituted and non-stoichiometrically mixed, creating a vast family of materials with exceptional tunability of optoelectronic properties, including light energy emission, bandgap engineering [82] as well as the occurrence of non-linear optics phenomena [83]. **Figure 18b** depicts the photoluminescence emission energy redshifting when various ions, such as Pb^{2+} , Cl^- , I^- or Sn^{2+} are incorporated in the MA^+ perovskite structure. In recent times, perovskites have been comprehensively examined, mostly attributed to their great efficiency growth from just around 3.8% in 2009 [84] to almost 25%. Furthermore, they exhibit other intriguing phenomena, streamlining the arrival of the new era of optoelectronic devices.

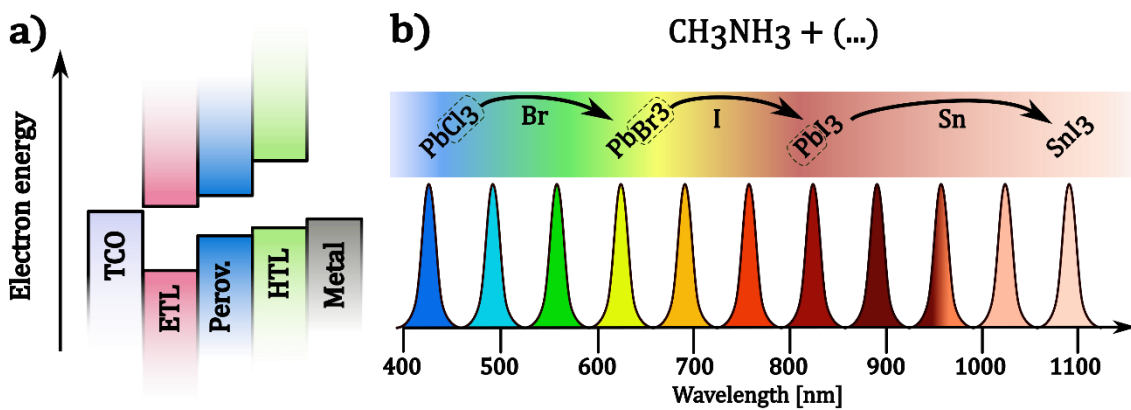


Figure 18 Perovskite cell energy diagram and bandgap tunability. a) Energy levels in an exemplary perovskite cell. Electrons due to the band energy move toward the TCO layer, whereas holes are transported to the metal contact. **b)** Sketch of the emission spectra for the MA^+ perovskite, depending on the stoichiometry and type of the metal cations. The top panel schematically shows the lowering of the bandgap while substituting cations. Adapted and updated from [85,86].

Moreover, the MA⁺ and FA⁺ perovskites can be produced using very affordable and scalable techniques, involving spin-coating, doctor blade, and sputtering, all available at very moderate conditions. Yet, the primary challenge in wide-spreading perovskite solar cells lies in their long-term instability, which manifests itself in significantly faster degradation compared to their silicon-based counterparts. Substantial efforts are put into optimizing their composition to enhance their water and photodegradation resistance.

This dissertation mainly focuses on third-generation solar cells, specifically perovskite cells, and the novel concepts to enhance their efficiency.

CHAPTER 2.

Transparent Electrodes

2.1. Electrical and Optical Properties

The primary role of the transparent electrode, as the name suggests, revolves around the effective photogenerated carriers collection while maintaining transparency within the relevant wavelength range. In the case of solar cells, this entails alignment with the solar spectrum maximum falling within the 300 – 800 nm range. Therefore, the optimal material for this task should possess a rarely seen dual nature – exhibiting high transmission and as low as possible resistivity. These attributes are found particularly pronounced in the selected oxide materials, such as zinc oxide (ZnO), indium-tin oxide (ITO), and cadmium-tin oxide (CTO). These materials are mainly deposited using various techniques, including chemical vapour deposition and physical vapour deposition techniques, depending on the final desired properties. Besides, efficient carrier collection can be achieved not only by the planar oxide layers but also through more sophisticated systems, such as metallic nanowires or grids. Within this chapter, the key desired properties of such systems and state-of-the-art concepts are discussed.

2.1.1. Transmittance and reflection

Most transparent conductive electrodes are wideband gap semiconductors that exhibit high transmission within the relevant visible wavelength range. Since the relationship between transmission (T), reflection (R), and absorption (A) can be expressed through the formula:

$$T = 1 - R - A, \quad (11)$$

reflection and absorption are the key factors constituting the losses that should be minimized to the lowest possible level. Typically, transmission of the transparent

electrode exceeds 85% – 90% within the visible wavelength range. The reflection of a planar oxide approximately equals 10% due to the refractive index difference in reference to the surrounding medium and the adjacent layer within a solar cell. A plethora of concepts and management strategies have been proposed to optimize this value. Absorption in the case of the direct bandgap semiconductors starts to increase abruptly above the bandgap, emphasizing the vital importance of the bandgap value to assert high transmission, particularly in the blue and ultraviolet range. For the practical use of the material as a TCE, its bandgap should exceed 3 eV. The bandgap value is an inherent property of the material, however, it could be slightly tuned using doping or some posttreatment. Another parameter that significantly influences the optical performance is the thickness of the utilized transparent conductive layer. As the thickness increases, so does the absorption and depending on the interference conditions, also reflection, inducing losses in the optical transparency. **Figure 19** presents the transmission curves of ITO. There are schematically shown regions of reflection losses, fundamental absorption losses, and lattice vibration absorption in the infrared region. All those losses reduce the overall performance, demanding some optimization and mitigation strategies.

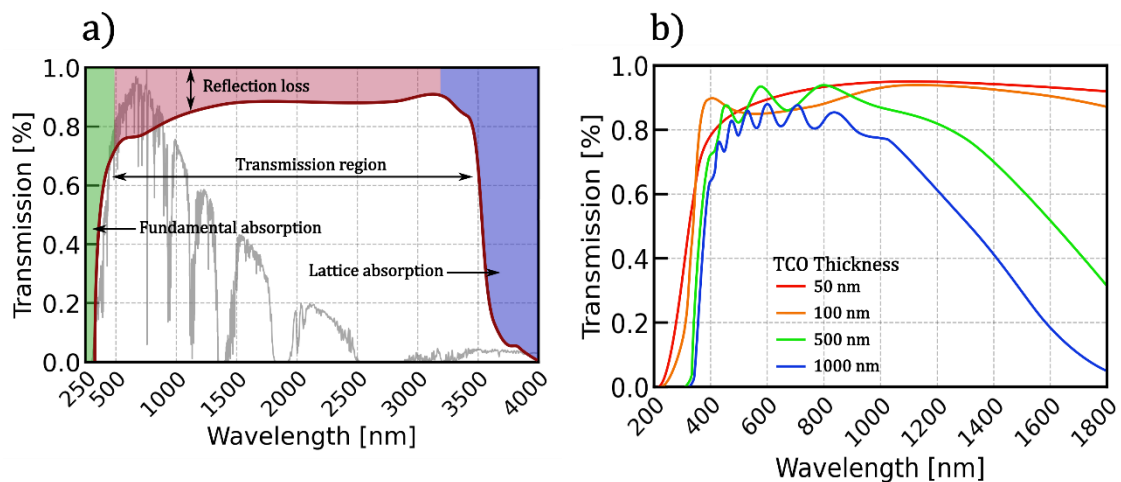


Figure 19. Optical properties of ITO thin film. **a)** Transmission spectra across the VIS-IR range of wavelengths alongside with AM1.5G spectrum. The reflection losses come mostly from refractive index mismatch. **b)** Transmission spectra showcasing varied thicknesses of an ITO thin film. As the thickness increases, the interference fringes along with a fast absorption in the IR range appear. The primary reason for the transmission attenuation is the electric permittivity falling below zero, resulting in metallic properties within this range. The transmission data was taken and visually adapted from [87].

The power flux of the solar spectrum reaches its maximum of approximately 600 nm, rendering the region around this wavelength the most significant.

Similarly, above 1800 nm wavelength, the power flux is becoming insignificant. Therefore the most relevant range lies between 400 – 1800 nm. Increasing the thin film thickness leads to the emergence of interference patterns and substantial absorption in the infrared range. Therefore, despite the enhanced conductivity of thicker layers, the thickness should be kept low to assert high transmission in the VIS-IR range.

2.1.2. Conductivity and Figure of Merit

Conductivity is a fundamental material property, that defines its electrical transport ability. It stems from the two basic parameters that the material can be described with: concentration of free carriers and their mobility. The formula for the conductivity, linking those properties is as follows:

$$\sigma = qn\mu, \quad (12)$$

where q – elementary charge, n – free charge carriers concentration, and μ – mobility of those charge carriers. Competitive conductivity requires sufficiently high values of both n and μ , aiming for a conductivity of at least 10^3 Scm^{-1} . These values are achievable for samples with very high carrier concentrations, exceeding 10^{19} cm^{-3} and mobility at least around $10 - 15 \text{ Vs/cm}^2$. These requirements heavily confine the pool of potentially appropriate materials to specific metal oxides, recently discovered and intensively studied 2D materials and metals. Increasing free carrier concentration density significantly affects the reflection and absorption of the light upon those carriers, leading to severe optical losses when the critical carrier density is reached. The reflection increase is induced by the screening of the electromagnetic field by the collective carrier movement (oscillation of the electron density). This effect prohibits the propagation of light within the material with frequencies lower than these collective oscillations. This oscillation frequency, known as the plasma frequency (ω_p), fundamentally describes the frequency threshold above which, the reflectance of the material approaches 1. The plasma frequency is expressed as follows:

$$\omega_p = \sqrt{\frac{nq^2}{\epsilon_0 m^*}}, \quad (13)$$

where ϵ_0 – the vacuum electrical permittivity, m^* – the effective mass of the charge carrier. **Figure 20** presents the reflectivity spectra of different materials with varying free carrier densities. As seen, the reflected wavelengths threshold is blue-shifted with increasing free carrier density up to the point where the whole visible spectrum is reflected as in the Al and Ag cases. Materials displaying plasma frequencies acceptable for transparent electrode application, exhibit carrier density around $10^{20} - 10^{21} \text{ cm}^{-3}$ and high reflectivity above 1400 nm wavelength.

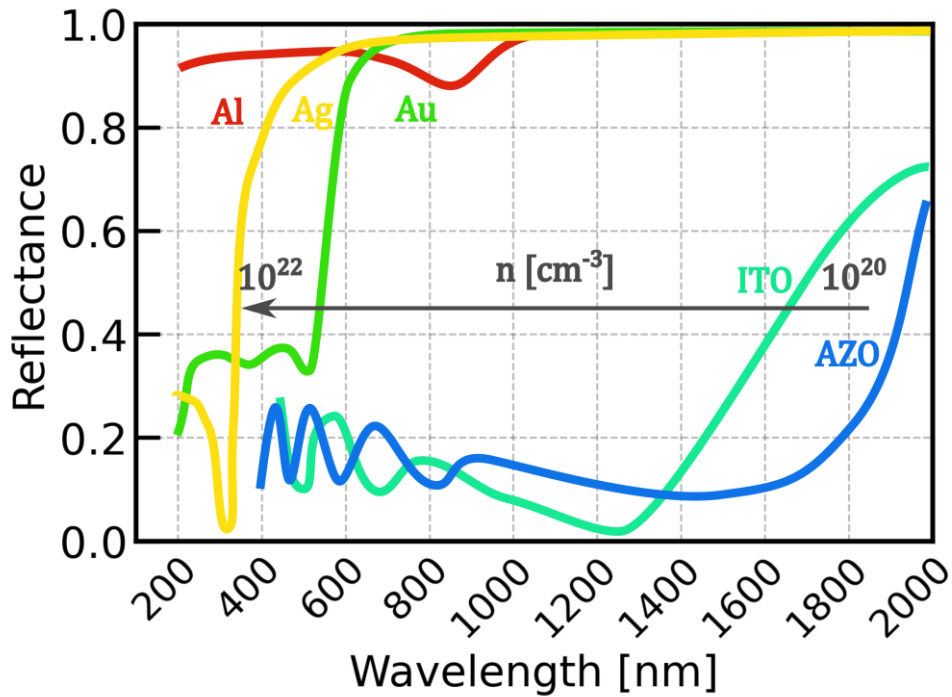


Figure 20. Reflectance alteration due to the different plasma frequencies in the selected, highly conductive materials. As seen, metals exhibit one order of magnitude more free carriers, yet they become highly reflective in the visible range.

ITO is currently the most widely used as a TCE for its superior electrical parameters and high transmittance. However, its scarcity elevates the production costs [88], inevitably limiting the economical feasibility of utilization of this material beyond multiple square kilometres scale. Therefore, there is an ongoing effort to optimize and introduce new concepts for transparent electrode application. While metals exhibit the best electrical conductivity across all the listed materials, they suffer from very high reflectivity, limiting their performance as transparent electrodes. Therefore, several, more advanced concepts trying to incorporate metals into the system, mitigating the losses stemming from their optical properties, have been proposed. **Table 1** displays the electrical parameters

of some of the commonly used materials as transparent electrodes such as metal oxides and metals.

Table 1. Electrical parameters (carrier concentration, mobility and resistivity) of the grown TCO samples with varying thicknesses and doping.

Material	T (avg.) [%]	n [10^{20} cm^{-3}]	μ [cm^2/Vs]	ρ [$\times 10^{-4} \Omega\text{cm}$]
<i>ITO</i>	86.3	1 – 10	20 – 80	2 – 8
<i>ZnO</i>	87.9	2 – 5	20 – 80	8
<i>SnO₂</i>	84.0	2 – 10	20 – 60	2 – 8
<i>Ag</i>	-	600	10 – 50	0.16
<i>Al</i>	-	2000	10 – 50	0.26

As the final performance of the material combines two essential properties: electrical conductivity and transmission, the metric that takes into account those attributes is introduced. One of the figures of merit, introduced by Haacke [89], simply interlinks the two fundamental parameters in the following form:

$$\Phi_H = \frac{T^c}{R_S}, \quad (14)$$

where T is the average transmission and R_S sheet resistance of the sample. The c exponent term determines the extent to which transmission is weighted to emphasize the detrimental effects of the absorption and reflection, present in the sample. Usually, c equal to 10 is used to introduce a substantial penalty for the transmission loss which severely decreases the figure of merit value when the sample exhibits average transmission below 85%. There have been proposed other figures of merits with more complicated formulas, involving the current density generated by the cell or more sophisticated parameters [90,91]. Those approaches are however much more complex, require more than direct measurements of transmission and resistance and in principle are aimed at more specific applications. **Equation (10)** is commonly used in practical scenarios, especially in assessing photovoltaic performance and is adopted throughout this thesis.

2.2. Performance improvement strategies

2.2.1. Thin layer interference

The light management strategies are crucial to further elevate the collection of photons within the system, mainly by reducing the reflection losses from the surface and the optical path enhancement in the active layer. One commonly employed method, proposed in numerous other applications, involves the single or multilayer antireflective planar layer coating. The main objectives of this coating are to match the refractive indices between the environment and the underlying TCE material and engineer such a stack that meets the criteria for destructive interference, thus suppressing the reflected waves. The first goal is achieved by adhering to the well-known formulas regarding the optimal refractive index (n_{ARC}) and thickness (d_{ARC}) for a given λ_0 wavelength:

$$n_{ARC} = \sqrt{n_1 n_2} \quad (15)$$

$$d_{ARC} = \frac{\lambda_0}{4n_{ARC}}. \quad (16)$$

This simple and effective approach has however a significant limitation, which is the tuning for the specific wavelength, leading to marginal improvement or even worsening within the remaining spectrum range. This scenario appears when the matching refractive index criteria lean towards constructive interference, increasing reflectance for the specific spectral range. To overcome this limitation, coatings consisting of multiple layers can be employed to match the refractive index closer, leading to smoother interface transitions and simultaneously adjusting the destructive interference conditions. The solution to this problem requires a computational approach such as the transfer matrices method applied [92] to find the best-performing thicknesses and refractive index combination. **Figure 21** presents the optical stack consisting of one and three antireflective layers along with the transfer matrix method simulations.

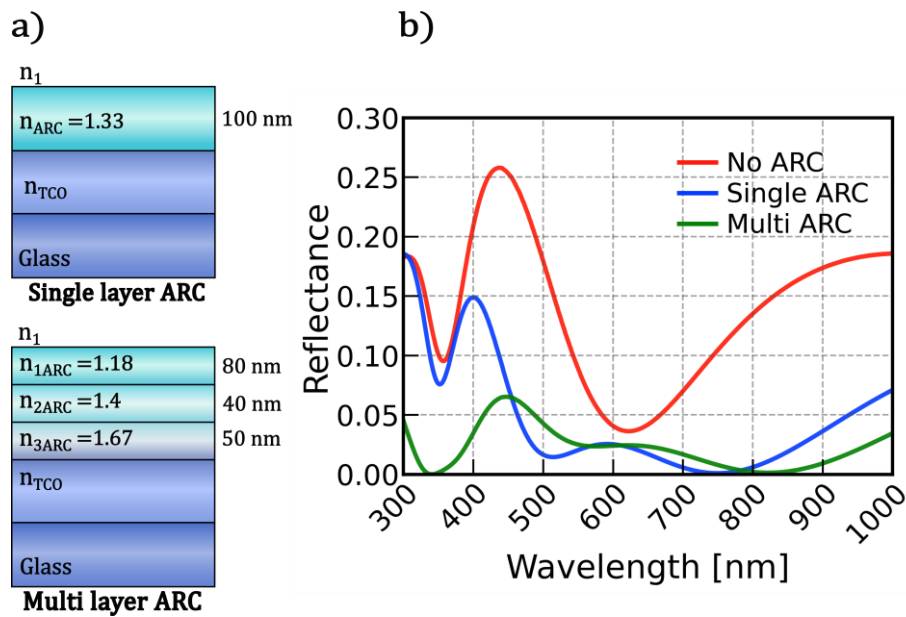


Figure 21. Planar layered antireflective coatings. a) A schematic drawing of a single and multi-layer antireflective coating placed on a glass substrate. **b)** Reflectance spectra of the systems. Multilayer antireflective coatings can further improve the transmission properties of the system, thus they involve more sophisticated structures, planning, and available materials.

Although the samples with a multilayer approach demonstrate high antireflective performance, they demand more computational and manufacturing effort, and in certain scenarios, tuning the stack for a wide wavelength range may pose a challenge. As depicted in **Figure 21**, introducing additional index-matched interfaces results in improvement compared to single-layer systems, however in certain regions, the reflectance is increased due to varied constructive interference conditions. Thus, this approach has its limitations, and beyond a certain number of layers, further complicating the structure might not yield noticeable benefits. Moreover, the planar layers do not substantially enhance the optical path length within the system, as the light enters into deeper layers with very similar angular distribution, without much scattering or diffraction.

Another explored idea involves constructing a trilayer stack made of both transparent conductive oxide (O) and a very thin metal layer (M) arranged in a sandwich-like stack with an O-M-O sequence to minimize reflection and increase the conductivity of such a composite material. Commonly exploited materials encompass ITO, SnO_2 , ZnO and their doped variations [93-96]. As for metals silver, copper, and gold are usually employed [97-102]. **Figure 22.** presents selected successful demonstrations of such systems along with their schematic drawings.

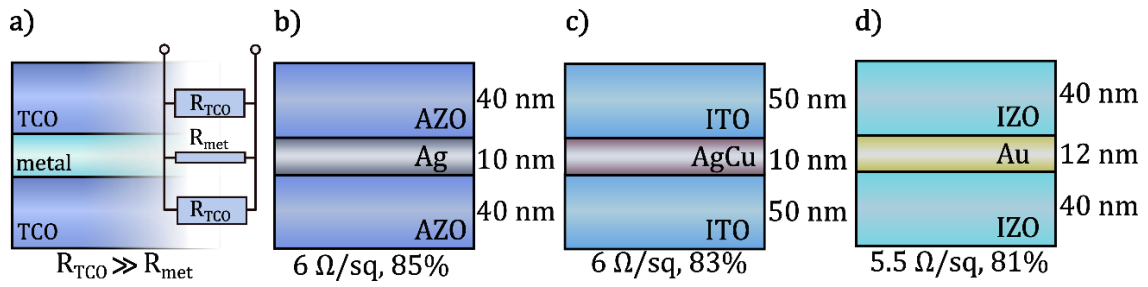


Figure 22. Selected TCO/metal/TCO optical stacks. a) The working principle of the TCO/metal/TCO electrode. The resistivity of the metal is much lower than the TCO part. Therefore, the preferred route for carriers runs through the thin metal layer. **b) – d)** Triple layer stacks with a variety of used oxides and metals. Below each stack, the achieved sheet resistance and average transmittance in the visible range are shown. Data taken from [103].

These stacks have shown promising results concerning both transmission and resistivity, suggesting a potential shift in the approach to TCEs. Besides the optoelectronic properties, there are arguments for this particular design over solely using ultrathin metal layers, mostly regarding the manufacturing ease. The composite electrode design enables ultrathin metal films deposition since mostly conductive oxides act as a wetting agent helping to deposit really thin layers below 10 nm. Also, such thin metal layers, tend to agglomerate into islands even after a few months of air exposure, hindering the conductivity of the layer [104]. Thus, such a sandwich arrangement helps to protect the structure of a metal thin film and facilitates the deposition of a continuous layer

For instance, in one of the pioneering works, M. Sawada [105] showed that the ITO/Ag/ITO triple layer stack demonstrates exceptionally low sheet resistance ($4.2 \Omega/\text{sq}$) retaining high transmittance (85%). However, their production demands more effort with thin layers of metal engineering with precisely defined thickness, adjusting wetting agents and dealing with the continuity of the films, which can be a challenging task, particularly when repeated several times within multilayer systems. As the transmission of the metal rapidly decreases with thicknesses above 6 – 8 nm, the high precision of the thickness control during the deposition is a critical condition. Furthermore, the metal atoms may diffuse over time into oxide layers, leading to degradation of the optoelectronic properties. This approach is further developed and investigated in **Section 4.4** using aluminium-doped zinc oxide (AZO) and silver multilayer stack.

2.2.2. Solutions beyond planar layers

A wide range of concepts aims to enhance conductivity and light management, which extend beyond planar layer approaches. A commonly explored idea involves silver nanowires randomly distributed across the surface. Silver's high conductivity and ease of large-scale manufacturing make such samples effective carrier collectors with low sheet resistance. However, shadow loss associated with the wires should be closely investigated to find the right balance between transmission and conductivity. **Figure 23** displays some prominent examples of this approach.

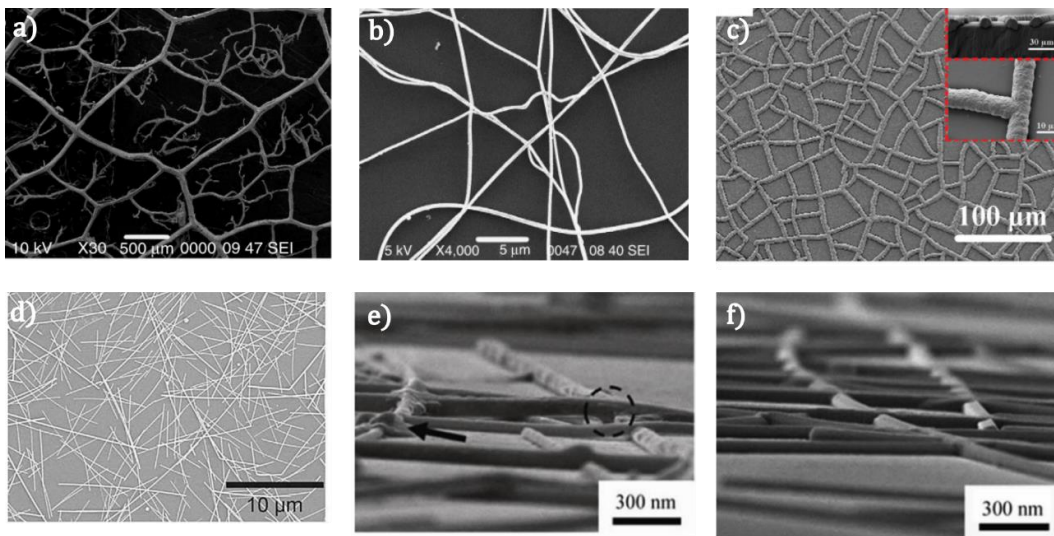


Figure 23 SEM images of silver nanowires transparent electrodes creating a randomly distributed conducting grid using a wide array of techniques. a) – b) Bioinspired patterns of imprinted leaf veins created by silver nanowires Image from [106], c) Percolating grid of silver ribbon network created with self-cracking technique. Image from [107] d) – f) Silver nanowires pattern with submicron thick silver lines. Image from [108]

For instance, Yu[109], Andres [110], and Leem [111] presented simple methods to manufacture randomly distributed silver nanowires samples with high figures of merit and sheet resistance reaching 6 – 10 Ω /sq, increasing the organic solar cells performance and allowing to be deposited on a flexible substrate.

More advanced concepts involve the structurization with the conductive lines, leading to a periodic, predefined arrangement. In this way, the main limitations of randomly distributed structure, such as excessive overlapping in certain areas and insufficient density in other regions are diminished. It allows for the precise definition of the desired structure and its subsequent evaluation and characterization. However, this method demands greater effort in the preparation

of the structures, relying on lithography techniques, which not only elevates costs but also creates risks of errors during the manufacturing process. Albeit, the realm of the structures that can find their place in these applications is still under thorough exploration. Mostly used structures are straight lines, rectangular grids or hexagons, exploring only a fraction of available geometries. **Figure 24** presents some of the proposed arrangements in the literature.

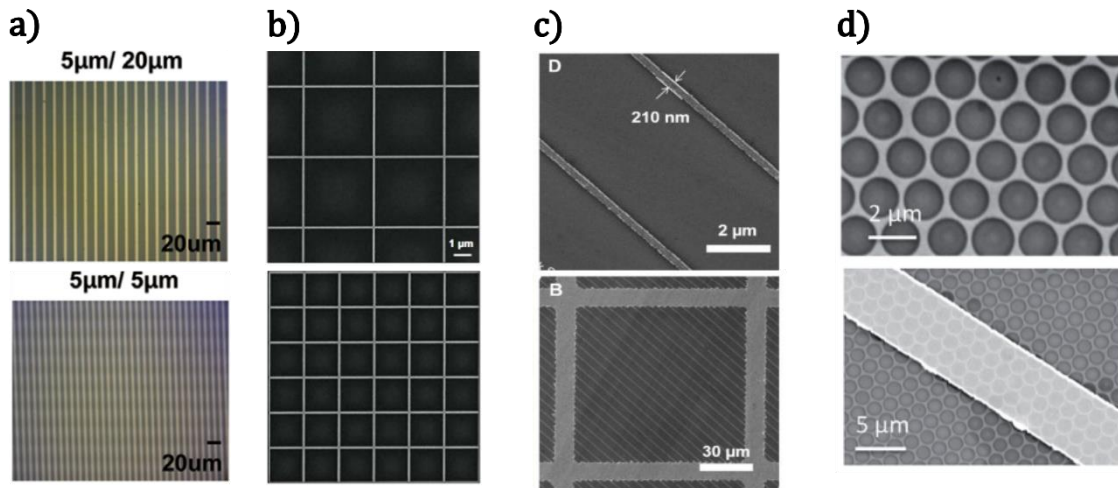


Figure 24. SEM images of periodic metallic structures, creating conductive patterns with a variety of shapes and configurations. a) Straight, parallel lines with different periods acting both as a conductor and diffractive gratings. Image from: [112] **b)** Rectangular grid with very thin conductive lines. Image from: [113] **c)** Hierarchical structure consisting of a square, hundreds of micrometer grid decorated with nanometer, diagonals crossing the meta structure. Image from: [114] **d)** Hexagonal grid decorated with metal nanomesh of hexagonal symmetry. Image from: [115]

These systems exhibit a conductivity comparable to metals with a competitive transmission of such systems since only a small fraction is covered by the metal. For instance, Gao [115] demonstrates a device with only $0.7 \Omega/\text{sq}$ sheet resistance and 81% transmission. Similarly, Hong [116] showcases a simple method of patterning silver thin films obtaining $9 \Omega/\text{sq}$ sheet resistance with over 92% transmission.

The metal grids, akin to nanowires introduce some shading losses. These can be minimized using an antireflective planar layer, showcased in **Section 2.2.1**, however, this approach does not efficiently address direct reflections from the metal structure, as it primarily serves for index matching purposes. The most sought-after systems should achieve both goals simultaneously by enhancing optical and electrical performance which renders a non-trivial engineering task. To meet those criteria, a more viable solution involves a multi-scattering antireflective texture to first scatter or diffuse the light, leading to a change in the angular

distribution of the incident light upon entering the active layer. Thus, the incoupling of the light is much more effective both in terms of reflective properties and optical path within the relevant segment of the cell. This asserts a very effective light harvesting with minimal reflection losses. This concept is extensively explored in the literature, **Figure 25** features some of the examples of such systems.

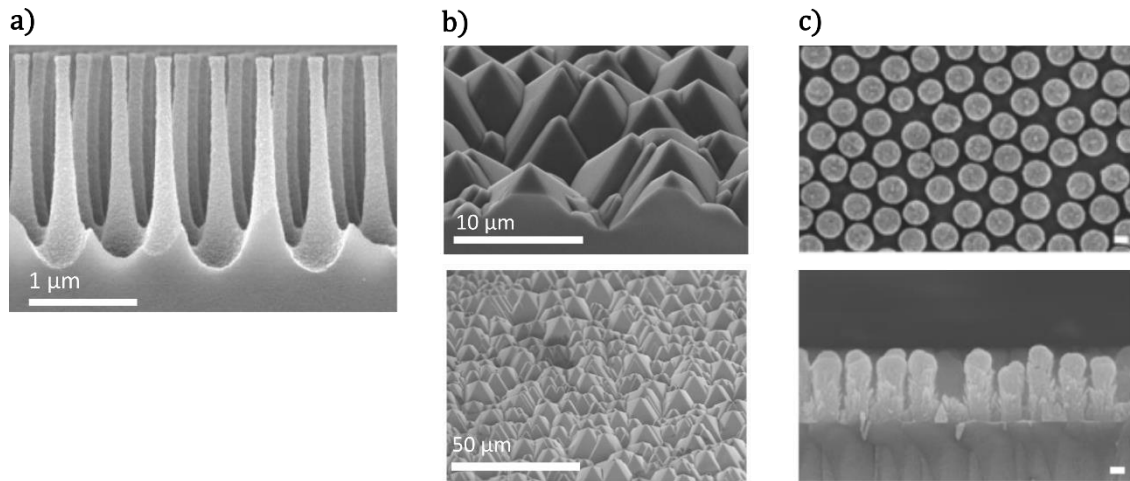


Figure 25. SEM images of antireflective textures for effective light incoupling. **a)** High-aspect ratio needle-like structure with a subwavelength period. Image from: [117] **b)** Micrometer-wide pyramidal shapes, used for reducing the reflection of the solar cell. Image from: [118] **c)** Tightly packed ZnO nanorod array, acting as a subwavelength antireflective structure. Image from: [119]

These systems can be manufactured using a variety of techniques including selective etching, photolithography, ion-reactive etching, bottom-up growth, or nanoimprint lithography. The wide range of available structures and manufacturing methods makes the selection of the right texture or structure a matter of elaborate simulations to optimize their performance for the given application. This considerable effort is rewarded with unparalleled antireflective optical properties of such structures. Moreover, these approaches enable further enhancement of absorption within the active layer, especially crucial for thin perovskite absorbers and silicon wafers in the IR region.

These more advanced concepts are the main point of focus within **CHAPTER 5.** and **CHAPTER 6.** and constitute the main research topic of this dissertation. These concepts are examined in detail to improve the performance of the solar cells.

CHAPTER 3.

Methodology

3.1. Atomic layer deposition

Atomic layer deposition (ALD) is a growth technique that enables the deposition of thin films of diverse materials from a vapour phase. It exhibits a few important features that render it advantageous over alternative, commonly employed deposition techniques such as chemical vapour deposition (CVD), molecular beam epitaxy (MBE), or physical vapour deposition (PVD). The electronic industry is evolving toward manufacturing sophisticatedly engineered nanometer structures such as Fin and Gate-All-Around Field Effect Transistors (finFET and GAAFET) that are manufactured through numerous photolithography, etching, metalization, and deposition cycles. Conducting all these steps results in an extremely complicated three-dimensional landscape, therefore the precise control and deposition over non-planar geometries play here a pivotal role. **Figure 26** illustrates the outcomes of the non-planar samples' growth mode using different deposition techniques. The sol-gel technique covers the samples from every angle, but it lacks precision in thickness control across the entire sample. In contrast, CVD and PVD are more directional techniques that cover specific parts of the sample, mostly the top, whereas the rest of the sample is either uncoated or coated insufficiently.

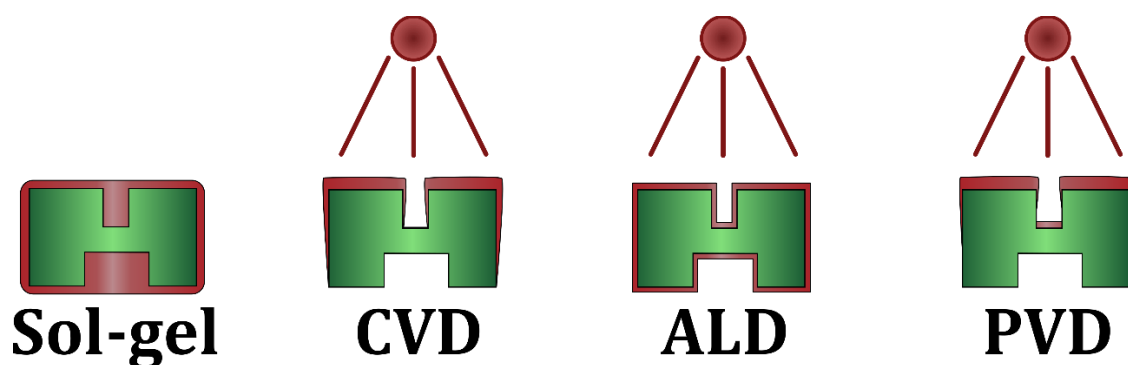


Figure 26. Various deposition techniques characteristics. During the deposition, different growth methods exhibit distinct results on texturized samples. ALD is characterized by a uniform deposition of different shapes, even with high aspect ratio geometry. Image inspired by [120].

ALD on the other hand provides precise control over the composition of deposited materials through a repetitive pulse and purge cycle in which precursor vapors penetrate the sample. Therefore, this technique allows for uniformly coated high-aspect ratio samples, which remain unreachable for sputtering techniques. ALD and its plasma-enhanced (PEALD) or spatial ALD (SALD) variants are employed to deposit a diverse range of dielectric and semiconductor materials, including oxides (e.g. ZnO, SnO, In₂O₃, CuO, Al₂O₃, HfO₂, MoO₃), sulfides (e.g. ZnS, MoS₂), nitrides (e.g. BN, AlN, GaN) and elements, metals in particular (e.g. Al, Co, Cu, Ag). **Figure 27** showcases notable applications and advancements in ALD. Currently, the ALD technique is employed in the mass production of the newest field effect transistors, LED, VSCEL, and many other nanostructure devices fabrication [121-126].

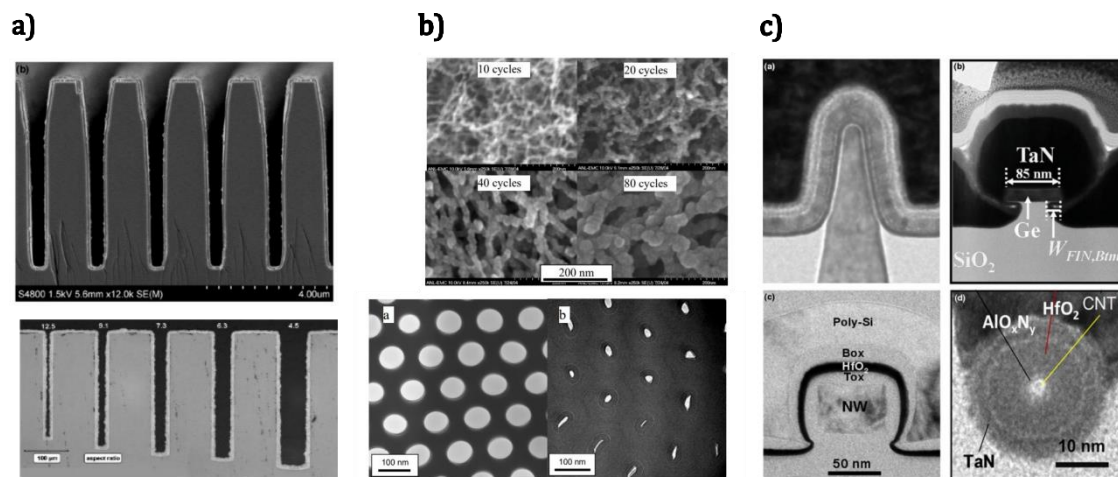


Figure 27. Selected literature examples of the ALD technique. a) High aspect ratio 3D structures uniformly coated with titanium oxide.[127] **b)** Conformal coating of nanoporous, high active surface materials.[128] **c)** Fin and Gate-All-Around Field Effect Transistor coated with hafnium oxide with a high dielectric constant for an effective gating [129].

ALD technique was developed in the 1970s and originally stemmed from a variety of CVD processes, as it shares many precursors for the deposition. A key distinction between those two techniques lies in the sequential exposure of the gaseous precursors that induce self-terminating reactions on the surface. In this way, the entire process is divided into half-reactions that stop when the substrate surface is devoid of the free sites ready to adsorb the precursor. The nature of the process leads to several, noteworthy advantages that may outweigh the decision to choose the ALD over other existing techniques. Additionally, when the growth conditions are properly chosen, the one cycle in the process yields exactly one

monolayer of the desired material, providing precise thickness control through layer-by-layer deposition. Another advantage is the conformality of the received layers. The precursor exposure time can be prolonged, allowing for a steady diffusion inside high-aspect ratio, complex structures, and cover it entirely with a pin-hole free, conformal coating.

The sequentiality and self-saturation of the process allow for compositional control and fine tailoring of the optoelectronic properties of non-stoichiometric films. The following sections discuss in detail the growth properties and dynamics of the ALD process.

3.1.1. ALD System Employed

The equipment employed to grow all the samples within this thesis is a commercially available ALD reactor Beneq TFS-200 model. It features up to 8 lines of different precursors, a 200 mm reactor chamber, allowing for coating multiple substrates at once and precise temperature control up to 500 °C. The setup is shown in **Figure 28**. The system enables both liquid and solid precursor usage. In the case of the last, a heating of the container as well as the precursor line is necessary. All the ALD-grown samples presented in this thesis are manufactured using this system.



Figure 28. ALD setup photo. The inset shows the reaction chamber which spans over 200 mm in diameter.

3.1.2. ALD growth dynamics and properties

The frequently emphasized advantage of the ALD is the precise control of the thickness of the sample, as the reactions occurring on the surface are self-terminatory resulting in the deposition of exactly one monolayer. The description of ALD process in previous section provides fundamental and illustrative form. In reality, this requires certain growth conditions, several requirements for precursors and reaction types. In principle, this requires certain growth conditions and reaction types to be fulfilled. Otherwise, the growth per cycle may strongly deviate from 1 monolayer, depending on the deposition temperature, which can lead to different deposition modes, such as CVD. **Figure 29** showcases different reaction types with different amounts of adsorbed material.

The self-terminating reactions pair is a prerequisite for any ALD process to take place. This term refers to the reactions that cannot further proceed when the free sites of the surface are saturated, consequently stopping the growth after one monolayer of the precursor is incorporated, without excessive growth beyond that point. Besides, for the self-terminating reactions to be fully controllable and yield an ALD growth mode, they should satisfy the following conditions [130-133]:

- no attachment of the precursors to its initial ligands,
- no desorption during the purge phase,
- non-reactive by-products of each reaction pair that are easily removed during purging,
- irreversible adsorption which is resistant to any etching processes during other phases and relies on chemisorption mechanisms, (ligand exchange or dissociation rather than physisorption).

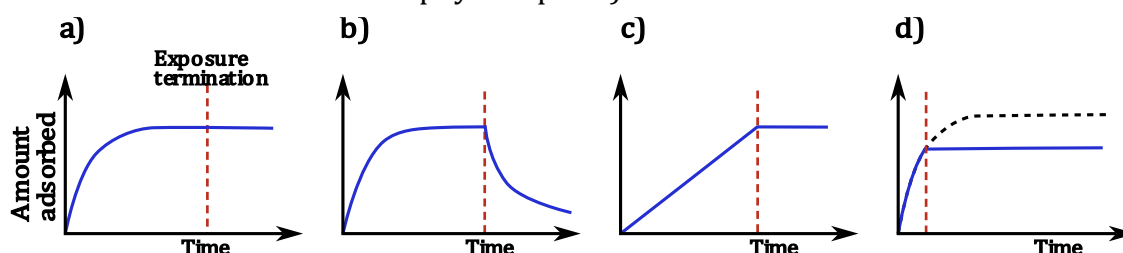


Figure 29. Different modes of adsorbing material in the ALD process, depending on the chemistry of the process. a) an ideal ALD process with irreversible, saturated adsorption, also called self-terminating reaction, **b)** reversible saturating reaction: after the exposure termination, the grown layer is etched, therefore the full monolayer is not reached **c)** irreversible, not saturating reaction: the example of CVD process where the thickness of the layer grows unstopably, **d)** irreversible adsorption stopped too early to saturate. Visually adapted from: [134-136]

During the physisorption process, numerous attractive interactions between molecules and layers are made, leading to weak bonding between many monolayers that can be easily broken or altered.

For instance, weakly bound atoms result in reversible reactions and slower deposition of the material. Similarly, an inadequately chosen precursor pair can cause non-saturated behaviour, where the precursor may react with the reaction by-product, causing excessive growth or, conversely, etching the just-incorporated layer (**Figure 29b**). The most desirable scenario for ALD is depicted in **Figure 29a**, where a true self-terminating reaction, leading to a plateau in the adsorbed material after some time, is shown. However, also the opposite in nature, non-saturating growth without the specific reaction termination moment can occur, causing an excessive deposition of the material.

The reaction dynamic is influenced not only by the reactants involved but also by the temperature of the process, which is one of the most influential and decisive parameters. **Figure 30** presents the deposition speed vs temperature with different regions marked outside the ALD growth mode, also referred to as the “ALD window” in which the ALD process takes place. Within this temperature range, the growth per cycle (GPC) is nearly constant and is equal to approximately 1 monolayer of the grown material.

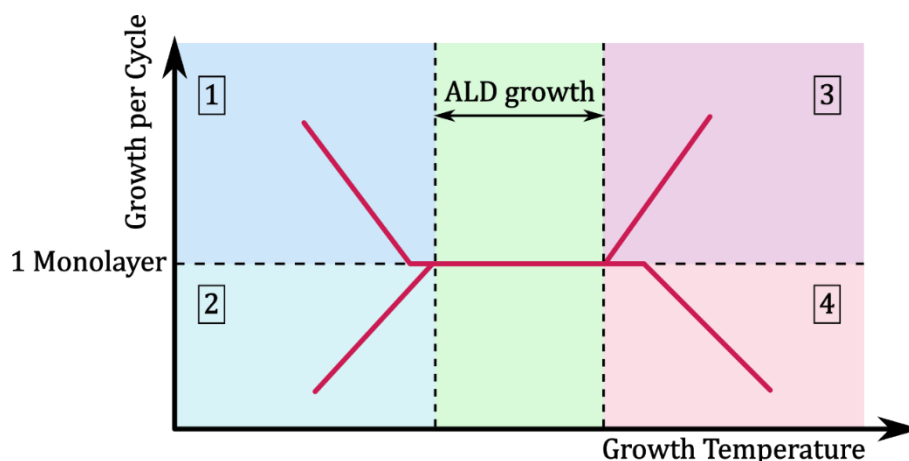


Figure 30. Different growth modes during the deposition. The ALD growth occurs only at a given temperature where we observe exactly one monolayer per cycle. In case of too low (regions 1,2) or too high temperature (regions 3,4), the deposition is either insufficient to cover the entire surface or due too excessive dopant amount, another layer is deposited. In both situations, the growth mode cannot be called an ALD deposition mode.

This allows for a self-terminating reaction despite some temperature variations and repeatable results, devoid of the undesired effects mentioned earlier.

Outside these conditions, an ordinary CVD process occurs, which is usually highly undesirable as it lacks control over the thickness and does not provide self-saturation of the reactions. As a result, this may lead to unintentional incorporation of byproducts and excessive growth ratios.

The deviations from 1 monolayer GPC can be categorized into four main regions, each stemming from different reasons [137-140]. Examining the GPC across a wide temperature range and observing its alterations allows for assuming one of the following reasons for the behaviour:

1. *Condensation of the precursor on the surface*

The temperature is too low to sufficiently decompose the precursor; therefore, physisorption becomes the dominant process, in which no ligand is released from the molecule. This mode does not qualify as a true ALD process, as the physisorption occurring in this mode is not self-terminated, and the layer continues to grow.

2. *Steric hindrance reduction*

With an elevation in temperature, an increased GPC is observed. That means enhancing the reactivity of the precursor, as more ligands are removed, and more molecules can be attached to the free sites on the surface.

3. *Ligands and reactions byproducts incorporation or lingering*

The temperature increase causes an excessive amount of by-products and ligands to either decompose into simpler compounds which cannot be easily purged or cause uncontrolled incorporation in the lattice. That causes GPC to exceed 1 monolayer. This process, similar to others, is not self-saturated and can proceed for a longer time.

4. *Monolayer desorption or ligand dissociation*

When the GPC decreases with increasing temperatures, the reason behind this is the decomposition of the monolayer into non-reactive compounds, which are needed for the next process step to occur. For instance, the functional methyl groups can be detached from the surface and joined together to form gaseous by-products, lowering the active free sites concentration important for the activation of the second half-reaction.

Maintaining the process nature within the ALD window is crucial to assert control over the process development, the final thickness of the material and

stoichiometry. However, even within this window, variations in the GPC can occur, resulting in less than monolayer per cycle growth [134-136]. These alterations come from the coverage ratio differences, i.e. how dense the atoms packed on the surface of the material are. The coverage within the process using the given precursors is not exactly constant and can be influenced by many factors. **Figure 31** presents the coverage ratio over time of exposure of the precursor. As seen, the curve approaches 1 with the elongated exposure times. Also, the mass gain occurs only at a specific point in time, namely the introduction of the precursor that takes place very quickly followed by the long purging phase, during which there is no mass gain.

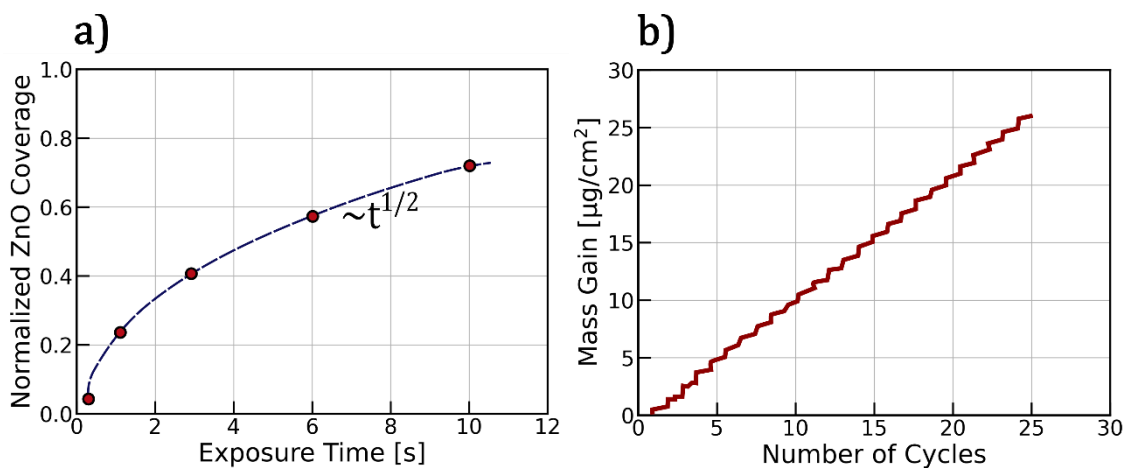


Figure 31. ALD growth characteristics. a) Coverage relation vs exposure time. In a proper ALD growth, the coverage is slowly converging to 1. The coverage can be approximated via the square function. **b)** Mass gain vs Number of Cycles. The deposition occurs only in a specific moment within the cycle, which is visible as the growth in mass deposited on the substrate. [120]

Several factors contribute to coverage curve shape as well as variations in the GPC. For instance, high steric hindrance of the ligands poses a challenge as not all free sites can be saturated, given that the ligands' physical dimensions are larger than the distance between the free sites. Therefore, the coverage equal to 1 does not necessarily mean the saturation of all free sites with the cation atom. The concentration of these free sites itself is regulated by the process temperature. It tends to decrease in higher temperatures, thus there are fewer reactive surface sites to be filled.

Besides, the reactivity of the substrate also influences the saturation effectivity. Initially, the layers are attached to the intrinsically or artificially

functionalized substrate, therefore GPC may fluctuate around some value until the entire substrate is covered. The growth mode typically assumed for an ALD process is the Stranski-Krastanov type, where the first few monolayers are filled by randomly saturating free sites. After this phase, the new material nucleates in island-mode, creating expanding islands that are joint together after reaching a critical number of pulses. Beyond this point, the GPC is expected to stabilize, and the thickness vs pulse number dependence should become linear. Another noteworthy reason for the variation is the geometry of the sample itself which can change during the growth due to the coverage of the thin film on the surface.

Considering all these reasons and process dynamics, designing the right precursors and associated reaction pathways that fulfil those requirements for an ALD process becomes a challenging task. Such precursors should be volatile enough to exhibit high vapour pressure in either room or slightly elevated temperature. Also, they should not decompose until they reach the surface at elevated temperature, and the reaction itself should be quick, and irreversible and the reaction product should be inert and gaseous. The dimensions of such precursor should be as small as possible (minimizing steric hindrance) to cover as tight as possible the surface. Due to these requirements, there are a limited number of precursors and processes that can be categorized as truly ALD. Nevertheless, the existing ones provide numerous advantages and unrivalled properties.

3.1.3. ALD Process Cycle and Reactions

This section illustrates the growth cycle of the typical ALD process. A single cycle results in the deposition of one monolayer of the desired material. This process itself consists of several steps, exploiting the fact that the involved reactions exhibit a self-saturating nature and occur only on the surface with the specific functional group. In addition, the substrate can be functionalized to enhance the precursor deposition if it contains insufficient natural functionalization. The exemplary process scheme is shown in **Figure 32** for a commonly used zinc oxide deposition. This scheme can be straightforwardly extended to any material, consisting of more than two elements.

The cycle starts with the first precursor – in this case, diethylzinc ($\text{Zn}(\text{C}_2\text{H}_5)_2$) – being introduced into the chamber (**Figure 32a**). The metalorganic nature of this precursor allows for an effective decomposition and adsorption of the cation on the surface, or more specifically with the functional groups present on the surface. The organic groups, in this case ethyl groups are detached upon contact

with the surface. The excessive amount of the precursor along with the by-products of the reactions are purged by the inert gas (nitrogen) in the following step (**Figure 32b**). The next precursor, water vapours, is introduced subsequently. The water reacts with the cation on the surface and substitutes organic groups, incorporating the oxygen atom into the lattice structure (**Figure 32d**). Once again, nitrogen is pumped to clear the chamber (**Figure 32e**). The entire process is cycled with zinc precursor until the appropriate thickness of the film is reached.

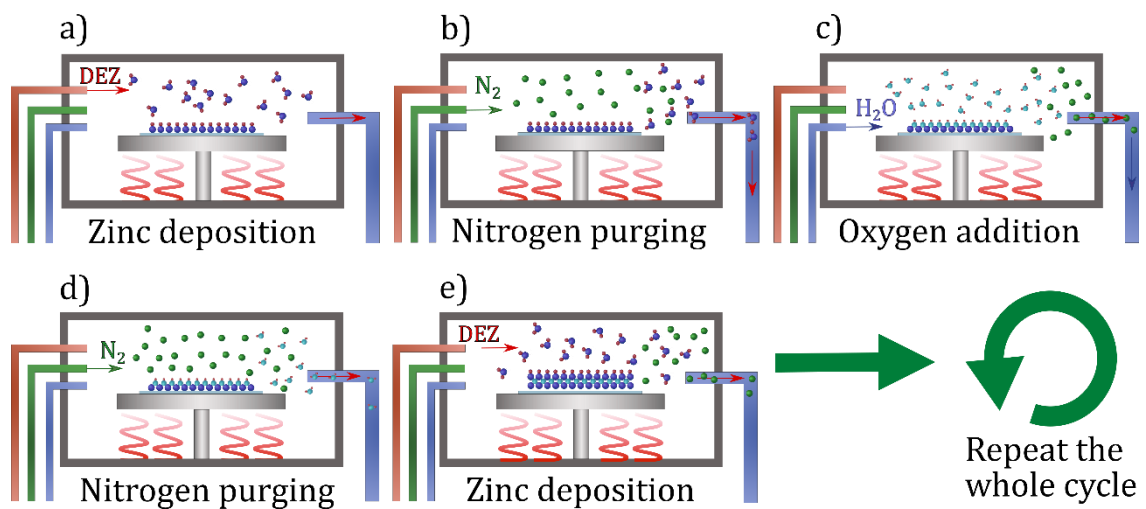
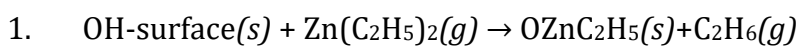
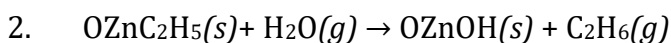


Figure 32. One cycle of ALD technique growth scheme. Each of the precursors is introduced to the chamber at a time and is purged before the next sub-step can occur. The thickness is achieved through the cycling of all the steps shown.

During ALD growth, the deposition is realized through at least two half-reactions. For instance, ZnO deposition using diethylzinc and water occurs in two steps, where the DEZ is adsorbed to the -OH group on the surface, detaching one ethyl group, resulting in C₂H₆ as a by-product gas. ZnC₂H₅ molecules with one ethyl group are attached to the surface. The second step removes this remaining group, substituting an oxygen atom, thus finishing the formation of the ZnO with a very reactive -OH group atop, ready to adsorb another precursor. Those two half-reactions are described below. The (*s*) and (*g*) letters indicate either the gaseous or solid state of the material, respectively:



N₂ purging step



Reaction (1.) stops when there are no more free sites present and the rest of diethylzinc cannot be effectively incorporated, and thus is removed in the purging phase. Similarly, reaction (2.) is stopped when the sites with ethyl groups are saturated.

The same procedure applies to the more complicated materials, such as ternary and quaternary compounds where more chemical reactions are involved. **Figure 33** shows such process with an example of doping zinc oxide with Al³⁺ cation.

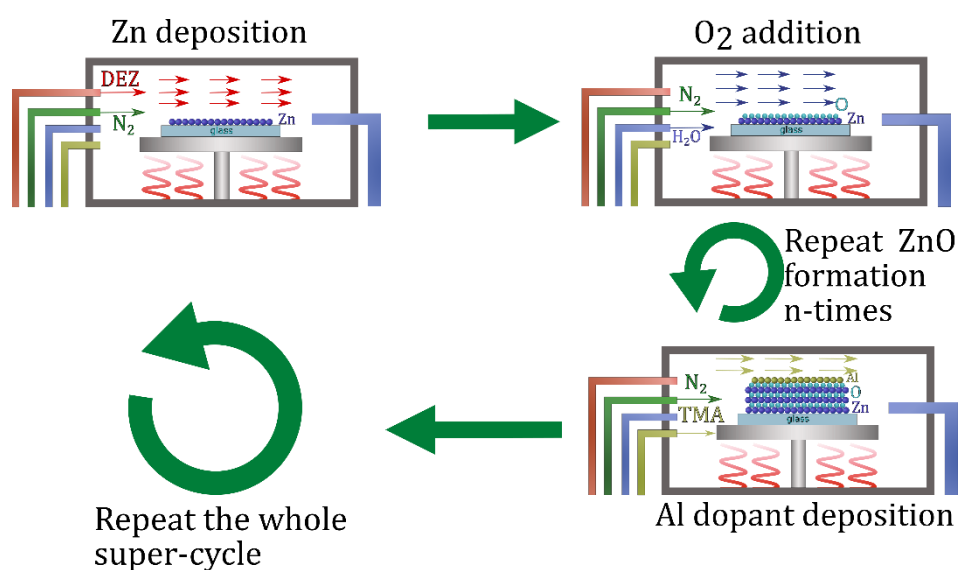
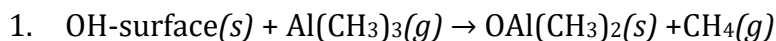
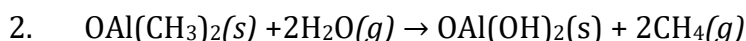


Figure 33. Doping through ALD technique scheme. After some number of ZnO cycle depositions, a certain dopant cycle is introduced, which constitutes a super-cycle. The process goes on until the desired thickness is reached. The n number controls the doping level.

In the following example, the precursor of the aluminium organometal compound trimethylaluminum (TMA) is utilized. In this case, the similar two half-reactions occur, where the TMA methyl group are substituted:



N_2 purging step



The amount of this precursor is controlled by adjusting the cycle number, instead of known from other techniques particle beam intensity or growth vapour pressure adjustments. Therefore, by varying the zinc cycle number, we change the doping in the material. Unlike the intuitive and simplistic view of this technique, the

cycle ratio does not necessarily correspond to the atomic ratio of the given element in the resultant material. This holds especially true for more complex compounds, made of 3 or 4 elements where the non-linearity of the cycle ratio vs. atomic ratio leads to hard-to-predict stoichiometry [140,141]. For instance, the content of oxygen, hydrogen, and zinc in ALD-grown ZnO samples varies depending on many factors, such as temperature, exposure time, and substrate even when the pulsing ratio remains the same. Therefore, determining the precise amount of the dopant incorporated requires further material characterization.

Figure 34 presents the cross-section of the differently doped ZnO with aluminium atoms, showcasing the distribution uniformity of the Al dopant for different concentrations.

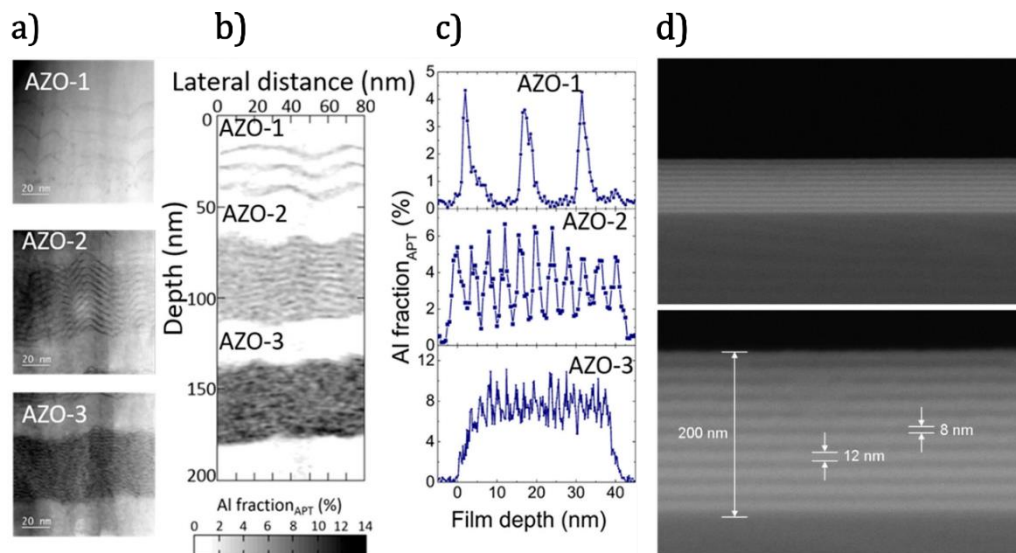


Figure 34. Cross-section of the ALD-grown samples. a) TEM image of a differently Al-doped zinc oxide. b), c) Al fraction within those samples. As visible, planar doping of the TMA precursor leads to diffusion of the element across the lattice structure, however, there are pronounced peaks in the Al atom content, meaning that the doping is not uniform below some critical doping level. [142] d) Cross section of nanolaminar sample of Al₂O₃ (dark) and HfO₂ (light).[143]

Determining the exact place and distribution of cations in the material involves more complicated characterization techniques such as secondary ion mass spectrometry (SIMS) or transmission electron microscope (TEM). However, the dopant atoms usually undergo a diffusion across the layers, and when the critical level in doping is reached, the sample approaches a state of uniform doping. As seen, very low doping ratios result in spikes in the measured Al concentration. Also, **Figure 34d** presents the possibility of growing very well-defined nanolaminate structures consisting of different materials.

3.2. Nanoimprint lithography

Nanoimprint lithography is a widely employed technique for fabricating micro- and nanostructures over large surfaces, possibly exceeding 20×20 cm. This technique enables the texturization of the surface with a diversity of structures under a moderate temperature range and environmental conditions. It primarily involves applying pressure to a moldable, semi-fluid resist that during this process is shaped according to the stamp. When combined with selective etching, nanoimprint lithography enables the manufacture of highly engineered patterns with a resolution below 50 nm, surpassing the resolution of deep ultraviolet photolithography. Several variations of this technique have been proposed, differing in conditions and assisted media, yet adhering to the same fundamental working principle. These variations include thermally assisted, UV triggered, flat stamp, or roller versions of the method, each tailored for specific applications [144-146]. Within the thesis, the employed variation of this technique is thermally assisted UV roller nanoimprint.

3.2.1. Nanoimprint method overview

The fundamental working principle of the nanoimprint technique is akin to a well-known embossing process, yet executed on micro- or nanometer-scale patterns. The entire method is based on mechanical forces acting on the semi-liquid resist by a soft stamp, therefore the resolution of the manufactured structures is not limited by the light source as in classical photolithography. The resolution can therefore exceed 50 nm, typically achieved through expensive equipment such as electron or ion beam lithography. By relying on mechanical forces, the whole process is consequently much faster than direct patterning or mask-based lithography which also encounters difficulties when applied to illuminate larger surfaces. This results in a high throughput of this method, especially when employing its roller variation, enabling fast and seamless integration into the production chain. This prerequisite is especially crucial due to the increasing demand for efficient cells in the photovoltaic industry. The process of pattern creation is depicted in **Figure 35**. The manufacturing process begins with defining the desired pattern for subsequent imprint and replication. The pattern should be placed on a rigid substrate, durable enough to withstand multiple presses against the stamp. Pattern manufacture can be done by at least several techniques, including e-beam, interference lithography, or direct laser writing. The interference

lithography holds an advantage in this process since it allows for a swift pattern origination across a large surface with a wide range of possible structure periodicity, spanning from 100 nm to even 100 μm . This method is particularly well-suited for creating periodic micro-textures, aligning with the objectives of our research. Within this thesis, the interference lithography technique was employed to manufacture the master structure, also called a shim.

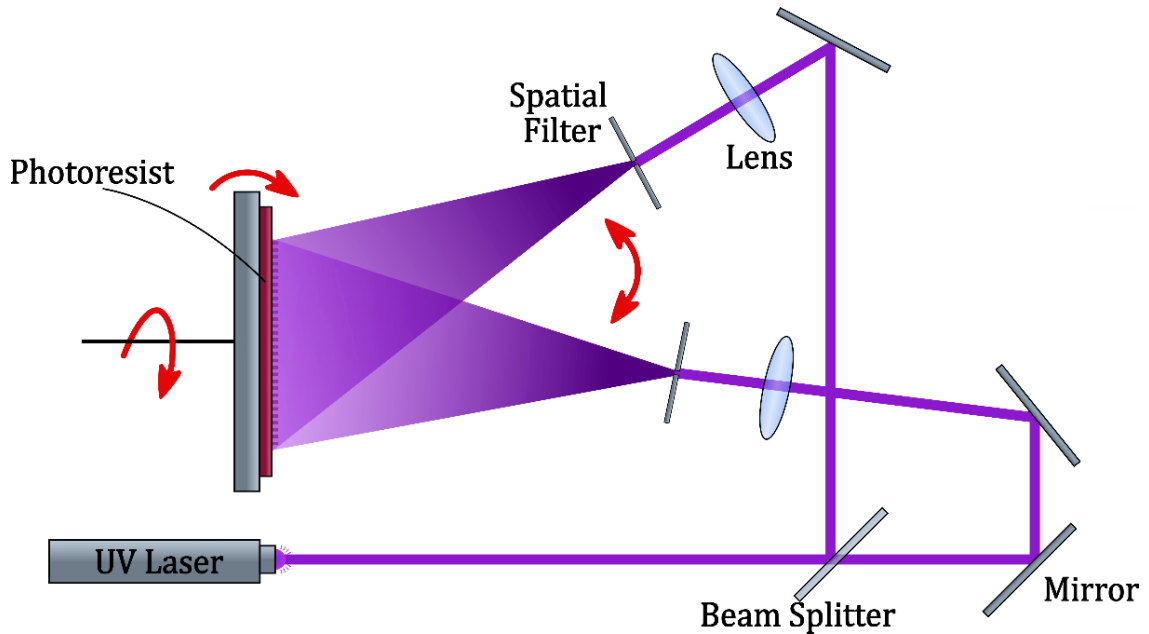


Figure 35. Interference lithography setup scheme. The red arrows depict the possible angle adjustment that determines the period and symmetry of the achieved gratings. Also, by tilting the whole substrate, non-vertical profiles can be originated. Inspired by the image from [118] and visually adapted.

During the interference lithography process, a photoresist is illuminated by two or more, previously split light beams. The interference pattern comes from superposition of those two coherent light beams illuminating the substrate at the certain angle. The period of those maxima is expressed by the following formula:

$$d = \frac{\lambda}{\sin(\theta)}, \quad (17)$$

where λ denotes the wavelength of the light and θ is the angle between the two interfering beams.

The phase shift and optical length differences adjust the position and contrast of the interference maxima within the photoresist, resulting in developed and undeveloped places, arranged in a periodic pattern. The intensity and the exposure time at a specific point on the surface determines the extent to which the

photoresist is exposed and consequently the depth of the resist that will be removed. Thereby with a fixed exposure time the light intensity defines the depth of the created cavity. Typically, a blue or UV laser light is used for this purpose, due to the shorter wavelength and thus higher resolution. In such a way, the resist is exposed in the controllable manner, by adjusting the period and symmetry of the linear interference pattern created by these superimposed beams. The period of the pattern is controlled by the phase shift between the two beams and their relative position, i.e. the laser wavelength and the angles of incident of those two beams. The rotation of the sample allows to further complicates the interference beam arrangement picture. For instance, two exposures with a 90-degree rotation, yield a square symmetry pattern, while three exposures, each separated by a 120-degree rotation, result in a hexagonal symmetry. After exposing the desired arrangement, the excessive photoresist is then removed, resulting in the 3D topography within the photoresist layer on the substrate. The acquired master structure in the photoresist is then electroplated with metal to obtain a durable and reusable metallic shim for mass production of stamps. Given these inherent properties of interference lithography working principles, certain desired patterns may be either very challenging or simply unachievable using this technique.

Once the shim with the replicated pattern is ready, the next step involves a PDMS replicate stamp from a master shim. **Figure 36** presents schematically all the necessary steps involved in the procedure with an exemplary honeycomb-like structure. The resulting shape is the negative of the master shim pattern.

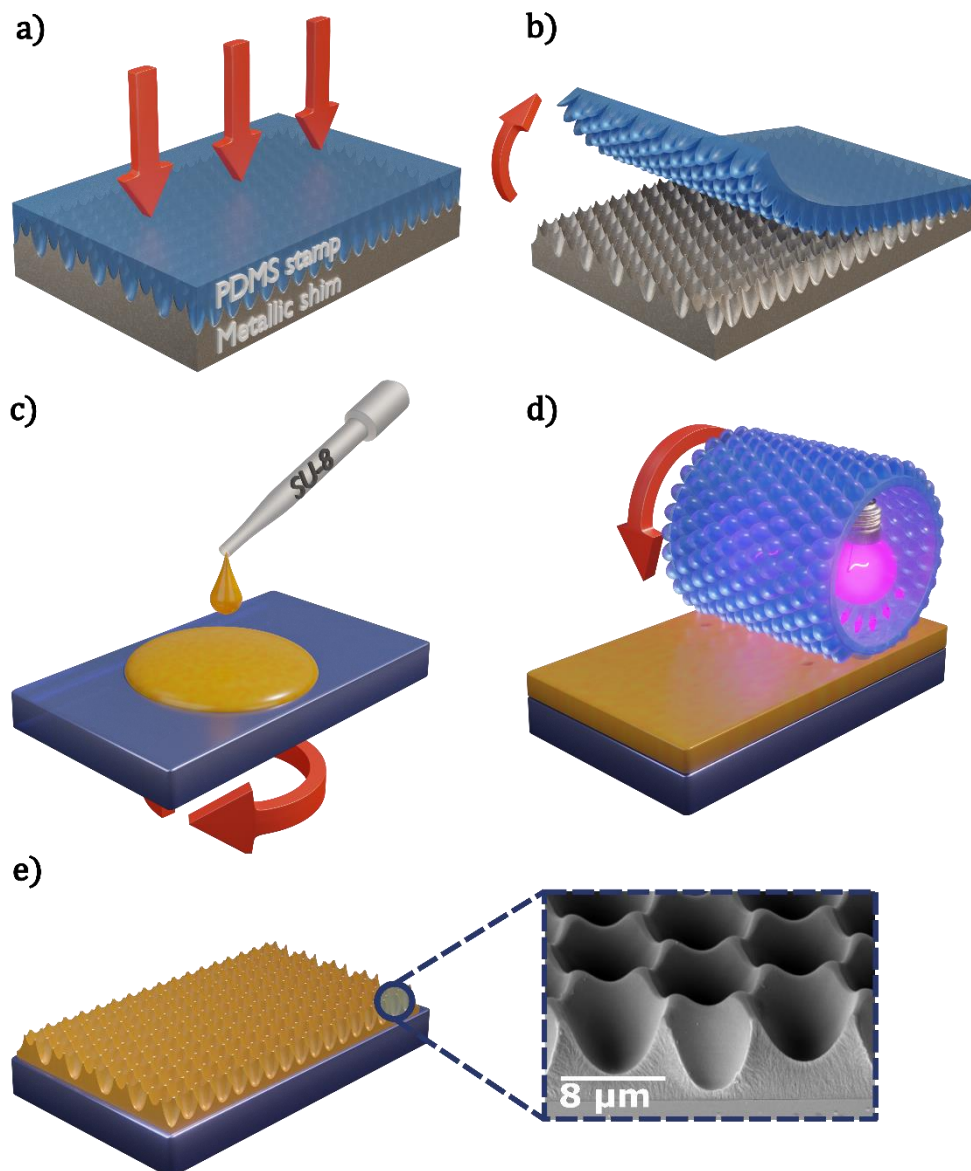


Figure 36. Thermally assisted Roller nanoimprint process scheme. a) The PDMS stamp replication b) Removing the ready-to-use stamp c) Spin-coating of the resist onto the substrate d) Rolling onto mouldable resist to imprint the negative of the stamp shape e) The finished sample along with the SEM image of an exemplary imprinted structure.

First, the liquid PDMS is dispensed over the metallic shim to slowly and thoroughly penetrate the master shim. Through applied pressure and elevated temperature of approximately 90 °C, the PDMS solidifies and becomes durable, with the exact pattern formed at its surface. Careful detaching yields a reusable, soft stamp that can be folded around the roller tube to later imprint the pattern into the photoresist. Each such created stamp can be used over 50 times, ensuring a highly efficient process. The photoresist is applied by spin-coating onto the desired

substrate. During the nanoimprint process, the PDMS stamp is slowly pressed against the photoresist-covered sample at the elevated temperature to make the resist soft and formable, under the weight of the rotating roller, forming the negative of the stamp pattern on the sample. As the photoresist is pressed and moulded, UV light triggers its cross-linking process. After the exposure and complete imprinting of the stamp, a brief post-baking is performed to finalize the crosslinking of the resist. As a result, a well-reproduced pattern of the original master shim is obtained within the resist.

3.2.2. Roller nanoimprint system

The scheme along with the photography of the setup is shown in **Figure 37**. In our case, the system used to nanoimprint the samples consists of a several kg roller with an installed UV lamp inside to allow an effective UV exposure of the sample beneath it.

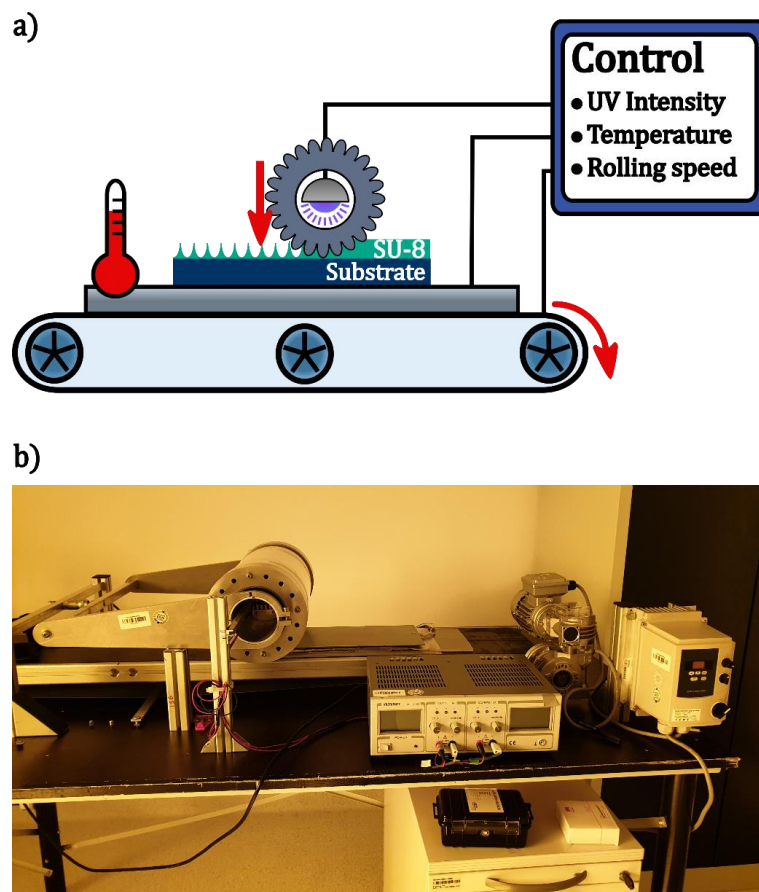


Figure 37. Roller nanoimprint system. a) A scheme with the most crucial parts including the tracer, hotplate and lamp depicted. b) The real appearance of the system.

Due to the geometry, only a small part of the stamp has contact with the surface at the time, amplifying the exerted pressure on one area. The sample itself is placed on a controllable hotplate to assert a valid temperature during the process. In this setup, the moving part is the treadmill with an attached hotplate, rather than the roller itself. The system operator has control over the UV illumination intensity, treadmill speed and hot plate temperature. The tuning of these parameters is crucial to obtain a repeatable and high-quality process. The whole system is placed in a room equipped with UV-blocking filters to rule out unintentional exposure of the photoresist.

This exact system used to nanoimprint the samples was designed and made from scratch by Dr Hubert Hauser. More details regarding this configuration can be found in ref. [118,147-149]. This system has been used to manufacture samples investigated in **CHAPTER 5**.

3.3. Characterization methods

This section comprehensively explains the phenomena behind each of the characterization methods used in the investigations presented in this dissertation. Additionally, it provides information about all the employed equipment and acknowledges the contribution of people, particularly in case the author of the thesis was not fully involved in the sample characterization process.

3.3.1. Scanning electron microscopy

Scanning electron microscopy (SEM) is a fundamental technique for the visualization and characterization of structures, offering resolution capabilities close to single nanometers, reaching magnification levels of approximately $\times 500,000$. This technique is vastly used across various scientific disciplines due to its versatility and the ease with which it analyzes the samples.

The SEM system consists of electron acceleration lenses and coils that precisely concentrate the beam in a very specific place of the sample with an accuracy down to a few nanometers. These accelerated electrons interact with the sample's surface providing information about the topography and composition of

the sample. The distinguishing feature of the SEM lies in the utilization of magnetic fields to focus and steer the high-energy electron beam, resulting in an orders-of-magnitude greater resolution compared to its optical counterpart. A schematic representation of the electron scattering and re-emission is depicted in **Figure 38**.

The source of the SEM signal comes primarily from the ejected electrons within the sample, usually from the K shell after being inelastic scattered. Those electrons are referred to as secondary electrons (SE) and they are ejected from or near the surface, typically from depths of no more than 50 nm, losing most of their initial energy during the scattering. Consequently, SEM is applied for imaging mostly the topography of the sample. Additionally, another scattering phenomenon known as elastic scattering is observed. The electrons involved in this process come from deeper regions within the sample and experience scattering on the atom nuclei as they travel toward the surface. These electrons are called backscattered electrons (BSE) since they undergo an elastic scattering, maintaining their initial high kinetic energy within the range of 2 – 30 keV. The cross-section of this process exhibits pronounced dependence on the atomic number Z. Consequently, the intensity of the signal is dependent on the elements composing the sample's surface, which is manifested as the appearance of bright regions corresponding to heavy elements and dark areas consisting of lighter elements.

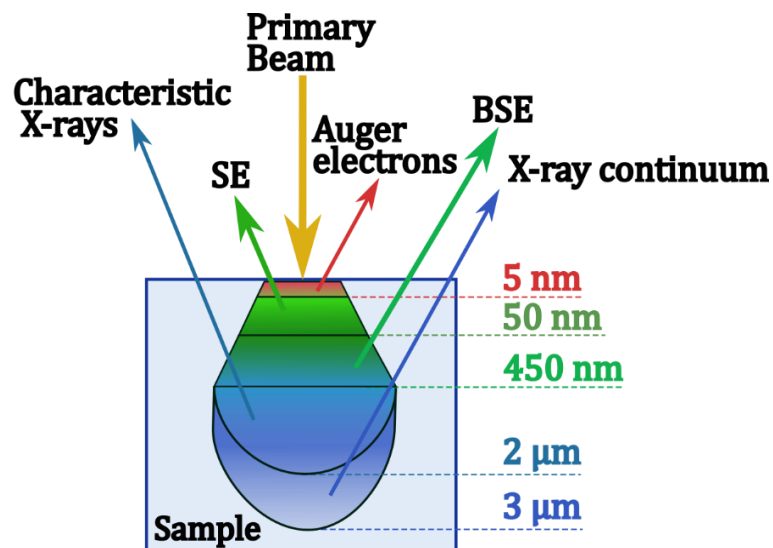


Figure 38. SEM electron beam scheme. In the picture penetration depths and reflections routes for different types of electrons and X-rays are indicated. Electron signals important for SEM, i.e. secondary electrons and backscattered electrons imagery are indicated in green, whereas X-ray generated light, particularly interesting for EDS is indicated in blue.

Besides electrons, the sample also radiates characteristic X-ray energies, originating from the electron transitions occurring between deeper shells of the atom, alike to creating electron-hole pairs in semiconductors, but with energy differences of the order of magnitude higher. Upon recombination, this energy is released in the form of X-ray radiation. Having the database of the characteristic X-ray energy emission, quantitative analysis of the elements present in the material with submicron resolution can be performed. This operational mode of the SEM system is called Energy-dispersive X-ray Spectroscopy (EDS).

Apart from the equipment itself, the acquisition of SEM necessitates the maintenance of high vacuum conditions since the electron beam can be very easily distorted when interacting with air molecules. The samples should be highly conductive to prevent the electrons accumulation on the sample's surface, which leads to electrostatic charging and severe image aberrations, deforming a sharp view of the sample. In the case of isolating samples (refer to **CHAPTER 5.** and nanoimprinted structures), a thin layer of sputtered metal atop is mandatory. However, when viewing TCO samples, no additional treatment is required thanks to their conductivity. It is important to emphasize that SEM is not a non-invasive technique and prolonged observation at one point may cause damage to the sample, which is particularly pronounced when dealing with organic materials.

In this dissertation, the results obtained with 3 different SEM systems are included:

- **CHAPTER 4.** The ALD-grown samples were characterized mostly with a Carl Zeiss Sigma HV field emission microscope at 15 kV accelerating voltage and around 3 mm working distance. These measurements were performed with the great help of PhD Piotr Wróbel.
- **CHAPTER 4.** Some of the ALD-grown samples were characterized with Helios Nanolab 600 Focus Ion Beam with high-resolution SE detector at 8 kV voltage and 5 mm working distance.
- **CHAPTER 6:** Perovskite and nanoimprinted structures were characterized using a Hitachi S-4700 system with 5 kV accelerating voltage and around 16 mm working distance.

3.3.2. X-Ray Diffraction

X-ray diffraction (XRD) is the technique used to extract information about the sample's crystal lattice. It is considered as a fundamental tool in every material science laboratory due to its capacity to characterize the structure of the investigated material from a multitude of perspectives. The information obtained through this technique involves, among other things:

- Crystal structure type and lattice constants, followed by the precise classification of the investigated material,
- Quality of the layer, including grain sizes and amorphicity,
- Thickness and strain present in the layer,
- Preferential growth directions.

XRD technique utilizes the atoms constituting the crystal structure to diffract incident monochromatic X-ray light, as these atoms function as a diffractive grating with an angstrom-like grating period that approximately matches the wavelength of the incident light. **Figure 39** provides a schematic representation of this technique along with an example of the XRD spectrum.

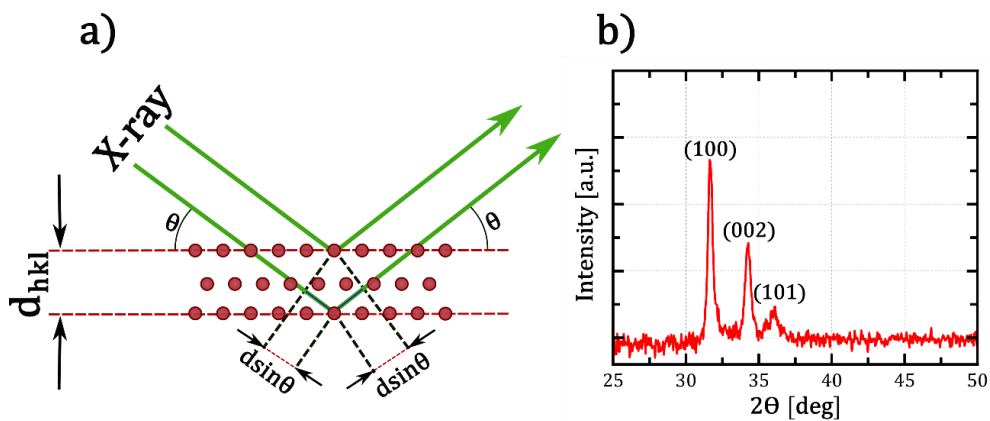


Figure 39. XRD operational principle scheme. a) An incident X-ray light is illuminating the crystal surface, undergoing diffraction on the atom's planes with interplanar distances indicated as d_{hkl} . **b)** An exemplary diffractogram of zinc oxide polycrystalline sample with peaks marked after Miller indices crystal planes.

Similarly to a diffractive grating operating in the visible range, the reflection peaks emerge at very specific angles, meeting the conditions for constructive interference conditions. In the context of crystals, the angles at which these peaks are observed depending on the interplanar distances within the crystal, thereby

providing valuable insight into its structure. The condition for the interference to occur is expressed by the Bragg's law[150]:

$$2d_{hkl}\sin\theta = n\lambda, \quad (18)$$

where d_{hkl} is the interplanar distance between the specific planes characterized by the Miller's indices, θ – the angle at which we detect the reflection, n – positive integer number and λ – the wavelength of the incident X-ray light.

The positions and intensities of the peaks in the diffractogram, show us the quality of a monocrystalline material along with the type of the investigated material. The X-ray light source must be both monochromatic and have sufficient brightness to prevent rapid attenuation within the sample. Usually, an electron charge lamp with a metal cathode is utilized for this purpose. In this setup, the electrons are accelerated by a high voltage and directed at the cathode, releasing X-ray light along with some other wavelengths, that are subsequently filtered out. As a result, a collimated and monochromatic light beam is achieved, being a mandatory condition for the accurate determination of the reflection peaks.

XRD measurements were performed using a Panalytical X'pert diffractometer equipped with a Cu X-ray tube with a characteristic wavelength equal to $\lambda = 1.542$ Å. The measurements were performed by PhD Mateusz Tokarczyk at University of Warsaw, Faculty of Physics.

3.3.3. UV-Vis-NIR Spectroscopy

For the optical characterization of the samples, the UV-Vis-NIR spectroscopy was employed. The scheme of the transmittance measurement employing a spectrophotometer is presented in **Figure 40**.

This technique was primarily used to determine optical parameters such as transmittance, optical bandgap, and reflectivity of the investigated samples. The spectrophotometer is a fundamental tool for this purpose, providing a spectrally resolved ratio of transmitted, absorbed and reflected light to the incident one. It consists of a well-defined light source covering the desired wavelength range, a high-quality dispersion element (such as diffractive grating) and a photodetector. Additionally, the instrument comprises a system of lenses and mirrors to direct and focus the light onto the right place.

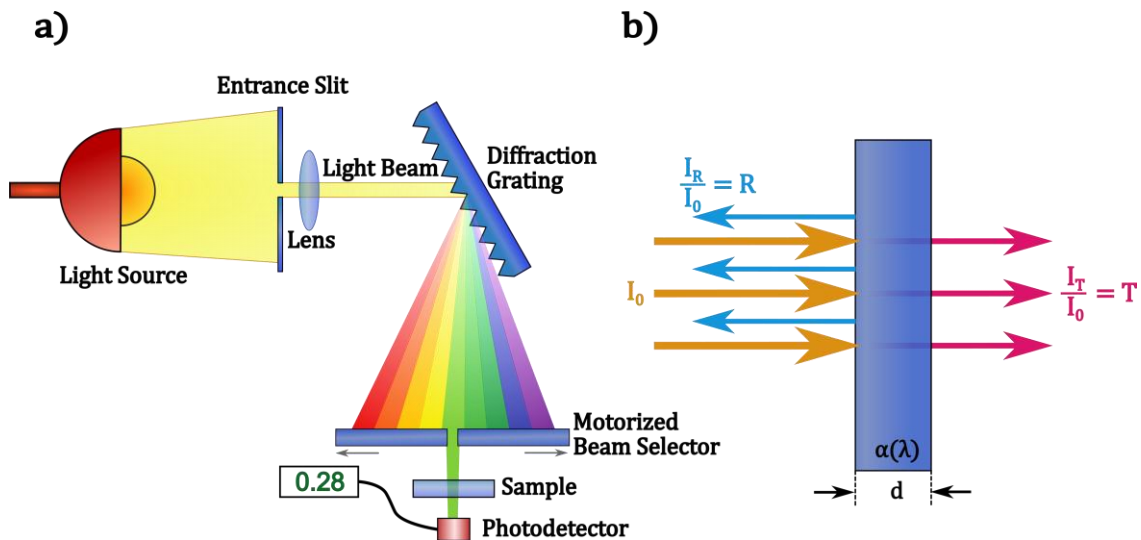


Figure 40 UV-Vis-NIR spectroscopy method scheme. a) Spectrophotometer operation and measurement scheme. The drawing depicts the essential parts of the instrument during its operation in transmission mode. **b)** Sketch of the light behaviour when encountering sample of thickness d and absorption coefficient $\alpha(\lambda)$ with the incident, transmitted and reflected beams indicated.

During the operation, the light first passes through the entrance slit and lens, where it becomes collimated. Then, it undergoes diffraction on the gratings, resulting in the generation of a spatially resolved spectrum. The motorized beam selector separates only a very specific wavelengths and transmits them to the photodetector. The selector moves during the measurement, to acquire a desired spectrum range. As a result, the relative intensity of the signal is acquired for each scanned wavelength. The obligatory condition for this technique to work effectively, is the well-defined source light spectrum, enabling the comparison of the initial and recorded signal. The instrument can also operate in reflection mode. In this mode, the instrument instead of collecting transmitted light, it captures only reflected light. When dealing with scattering samples, the presence of an integrating sphere is necessary to collect all the signals reflected from the sample at various angles.

The reflectivity and transmittance are expressed as relative light intensities to the incident one, which are defined by the following formula:

$$R(\lambda) = \frac{I_R(\lambda)}{I_0(\lambda)}, \quad (19)$$

$$T(\lambda) = \frac{I_T(\lambda)}{I_0(\lambda)}. \quad (20)$$

Once those parameters are obtained, absorption of the sample can be determined by the following formula:

$$A(\lambda) = 1 - R(\lambda) - T(\lambda), \quad (21)$$

Assuming the known thickness of the sample and meeting the requirement of $ad \gg 1$ which is asserted for the measured samples, the full absorption coefficient dependence can be calculated using this formula [151]:

$$\alpha(\lambda) = -\frac{1}{d} \ln \left(\frac{T(\lambda)}{1 - R(\lambda)} \right). \quad (22)$$

Those parameters are crucial in characterizing both solar cells and TCO materials, since they provide information on the optical properties of the sample, specifically about what part of the incident light is either transmitted, absorbed, or reflected. Additionally, a very convenient value is the weighted transmission and reflectance with respect to the standard solar spectrum. The spectrum was taken from NREL data [49] – a widely adopted source of the standard spectrum. The formula for R_W is equal to:

$$R_W = \frac{\int R(\lambda) \Phi_{AM1.5}(\lambda) d\lambda}{\int \Phi_{AM1.5}(\lambda) d\lambda} \quad (23)$$

where $R(\lambda)$ is the reflectance of the sample and $\Phi_{AM1.5}$ is the photon flux of the AM1.5g solar spectrum.

In this thesis, two different spectrophotometers were employed:

- **CHAPTER 4.** Transmission spectra of the ALD-grown samples were collected at room temperature, with a Varian Cary 3000 spectrophotometer setup in the 250 – 1100 nm range with a 1 nm step with a light beam dimension of around 3 mm × 3 mm. Since the scattering within those samples is negligible, there was no necessity to employ an integration sphere.
- **CHAPTER 5:** Reflectance and transmittance spectra of the imprinted structures were measured using a Perkin Elmer UV/VIS/NIR Lambda 950 Spectrometer with an integrating sphere to assert full signal collection. The spectra were collected in 2 nm steps from 300 to 1200 nm with light beam dimensions around 4 mm × 4 mm.

3.3.4. Hall effect measurements

The electrical parameters of the samples such as resistivity, carrier concentration and mobility were determined through Hall effect measurements. The electrical properties study using Hall effect and van der Pauw method is routinely used in numerous experimental research dealing with semiconductor physics and material science. The measurements were conducted at room temperature, utilizing an Ecopia HMS-3000 Hall Effect Measurement System with 0.532 T neodymium built-in magnets. Uncertainties of the electrical parameters were determined based on data provided by the manufacturer, as well as the measurement setup and sample geometry. The measurement setup is illustrated in **Figure 41**.

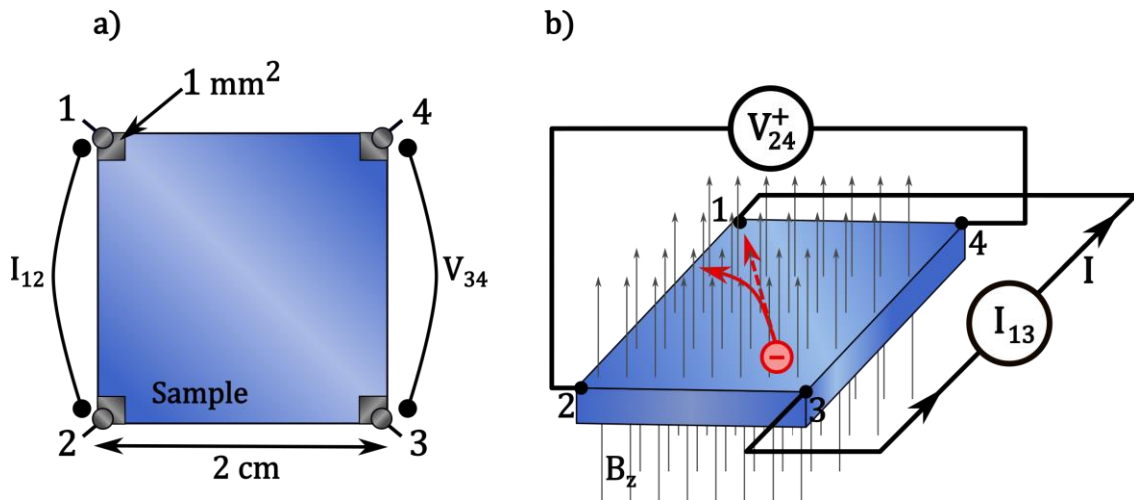


Figure 41. Hall effect and van der Pauw measurement setup. a) Sample with contact scheme and applied voltage. Such connected wires define resistance termed as $R_{12,34}$. b) Hall effect measurement setup with directions of magnetic field, current and charges detraction indicated, being the source of measured Hall voltage, indicated here as V_{24}^+ . The final value of the Hall voltage is the average across the varied magnetic field and current polarization.

The TCO samples used in the study were squares measuring 2 cm \times 2 cm with four silver paste small droplets placed at the corners, each with an approximate area of 1 mm². Such metallic pads provide ohmic contact minimizing parasitic resistances. To determine sheet resistance and the resistivity of the samples, van der Pauw method was employed [152]. This method involves several measurement steps.

First, a set of 8 combinations of resistances is measured, adapting the following naming convention:

$$R_{12,34} = \frac{V_{34}}{I_{12}},$$

$R_{12,34}$ represents the resistance measured by the potential difference between points (3) and (4) with current flow from point (1) to (2). The resistivity measured with reversed voltage and current polarities is – following the convention – denoted as $R_{21,43}$. Measuring the resistances for both polarities minimizes the error arising from any non-uniformities and voltage misalignments present in the sample. Vertical and horizontal resistances are defined as follows:

$$R_V = \frac{R_{12,34} + R_{34,12} + R_{21,43} + R_{43,21}}{4} \quad (24)$$

$$R_H = \frac{R_{23,31} + R_{41,23} + R_{32,14} + R_{14,32}}{4}$$

Determining sheet resistance (R_S) involves solving the following equation, which can be done only by using numerical methods, for example extensively described in [153].

$$e^{-\pi R_V/R_S} + e^{-\pi R_H/R_S} = 1 \quad (25)$$

Once R_S is calculated, other electrical parameters can be obtained utilizing the Hall effect. By applying a constant magnetic field, charges are deviated from their linear path, inducing imbalanced charge distribution and appearance of the voltage between the two sides of the sample, termed as Hall voltage. This voltage is directly proportional to the mobility of the carriers and inversely proportional to their concentration. Similarly, to the R_S establishing process, determining Hall voltage requires measuring voltages for both polarities with constant current flow. The final value is the average of all these measurements:

$$V_H = \frac{V_{13} + V_{24} + V_{31} + V_{42}}{8},$$

where:

$$V_{ij} = V_{ij(P)} - V_{ij(N)},$$

marks the voltage difference with positive and negative polarity of the applied magnetic field. The final parameters are defined by the following relations:

- The Hall coefficient:

$$R_H = \frac{d}{4IB} V_H, \quad (26)$$

- Carrier concentration:

$$n = \frac{1}{R_H q} \quad (27)$$

- Carrier mobility:

$$\mu = \frac{R_H}{R_S d} \quad (28)$$

Van der Pauw's method is susceptible to uncertainties arising from the contact placement and geometry of the sample. The proposed model works most accurately when the sample is considered as a uniform, pin-hole-free conductor without any thickness variations. Metal pads, serving as contacts, should be as small as possible and placed in the corners of the sample, at the same time providing ohmic contact [154]. Additionally, the magnetic field value should be well-determined and uniform across the whole sample to assert valid calculations using **Equations ((27) and ((28)**. In the case of the measurements, all the abovementioned precautions to minimize the uncertainties were applied.

3.3.5. J-V Characteristics and External Quantum Efficiency

J-V characteristic is the fundamental indicator of solar cell performance and its significance has already been discussed in **Section 1.3**. Here, only the experimental details about measurement are presented. J-V characteristics were collected using a Xenon lamp with its brightness calibrated to a reference silicon cell sample to assert a stable illumination power density of 100 mW/cm² for each sample. During the measurement of a given cell, all area outside the solar cell was covered with a black mask to eliminate the unintentional over-illumination of the sample. In the case of textured surfaces, which may induce incoupling of the light beyond the chosen area, no significant influence was found. This approach aligns with the work of M. Jošt et al.[155] where similar type of samples was investigated, without significant uncertainties reported. The mismatch factor was not considered; however, it influences the result in a very negligible way. J-V curves were recorded using a Keithley 2400 source meter in forward and reverse scan direction (range – 0.1 V to 1.2 V, step width 20 mV, scan speed 20 mV/s). A few

measurements were taken until the stabilization of the J - V curves, which is a commonly seen phenomenon, then the latest result is presented.

External Quantum Efficiency (EQE) refers to the ratio of incident photons to photogenerated electrons collected at the electrodes of the solar cell. This is a critical metric showing the capability of solar cells to convert the photon flux into a usable electron flow. It quantifies the ratio between the charge carriers collected and the number of incident photons at a given wavelength, expressed via:

$$EQE(\lambda) = \frac{\text{collected electrons / sec}}{\text{incident photons / sec}} \quad (29)$$

This ratio includes optical losses, arising from reflection and transmission, therefore this is the most reliable indicator of the solar cell optical performance. While an ideal cell would exhibit EQE equal to 1 for all wavelengths in the solar spectrum, this value is always only approached but never reached, especially for the wavelengths below the bandgap. Also, the integral of EQE and solar spectrum directly yields the current density generated by the cell:

$$J_{SC} = q \int_0^{\infty} EQE(\lambda) \Phi_{ph}^{AM1.5}(\lambda) d\lambda \quad (30)$$

EQE measurements were collected with an in-house built setup in 10 nm steps from 300 to 900 nm. The light source is a Xenon lamp that is subsequently chopped at a frequency of 133 Hz and directed to a double monochromator. A transimpedance amplifier connected in series converted the measured current signal to a voltage signal and finally, the lock-in amplifier filtered and detected the signal despite the noise. The samples were measured with no additional bias light. The EQE data were normalized to the J_{SC} obtained from J-V measurements.

3.4. Numerical methods

Numerical methods were employed to describe the behaviour of simulated thin film samples and solar cells. Two main methods were used: transfer-matrix method (TMM) for planar, homogenous layers and more computational demanding rigorous coupled-wave analysis (RCWA).

3.4.1. Transfer-Matrix Method

This method describes the propagation of light by assigning a matrix that connects the amplitude of the electric and magnetic- field component of the incident, transmitted, and reflected light while traveling through the given medium. It is a very fast method that relies on implementing Fresnel equations and continuity conditions described by Maxwell's equations. For its low computational consumption power, it is used for solving optimization problems such as thickness and refractive index tuning in complicated optical stacks.

Figure 42a presents electromagnetic wave propagation through a medium as a superposition of two waves travelling in opposite directions on both sides of the medium. The wave before and after propagating through a medium is connected by the following relation:

$$\begin{pmatrix} E_L^2 \\ E_R^2 \end{pmatrix} = M \begin{pmatrix} E_L^1 \\ E_R^1 \end{pmatrix}, \quad (31)$$

where $E_L^1, E_R^1, E_R^2, E_L^2$ are amplitudes of the respective electric field, and M is the transfer matrix.

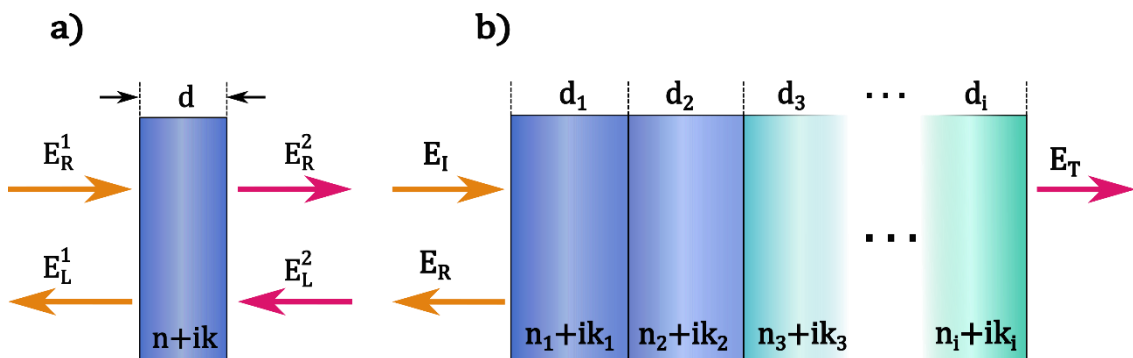


Figure 42 Transfer matrix method scheme. a) Schematic illustration of electric field amplitudes of the EM waves propagating through isotropic medium of thickness d . **b)** Scheme of multilayer optical stack consisting of i layers. E_I, E_R and E_T are the amplitudes of incident, reflected and transmitted electric field, respectively.

In the case of a wave propagating only from the left direction, the amplitudes of E_L^2 is equal to 0. Its amplitude can be normalized to be equal to 1 In this case and are transmission (t) and reflectance (r) coefficients, respectively.. It results in a following equation, describing optical response of the system:

$$\begin{pmatrix} t \\ 0 \end{pmatrix} = M \begin{pmatrix} 1 \\ r \end{pmatrix} = \begin{pmatrix} M_{11} & M_{12} \\ M_{21} & M_{22} \end{pmatrix} \begin{pmatrix} 1 \\ r \end{pmatrix} = \begin{pmatrix} e^{ik_z d} & 0 \\ 0 & e^{-ik_z d} \end{pmatrix} \begin{pmatrix} 1 \\ r \end{pmatrix}, \quad (32)$$

with k_z equal to:

$$k_z = \sqrt{\frac{\omega^2}{c^2} (n_i + ik_i)^2 - k_{\parallel}^2} \quad (33)$$

where M is a propagation matrix for a medium of thickness d with k -vector k_z , wave vector parallel to the propagation direction. k_z depends on: ω – frequency of the incident light, n_i+ik_i – the complex refractive index of the medium and k_{\parallel} – k - vector component parallel to the medium surface.

In the case of a multilayer system, the continuity requirements described by Maxwell's equation must be taken into account when the wave crosses an interface within the system. That puts constrains onto the vector components that are expressed by additional interface 2×2 matrices multiplication, which leads to the following expression for the optical response of the whole system, consisting of N layers:

$$M^{sys} = \left(\prod_i M_{i,L}^{int} M_i \right) M_{N,R}^{int}, \quad (34)$$

where $M_{i,L}^{int}$ – left interface matrix between $(i - 1)$ -th and i -th layer, M_i – propagation matrix of i -th layer and $M_{i,R}^{int}$ – right interface matrix between $(N - 1)$ -th and N -th layers.

In fact, the whole system calculates the phase accumulation and attenuation of the field for a plane wave propagating distances d_i with n_i refractive indices. Thus, the full description of the optical response of the system consisting of N planar, homogenous media is reducible to solving 2×2 matrices multiplication and solving a set of 2 linear equations to obtain r and t coefficients, according to **Equation (32)**.

All presented numerical simulations in **CHAPTER 4**. were conducted using the already implemented TMM method in *tmm* python library written by Steven Byrnes [156].

3.4.2. Rigorous coupled wave analysis

This method is developed to efficiently calculate the properties of a system with periodic structures, currently vastly explored for many photonic and optoelectronic devices. This method effectively computes the diffraction efficiencies and diffracted amplitudes of a periodic system, namely diffraction gratings and their stacks. Additionally, it gives transmission, reflectance, absorption coefficients and EM field distribution within the system. The method utilizes the Fourier expansion of the real space into k-space and similarly translates the problem of solving Maxwell's equation in real to Fourier space. For RCWA calculations, the "reticolo" MATLAB implementation provided by Lalanne, Hugonin et al.[157-159] was employed.

This implementation allows to define 3D elementary cell of a periodic structure with $L_x \times L_y \times L_z$ dimensions with a complex refractive index profile, consisting of multiple textures stacked in z-direction and investigate its diffraction properties. Within each texture, the refractive index is constant in direction z, but can vary in x- and y-direction. The RCWA method is of huge importance especially in the solar cells where the angular redistribution of the incident light is a key feature in enhancing the absorption within the active layer. The dielectric constant and electric field (exemplary shown for x-component) can be expressed as Fourier series by the following equations:

$$\varepsilon_r(x, y) = \sum_{m=-\infty}^{\infty} \sum_{n=-\infty}^{\infty} a_{m,n} e^{i(m\mathbf{G}_x+n\mathbf{G}_y)\cdot\mathbf{r}}, \quad (35)$$

$$E_x(x, y, z) = \sum_{m=-\infty}^{\infty} \sum_{n=-\infty}^{\infty} S_x(m, n; z) \cdot e^{-i[k_x(m,n)x+k_y(m,n)y]}, \quad (36)$$

where $a_{m,n}$ are the Fourier coefficients in the expansion within the $\mathbf{G}_x \times \mathbf{G}_y$ the reciprocal lattice of elementary lattice, similar as $S_x(m, n; z)$ are the coefficients of electric field expansion.

By including more m, n terms, Maxwell's equations solution for electromagnetic field distribution, E_x, E_y, E_z is closer approximated. The solution is therefore a set of planar wave basis with different $k_x(m, n)$ and $k_y(m, n)$ values modulated by $S_x(m, n; z)$. The intensities of the S-terms describe the intensity of the mode propagated in the system. Also, it provides direct insight into diffraction powers and propagation direction of each mode.

Figure 43 depicts an exemplary elemental cell with the staircase approximation used, where the whole structure is cut layer by layer and approximated with a step-like boundary.

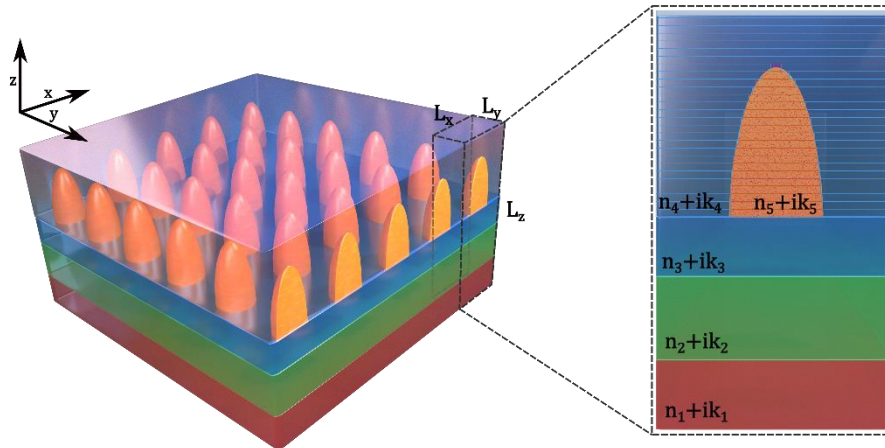


Figure 43 Elementary cell of a diffractive texture used in RCWA calculations. The whole area is sliced by the z -planes, across the refractive index, $n+ik$, is constant. The 3D structure is defined in xy planes.

As the number of these layers grows, the calculation time may be unfeasible to perform the calculations in the finite time domain. Therefore, the layer thickness must be chosen to accurately reflect the structure at the same time not overflow the machine. Also, the calculation time highly depends on the elementary cell size, since we need to include more terms (m, n) in the computation of the solution, exploding into excessive amounts of needed computational power to calculate problems that demand fine discretization of the space. The problem scales as $O(n^3)$, where n is the number of plane waves used. Therefore, a convergence analysis was also done to choose the scaling factor of the cell, ensuring a close approximation of the behaviour of the experimental system with minimal computational resources demands.

RCWA method was used to calculate the reflectance and transmittance of the systems described in:

- **CHAPTER 5. Nanoimprinted Perovskite Solar Cell**, consisting of the thin film perovskite cell and the anti-reflective texture atop
- **CHAPTER 6. Transparent Electrodes with Embedded Nanomeshes**, consisting of perovskite solar cell, TCO layer with nanomesh structure and anti-reflective texture atop

3.5. Summary

This chapter provides an introduction to the two main manufacture methods used in this thesis, which are atomic layer deposition and nanoimprint lithography. With a strong emphasis on the physical and chemical processes occurring during the atomic layer deposition growth along with its prominent applications examples, this chapter can be useful for every student who wants to grasp the fundamentals of this technique to further deepen his/her knowledge. Also, the nanoimprint technique is presented in an approachable way, showcasing the entire process chain from the design to obtaining the final structures reproduced in the photoresists.

Besides, the main characterization techniques are explained in detail and stated with the exact equipment employed in the study with, if applicable, stated explicit formulas that were used to analyze the data. The two numerical methods used throughout the thesis are also described: transfer matrix method and rigorous coupled wave analysis. These two techniques helped to design the optimized optical stacks to help improve solar cells. If possible, the numerical findings are accompanied by the experimental validation.

CHAPTER 4.

ALD-grown ZnO as a Transparent Conductive Electrode

The researches described here were the basis for the subsequent publication: Maciej Krajewski et al., *Structural, Optical, and Electrical Properties of Hafnium–Aluminum–Zinc-Oxide Films Grown by Atomic Layer Deposition for TCO Applications*, ASC Omega, 2023 [160]. The measurements were performed by the author of this dissertation, if not stated otherwise.

4.1. Zinc oxide selected properties

Zinc oxide (ZnO) is a compound naturally found in nature, crystallizing in the hexagonal wurtzite structure. The elementary cell is depicted in **Figure 44**. The dimensions of the elementary cell are as follows: $a = 3.25 \text{ \AA}$, $b = 3.25 \text{ \AA}$, $c = 5.21 \text{ \AA}$. The c-axis is usually a preferential growth during most of the growth types, creating a hexagonal nanorods or nanowires that are joined together, creating a forest-like structure with well-aligned c-orientation. The elementary cell is made of 2 ZnO molecules, where oxygen atoms are placed in tetrahedral configuration, with slightly shorter Zn-O distance along the c-axis (0.19 nm, vs. 0.198 nm respectively).

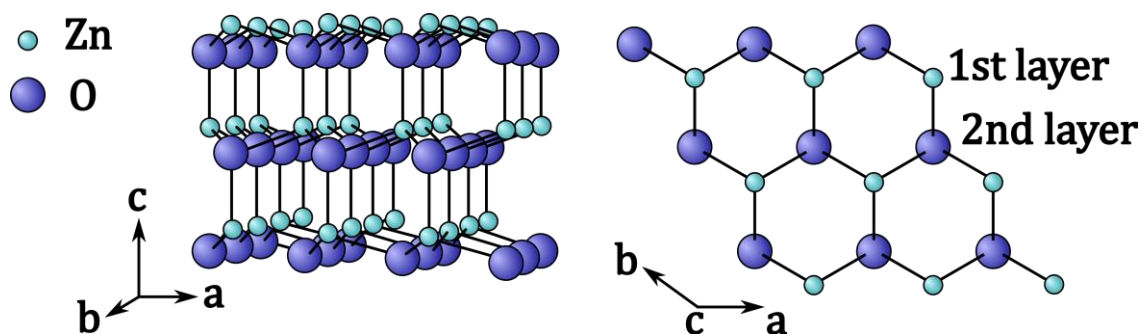


Figure 44. ZnO crystal Structure. Left: the view from side, Right: view from top.

ZnO constitute one of the most popular material employed to transparent conductive electrodes role. It exhibits a typical in the similar oxide materials n-type conductivity with intrinsic charge concentration exceeding 10^{19} cm^{-3} . and a direct bandgap of 3.3 eV at room temperature. These features make it both a very good electrical conductor remaining transmissive in the visible range. Additionally, both of these properties can be varied in the wide range by an appropriate doping, what is the subject of the following sections. Due to wide bandgap, the main source of the free charges are the intrinsic or induced point defects present in the lattice structure that disrupt the ideal crystal structure by displacement or removal of the atoms [161-163]. Zinc oxide exhibits an abundance of different defects, placed at different energy levels in the band gap. **Figure 45.** illustrates this rich landscape along with the estimated ionization energies of each of the donors. The exact energy of each impurity is still a matter of an extensive debate and varies, depending on the author claiming these values. Within this thesis, the adopted notation is the Kröger–Vink's.

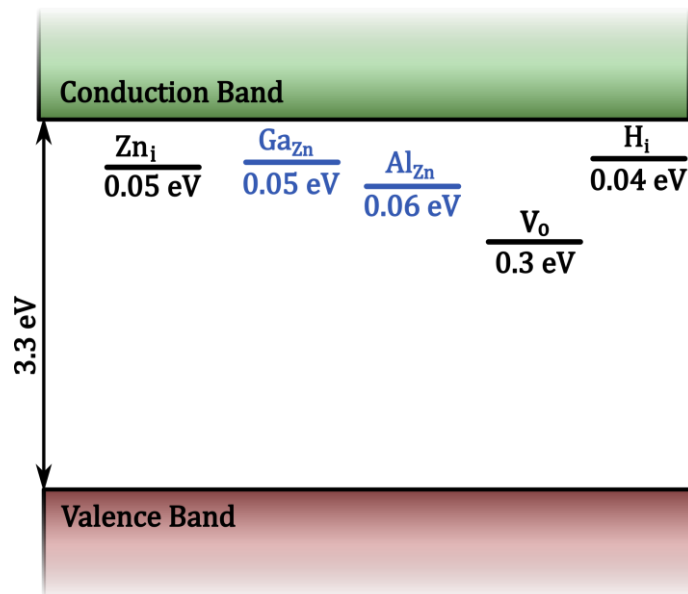


Figure 45. ZnO valence and conduction bands energy levels along with the most commonly met donors and their positions in the bandgap. The bars indicates the energy levels of the either intrinsic or extrinsic donor.

The intrinsic point defects consists of vacancies, interstitials and antistites. In case of ZnO there are six possible point defects that determine the electrical properties of the material. These are denoted as V_{Zn} , V_{O} , Zn_i , O_i , Zn_o and O_{Zn} and can also exhibit varied charge values, depending on the ionization level. Due to the

much lower energy formation of donors and thus their higher concentration, the achieving of p-type ZnO is challenging and demands a lot of precise engineering and tailored growth conditions [164]. The dominant defect responsible for intrinsic n-type doping in ZnO is according to many authors either interstitial zinc atom or oxygen vacancy [165-168]. This matter itself raises a lot of divided opinions and is still under discussion which one holds more significance. Another important element that contributes to the conductivity is hydrogen atom, which is often incorporated in the lattice during growth from vapours, adding one loosely bound electron [169]. **Figure 45** shows also some of the extrinsic dopants like Al^{3+} and Ga^{3+} . These dopants are substituted to Zn position and contributes one extra electron, comparing to Zn^{2+} . The influence of these dopants on the optoelectrical properties of ZnO is discussed in the subsequent sections of this chapter.

4.2. Aluminum doped zinc oxide ALD growth

Zinc oxide stands out as a semiconductor with a very good conductivity whose properties can be easily tuned by introducing various dopant atoms into its lattice structure. Numerous studies have demonstrated successful doping within the low concentration range (below approximately 7%) using metals from the IIIA group, such as Al, Ga, and In [170-175], transition metals like Ag, Cu, Mn [176-178] and even rare earth elements such as Ce and Er [179,180]. In these cases, the introduced metal substitutes the zinc atom within the structure, thereby contributing an additional ionized electron to the conduction band. Among the commonly employed dopants, aluminum is one of the most prominent element [181,182], as it enables injecting additional electrons into the conduction band through a precise controllable process. Besides, aluminum holds significance as a cation due to its abundance, affordability and non-toxicity with well-established track-record of its usage in transparent conductive oxide applications. The primary objective of this chapter is to demonstrate a growth of aluminum-doped zinc oxide (AZO) thin films that are not only highly conductive but also transparent using atomic layer deposition technique. Furthermore, these studies aim to explore the widest possible doping range, achieving the most versatile tuning of optoelectronic parameters.

4.2.1. ZnO growth parameters optimization

The atomic layer deposition growth dynamics and in consequence the resultant material structure and properties, highly depend on a several growth parameters governing the physics within the reactor volume. Through the optimization process, one of the main objective was to adjust the growth conditions to obtain the samples exhibiting optimal performance in terms of both electrical and optical parameters. The parameters that have been subjected to adjustment include:

- Growth temperature
- Precursor pulsing time
- Precursor purging time
- Aluminum dopant content

These parameters spans a multidimensional space of which experimentally probing step-by-step is unfeasible to conduct. However, this exhaustive exploration is not necessary, since the relevant trends in the samples' behavior can be revealed by isolating and varying a single parameter while holding all others constant. The literature provides a very wide range of recommended values for these parameters, however their transfer to a specific ALD system is not straightforward. Precursor dosing and purging times are influenced by factors such as the volume of the reactor chamber, length of the lines delivering the chemicals, and also pump efficiency. Similarly, the growth temperature and aluminum dopant content vary based on system limitations and the specific applications being targeted. Therefore, this process needs to be tailored for each specific ALD system and grown material, despite the abundance of literature data.

Once an optimized value for the varying parameter is reached, subsequent parameters are tested, building upon the knowledge on previously optimized parameters. This approach allows to reach the desired properties without the need of excessive number of growths.

Table 2 shows these parameters along with their respective variation ranges used during the growths. The dataset collected for the optimization process comprises over 100 individual growths with over 600 samples measured. Such an extensive amount of data provides a statistically significant number of measurements, effectively mitigating chance errors and outliers. **Figure 46 – Figure 49** show the collected data illustrating the relationship between a

specific parameter and its influence, disregarding the impact of other parameters. The electrical parameters were measured using the method described in **Section 3.3.4**. As the thickness of the sample introduces another variability in its structure, all the samples had the similar thickness of approximately 200 nm to minimize this effect.

Table 2. Investigated growth parameters and their respective ranges.

Growth Parameter	Range
Aluminum dopant content	0 – 15 %
Temperature	120 – 250 °C
Diethylzinc (DEZ) pulsing time	50 – 500 ms
Purging time	2 – 12 s

The parameter that significantly influences the structural and optoelectronic attributes of the sample is the growth temperature. As has been discussed in **Section 3.1.**, the temperature determines the growth mode in the reactor, changing the occurring reaction speed and mobility of precursors molecules. **Figure 46.** presents electrical parameters of the grown samples for varying growth temperature for each measured sample.

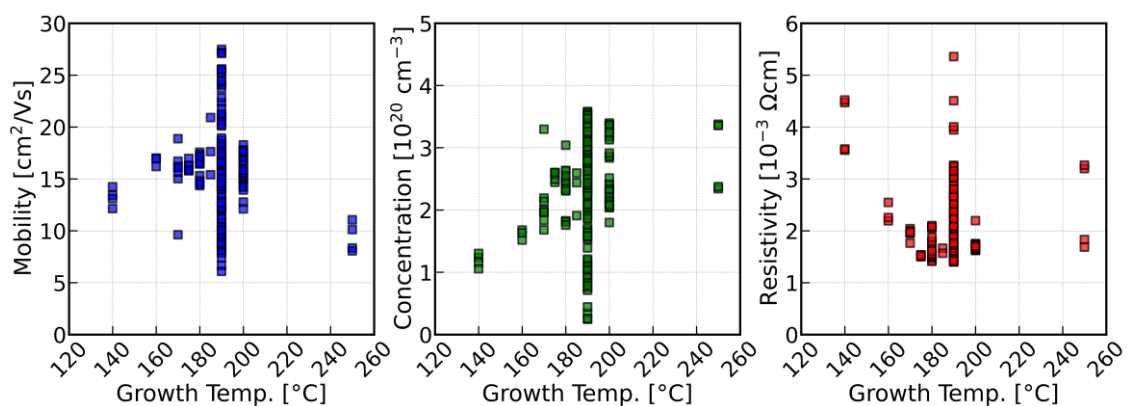


Figure 46. Electrical parameters of ZnO and AZO thin films for varying growth temperatures. These graphs disregard the influence of other growth parameters.

A temperature that is too low leads to reduced reactivity of the precursors, in consequence obtaining the insufficient concentration of incorporated atoms, not

yielding the whole monolayer. On the other hand, excessively high temperature may trigger decomposition of the precursor before it reaches the ligands on the surface or remove the ligands already present on the surface that are important for the next step reaction. Therefore, it is crucial to find a balance where the full monolayer is obtained with intended subsequent reaction steps.

Note that **Figure 46** presents the data without other growth parameters kept constant, thus there are some processes with ranging precursor dosing and purging time, influencing the outcome. The samples exhibit a wide range of mobility values, spanning from 5 to 28 cm²/Vs. Interestingly, at 190 °C, the results show considerable divergence due to the biggest ensemble of measured samples, encompassing both different free carrier concentrations and mobilities. Carrier concentration achieve levels of 3.7×10²⁰ cm⁻³ for the optimal temperature range of 190 – 200 °C. As can be seen, the lowest resistivity, being the product of the concentration and mobility, is obtained for the same temperatures around 190 – 200 °C, indicating the most favorable conditions for the desired electrical properties.

Figure 47 presents the electrical parameters for different precursor dosing at 190 – 200 °C temperature, which was established as the best performing one.

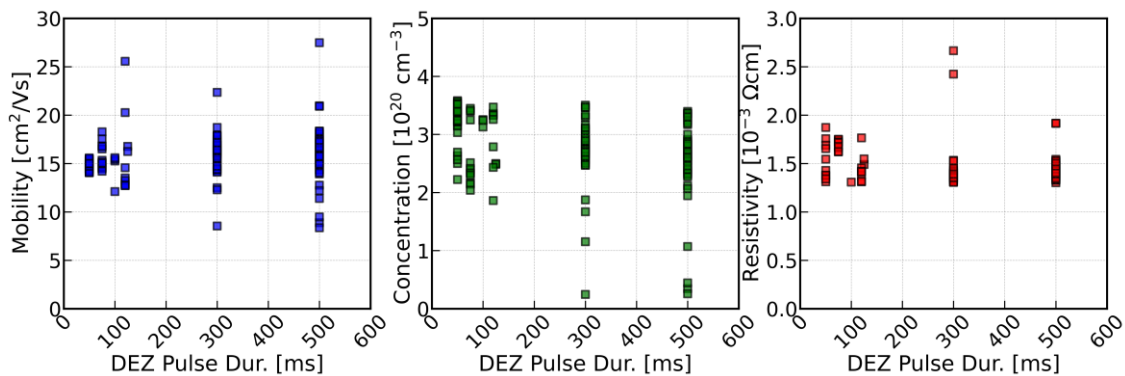


Figure 47. Electrical parameters of ZnO and AZO thin films for varying diethylzinc precursor pulse duration at 190 – 200 °C growth temperature, 200 nm thickness.

The pulsing time determines the duration for which the precursor valve is open, allowing the carrier gas mixing with precursor and then enter the chamber. When the precursor pulse is too short, the dosage of the chemical is insufficient to cover the whole surface, leading to not-saturated process – the surface coverage remains low, resulting in an incomplete monolayer formation. Conversely, pulses of excessive duration, introducing too much precursors amount, are not recommended either. This excessive dosing not only leads to unnecessary

precursor consumption but also complicates the purging of the precursor molecules thus, hindering the growth of the material, similar as too short purging times. As explained in **Section 3.1.**, that may sometimes lead to deterioration of the quality of the growing monolayers. Therefore, we need to minimize dosing to the point when the stable, monolayer and pinhole-free growth is attained.

Finding a balance in precursor pulse duration is therefore crucial to ensure optimal surface coverage without chemical wastage. As depicted in the figure, there is no visible correlation between the precursor dosing time and the electrical parameters, unlike for growths at different temperatures. For instance, there is no significant resistance minimum shift between 100 and 500 ms of DEZ precursor dosing time. Similarly, the concentration values remain consistent regardless of the dosing time. A slight discrepancy is noticeable for mobilities, where 50 and 75 ms seems to have a detrimental effect on the achieved maximal values. Also, some of the samples exhibit slight undersaturation, depending on the position within the reactor chamber. To ensure stable growth and avoid excessive precursor dosage, the optimal diethylzinc precursor has been determined to be 120 ms.

Similar to pulsing, the optimization of purge duration time was investigated. The purge time should be sufficient to remove all residual molecules of the preceding precursor but at the same time, it should not excessively elongate the growth process. As depicted in **Figure 48**, purge times below 4 seconds appear to result in slightly lower values in concentration or mobility, probably due to limited cleansing of residual molecules. Although, the difference in the minimum resistivities are not striking, for precautionary measures, asserting removal of the reaction by-products and lingering precursor, the optimal purge duration has been set at 8 seconds. Again, note that **Figure 48** shows measurement points with varying pulse dosages that may cause diverse results.

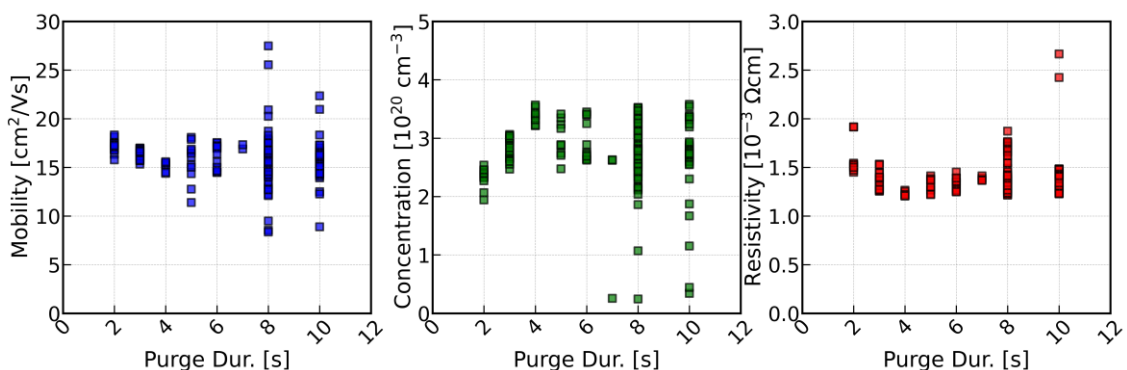


Figure 48. Electrical parameters of ZnO and AZO thin films for varying purge duration at 190 – 200 °C growth temperature, 200 nm thickness.

Upon necessary optimization of those parameters, we may study the properties of the obtained films. This enables a comparative analysis as the dopant concentration and type are varied. In this thesis, the following growth parameters are used while growing all the samples, presented in **Table 3**.

Table 3. Established optimal growth parameters for AZO thin films using atomic layer deposition.

Growth Parameter	Range
Temperature	200°C
Diethylzinc (DEZ) pulsing time	120 ms
Trimethyloaluminum (TMA) pulsing time	120 ms
Purging time	8 s

The impact of cation dopants introduced into the crystal lattice of zinc oxide defines the primary point of interest within this study and is significantly extended in **Section 4.3**. Here, the primary trend of behavior is highlighted. By keeping the other growth parameters constant, the influence of doping aluminum atom is clearly seen. **Figure 49** shows the electrical parameters for varying aluminum content after optimizing other parameters. Doping with aluminum to create a ternary compound is realized by adhering to the method described in **Section 3.1**, where the trimethylaluminum pulse is introduced between the diethylzinc and water cycles to achieve the desired zinc-aluminum ratio. Note that this number express the ratio between the TMA and DEZ precursors pulses and it controls the doping ratio within the resultant material, however in principle it does not mean the exapt atomic ratio between aluminium and zinc in the resultant material.

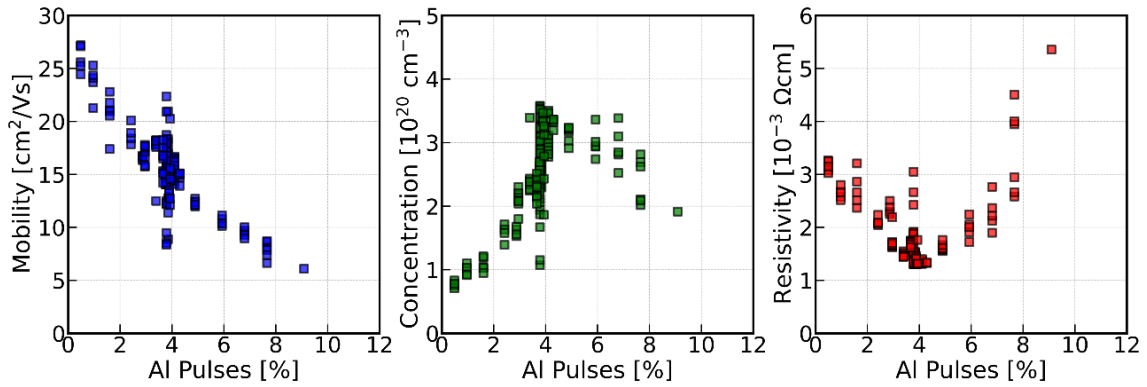


Figure 49 The electrical parameters obtained for varying aluminium cation pulse ratio with all the other growth parameters kept constant at the optimum, previously established levels.

Starting with an almost pristine ZnO material, the mobility is at its maximum, while the concentration remain below 10^{20} cm^{-3} , resulting in relatively high resistivity of approximately $3 \times 10^{-3} \Omega \text{ cm}$. As doping increases, the mobility decreases due to a higher scattering centers concentration. However, the introduction of aluminum cations contributes additional electrons to the conduction band, ultimately reducing the resistivity. At approximately 4% this effect reaches a saturation and with monotonically declining in the mobility, the overall resistivity starts to grow, quickly reaching high values. In **Figure 49**, some outliers are also visible, especially pronounced at around 4% of aluminum content. These discrepancies should be regarded as the effect of the substantial number of samples measured and in principle they do not contradict the general trend revealed within the study and optimal growth parameters established.

4.2.2. Structure and optical properties

Thin film samples of doped zinc oxide, each 200 nm in thickness, featuring varying aluminum dopant content, were grown. **Figure 50**. presents the surface morphology of the selected samples. Across all structures, randomly scattered, double-wedge crystallines are present, resembling grains of rice with approximately 50 nm in length. As a result, a tight-packed picture of disordered polycrystalline structure is formed. This picture seems to be maintained across wide range of doping levels. After the certain doping threshold (approximately 15%), a notable change in morphology occurs, transforming the crystalline grains into more circular and smaller shapes. That may stems from the excessive amount

of extrinsic doping in the lattice, which leads to the deterioration in the crystal quality.

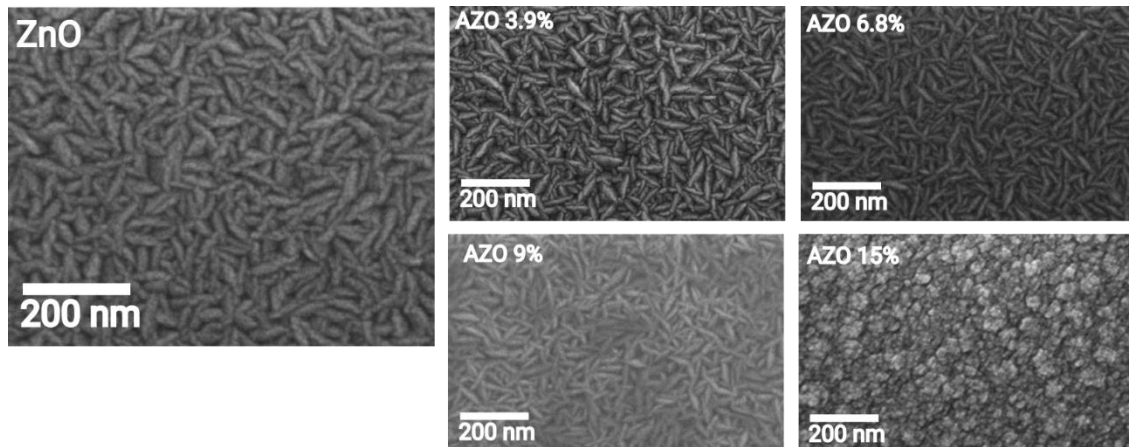


Figure 50. SEM images of zinc oxide with various aluminum dopant content. The pictures reveal the morphology of the thin films and the distortion in the lattice visible after critical doping is reached.

To trace the growth dynamics and grains formation process, the depositions of materials with varying thickness were conducted. In **Figure 51**, the morphology of the samples with the same aluminum cation content, equal to 4%, is depicted. This consistency in dopant concentration was maintained to eliminate the influence of different doping levels on the material.

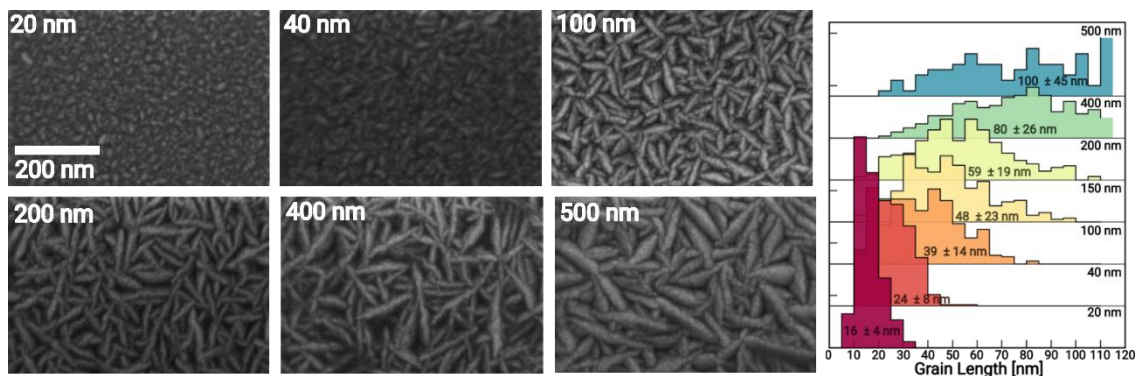


Figure 51. Morphology of the AZO thin films with 4% of aluminum content for increasing material thickness. On the right of each histogram, the average value of the grain length along with the standard deviation is presented.

As displayed, the thin layers of 20 nm and 40 nm thickness show crystal grains in a circular shape, typically not exceeding 25 nm in length along the longer axis in the horizontal plane, as evidenced by the SEM images. However, even the 20 nm

thickness of grown zinc oxide forms the pin-hole free layer, covering tightly the surface. Also, with increased thickness, the grains gradually exhibit an elongated shape, eventually forming the distinctive double-wedge polycrystalline landscape described earlier. **Figure 51** also presents the granulometry studies associated with the specific layer thickness. Additionally, each histogram features the average grain sizes with one standard deviation. The thinnest layer, measuring 20 nm layer exhibits a very narrow histogram with only 4 nm deviation in grain sizes. The histograms shift towards the longer grains with thicker grown layers, reaching 100 nm long grains for 500 nm thick layer. Also, they tend to be wider and more spread, as visible from the relative standard deviation starting from 25% for 20 nm samples and reaching 45% for 500 nm material. These studies reveal that thicker samples consists of grains of bigger sizes, compared to those of 100 nm – 200 nm, which may results in less pronounced grain boundaries scattering that overall has a beneficial effect on the electrical transport properties. **Figure 52** presents SEM cross-sections of 500 nm thick aluminum doped zinc oxide thin films. As visible, the grain morphology seen in **Figure 51** is propagated down to the bottom of the sample, showing the columnar growth mode with clearly oriented direction and order, resulting in overlapping of the grains, visible on the surface. The surface, when seen from tilted angle, reveal that the rough cap of the grains spans only over the small fraction of the whole layer.

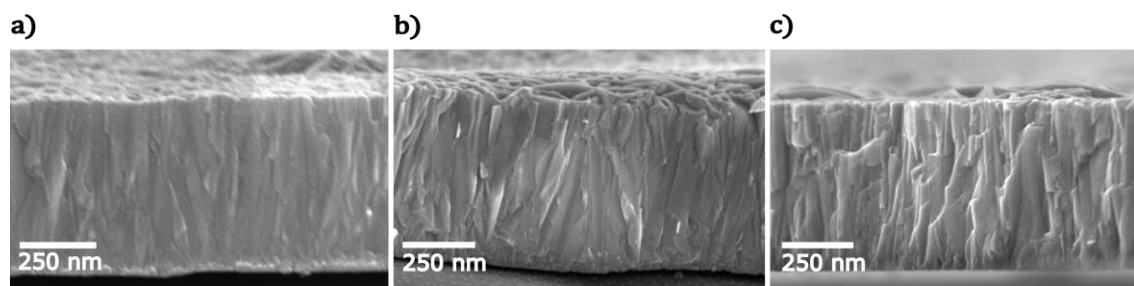


Figure 52. SEM cross-sections of 500 nm aluminum doped zinc oxide (4%) at different angles.

Another crucial property under investigation is the optical transmission in the most relevant range, specifically from 300 to 1000 nm. This range encompasses wavelengths critical for efficient solar cell operation, as it covers the solar spectrum necessary for the functioning of TCEs layers. **Figure 53** depicts the real appearance of the samples with visible changing colours due to varying thickness, whereas **Figure 54** shows the transmission spectra for those layers along with the glass reference spectrum. As seen, the samples exhibit high transparency even for the thicker material layer.



Figure 53. Real appearances of the samples with different thicknesses. The images were taken with the same camera setup and lighting conditions. The white piece of paper for comparison.

The increase in material thickness leads to the appearance of characteristic thin film interference effect with several minima and maxima present in the spectrum. In thinner samples ranging from 20 nm to 40 nm in thickness, the absorption edge experiences only slight shifts, as the exhibited absorption is insufficient to determine a sharp absorption edge. However, in thicker samples, this edge becomes apparent at approximately 350 nm where the attenuation of the transmission begins. Due to their thickness, they exert subtle effects on the transmission spectrum which is particularly evidenced by the convergence with the glass absorption edge at around 280 nm.

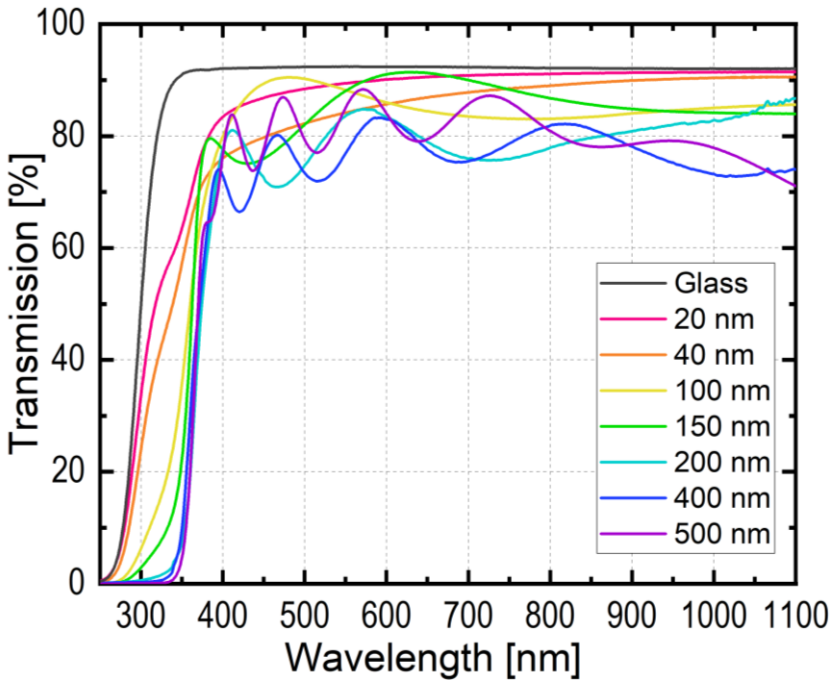


Figure 54. Transmission spectra of 4% AZO thin films for varying thickness ranging from 20 to 500 nm grown on a glass substrate. The interference effect clearly manifested by the maxima in transmission spectra is visible.

A slight decrease in transmission, from the initial 90% for glass to approximately 85% for shorter wavelengths, is visible. As the samples become thicker, stronger absorption in the infrared region is observed, leading to values below 80% transmission. The average transmittance within the commonly used range (around 150 – 200 nm) aligns with findings in existing literature and remains at 86%[87] The study shows that zinc oxide remain transparent even for thicker layers, establishing it as a highly suitable material for TCE applications. In the next section, the interplay between two different dopant cations and the consequences of this approach is discussed.

4.3. Co-doping of aluminium zinc oxide

As described in the previous section, the properties of the transparent conductive oxide films can be widely tuned by changing various factors such as their growth parameters, composition, doping amount, and post-deposition treatment. A careful approach should be taken to establish a precisely tuned material with the desired properties optimized. The properties of singly-doped ZnO have been thoroughly investigated over the last three decades, receiving a deep insight about the resulting alloy. Nevertheless, there still remains undiscovered potential in co-doping ZnO with two elements simultaneously. This approach lead to the growth of quaternary material with novel, not yet known optoelectronic properties, offering new pathways for tuning with additional degree of freedom.

The co-doped ZnO is present in literature and usually promises enhanced properties comparing to the singly-doped version. For instance, Kang et al.[183] have shown that Al/F codoping passivates trapping defects such as oxygen vacancies and thus increase the mobility of the sample resulting in a exceptionally low resistivity equal to $5 \times 10^{-4} \Omega\text{cm}$. Besides, elements pairs comprising of Al/Sn, Al/Ti, Al/Th, or Al/Mn were also reported to exert beneficial influence on the material optoelectronic properties. The beneficial influence of codoping using two elements from different groups, such as IIIA and IVB is also present in the literature [184-190]. Simultaneously introducing elements from those two groups may not only lead to enhanced long-term stability in air but also further promote the mobility and concentration of the carriers in the material. Therefore, this chapter demonstrates a co-doped zinc oxide employing two different cations by combining elements from IIIA and IVB groups i.e. quaternary hafnium-aluminum zinc oxide films (HAZO), utilizing the ALD technique.

Aluminum is widely used in the industry, whereas the utilization of hafnium is presently infrequent in the literature, although there are several arguments in favour of the implementation of hafnium that justify the investigation of this element. Some reports investigate doping ZnO with IVB elements such as Hf, Ti, and Zr, which enhances the material's electrical stability, modifies the conduction band minimum, and fills the oxygen vacancies states. Additionally, it contributes four valence electrons stemming from $5d^26s^2$ electron configuration. As Hf^{4+} ion substitutes Zn^{2+} ion, which gives 2 additional electrons that contributes to free carrier concentration. Hf^{4+} ion possess also atomic radius close to that of Zn^{2+} (0.78 Å and 0.74 Å, respectively). The incorporation of this cation is less detrimental to the crystal lattice, since it causes less lattice constant changes. Hence, exploring the potential of co-doped ZnO emerges as a highly intriguing and valuable research activity, opening door to a new realm of material design. In the following sections, the surface morphology, optical and electrical properties are discussed over a wide range of dopant concentrations to optimize the structure and compare its properties with singly doped zinc oxide. The obtained material might hold significant importance as a TCE for photovoltaic applications. As the main goal of this thesis is to propose the solutions for enhanced photovoltaic architecture, such improvement may lead to better photogenerated carrier collection and in result, higher current density.

4.3.1. Samples and Morphology

Thin films of singly-doped (aluminum zinc oxide) and co-doped (hafnium-aluminum zinc oxide) were grown for varying doping of cations. **Figure 55** presents the scheme of the pulses sequence during the growth. Note that the dopants, due to inter-diffusion, are uniformly or close to uniformly distributed in the structure and do not create planar layers. Co-doped zinc oxide is doped with the same number of both precursors being introduced in the material which means that HAZO 6% consists of 3% Hf and 3% Al cycles. We employed two thickness: 170 nm and 570 nm. The first one is in the range of optimal transmission and it is commonly used as TCO layer in numerous applications. The second one, thicker has been grown to demonstrate the resistivity decrease in even more pronounced way, since it is well known that thicker oxide samples exhibit lower resistivities.

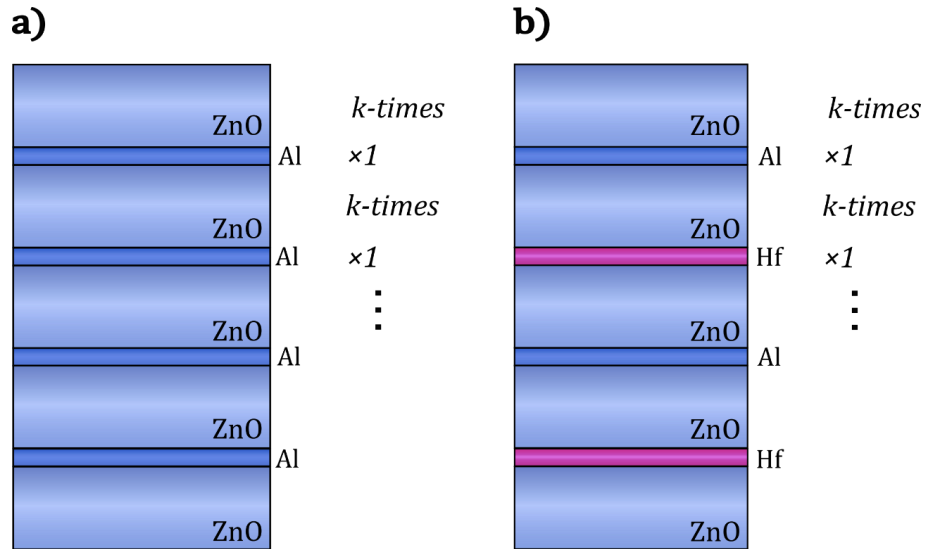


Figure 55. Sample growth scheme with varying dopant content of a) ZnO:Al (AZO) and b) ZnO:Hf:Al (HAZO). By controlling the k -number the right doping amount can be adjusted.

The samples were grown after the optimal growth parameters have been established. The TEMAH (tetrakis(ethylmethylamido)hafnium) precursor was heated to 80 °C to provide sufficient vapor pressure for this growth to occur and the pulse time was selected to be 500 ms. **Figure 56** presents the morphology of the selected samples with varying dopant contents. As can be seen, the 170 nm thick samples exhibit similar grain structure, resembling elongated double wedges with around ~50 nm in length, previously seen in **Figure 51**. It is hard to point out a pronounced distinctions between AZO and HAZO samples, as they exhibit similar morphology across wide range of dopant incorporated. The granulometry studies were conducted to reveal a more subtle differences between those two materials, especially in the grain sizes. Herein, the horizontal grain lengths (longer axis of the grain) visible in SEM images are investigated. The average grain size values distributions are depicted in **Figure 57**, with both materials demonstrating stable grain lengths throughout the studied dopant concentration in the range of approximately 45 – 58 nm.

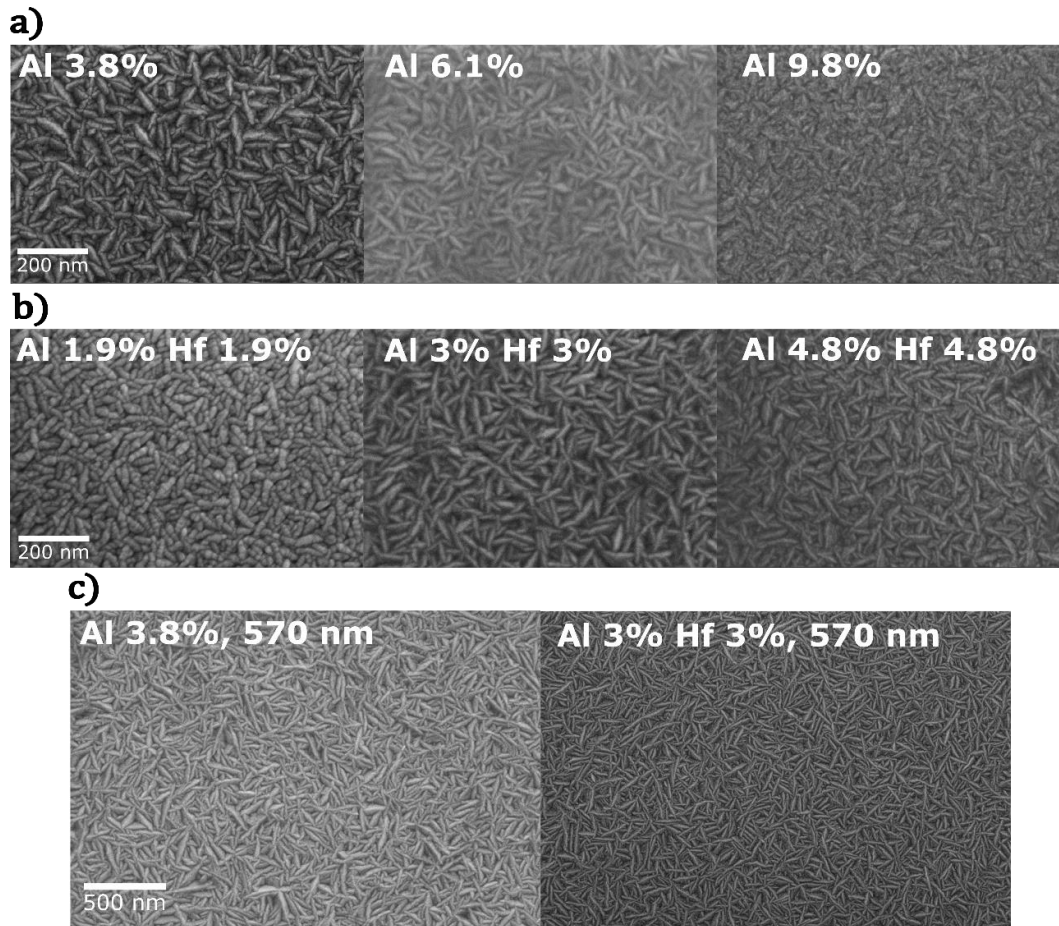


Figure 56. SEM images of ALD-grown thin film ZnO samples. a) – b) AZO and HAZO samples with different Al or Hf cation content and HAZO 170 nm thin films samples grown on glass. c) AZO and HAZO samples of 570 nm thickness with 3.8% and 6% of dopant contents, respectively.

The shape of the received histograms is similar throughout the studied samples, with a clearly marked middle point. The pure ZnO sample presents an average grain length of approximately 58 nm, slightly higher than the AZO and HAZO samples which exhibit an average of 48 – 52 nm and 55 – 57 nm, respectively. The size distribution of AZO grains is slightly more varied, showing a relative standard deviation ranging from 28% to even 48% for some AZO samples, whereas the HAZO samples typically demonstrate lower relative variance in grain sizes, with a very stable standard deviation in the 30% – 34% range.

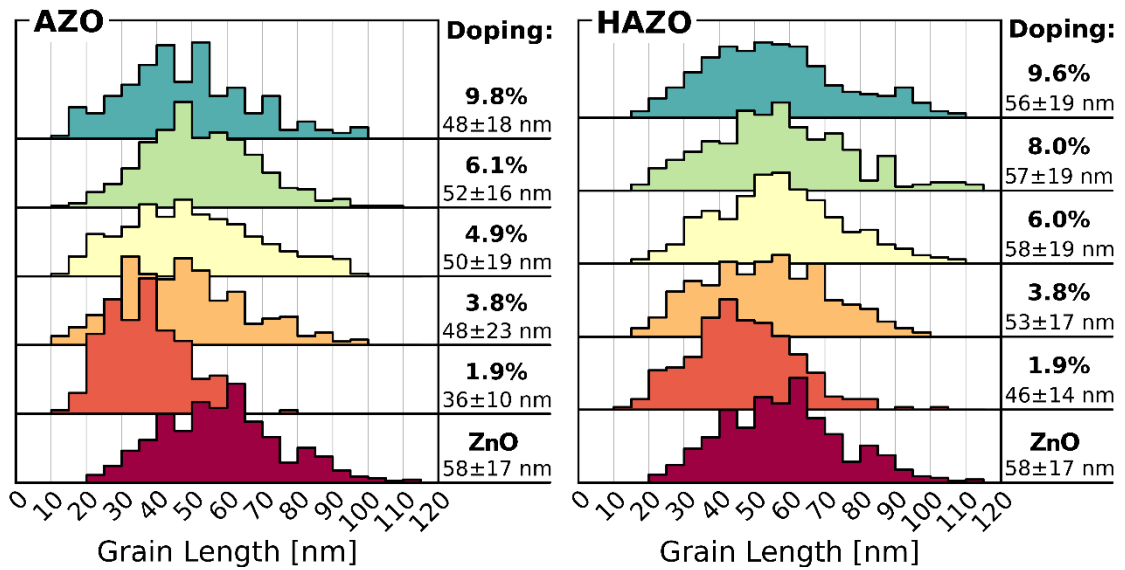


Figure 57. Granulometry results obtained from SEM images for both types of dopant samples with varying concentrations. On the right of each histogram, the average value of the grain length along with the standard deviation is presented.

As a result, co-doped samples exhibit consistently longer grains, therefore with less pronounced grain boundaries and less scattering centers. The one hypothesis regarding this notable distinction in growth modes is the ion radius mismatch which is very low for Hf^{4+} ion, thereby streamlining the process of grain formation, in contrary to Al^{3+} ion. In the case of thicker samples (**Figure 56c**), the grains are notably longer, reaching around 100 nm with a very similar, previously seen double-wedge polycrystalline landscape.

Another technique used to investigate the morphology, in particular the surface roughness, of the samples is atomic force microscopy (AFM). The surface roughness is investigated with respect to the dopant concentration (depicted in **Figure 58**). SEM and granulometry studies reveals that dopant concentration can influence the grain dimensions and thus the roughness of the materials. The root mean square (RMS) roughness values of 2.0 – 2.3 nm and 2.7 – 3.4 nm were established for AZO and HAZO samples, respectively, aligning with the values reported in the literature [191,192]. The introduction of hafnium ion in the lattice structure, seemingly affects the surface roughness, increasing it slightly. Both morphology studies indicate that aluminum and hafnium are incorporated in similar manner, without forming non-stoichiometric aggregates and other phases. The correlation between grain sizes and dopant percentage implies that surface roughness could also be influenced by the organization pattern of these grains, including their steepness and directional alignment.

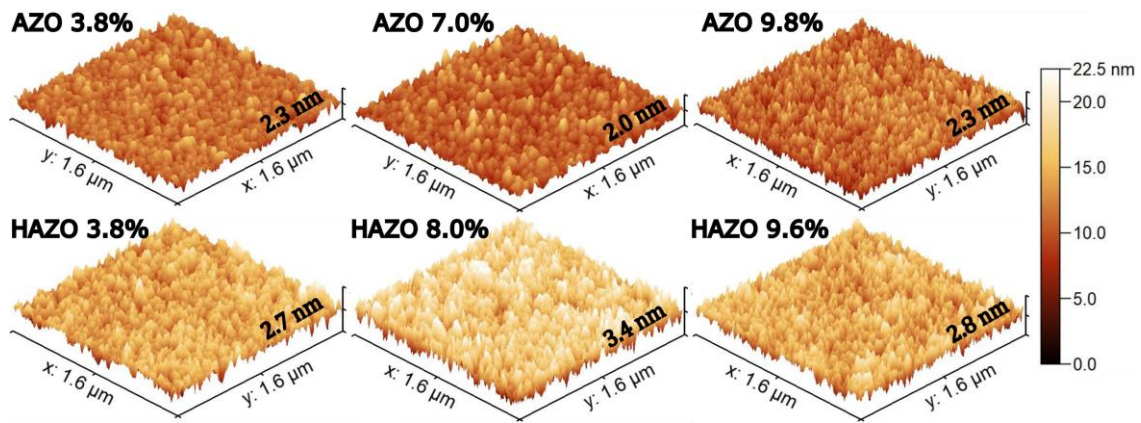


Figure 58. Atomic Force Microscopy images in 3D projection of the samples, showing the surface morphology and roughness of each sample with different dopant concentrations. On the side of each image, the RMS roughness is stated.

Besides the surface, the crystal structure is influenced as well by the amount and type of the used dopant. The polycrystalline nature of the grown samples has been confirmed by XRD studies. **Figure 59** presents diffractograms of the thin film samples with varying dopant content.

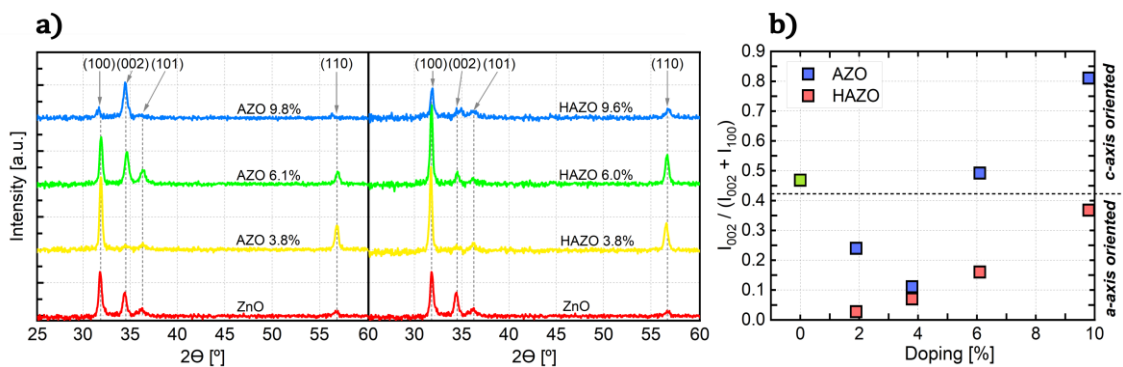


Figure 59. X-Ray Diffraction studies. a) Diffractograms of as deposited AZO (left) and HAZO (right) selected thin films on the glass substrates. ZnO results are shown as the reference. **b)** Intensity relationship between (002) and (100) peaks in AZO and HAZO samples showing the preferred orientation of the crystallites in the thin film. The dotted line represents the theoretical threshold for either a- or c-axis oriented sample. Pure ZnO is marked as a green square.

The absence of other peaks attributed to Al_2O_3 or Hf_2O phases, as well as not altering wurtzite structure indicates the successful incorporation of cations even for quite high concentration, reaching approximately 10%. The diffraction peak positions are in agreement with the reference ZnO pattern taken from JCP2.2CA 01-079-2205. The introduction of dopants does not notably shift the peaks, which remain stable across wide range of the concentration, close to the initial position of

pure ZnO material. Some subtle shifts are present for the (002) and (110) peaks at 6.1% and 9.8% aluminum content in AZO samples, possibly due to the slight lattice changes. Taking into account that ionic radius of Hf^{4+} is very similar to Zn^{2+} ion which it substitutes in the crystal lattice, its incorporation does not cause significant stress and significant lattice alterations. Although the introduction of Al^{3+} ions theoretically induces compression stress, there is the possibility of the expansion of the lattice in case of interstitial incorporation of Al^{3+} ion[193]. None of such behavior is observed in this case, therefore we may conclude that most of the ions are incorporated as the substitutional positions. Those findings are also coherent with literature reports where even the highly doped structures do not exhibit much lattice changes (above 1%)[184,194]. The relative intensity of the (100) and (002) peaks corresponds to the preferred growth direction, providing insights into crystallite vertical or horizontal orientation. The variation in the intensity of these peaks indicates the dominance of different growth orientations, depending on the dopant concentration and the material. **Figure 59b** presents the intensity relationship between those two peaks. Dominant intensity of (100) peak is related to the a-axis preferred crystallites (horizontal growth), whereas (002) is the indicator of c-axis oriented growth (vertical). As can be seen, the HAZO samples remain in the realm of a-axis growth, regardless of the doping level. On the other hand, hafnium addition seemingly leads to preferred a-axis growth. Furthermore, the absolute intensity of the peaks is attenuated with the higher dopant addition, implying an ongoing amorphization process. This observation aligns with the SEM images and electrical transport parameters, which also indicate the deterioration of the crystalline quality for high dopant concentrations.

4.3.2. Electrical properties

The electrical transport properties are described with the well-established parameters, such as carrier mobility, concentration and resistivity. These fundamental physical values primarily define the material's suitability as a TCE. **Figure 60** presents these parameters for two differently doped materials with varying cation content along with undoped ZnO results. As anticipated, the mobility displays a linear decrease from $28 \text{ cm}^2/\text{Vs}$, recorded in the sample without extrinsic doping, to around $6 - 8 \text{ cm}^2/\text{Vs}$ at higher doping ratios. This decline mostly stems from the abundance of ionized dopant atoms acting as scattering centers, thereby leading to the higher scattering probability [195].

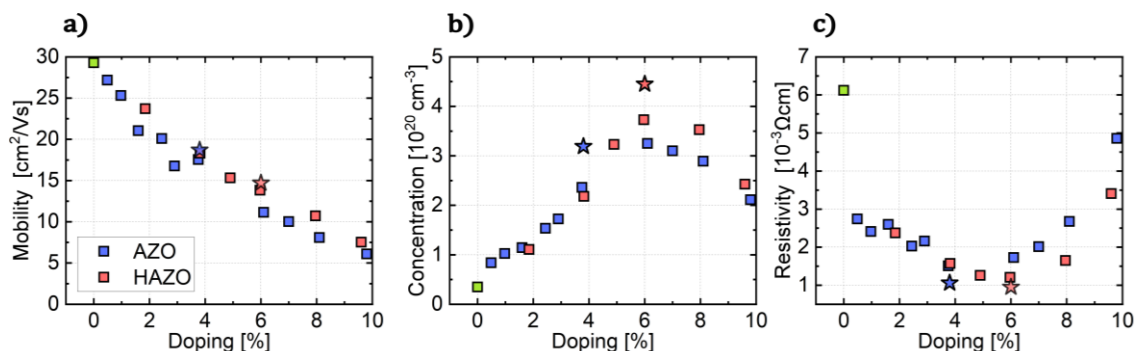


Figure 60. Electrical parameters of the studied materials for varying cation metal content. Pure ZnO sample (i.e. with 0% doping) is indicated with a green square. The stars indicate the 570 nm AZO (blue) and HAZO (red) samples.

Furthermore, increasing the free carrier concentrations intensifies carrier-carrier scattering, thus reducing the mobility. The results clearly indicate that at the comparable doping level, HAZO consistently achieves higher mobility than AZO. These results suggest the beneficial influence of maintaining larger grains size, that have been shown in granulometry studies in **Figure 57**. While the disparity is not very substantial, as it reaches approximately 3 – 4 cm²/Vs across the most relevant doping content, it beneficially affects the performance of the new proposed material. Incorporating 3⁺ or 4⁺ valence cations in both materials results in remarkably high free carrier concentrations. Starting from approximately 2×10¹⁹ cm⁻³, it reaches levels as high as 3.3×10²⁰ cm⁻³ and 3.7×10²⁰ cm⁻³ for AZO 6% and HAZO 6%, respectively. Further doping the materials fails to provide additional free carriers, as the carrier concentration starts to decline, possibly due to the introduction of a significant number of trapping states, that effectively limits the growth in carrier concentration. However, once more, co-doped zinc oxide exhibits slightly more favorable values for comparable doping, mainly attributed to additional electron provided by Hf⁴⁺ ion.

The resistivity of the films – resulting from the product of two formerly discussed values – demonstrates a V-shape when plotted against varying dopant concentration. At first, the resistivity decreases with increasing cations content, reaching minima corresponding to the previously discussed concentration maxima. Specifically, the resistivity minima are observed at 4% for AZO and 6% for HAZO, reaching 1.5×10⁻³ Ωcm and 1.2×10⁻³ Ωcm, respectively. Beyond these doping ratios, the resistivity starts to grow due to simultaneous decrease in mobility and carrier concentration. Therefore, the optimal electrical properties have been established at

6% of cation doping level for co-doped HAZO samples, surpassing the singly-doped AZO.

Additionally, to explore further conductivity enhancements, two additional growths were performed for optimized parameters on substantially thicker samples (570 nm) for both AZO and HAZO materials. These samples yielded even lower resistivities values, equal to $1.05 \times 10^{-3} \Omega\text{cm}$ and $9.5 \times 10^{-4} \Omega\text{cm}$ for AZO and HAZO samples, respectively. This result is understandable taking into account the the crystal quality improvement with thicker samples. **Table 4** provides a summary of the electrical parameters.

Table 4. Electrical parameters (carrier concentration, mobility and resistivity) of the grown TCO samples with varying thicknesses and doping.

Material	Thickness [nm]	Doping [%]	n [cm^{-3}]	μ [cm^2/Vs]	ρ [$10^{-3} \Omega\text{cm}$]
<i>AZO</i>	170	0	0.35	29.3	6.12
		1.9	1.14	21.1	2.60
		3.8	2.36	17.5	1.51
		6.1	3.25	11.1	1.72
		9.8	2.11	6.1	4.86
<i>HAZO</i>	170	1.9	1.11	23.7	2.37
		3.8	2.18	18.3	1.57
		6.0	3.73	13.8	1.21
		9.6	2.43	7.5	3.41
<i>AZO</i>	570	3.8	3.19	18.7	1.05
<i>HAZO</i>		6.0	4.45	14.7	0.95

4.3.3. Optical properties

The optical properties of the thin films, namely the transmission and reflectivity are crucial attributes that determine the further applicability of the material as a TCE. Transmission spectra of the selected, representative samples are shown in **Figure 61**. for AZO and HAZO samples with different dopants concentrations along with the glass reference spectrum. The samples regardless of the dopant type exhibit an average transmittance of 86% in the 300 – 1000 nm wavelength range.

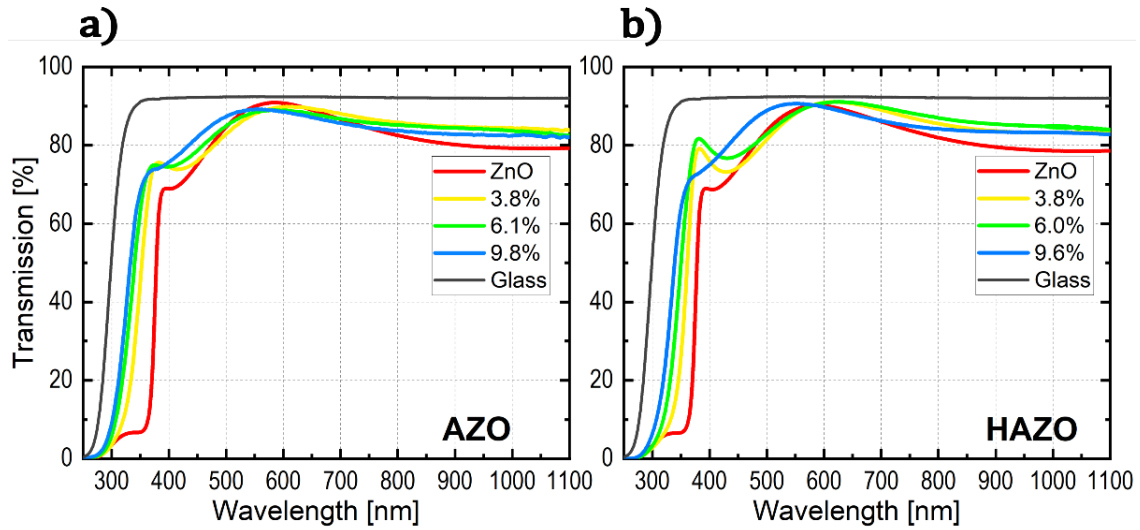


Figure 61. Optical transmittance spectra of: a) AZO and b) HAZO thin films with different dopants concentration deposited on a glass substrate (included in graph).

As the cation concentration increases, a noticeable blueshift of the absorption edge is visible due to bandgap widening, caused mostly by the Burstein-Moss effect since the free carriers of significantly increased concentration fill the lower states in the conduction band, disallowing typically available interband transitions. Consequently, this results in an increase in transmission within the 400 – 500 nm range. To precisely quantify this widening, the transmission spectra were plotted in Tauc convention (**Figure 62**), following the relation:

$$\alpha h\nu = A(h\nu - E_g)^{1/2} \quad (37)$$

where α is the absorption coefficient, h is the Planck constant, ν is the radiation frequency and A is the proportionality constant. The exponent value equal to $\frac{1}{2}$ denotes direct allowed transitions, characteristic for direct energy gap

semiconductors, which is the case for ZnO. Here, the assumption that ZnO bands are approximately parabolic is implemented, which is in accordance with many reports for low dopant concentration [181,184,196,197].

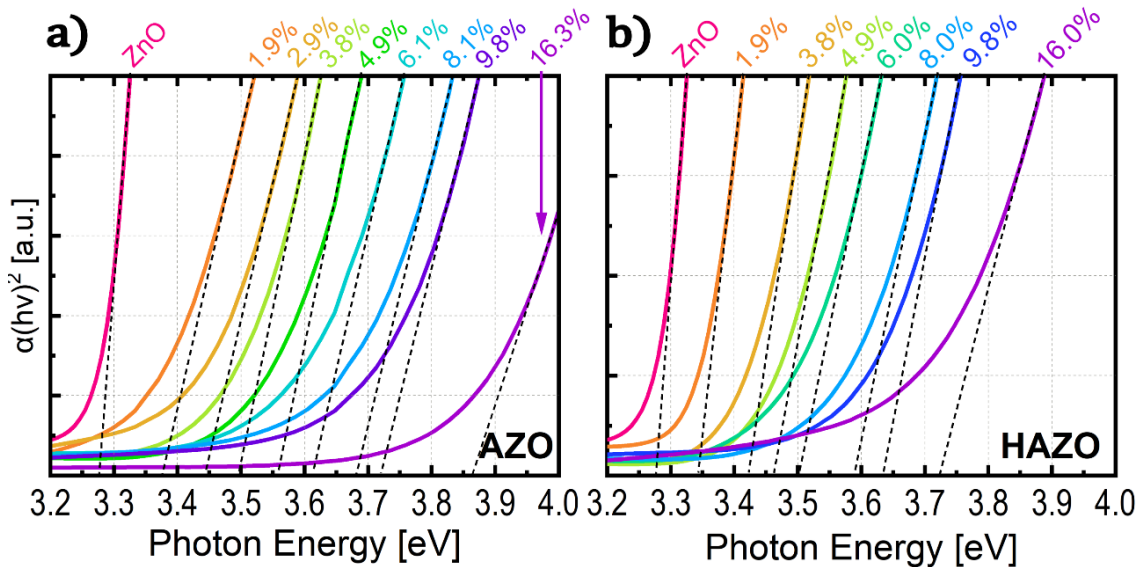


Figure 62. Tauc plots obtained from transmittance spectra of a) AZO and b) HAZO thin films with varying dopant concentrations together with linear fits pointing toward optical bandgap value (dashed lines) obtained using Equation ((37) and extrapolated.

Despite certain limitations of this method, as it was originally developed for non-direct interband transitions in amorphous bulk semiconductor [198], the predictions for optical bandgap acquired with this method corresponds with the literature findings derived from different methodologies. We should note that determining the real bandgap in such systems is a challenging task, since it's value is influenced by defects states near the band edges, excitonic effects and previously mentioned Burstein-Moss effect.[199] Tauc plots in case of highly doped ZnO help to determine the absorption edge and optical band gap. Nevertheless, when this approach is systematically applied to samples within a single ensemble, it reliably reveals trends and enables comparisons between different samples. As illustrated in **Figure 62**, the bandgap monotonically widens with increasing dopants concentration, regardless of the introduced dopant type. Specifically, for singly-doped material, AZO, bandgap alterations of 0.57 eV were obtained, whereas for HAZO the obtained range spans across 0.4 eV.

For high carrier concentration, the bandgap narrowing term should be taken into account that originates from many-body interactions, in particular electron-electron and electron-impurity scatterings effects [200] As many reports

show,[201,202] the deviation from the Burstein-Moss effect is increasing with dopant concentration, suggesting the amplification of those effects along with the non-parabolicity of the conduction band in ZnO. The bandgap value vs doping content and carrier concentration measured using van der Pauw method are presented in **Figure 63**. The dashed lines presented in **Figure 63b** graph are determined using the following formula:

$$\Delta E_g = \frac{3\pi^2}{2m_e^*} n^{2/3} + E_{BN}(n), \quad (38)$$

where m_e^* is electron effective mass, n is electron concentration and E_{BN} is a band-narrowing term with non-trivial dependence on the carrier concentration and dopant ion radius. This term takes into account narrowing effects that occur in the material [181,200]. The exact determination and theoretical examination of this term is beyond the scope of this thesis. Instead, it is included to collectively encompass those effects that cause deviation from the treated Burstein-Moss formula with $n^{2/3}$ dependence.

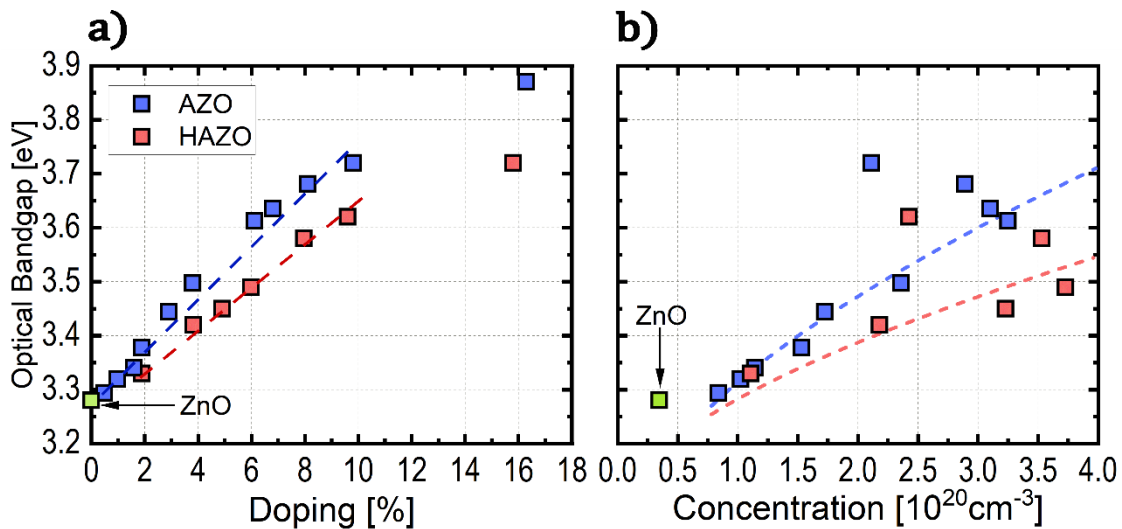


Figure 63. Optical bandgap of the thin film samples determined from Tauc plots. a) for varying dopant concentration. Dashed lines are a linear guide for the eye. **b)** for the carrier concentration obtained from Hall measurements. Dashed lines are calculated according to **Equation (38)** and tries to estimate the deviation from the Burstein-Moss effect.

The primary factors contributing to these deviations include the Coulomb interaction repulsion between the electrons, leading to the effective attraction of the holes and shifting the energy of the band downwards. Additionally, the excessive amount of electrons from donor ions in the zinc position alters the charge distribution, disrupting the parabolicity of the conduction band[203]. In our case,

the data was fitted using **Equation ((38))** with simplified term responsible for band narrowing. However, as previously mentioned, quantifying the exact contribution of these effects is challenging and experimentally laborious process, therefore, the dashed curves should be regarded as an initial attempt to incorporate these apparently existing effects in the studies.

In **Figure 63a**, both materials display a consistent, monotonic widening of the band gap, exhibiting a nearly linear relationship in the low doping regime. However, beyond the 8% dopant concentration level, the widening slows down notably, but it still occurs which cannot be explained solely by the carrier concentration increase (Burstein-Moss effect), as discussed before but might be influenced by structural changes. In particular, lattice stress from high dopant concentration may be the cause of the deterioration of the crystal. As the dopant atoms such as Al (or Hf) incorporates in the lattice sites of ZnO [168,204,205], replacing zinc atom with dopants that contribute 3 (or 4) additional electrons to the conduction band. Adding such amount of free carriers results in shifting upward Fermi energy and accordingly, lowering the defect formation energy of some intrinsic acceptors and electron trapping states, such as oxygen vacancies. This mechanism, known as self-compensation is widely recognized in semiconductor physics as it is the main cause of free carrier saturation in a variety of materials.

AZO demonstrates a slightly wider bandgap, reaching up to approximately 3.7 eV for 9% of Al doping compared to HAZO, which shows bandgap of 3.62 eV for with 5% Al and 5% Hf content, respectively. Moreover, 3.5 eV and 3.62 eV bandgaps are observed at their respective resistivity minima, i.e. 4% and 6% for AZO and HAZO. An intriguing aspect is the comparatively slower bandgap widening, despite higher carrier concentrations measured. This phenomenon could be attributed to the presence of optically active states below the Fermi level, induced by hafnium incorporation that may lower the recorded optical bandgap.[206] This effect along with many-body interactions described before, counteracts the pure Burstein-Moss effect, thus causing the bandgap narrowing more prominent.

To extensively study the optical properties of the grown samples, the ellipsometry studies were performed. This method allows to precisely track the changes in the refractive indices based on the used dopant and it's amount. The ellipsometry measurement and the subsequent model tuning based on the received data have been done by PhD Piotr Wróbel. **Figure 64** illustrates the real and imaginary components of the complex refractive index $\hat{n} = n + i \cdot k$ of AZO and HAZO plotted against the wavelengths for different aluminum content.

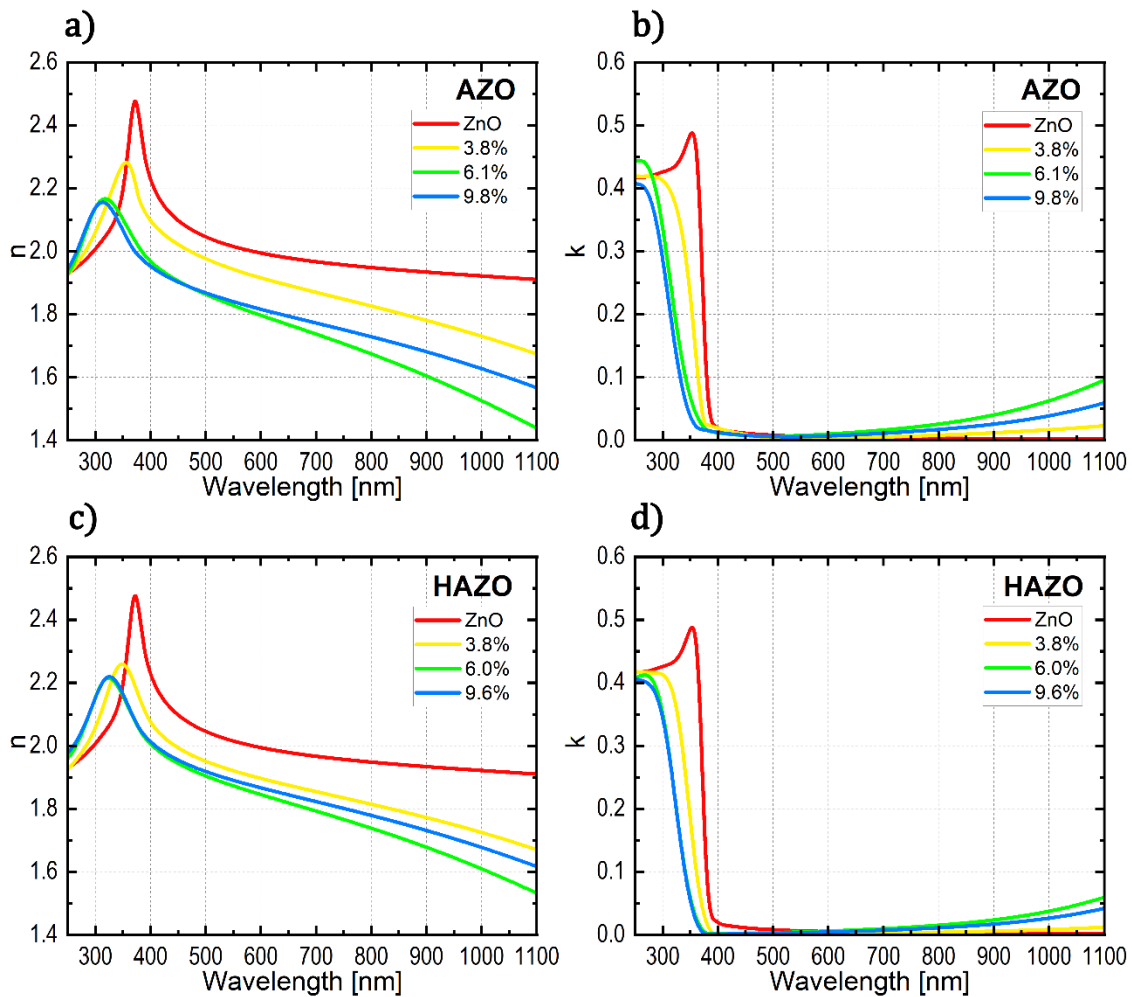


Figure 64. Complex refractive index extracted from the ellipsometric measurements of a) – b) AZO and c) – d) HAZO. Subplots a) and c) present the real component of the refractive index, whereas subplots b) and d) present the imaginary component of the refractive index.

Both materials exhibit comparable behavior in the presented spectral range. In the UV spectral region, electronic transitions lead to significant absorption, reaching peak values for the extinction coefficient (k) and the real part of the refractive index (n). Beyond that peak, the k abruptly decreases to a very low values, indicating high transparency. Within the VIS-NIR range, ZnO demonstrates near-zero values of k , while the refractive index n slowly decreases from approximately 2 – 2.1 to around 1.5 – 1.9, depending on the cation doping ratio.

The introduction of a dopant, either aluminum or hafnium, induces a decrease in the real component of the refractive index, which coming down from around 2.5 to 2.1 for highly doped samples. Besides, the refractive index peak itself is getting broader. At the same time, shifting of the both complex refractive index components

towards shorter wavelengths is visible. The increase in the carrier concentration leads to an observed increase in the extinction coefficient within the NIR range, especially prominent above 900 nm range. This pronounced increase is attributed to free carrier absorption, described by the Drude term, alongside absorption originating from phonons or defect states, which are included within the model as Gaussian oscillators. The patterns and trends revealed by the ellipsometry studies are very alike for both of the materials. However, there are some differences when the changes of the dynamics are examined. For instance, HAZO displays better refractive index consistency across the doped samples, which are around 0.14 at 500 nm wavelength and around 0.31 at 1000 nm. AZO samples on the other hand, exhibits at the same wavelengths the relative changes equal to 0.19 and 0.41, respectively. This attribute make it less susceptible to unintentional refractive index change due to alterations in doping. The noteworthy attribute of HAZO is the enhanced transmission in the IR range, as it reaches half of the k value observed for comparable doped AZO samples.

4.3.4. Outlook and prospects for co-doped ZnO

Aluminum doped zinc oxide and hafnium-aluminum doped zinc oxide thin films were grown employing ALD technique with different dopant ratios. Comprehensive studies were conducted to deeply investigate the optoelectronic properties of these films. Doping – regardless of the type of the cation – induced significant changes in the samples' electrical and optical properties, notably enhancing conductivity and blue shifting the optical bandgap. These enhancements primarily stem from increased concentrations of free carriers within the material, along with slightly larger grain lengths observed in thin films doped with hafnium.

Given the exceptional conductivity and versatile tunability, the proposed material can be employed as a part of future electronic devices utilizing TCO films. Although there are reported results of other conductive oxides that achieve even better performance, with exhibited resistivities as low as $\sim 2 - 4 \times 10^{-4} \Omega\text{cm}$ [207-209], these materials are usually obtained with RF sputtering or evaporation techniques and demands some post-growth treatment. Their presence should not diminish the benefits offered by ALD. This technique presents high throughput, cost-effectiveness which are indispensable for future, large surfaces solutions and applications such as photovoltaics. In addition, this method enable the uniform coating of high-aspect ratio structures, unreachable for sputtering techniques. Also,

the achievable refractive index range is sufficient for the design of efficient Bragg gratings and other photonic components based on the optical constants modulation.

4.4. Performance optimization using multilayer TCE

As described in **Section 2.2**, various strategies have been explored to enhance the performance of TCEs, focusing on improvements in both electrical conductivity and optical characteristics. The one noteworthy concept involves incorporation of a very thin layer of metal, creating a multilayer, sandwich-like composite electrode. Such an idea has been demonstrated to be a very promising approach to substantially enhance the material conductivity while minimally impacting light transmission, offering a reasonable trade-off resulting in the improved TCE performance. The critical aspect lies in the precise tuning the individual layers thicknesses to find optimal interference conditions minimizing optical losses due to reflection. At the same time, the very high conductivity of the metal provides an efficient photoinduced carrier collection and undisturbed transport. In this section, the numerical and experimental findings of the multilayer oxide-metal-oxide composite electrode are discussed.

4.4.1. Numerical Findings – TMM Results

The main method used here to simulate the optical behavior of the samples is TMM (described in **Section 3.4.1**). Dielectric functions of considered materials were determined ellipsometrically and implemented in the python code. First, the planar AZO layer deposited on the glass substrate was simulated to establish a reference point in the further studies. **Figure 65** presents the calculated transmission of the AZO layer with varying thickness.

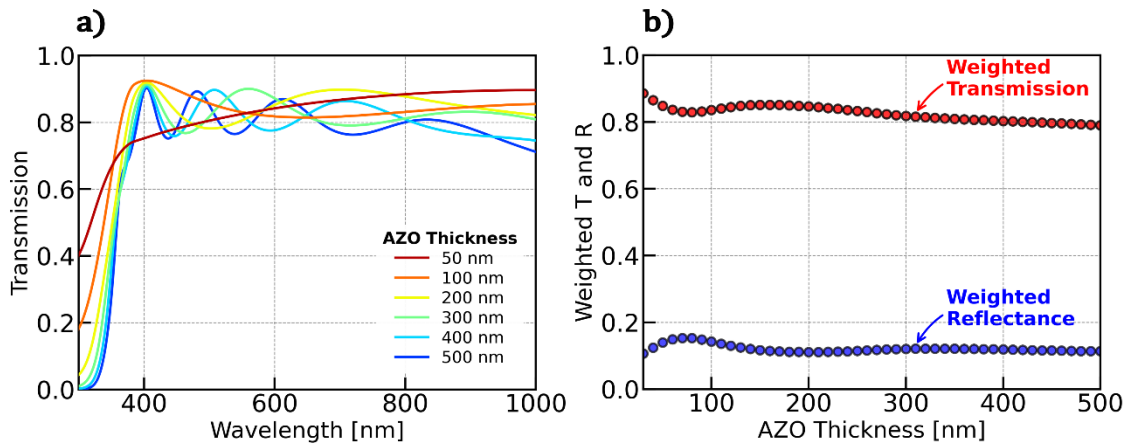


Figure 65. TMM calculations results. a) AZO thin film deposited on the glass substrate for thicknesses ranging from 50 to 500 nm. **b)** Weighted transmission and reflectance to AM1.5G standard spectrum for the same samples. Maximum transmittance is exhibited at 140 nm of AZO.

The transmission for thicker samples starts to exhibit typical interference patterns, consistent with those observed in experimental data. **Figure 65b** presents the AM1.5G standard solar spectrum weighted transmission and reflectance, calculated according to **Equation ((23))** within 300 – 1000 nm range. In this way, the information on the applicability of the material as TCE is received. As seen, the typical transmission of the layer is about 82 – 86%, reaching its maximum at 140 nm of thickness. The bare planar layer suffers from the relatively high reflectance and not optimal transmission. The multilayer approach promises to overcome those shortcomings with carefully designed stack composition.

The commonly adopted approach employs the sandwich-like structure made of 3 layers in the following order: oxide-metal-oxide. Such a composite stack is also the easiest to manufacture. In addition to the analysis of the entry-level structure, this study investigates optical properties of more complicated structures, which are made of 5 and 9 alternating metal-oxide layers. **Figure 66** presents the stack schemes along with weighted transmission and reflectance heat maps, where warmer colors indicate higher transmission and lower reflectance, respectively. The thicknesses of AZO and Ag layers were tested across the 20 – 120 nm and 0 – 20 nm ranges, respectively. The best layers combination is marked with the yellow arrow. As seen, adding additional bilayers of oxide-metal does not bring beneficial results, since the highest transmission is exhibited by the triple layer made of AZO-Ag-AZO. Thicker, more complicated samples tend to absorb more light without mitigating the reflection.

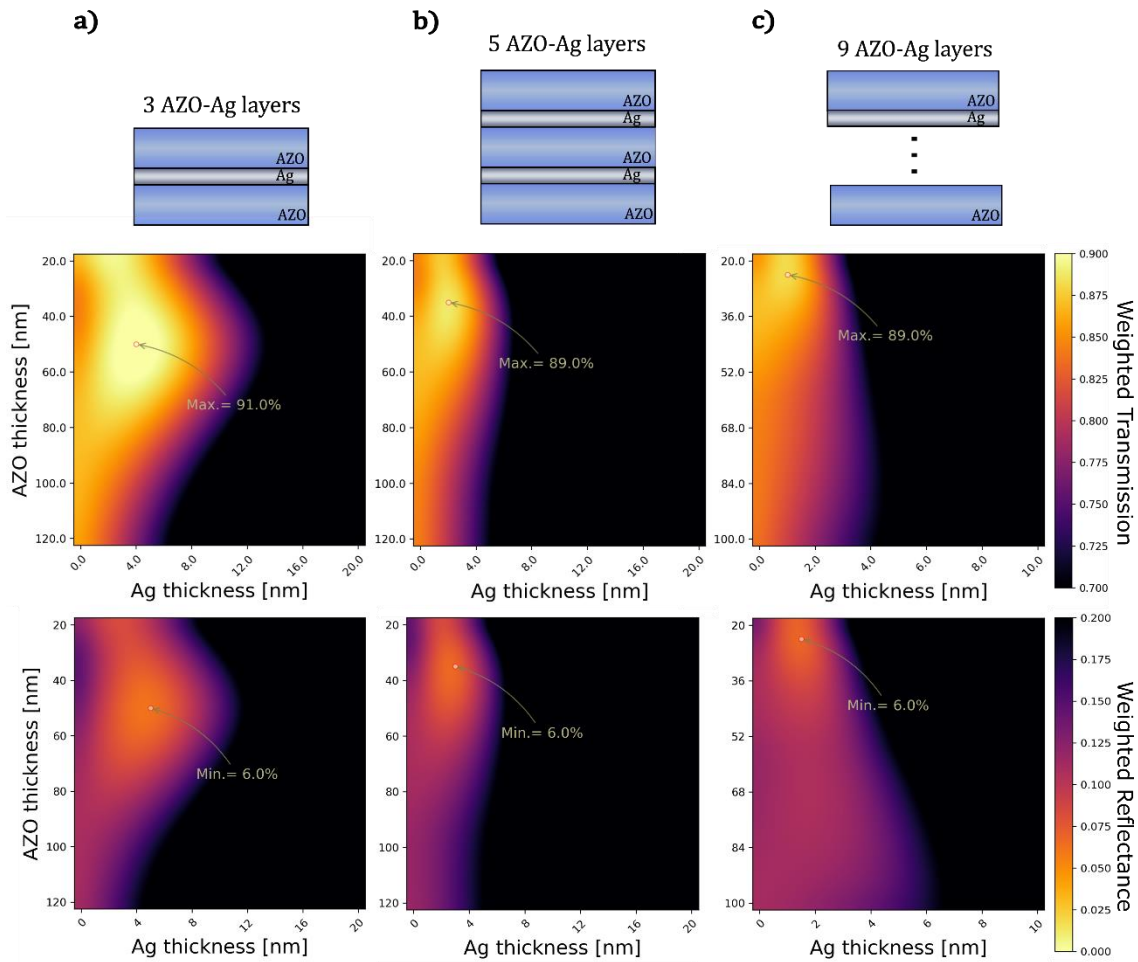


Figure 66. T_w and R_w based on TMM calculations for different composite, multilayer systems comprising of a) 3-layer stack of AZO-Ag-AZO, b) 5-layer stack and c) 9-layer stack. Maximum performance for both transmission and reflectance is marked with arrow for the best performing AZO, Ag thicknesses.

Furthermore, apart from the increased complexity in fabrication, the individual layers become thinner, posing challenges in manufacturing such a system. The best performing optical stacks are made of layers with thickness equal to 52 nm of AZO (4% Al content) and 4 nm of Ag, resulting in 91% of T_w and 6% of R_w . Those results are 5% and 4% better than bare AZO layer, respectively. To further demonstrate the limit of this system, the simulations with antireflective layer made of MgF_2 were performed. MgF_2 is a low refractive index (around 1.37 in the visible range) material used to minimize reflections on the interface due to better index matching. The results employing this additional layer are depicted in **Figure 67**.

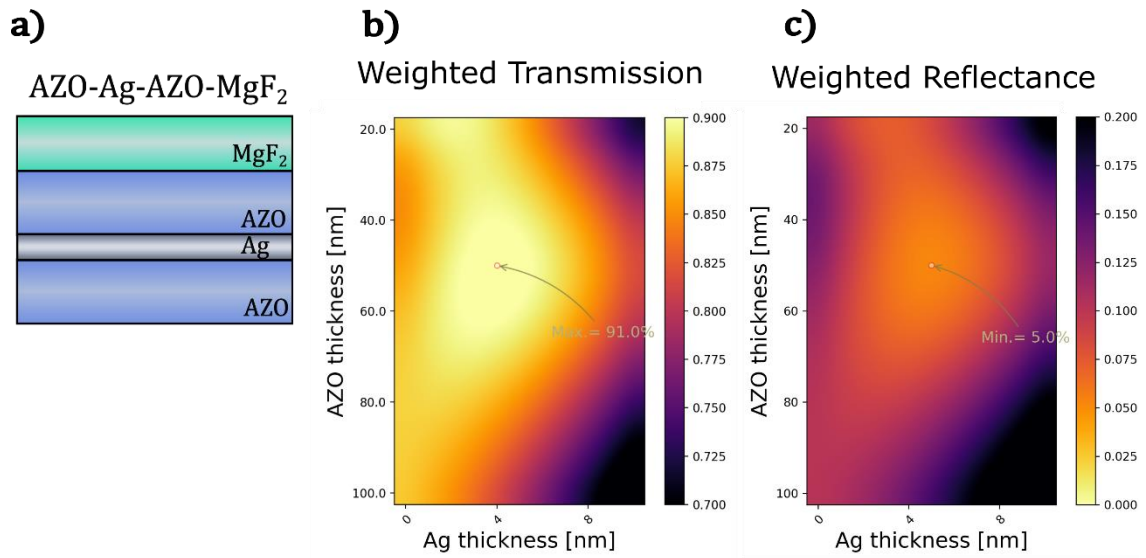


Figure 67. T_w and R_w based on TMM calculations for 3-layer stack of AZO-Ag-AZO with antireflective MgF_2 coating. a) stack scheme, b) T_w with marked maximum performance, c) R_w with accordingly marked maximum.

T_w reaches maximum for very thin silver layer, equal to 4 nm and 52 nm of AZO. Similarly R_w reaches minimum for 5 nm of Ag and 52 nm. Such modified layer yields slightly better reflectivity results, achieving only 5% of R_w , whereas the transmission stays at the same level. **Table 5** summarizes the optimal parameters of each of the stack.

Table 5. Optical performance of the optical stacks proposed as a transparent conductive electrode with varying stack structure.

Optical Stack	Thickness [nm]	AZO thickness [nm]	Metal thickness [nm]	T_w max.	R_w min.
AZO	140	140	0	86%	10%
AZO-Ag (3-layer)	108	52	4	91%	6%
AZO-Ag (5-layer)	112	36	2	89%	6%
AZO-Ag (9-layer)	124	24	1	89%	6%
AZO-Ag (3-layer + MgF_2)	108	52 + 110 MgF_2	4	91%	5%

Given the promising outcomes from these numerical simulations, the next step involved experimental validation of the proposed stacks using a combination of ALD and PVD techniques to manufacture the composite structures. The main goal of this experiment is to assess both the feasibility and performance of such designed structures.

4.4.2. Experimental Realization

The simulation results suggest that adding thin layer of metal could indeed significantly improve the transmission of the stack. These findings are also supported by the numerous literature examples (see **Section 2.2**). Thus, the trilayer samples made of AZO/Ag/AZO stack with the parameters close to the optimized layers received in simulations were performed. The thin layer of the silver was evaporated using PVD75 e-beam evaporation system delivered by Lesker. This process was performed by PhD Piotr Wróbel. The images of the samples are depicted in **Figure 68**. The samples underwent the basic optical and electrical characterization to potentially validate the findings of the employed model.

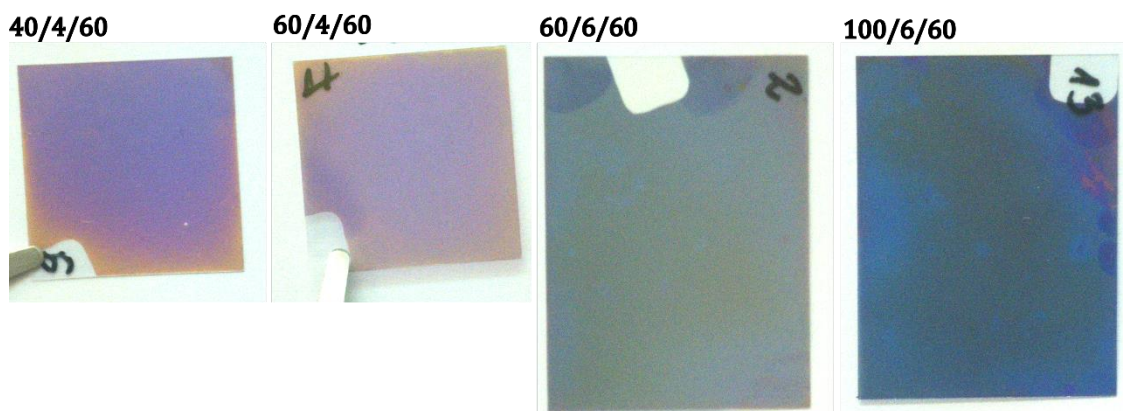


Figure 68. Real appearance of the multilayer composite electrodes. The numbers above each of the sample marks the layer thickness following the convention: AZO/Ag/AZO. All the samples – even the ones with a very thin silver layer – seem to be insufficiently transparent to be an efficient transparent electrode material.

It is evident that the samples exhibit dark bluish or light violet color, indicating high reflection within this range. The appearance of the samples suggest that the transmission of them might not be adequate for creating a high-quality transparent electrode. To investigate the impact of incorporating a metal layer, transmission measurements were conducted (**Figure 69**).

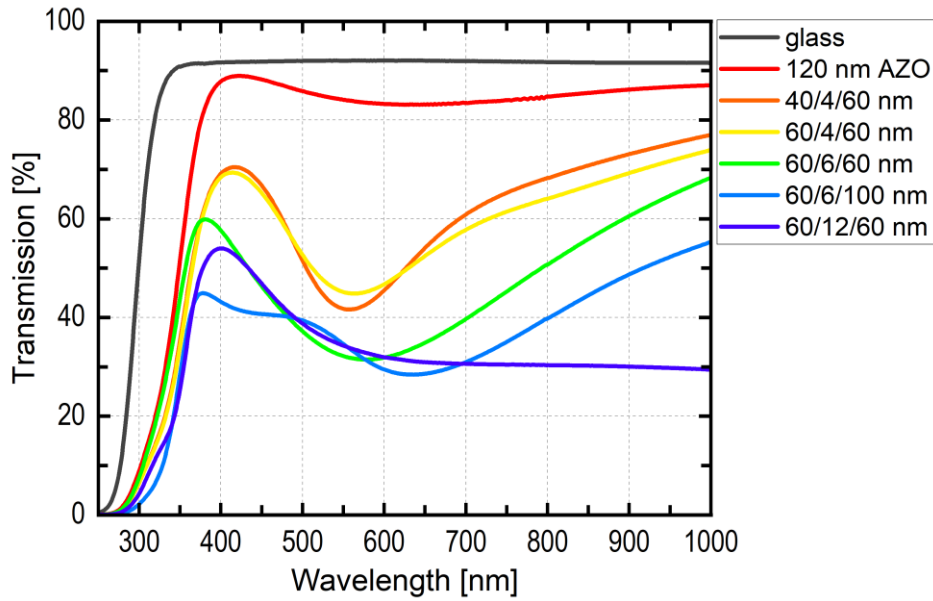


Figure 69. Transmission spectra of different AZO/Ag/AZO stacks, deposited on the glass substrate. Legend shows the thickness of the individual layers where the middle one marks the metal thickness, and two other AZO thickness. The glass and 120 nm AZO curves are shown for comparison.

The optical performance, as seen in the presented figures, falls well below the expectations and TMM model predictions. The weighted transmission values change from approximately 64% to 33%, mostly influenced by the silver layer thickness within the material. Notably, the visible maximum in transmission is blue shifted with increased silver thickness layer between the AZO layers, indicating a tuning potential by selecting the right silver thickness. The reason for such discrepancy may stem from the fact that evaporation such thin layer of silver make it prone to agglomerating into nanoparticles, rather than forming the desired thin, uniform planar layer. In such structures, the presence of localized surface plasmons (LSPs) can induce undesired effects and an optical response unsuitable for the intended application, particularly leading to increased absorption at the resonance frequency of the plasmon. On the other hand excitation of LSPs on metal nanoparticles immersed in ZnO medium might lead to generation of hot electrons and their injection into the TCO [210-212] resulting in the increased concentration of charge carriers and thus improved performance of the entire photovoltaic system. Surprisingly, the electrical performance of the samples, is minimally affected by this modification up to relatively thick layers of silver, as high as 12 nm. In this case, the resistivity drops down to $3.7 \times 10^{-4} \Omega\text{cm}$, whereas for samples with 6 and 4 nm the results are very similar to the ones without any metal embedded. **Table 6** summarizes the electrical resistivity and optical performance.

Table 6. Composite electrode resistivity and transmission values. The first column presents the structure of the sample following the relation: AZO/Ag/AZO.

Sample thickness [nm]	ρ [$10^{-3} \Omega \text{ cm}$]	Tw [%]
120/-/-	1.48	85.0%
40/4/60	1.85	63.9%
60/4/60	1.57	62.0%
60/6/60	1.5	50.3%
60/6/100	1.26	41.9%
60/12/60	0.37	32.7%

It appears that the key factor for success is obtaining a pin-hole-free silver layer, leading to the efficient transport of carriers. However, achieving such a thin, pristine surface renders to be challenging, in particular on the rough surface formed by the underlying AZO layer. Adding ~ 1 nm germanium or nickel wetting layer may be a solution, though it induces some absorption losses and this approach will be investigated in the future. Additional difficulty may come from the silver diffusion and reconfiguration, phenomena observed in similar systems being exposed to elevated temperature in oxygen rich temperature [213-215]. Under these conditions, oxygen may diffuse into silver and degrade it. Another undesired effect is the agglomeration of silver into larger islands that disrupt the continuity of the thin film. These two main effects lead to the deterioration of interfacial properties, increasing light scattering and absorption, as well as reducing the conductivity of the system.

These attempts yielded moderate results, falling short of the promising effects calculated in simulations. Therefore, the approach involving Oxide-Metal-Oxide architecture, was not further developed due to the extensive time and labor involved, outweighing the benefits. The next efforts were redirected towards texturized geometries and their antireflective properties.

4.5. Summary

This chapter presented the laborious and time-consuming process of the optimization procedure to obtain the best-performing ZnO and ZnO:Al thin film samples, showing the importance of the equipment-specific protocol development and the large parameter space to optimize.

It is worth mentioning that the ALD setup was delivered to our Faculty as a brand-new, therefore the whole process chain which is not described here has been developed from the very beginning. Many of the steps undertaken within the procedure being developed in the initial period have not been discussed here, but taking these steps was essential to assert the full operation of the setup and its reproducibility of the results.

This part also presented the various effects that the doping of the two different dopants have. One is the obvious change in electrical resistivity, coming from the additional free carriers introduced by substitutional atoms, either aluminum or hafnium. The co-doping of ZnO has been done before, but this field is still mostly unexplored, therefore a new insight into it is useful and helps to find the best working pairs in this complex environment. The co-doping proved to raise better electrical performance especially in terms of enhanced carrier concentrations, promising new material for transparent electrode applications.

Moreover, this chapter delved into the more advanced concepts presented in **Section 2.2.1** such as oxide-metal-oxide structures. First, the numerical models specially tailored to reflect the efficiency driven approach were tested for a wide array of configurations to find the best parameters for later experimental validation. Some of the samples raised a very promising results, expanding the performance of just planar transparent conductive oxide layer. Nevertheless, the experiment went much below the expectations, probably due to the difficulty in preparation of a few nanometer thin metallic layer.

CHAPTER 5.

Nanoimprinted Perovskite Solar Cell

5.1. Introduction

In the previous chapter, we focused on the reflection mitigation losses as well as proposing the novel TCE materials, aiming for enhancing the performance of the solar cells. The properly designed top layer that enhances the charge collection is inevitable in the efficient solar cell design. In this chapter, another concept of enhancing current generation and reflection loss is demonstrated by nanoimprinting the ARC onto perovskite solar cell. Asserting the best light management is important to achieve high performance in all photovoltaic technologies and can be done by taking two basic approaches. The first one is the reflection losses reduction, whereas the second one is the elongating the optical path length within the active layer of the absorber. There have been many proposed concepts of dealing with this, notably to mentioned are planar ARC, structured surfaces such as random nanorods[216,217], biomimetic moth-eye patterns[119,218,219], micro lens arrays[220] or applying texturized foils[221-224]. By nanoimprinting the structure on top of the perovskite solar cell, we aimed to simultaneously reduce the reflectance and improve the absorption within the active layer.

Perovskite solar cells have experienced an astonishingly rapid evolution over the past decade, starting with the efficiency of just 3.8% in 2009 [84] to current 25% [225] record breaking devices [225]. The extensive research and efforts are motivated also by their exceptional bandgap tunability, achieved through compositional adjustments within an energy range of 1.2 to 3.0 eV [226,227]. Furthermore, the manufacturing process of perovskite solar cells employs simple methods solution-based synthesis that enables a cost-effective production.

In this chapter, we present the detail description of the nanoimprint process, proposed structures and the influence on the optical and electrical parameters of such modified perovskite solar cells. We demonstrated that the whole nanoimprint process chain is safe enough to not alter the perovskite solar cell, which may results in its severe damage and performance deterioration. To the best of our knowledge

nanoimprint lithography, has been never directly applied to create such or similar structures on top of perovskite cell a roller nanoimprint technique. Furthermore, this chapter discuss the limits of light harvesting improvements using proposed honeycomb structure. The researches described in this chapter served as the foundation for the publication in Maciej Krajewski et al. *Roller Nanoimprinted Honeycomb Texture as an Efficient Antireflective Coating for Perovskite Solar Cells*, *Advanced Materials Interfaces*, 2023 [228]. The measurements were performed by the author of this dissertation unless otherwise stated.

5.2. Proposed structures

The nanoimprint process begins with spin-coating of the moldable photoresist that get soften in elevated temperature of 90 – 120 °C. The used resist was the commercially available SU-2002 epoxy negative photoresist (purchased at Microchem company [229]). The thickness of received layer is controlled by the rotation speed during the spin-coating process and was also investigated throughout the study. After the spin-coating the samples were preheated at 60 °C for 90 seconds and kept in dark place to rule out the accidental light exposure. The samples were then placed on a roller nanoimprint setup that provide temperature of 90 °C and UV light exposure. During the process the sample slowly slides under the roller and the structure itself get imprinted within the soft resist and get cross-linked due to UV radiation. After the curing of the resist, the sample is left for 2 minutes bake to let the process finish. Three fundamental regimes of operation were tested to choose the best performing structure, schematically pictured in **Figure 70**.

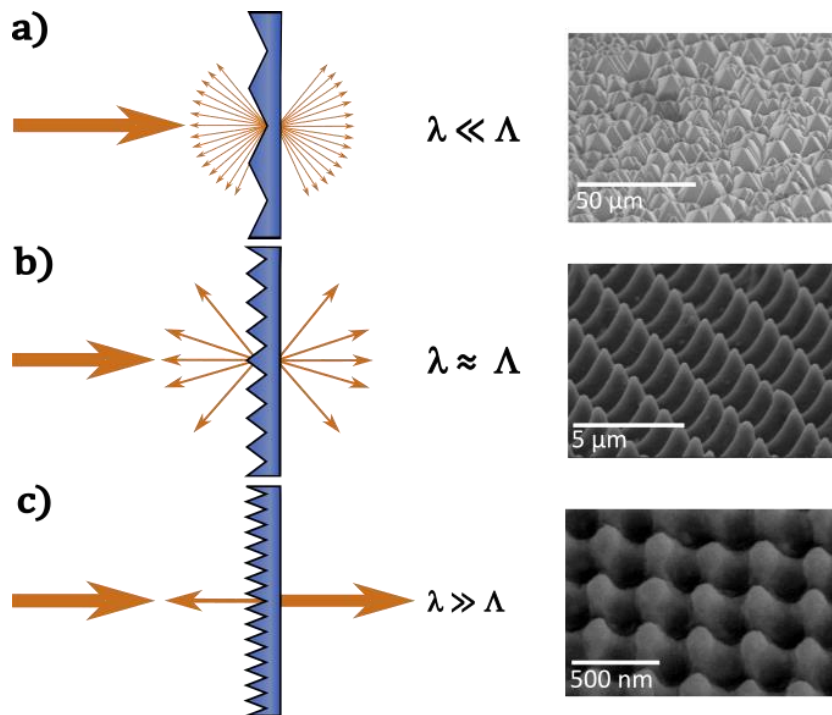


Figure 70. Schemes and SEM images of different textures with varying spatial periods and features size. a) large structures allow many diffraction orders to propagate **b)** intermediate structures with periods comparable to wavelength **c)** structures with a very small features sizes, acting as an effective medium with different refractive index

The roller nanoimprint technique was applied to manufacture a wide array of different textures, all aiming to modify the optical properties of the solar cell, namely to reduce its reflectivity. Large features such as pictured in the SEM image cause the light to diffract in many channels, leading to the geometry or ray optics approximation feasible. Such structures reduce the reflection by multiple internal reflections within the texture and therefore increasing the path length in the active layer, profoundly improving the absorption. When the features size are close to investigated wavelengths, the Snell's law and ray tracing is no longer valid, since the diffraction start to dominate the distribution of light power, the proper approach entails rigorous Maxwell equation solving using finite-difference time-domain (FDTD), RCWA or similar techniques. Going down with features size, the light wavelength is much longer than the period of the structure, which becomes unresolvable for the light and therefore the light acts as if it travels through a medium with a gradient refractive index, minimizing the reflection through the index-matching phenomenon.

To effectively explore the performance and potential applications of those three regimes, several structures using nanoimprint technique were prepared onto glass substrate to validate the antireflection properties, depicted in **Figure 71**.

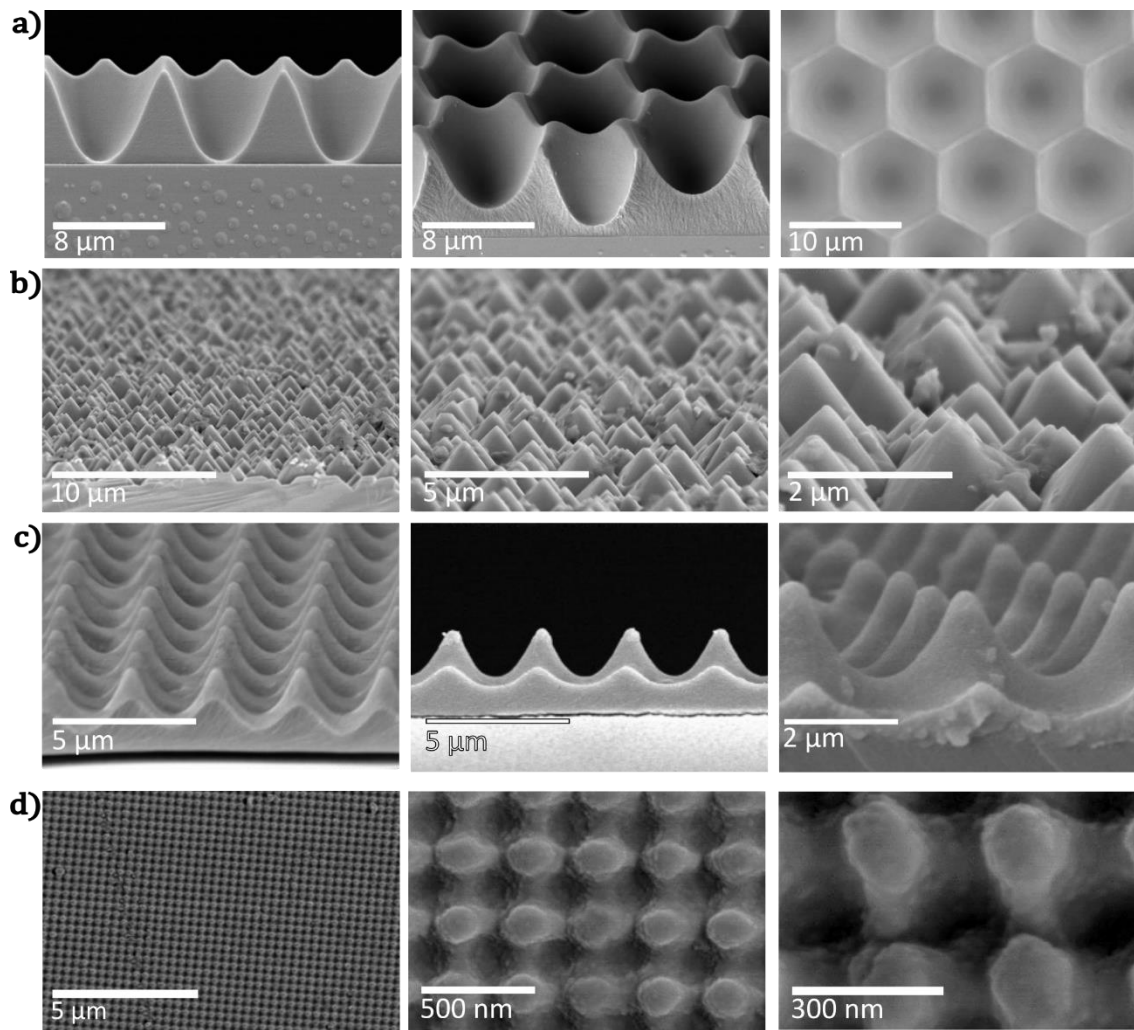


Figure 71. Different textures imprinted on top of the glass substrate visible under different angles and magnifications. a) Honeycomb structure b) random pyramids c) needle-like structure d) moth-eye structure

The textures vary in terms of their period, symmetry and employed shapes. Starting from a several micrometers period in case of the honeycomb structure, through a 2 micron pyramids and needle-like structure down to moth eye structure with the period of approximately 300 nm, which constitutes the subwavelength properties of such structure. The structures cover different regimes of light propagation, however their main goal is the same, i.e. lowering of the reflection from the top surface of the solar cell. Additionally, most of them, namely honeycomb, pyramids and needle-like structures enhance the optical length within the active layer, due to introducing the light inside the solar cell at different angles. In the moth-eye texture, those effects are less pronounced. Some structures due to smaller features are harder to replicate, resulting in degenerated shape of the outcoming structure. Also, the right thickness of the resist, controlled by the spin-

coating speed is the key factor for the right replication of the structure. **Figure 72** presents some of the poorly replicated results due to different factors such too thin layer of SU-8 photoresist, too much pressure during the imprint or insufficient UV exposure. Proper optimization of all these parameters is the precondition for replicating the structures with a sufficient quality.

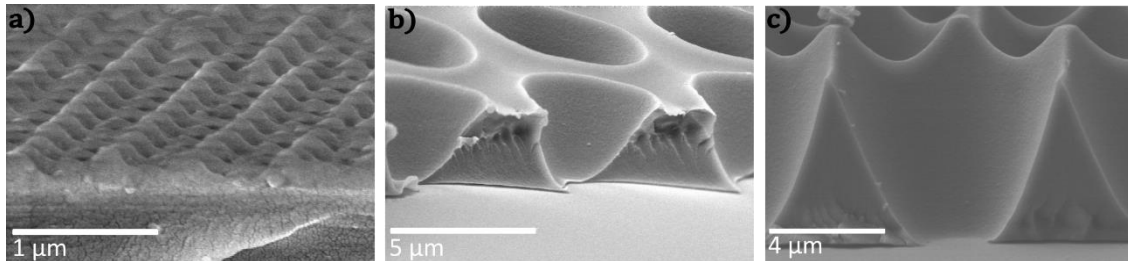


Figure 72. Examples of poorly replicated structures. a) collapsed, not cross-linked resist after moth-eye stamp imprint **b)** vertically squished honeycomb texture due to insufficient thickness of the resist with visible holes in the bottom **c)** defected honeycomb structure

5.2.1. Optical Studies of the Imprinted Structures

The best as possible replication is indispensable for the efficient light incoupling and the performance of the texture as an anti-reflective coating. **Figure 73** presents the influence of the rotation speed on the reflectivity of the honeycomb structure. With thinner layer, there are some holes visible that do not contribute to the antireflective properties of the layer. The optimal spin-coating speed is 300 rpm. This corresponds to resist thickness of around 5 μm, as determined via SEM imaging. After the optimization of the nanoimprint process, all the abovementioned structures were nanoimprinted onto the soda-lime glass substrate to firstly evaluate their antireflective performance.

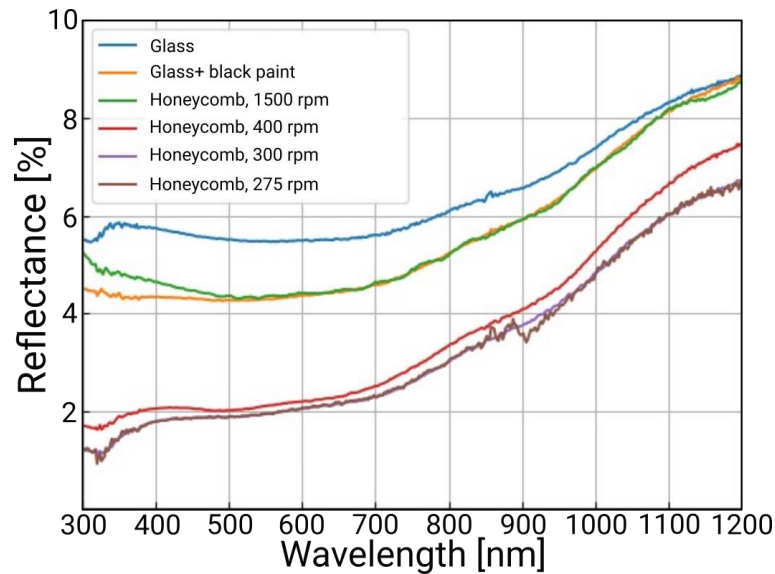


Figure 73. Reflectivity for the honeycomb structure with different spin-coating speed. The differences stem from the differently coated surface for high rotation speed samples.

The results are presented in **Figure 74**. To eliminate the backside reflection coming from the glass that may interfere with the true optical properties of the given structure, the glass was coated with a black paint that effectively absorbs in the visible range. However, the paint itself reflects some of the light in the infrared region which is visible in the graph above 800 nm wavelengths. The increased signal within infrared range originating from this black paint reflection is replicated across all the investigated samples. The results reveal that to a greater or lesser extent, all the investigated structures decrease the reflectivity of the sample, pushing it below 4% in the visible spectrum. As can be seen in the **Figure 74** the lowest reflectivity is exhibited by the honeycomb structure, reaching as low as 2%, followed by the needle and moth eye structures, however the moth eye structure exhibit some interference pattern where the maxima exceed the needles reflectivity. The best-performing structures, i.e. needles and honeycomb were selected to process further on the real perovskite solar cells to check their performance on the device.

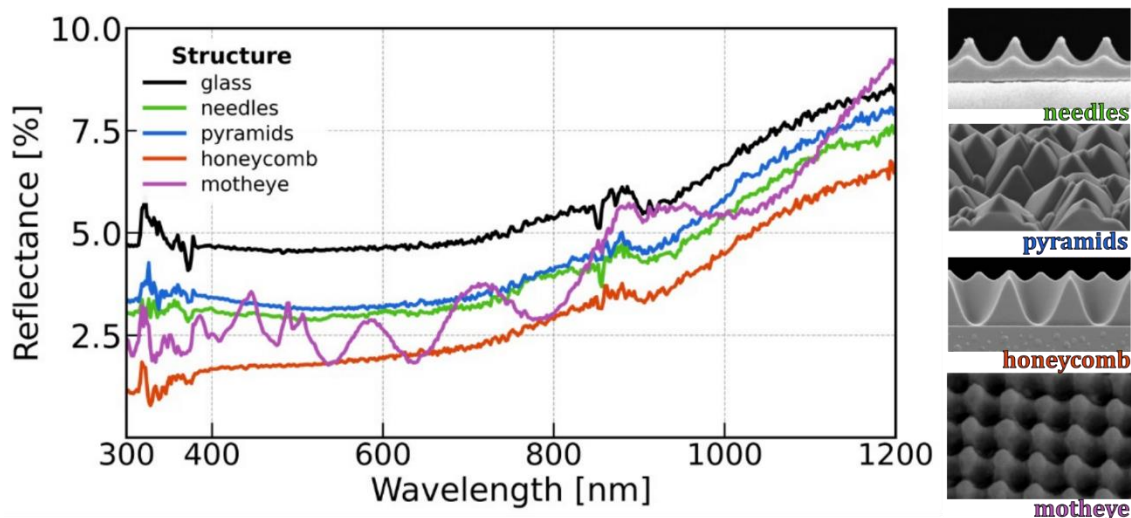


Figure 74. Reflectivity results for the imprinted samples on the glass substrate with black paint on the bottom surface. The increase in reflectivity above 800 nm in case of glass is caused by some residual reflectance coming from the non-ideal absorption in the infrared region.

5.3. Perovskite Solar Cell Imprinting Process

The imprint process on the glass or silicon substrate has been previously demonstrated in literature [230,231]. However, the imprint technique may be invasive when applied to other surfaces, especially sensitive to corrosive chemicals, like perovskite active layer. Therefore, the transfer of this technology to the perovskite layer was the first challenge and when successfully demonstrated, that would be one of the first attempts of doing so on such a delicate substrate.

5.3.1. Fabrication and Characterization of perovskite solar cell

The perovskite solar cells were manufactured by Minasadat Heydarian (Fraunhofer ISE) using the procedure described in detail in Ref. [228]. The outcoming layer was the cesium-lead-iod-bromium perovskite active layer of exact formula $\text{Cs}_{0.15}(\text{FA}_{0.8}\text{MA}_{0.2})_{0.85}\text{Pb}(\text{I}_{0.8}\text{Br}_{0.2})_3$ with a bandgap of 1.66 eV suitable for perovskite-silicon tandem solar cell. The active layer is placed between transparent conductive electrode made of ITO and ETL, HTL layers. The cell consists of 4 independent subcells (commonly referred as the pixels) with 5×5 mm area. The electrodes of evaporated Ag consisting of busbar surrounding each of the subcell

and two pads to connect the measurement setup. The SEM cross-section image and the scheme of the layers stack are depicted in **Figure 75**, whereas the image of the ready device is depicted in **Figure 76**.

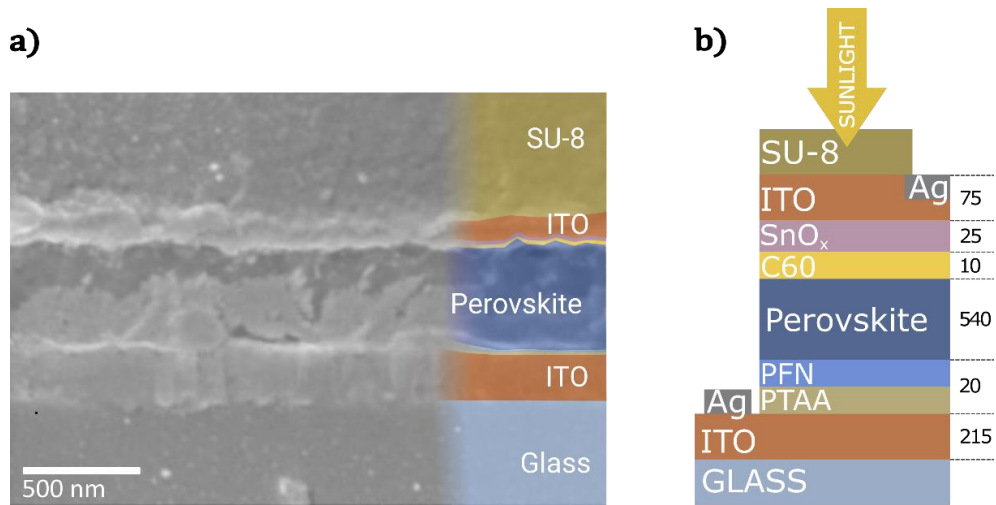


Figure 75. Perovskite solar cell cross-section. a) The SEM cross-section with SU-8 resist on top of the cell **b)** scheme of the perovskite cell with the direction of incident solar light depicted and exact thickness of each layer stated in nm

The imprint process on the ready device is different to that on top of the resistant and durable material such as glass or silicon. The first step in transfer is the optimization of the process using nanoimprint technique. **Figure 76** shows the peeled of and destroyed perovskite solar cells of first attempts in transferring the technology on the perovskite solar cell using planar stamp nanolithography setup shown in **Figure 37**. The tries of adapting different pressure, UV exposure and other parameters proved to be insufficient and no successful attempt was done using the tool. The main reason for this failure is the high pressure generated exert on the solar cell and strong adhesive forces that are keeping the stamp and cell together too tight, making it very fragile to peeling of the whole optical stack.

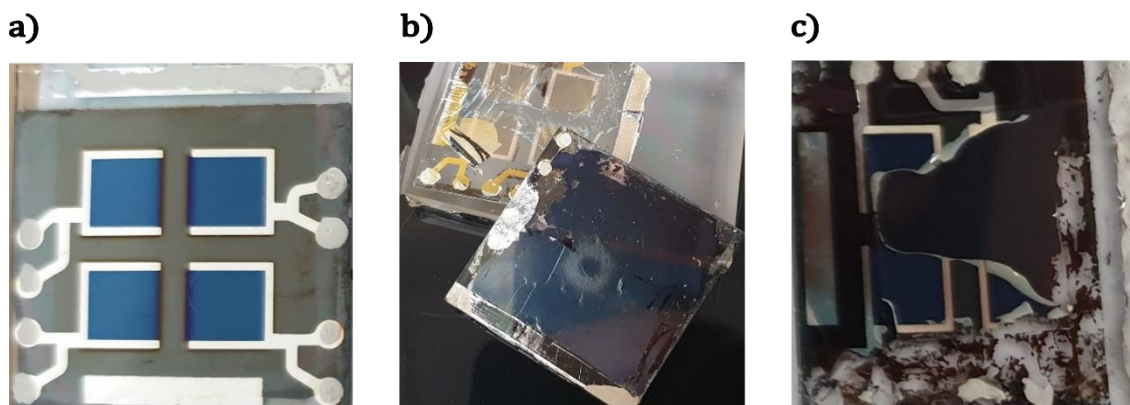


Figure 76. The real appearance of the perovskite solar cells. A) as manufactured **b)** and **c)** after unsuccessful nanoimprint process, showing severe degradation and peeling off.

Therefore, the next step was to try the roller nanoimprint setup, already described in **Section 3.2.2** where the pressure is applied in more controlled way and with slowly departing it from the surface, making the stress generated less pronounced. This approach proved to be the key factor in successful texture imprinting on the solar cell. The SEM images of the such imprinted layers along with schematical cross section of the cell are depicted in **Figure 77**.

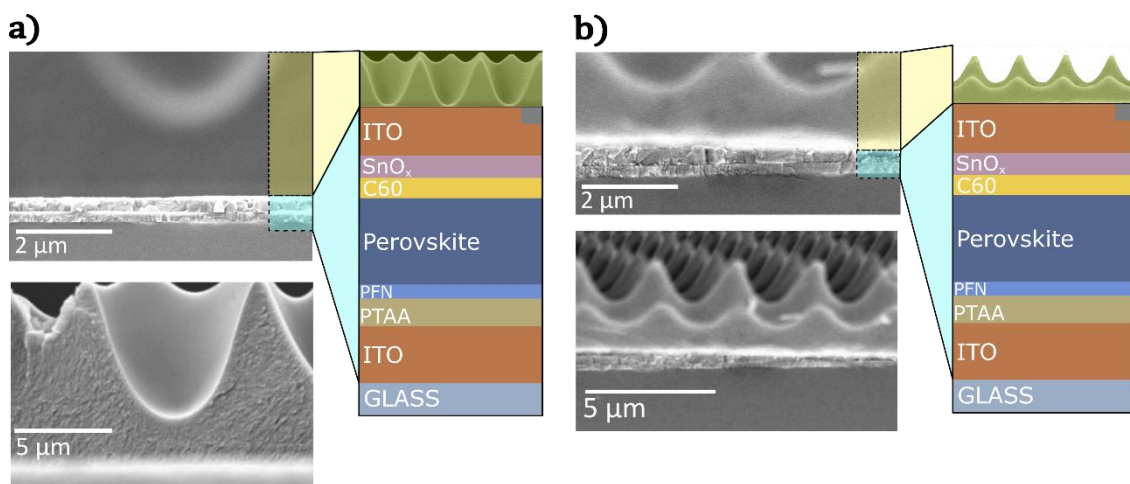


Figure 77. SEM cross-sections of perovskite solar cells with two different nanoimprinted structures along with their schematical drawing. a) honeycomb b) needle-like

The solar cell sample with spin-coated resist was placed in the roller nanoimprint system and heated to 90 °C for a few minutes to let the photoresist become formable. Then, the sample is slowly pressed against the stamp by slowly

moving tape, which results in forming the negative stamp pattern on the sample, simultaneously exposing it to the UV radiation. This triggers the cross-linking process and hardening of the resist. After the exposure, the sample is left for post baking for 3 minutes to finish the cross-linking and hardening processes. Two, most promising structures based on the previous reflectance research were imprinted onto perovskite solar cell to check its real performance as the anti-reflective layer.

As can be seen in those two cases, the imprinted layer is tightly attached to the perovskite solar cell, proving the whole procedure was successful. The structures itself are much bigger than the whole optical stack of the perovskite cell, which emphasizes that the proper attachment to such delicate layer demands special attention. As can be seen from the SEM image, the procedure of applying the texture is harmless for the cell, leaving the whole stack in place and untouched. Such modified cells were subjected to the reflectance measurements, depicted in **Figure 78.**, to determine the antireflection properties of the applied layers and chose the best performing one for further processing.

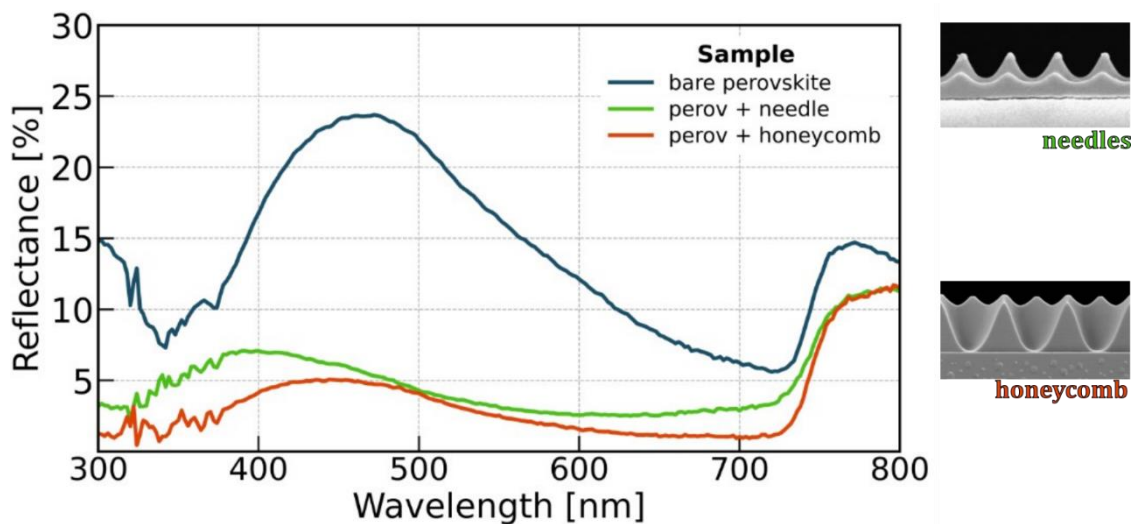


Figure 78. Reflectance measurements of a perovskite solar cell with two different nanoimprinted textures applied: needle-like and honeycombs.

Both textures have an exceptionally well influence over the reflectivity of the solar cells, reducing the reflectance across the wide range of wavelengths. Such designed structures diffract the incident light, forming some kind of a waveguide, making it harder for light to escape, effectively increasing the absorption within the active layer. The most pronounced outcome is the reduction from around 24% at 480 nm to well below 10% level. Also, beyond 500 nm, the reflectance is close to 3%, making little room for further improvement. The rise beyond 740 nm is related

to the bandgap of the perovskite layer after which, the absorption is severely diminished. By comparison of those two structures, it is clear that the better performing one is the honeycomb texture due to subtle, but visible differences in the reflectance where the recorded value fall below 5% across the whole range. Due to limited number of samples, our goal is to transfer only the best performing structures onto real, working devices. Therefore, the ongoing analysis and processing is done for the champion texture which is honeycomb structure.

5.4. Optical and Electrical Parameters

5.4.1. Effect of the ARC on the optical performance

Reflectance spectra were collected for three different samples: as manufactured perovskite cell without any ARC, planar 100 nm MgF₂ layer as the representation of commonly used ARC and nanoimprinted honeycomb texture. The stacks and real images of the investigated samples are presented in **Figure 79**.

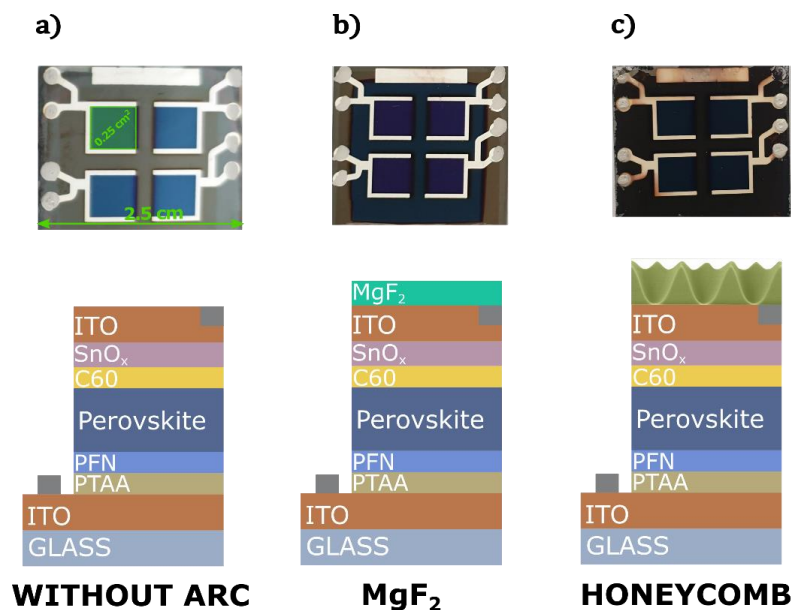


Figure 79. Real images of the perovskite solar cells with varying top surfaces. a) as manufactured cell without any ARC **b)** evaporated 100 nm MgF₂ planar layer **c)** nanoimprinted honeycomb structure

All the pictures were taken under similar lighting conditions and white balance setup. As seen, the uncoated device has a uniform light-blue color, reflecting

substantial part of shorter wavelength light. On the other hand, honeycomb structure has dark indigo color, indicating that the most of the light is absorbed by active layer. What is also worth mentioning are the contact pads that underwent the imprinting procedure are without any visible damage.

The reflectance measurements along with the simulation results of all investigated samples are shown in **Figure 80**. The details concerning the numerical calculations are exhaustively described in **Section 5.6**. Simulations using RCWA method along with the convergence studies were done utilizing Fraunhofer ISE computational cluster with a great help and supervision from Adrian Callies.

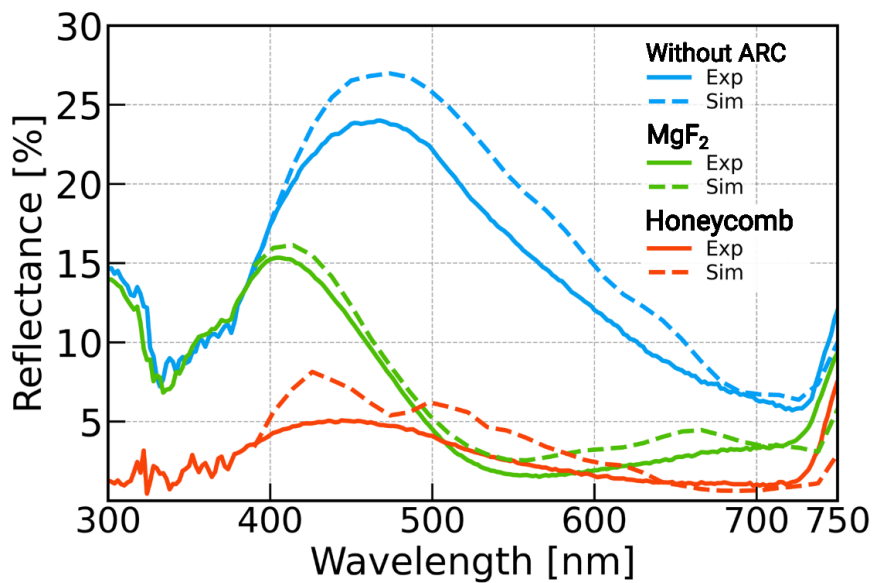


Figure 80. Reflectance results of the perovskite solar cell (solid line) along with the spectra obtained from the RCWA simulations (dashed lines).

The uncoated, reference sample exhibit high reflection losses, reaching above 10% in most of the relevant wavelength's spectrum of 350 – 600 nm. The sample with the MgF₂ top layer exhibit much lower reflection losses, with visible wavelength-dependent behavior with constructive interference maximum reaching 15% at around 400 nm. Although the sample reflectance is profoundly reduced below 5% in the 500 – 700 nm range, there is substantial loss of approximately 10% in the shorter wavelength range of 350 – 500 nm. On the other hand, the sample with the honeycomb texture exhibits a uniform, wavelength-independent spectrum, with the recorded loss below 5% across the most relevant wavelength range for perovskite solar cells (400 – 740 nm). That clearly shows the high applicability for this concept. The simulated spectra closely follow the experimental data. They show proximity to the measured values, and in particular the relative changes caused by the different approaches are well reproduced. Some deviations

toward higher reflectance can be explained by the assumption of perfectly planar layers and surfaces made in the simulation, whereas in reality there is some microroughness present that influence the reflectance results.[232] As the main goal is to quantitatively evaluate the ARC influence, the AM1.5g photon flux solar spectrum weighted reflectance, R_w , was calculated using **Equation (23)**.

To estimate the maximum generated current assuming perfect external quantum efficiency, the following formula is used:

$$J_{ph} = q \int (1 - R(\lambda)) \Phi_{AM1.5}(\lambda) d\lambda, \quad (39)$$

where q is the elementary charge.

The planar solar cell without ARC exhibits 13.6% of weighted reflectance in the 300 – 750 nm range which translates to 3.2 mA/cm² current density loss. Applying a planar anti-reflective layer of 100 nm MgF₂ decreases this loss to around 4.9% (1.2 mA/cm²). With the honeycomb pattern presented in this work, the reflection loss can be further reduced to a value of 2.7%, which corresponds to a loss of 0.6 mA/cm². These results show profound increase in J_{sc} generation upon applying the novel nanoimprinted structure, even though the SU-8 resist is not properly index-matched to the rest of the solar cell, leaving some room for improvement when correctly addressed. To investigate the full potential of the proposed structure, additional RCWA simulations were carried out, depicted in **Figure 81**:

1. Modeling of the same geometric structure, but with an idealized photoresist with no absorption and a real part of the refractive index equal to the ITO top layer. This assumption aims to remove the reflection at the structure-cell interface, leading to even better performance. This simulation provides an outlook on what can be achieved by further optimizing the optical properties of utilized resist.
2. Modelling the structure with optimized refractive index equal to that of ITO with a module glass on top. That approach closely replicates the actual use case in the module. In the real device, the cells are protected from detrimental environmental conditions by the front glass.

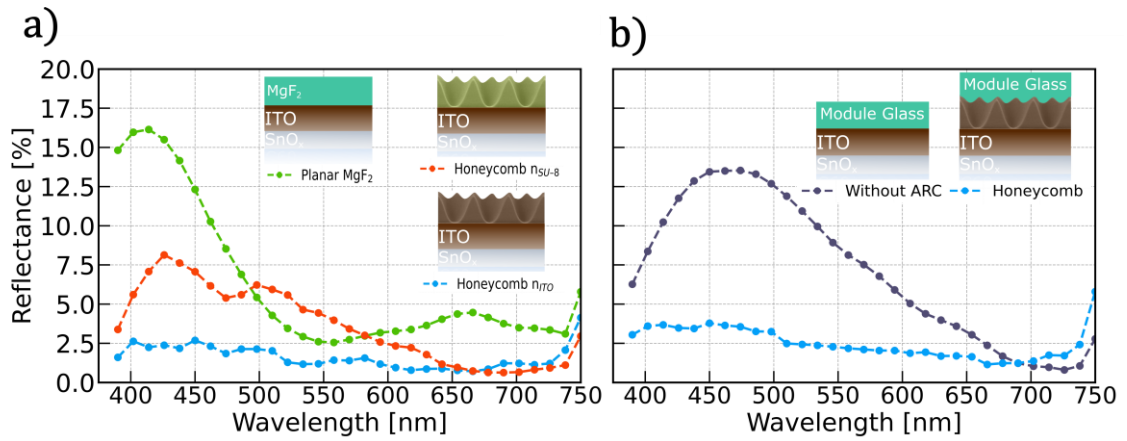


Figure 81. Simulated reflectivity results along with the simulated optical stacks schemes of a) planar MgF₂ layer and honeycomb samples with different refractive indices. The red line indicates the honeycomb structure imprinted in SU-8, and the blue indicates the honeycomb structure with a refractive index equal to this of ITO. **b)** honeycomb structure implemented as a part of the whole module (blue line) along with the module without any ARC (grey line).

As can be seen in **Figure 81a**, the properly matched refractive index leads to a beneficial reflectance effects, with the reflectance spectrum falling below 3% throughout the whole range of relevance. Therefore, a very promising weighted reflectance value equal to 1.6% has been achieved, which translates to only 0.4 mA/cm² J_{sc} loss, showing that this structure would absorb virtually all the reflection from the cell. For the scenario of module integration, the results seem to be very promising as well, raising only 2.5% R_w . That means the honeycomb structure can play a beneficial role when applied to the real module stack devices as well. These results are summarized in **Table 7**.

Table 7. Weighted reflectance (R_w) and associated with this current density loss for varied ARC integrated into perovskite cells. (*) marks the RCWA simulation results.

Sample	R_w [%]	J_{sc} loss [mA/cm ²]
Without ARC	13.6	3.2
MgF ₂ ARC	4.9	1.2
Honeycomb, n _{SU-8}	2.7	0.6
Honeycomb, n _{ITO} (*)	1.6	0.4
Honeycomb, module glass (*)	2.5	0.6

5.4.2. Effect of the ARC on the EQE and J-V performance

EQE measurements were performed to investigate the influence of the ARC on the electrical properties of the cell, in particular the number of electrons generated from the incident photons. Perovskite solar cells rarely exhibit exactly the same EQE response due to some slight details during manufacture, resulting in subtle deviations in their electrical properties. Therefore, the best approach is to compare the obtained results before and after application of the specific ARC for precise evaluation of their enhancement. EQE results are presented in **Figure 82**. The as collected EQE data were calibrated with the J_{sc} obtained from the J-V measurements that will be discussed later in this section. This approach is necessary in order to obtain precise value of EQE, coherent with the current generated from the cell. The spectra were taken over the range of 300 – 800 nm to fully cover the perovskite absorption range.

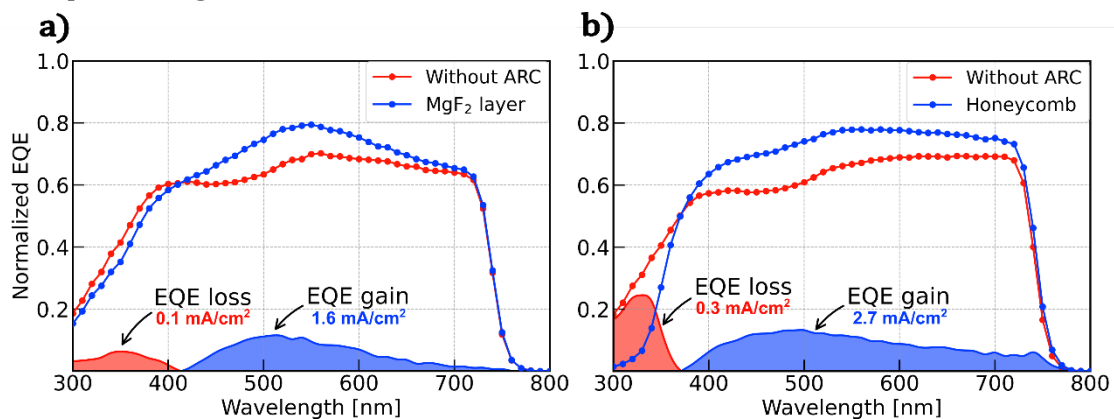


Figure 82. External quantum efficiency spectra normalized to J_{sc} received in J-V measurements of a perovskite cell a) with and without MgF₂ layer and b) with and without honeycomb texture. At the bottom of each graph absolute difference between modified and unmodified structures is shown. Gain is depicted as a dark blue region whereas the loss is depicted as a red region. Also, the change in calculated J_{sc} after ARC application using Equation ((30)) is stated.

In both of the modified samples, featuring either MgF₂ or a honeycomb structure, we observe an enhancement in EQE within the spectral range of 400 – 750 nm, yet the honeycomb structure visibly surpasses the performance of the MgF₂ thin film alternative. The MgF₂ EQE spectrum has a noticeable maximum at approximately 550 nm which corresponds to the minimum in reflectance as depicted in **Figure 80**. In contrast, the honeycomb texture exhibit more uniform, broadband EQE enhancement across the extended range of 370 – 750 nm. Within the 430 – 560 nm range, the EQE improvement exceeds 10%, and in the region up

to 740 nm it remains above 5%. This improvement corresponds to the profound reduction in the observed reflection, already described in **Section 5.4.1**. Noteworthy, in both ARC configurations, there is an EQE reduction, 300 – 370 nm wavelength region, compared to the untreated solar cell. However, it is much more pronounced for honeycomb modified structure that suffers from parasitic absorption in the SU-8 layer. On the other hand, the MgF₂ ARC exhibits a constructive interference, enhancing reflection in this region, leading to a similar behavior. However, the loss-gain balanced out in favor for both structures, leading to overall 2.4 mA/cm² and 1.5 mA/cm² gains increase for honeycomb and MgF₂, respectively. The losses and gains of the EQE are shown as a red- and blue-filled curves in **Figure 82**. The general conclusion from the EQE measurement is that they both exhibit enhanced electrical properties, however honeycomb structure outperforms MgF₂ planar layer.

Similar to EQE, *J-V* characteristics of the cells were measured before and after the application of the MgF₂ layer and the honeycomb texture, as illustrated in **Figure 83**. The shapes of the curves undergo minimal differences depending on the sweeping direction, indicating minimal hysteresis in the *J-V* curves.

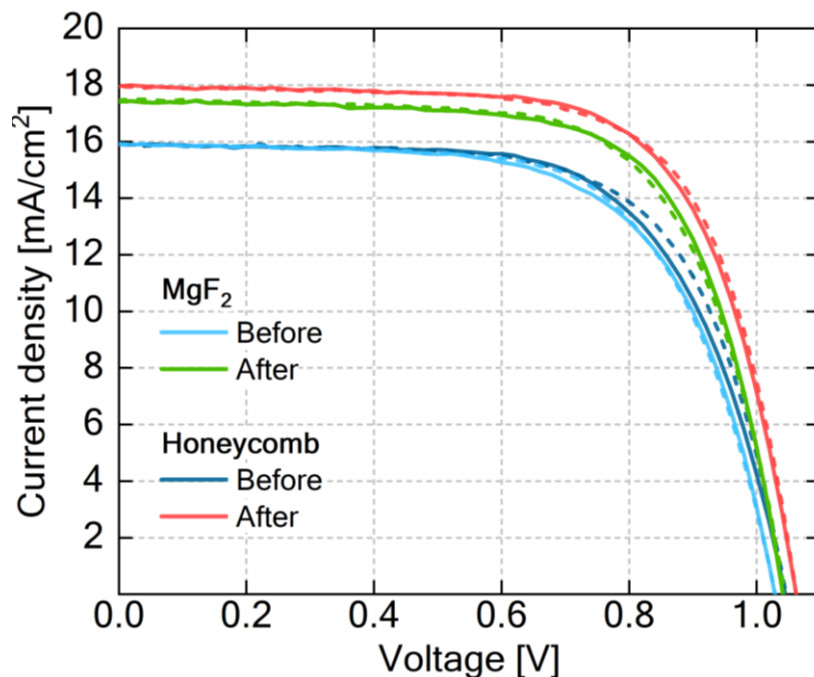


Figure 83. *J-V* curves of the studied solar cells samples under standard AM1.5g solar spectrum illumination conditions. Solid lines represent measurements in the forward direction, whereas dashed lines the reverse direction.

Solar cells electrical and optical parameters are summarized in **Table 8**. Following the application of ARC, the J_{sc} is increased in both cases. Specifically, the honeycomb structure exhibits a notable increase of 2.1 mA/cm², while 1.6 mA/cm² increase is observed for the thin film MgF₂ layer when sweeping in forward direction. The increase in current density is very similar in reverse direction, achieving 2.0 mA/cm² and 1.5 mA/cm² for honeycomb and MgF₂, respectively. The current increase leads also to V_{oc} enhancement by 12 mV to 16 mV and the FF by 2 – 3 percent.

In both cases, the current density enhancement was equal to 2.4 mA/cm² which closely matches the 2.1 mA/cm² increase observed in the experiment. This alignment leads to the conclusion that the honeycomb structure achieved the most significant improvements in J_{sc} and PCE, primarily attributed to its minimal reflection losses.

Table 8. Summary of the examined solar cell electrical parameters. Forward (fwd) and reverse (rev) scan direction along with reflectance performance (weighted reflectance – R_w) are shown.

Sample	R_w [%]	V_{oc} [V]		J_{sc} [mA/cm ²]		FF [%]		PCE [%]	
		fwd	rev	fwd	rev	fwd	rev	fwd	rev
Before honeycomb	13.6	1.045	1.046	15.9	15.9	65	67	10.8	11.1
After honeycomb	2.7	1.062	1.062	18.0	17.9	68	69	13.0	13.1
Before MgF ₂	13.6	1.029	1.029	15.9	15.9	65	65	10.7	10.6
After MgF ₂	4.9	1.044	1.041	17.5	17.4	67	68	12.3	12.4

The absolute efficiency value achieved by the best-performing cell still falls below expectations, given that the current records for perovskite single junction cells exceeds 25% [233], which is almost twice the efficiency achieved in this study. It is therefore noteworthy to emphasize that the cell's efficiency as such in isolation may not serve as a definitive indicator of its quality and potential. In this case, the used perovskite absorber is a wide bandgap semiconductor, that is optimized for the use in a tandem solar cell, leaving a substantial part of solar spectrum unabsorbed. Thus, series resistance (influencing FF) as well as current density are not optimal for single junction operation. Nevertheless, the open circuit voltage of the device shows that the device has high quality, as it is comparable to the V_{oc} shown in literature [234] for such cells. It also shows that this technique may find its place when enhancing perovskite-silicon tandem devices in future.

5.5. Summary

Within this chapter, we have successfully demonstrated the application of a nanoimprinted structure on top of the perovskite cell. This marks the first successful attempt at the direct imprinting of an ARC onto such sensitive absorber without deteriorating the layer.

Utilizing the roller nanoimprint technique has led to a significant enhancement in the antireflection properties of the perovskite solar cell, achieving an impressive reduction to as low as 4.7% in weighted reflectance. This reflection decrease is correlated to J_{sc} and PCE increase, equal to 2.1 mA/cm² and 2.2%, respectively. These results unveil the potential for further exploration of this path, with the prospect of discovering an even more index-matched photoresist that can reduce reflectivity to as low as 1.6%, as indicated by numerical analysis.

Among the various advantages of employing nanoimprint technique for photovoltaics, one of the foremost is its potential in the context of perovskite silicon tandem cell devices. This possibility holds profound significance as perovskite-silicon tandem cells represents one of the most rapidly advancing technology in photovoltaic research [224,235,236]. The technique presented here promises construction of perovskite-silicon tandem devices with the exceptional antireflective and light trapping properties, thus opening the way towards new record breaking photovoltaic devices in future.

5.6. Appendix to CHAPTER 5: RCWA calculations details

The reflectivity simulations were performed using RCWA method, “reticolo” MATLAB implementation, described in **Section 3.4.2**. As the calculation time depends highly nonlinearly on the unit cell size, the simulation of $8.8 \times 15.4 \mu\text{m}$ unit would consume immense calculation power and time. Therefore, the structure was scaled down with fixed proportions to streamline the calculation process without losing the attributes of the geometry. Convergence analysis has been performed for this scaling factor value to find the most efficient value without sacrificing the close approximation of the light behavior within the system. Adhering to the guidelines in RCWA simulations, it is advised to use the period that is at least 4 times larger than the longest simulated wavelength, therefore the scaling factor was chosen to be 0.3. This approach is adapted in those simulations, proving to be a reasonable assumption, raising results closely following the experimental findings. **Figure 84** presents the unit cell used in simulation before scaling down.

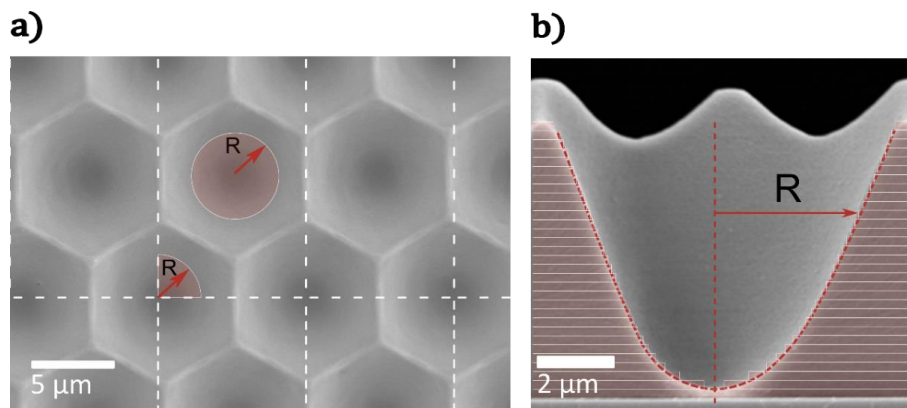


Figure 84. RCWA simulation setup. a) Elementary cell used in calculations with the radii of the given layer depicted, top view **b)** Stair-case approximation of honeycomb structure, side view. Dashed line depicts the cosine approximation of the honeycomb profile.

The honeycomb profile was approximated using cosine function, which is proved to be a close representation of the slanted surfaces of the unit cell. The structure itself was replicated using staircase approximation with predefined single layer height z . This value also has undergone a convergence studies, shown in **Figure 85**.

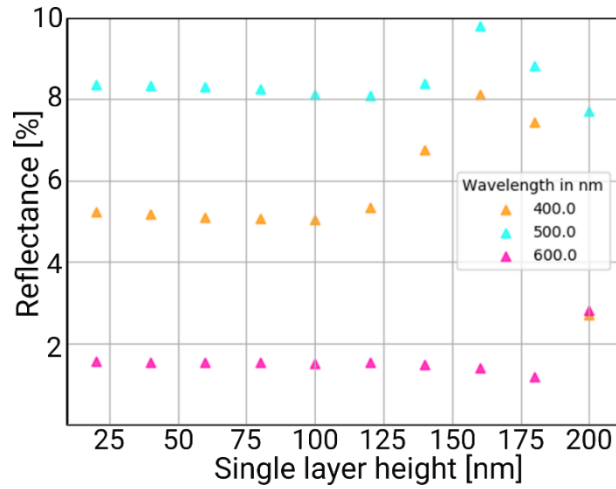


Figure 85. Reflectance results for three different wavelengths obtained for varying layer heights.

The optimum layer height that raises stable reflectivity results with acceptable calculation time was determined to be 75 nm. With this approach we reproduce the shape of the slope and those residual shapes on top of the structure. The exact function used to represent the radius of the described honeycomb structure takes the following form:

$$R(z_n) = S \times Re \left(\arccos \left(\frac{\frac{z_n}{S} - x_0}{z_0} \right) \right), \quad (40)$$

where S –geometrical scaling factor, z – coordinate of the n-th layer and x_0 and z_0 are the coefficient used to closely fit the exact function.

CHAPTER 6.

Transparent Electrodes with Embedded Nanomeshes

6.1. Introduction

In previous chapters, we focused on the concepts of enhancing the operation of solar cells by modifying the top layer of the cell either by proposing a new TCE material (**CHAPTER 4.**) or by top surface texturization (**CHAPTER 5.**). Herein, we propose combining these two concepts by modifying the TCO top electrode with with the embedded nanomesh patterns that facilitate the photogenerated charge collection. Additionally, the texturization of the top surface and its antireflective properties is investigated.

The concept of incorporating a metal grid structure within the TCO layer has been a topic of discussion in the literature for at least one decade. The addition of a microgrid pattern elevates the material conductivity while retaining acceptable transparency. However, finding the right balance between the shading ratio and enhancing conductivity remains a challenge while taking this approach. Much of the existing literature focuses on rectangular grids or simple line designs [113,114,237,238], leaving a substantial part of the geometry landscape unexplored, particularly in the domain of more sophisticated configurations, such as fractal geometries.

Within this chapter, we introduce a model that aims to find the nanomesh geometries, offering the best optoelectronic enhancement for a specific solar cell architecture. Our approach takes into consideration solar cell's thickness, diffusion length of the photogenerated minority charges and refractive index, expanding the usually used approach that focuses solely on the geometry of the mesh. These numerical findings contribute to the understanding of the nanomesh design for improving the top electrode layer in third generation photovoltaics. Furthermore, we conducted RCWA analysis of the optical properties of nanomesh structures with ARC texture on top of them to determine the overall impact on the performance of such modified solar cells.

6.2. Proposed Model

Photogenerated electrons and holes should be collected at the respective electrodes to provide a working solar cell. To maximize the number of the carriers being collected, the electrons should reach the metal as soon as possible. Therefore, the minimization of the distance travelled to the electrode is crucial to assert effective carrier collection. Two models of this process were proposed: one represents a purely 2D approach, whereas the 3D model, takes into account also the thickness of the active layer. **Figure 86** presents the scheme of the photogenerated carrier behaviour within the active layer for both 2D and 3D cases. Atop the surface, the metallic nanomesh is placed.

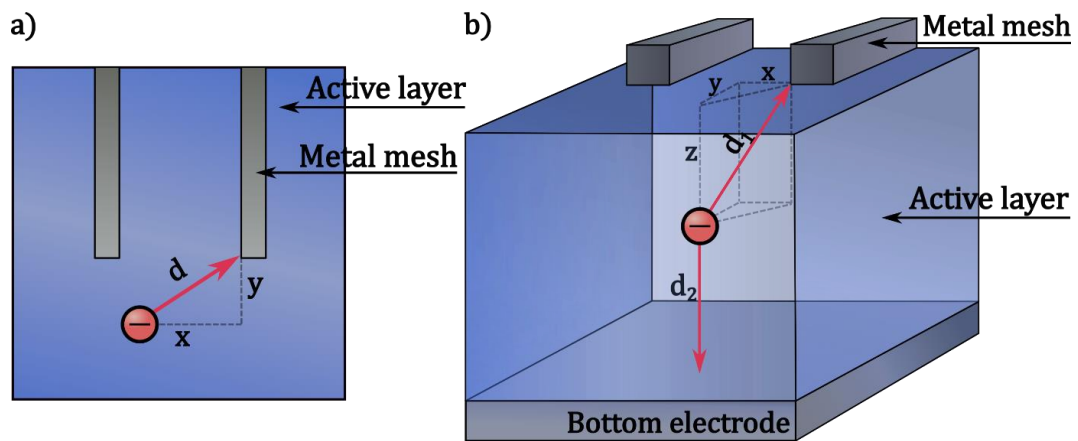


Figure 86. Schematic drawing of two proposed models of photogenerated carriers' behaviour. a) 2D model and b) 3D model.

In the 2D model, it is assumed that photogenerated carriers follow the shortest available path to reach the metallic electrode. As known from semiconductor physics, the photogenerated carriers undergo diffusion and travel through the material at a specific distance before recombination with the opposing carrier. This distance is called a diffusion length, or mean free path and is related to the probability of finding the particle at distance d from the generation place:

$$p(d) = e^{-\frac{d}{\gamma}}, \quad (41)$$

where d – distance to the metal electrode and γ – diffusion length defined as the material parameter, dependent on the bulk recombination rate of the minority carriers.

This simplified model is widely adopted as the first approximation of the dynamics of photogenerated charges in solar cells. To gain a more insightful view,

it is important to note that the photogeneration process takes place at different depths within the solar cells, thus the charges have different distances to traverse to reach the electrode. Therefore, the photogenerated carriers' density distribution itself is governed by the absorption of the solar cell.

Furthermore, the absorption process results in the electron-hole pairs creation, which must undergo separation and collection at the opposite electrodes. That creates a situation where the hole and the electron have different distances to travel to the respective electrodes, depending on the depth of the photogeneration process (see **Figure 86**). It is therefore important to account for that fact in calculations, taking the lower value of the collection probability.

The proposed 3D model employed the following assumptions:

- a) The mean free paths for photogenerated holes and electrons are equal. This assumption is consistent with the experiment and has been confirmed in real-world devices employing perovskite and organic active layers.[239-241]
- b) The electrons and holes take the shortest possible path to the metal electrode placed on top of the cell and to the bottom unstructured electrode respectively. The lower collection probability related to longer distance to the electrode of one of the carriers is taken into calculation.
- c) The photogenerated carriers spatial distribution is equal in the x-y plane whereas for the z direction, it is related to the absorption probability of photons within the solar spectrum taking into account architecture of the optical stack, described in the next section.

Following these assumptions, the distance to the top structured electrode is equal to $d_1 = \sqrt{x^2 + y^2 + z^2}$, whereas $d_2 = z_0 - z$ is the distance to the non-structured bottom electrode of the cell, where z_0 is the active layer thickness. The collection probability for the charge carrier generated at the given point, distant from the electrode by x, y and z in the spatial directions is equal to:

$$p(x, y, z) = G(z)e^{-\frac{\max [d_1, d_2]}{\nu}} \delta(x, y), \quad (42)$$

where $G(z)$ is the normalized z-dependent generation rate, equal to the ratio between all absorbed photons to the absorbed photons in the given z-th layer defined according to the optical response of the absorber layer, assuming a standard AM1.5G solar spectrum illumination:

$$G(z) = \int_{\lambda_{min}}^{\lambda_{max}} \alpha(\lambda) e^{-\alpha(\lambda)z} \times AM1.5G(\lambda) d\lambda, \quad (43)$$

where the exponent term is a representation of Beer-Lambert law, describing the attenuation of the light traversing through the medium. It describes how the light is absorbed within the material, thus after normalization, it describes the photogeneration carrier distribution in the z-direction. During the calculation, the discretization of the $G(z)$ function is assumed. In the calculations, the z-direction is divided into 51 points, streamlining the calculations and asserting a close approximation of the function. Also, the $\delta(x, y)$ term determines the coverage of the points by metal, to exclude shaded points, as they do not yield any photogenerated carriers. It is defined as:

$$\delta(x, y) = \begin{cases} 0 & \text{for metal covered points} \\ 1 & \text{for not covered points} \end{cases} \quad (44)$$

The most significant parameter that can be obtained is the average probability collection across the whole structure which directly translates to the structure effectiveness and generated current. To obtain the efficiency of this model, the integral over the entire volume cell is introduced, and divided by the unit cell area to normalize it. This computation results in the mean probability collection, denoted by **Equation (45)**. When a point in the unit cell is shaded, it cannot generate the photocarriers and therefore the carrier collection probability at this point is equal to zero. The formula is expressed as follows:

$$S = \frac{\iiint_{\text{volume}} p(x, y, z) dx dy dz}{\text{Unit cell volume}} \quad (45)$$

The primary objective of the model is to predict the performance of the designated structure functioning as a transparent electrode. The final assessment of the structure's efficiency is closely linked to the optical losses inherently induced by the nanogrid placed atop the cell. The final efficiency term resembles the well-known figure of merit first introduced by Haacke[89] which was later on adopted by the scientific community (presented in **Section 2.1.2**). This formulation underlines the influence of the transmission (T) by raising it to the tenth power, serving as the predominant factor for the final performance as TCE. Following this reasoning, the final evaluation is expressed through the below formula:

$$\varepsilon = S \times T^{10}, \quad (46)$$

The ε parameter undergoes examination and subsequent optimization to identify the best-performing geometry and design guidelines for the implementation of these grids in real devices. The model takes into account the active layer features such as its thickness, diffusion length of minority carriers, and refractive index. This approach significantly extends the 2D model results, offering nanomesh structure parameters for the specific active layer attributes.

6.3. Calculations examples and model predictions

The collection probability results for an exemplary structure (in this case, a space-filling fractal) and three different diffusion lengths are shown in **Figure 87**. The calculation procedure first assigns the probability collection value to each point in the unit cell according to **Equation (43)**, resulting in a probability heatmap for the whole elementary cell area.

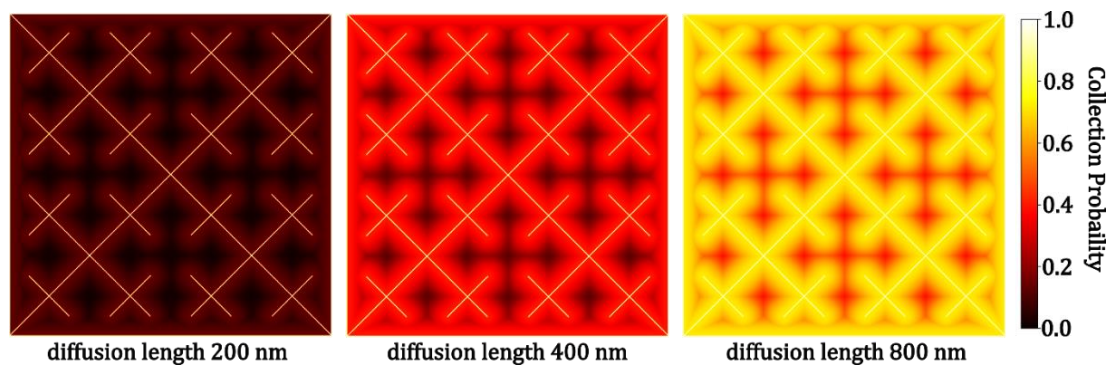


Figure 87. Collection probability heatmaps of the space-filling fractal for varying diffusion lengths. The rest macroscopic parameters in the simulation are kept constant, highlighting only the influence of the diffusion length elongation.

As expected, the resulting efficiency for the same geometry is directly proportional to the diffusion length of the photogenerated carriers. The impact of the mobility of the carriers aligns with the intuitive view, seen in the real devices where the longer diffusion length results in a higher collection probability. To better illustrate its influence, a series of simulations were performed over a wide range of this parameter, spanning from 200 to 4000 nm. **Figure 88a** presents the collection probability histograms with data derived from the heatmaps calculated with the previously presented approach. Also, the normalized efficiency based on

Equation ((46)) is received. As the diffusion lengths increase, the distribution of values becomes narrower, tending towards higher mean values – approaching 1 – which are marked with triangles. Moreover, the rate of increase tends to slow down beyond a certain threshold. For instance, a noticeable saturation is observed after reaching 1500 nm, as depicted in **Figure 88b**. By inspecting these results, it is clear that the diffusion length dictates the behaviour of the charges within the system, regardless of the employed geometry. Consequently, to compare the influence of the different geometries on effectiveness, the diffusion length parameter should be kept at the same value.

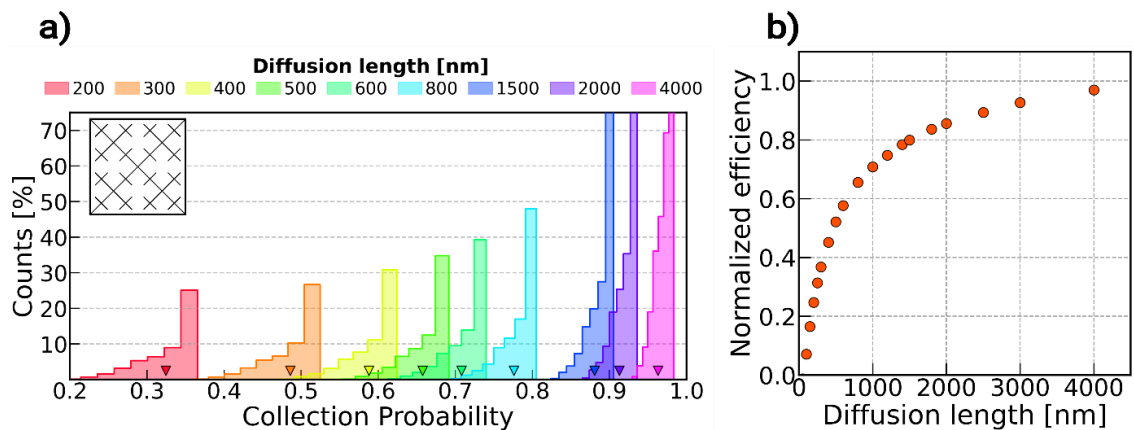


Figure 88. Collection probability of the structure for varying diffusion lengths. **a)** Histograms of the values received from the heat map along with mean values of each map (triangles) and **b)** Normalized efficiency of the structure with diffusion lengths, defined as the average value of the histograms without taking zeros values into account.

The next aspect to be explored is the influence of the diffusion length on the predicted nanomesh complexity. Intuitively, higher mobility of charges would require a less complicated structure to be effectively collected. Therefore, even small changes in the diffusion length parameter may lead to substantial changes in the optimal arrangement returned by the model. **Figure 89** illustrates the efficiency for different diffusion lengths in relation to the line number per unit cell for an exemplary geometry. Diffusion length impact becomes especially pronounced when considering the overall complexity of the structure, such as the number of lines per unit cell (pitch of the structure).

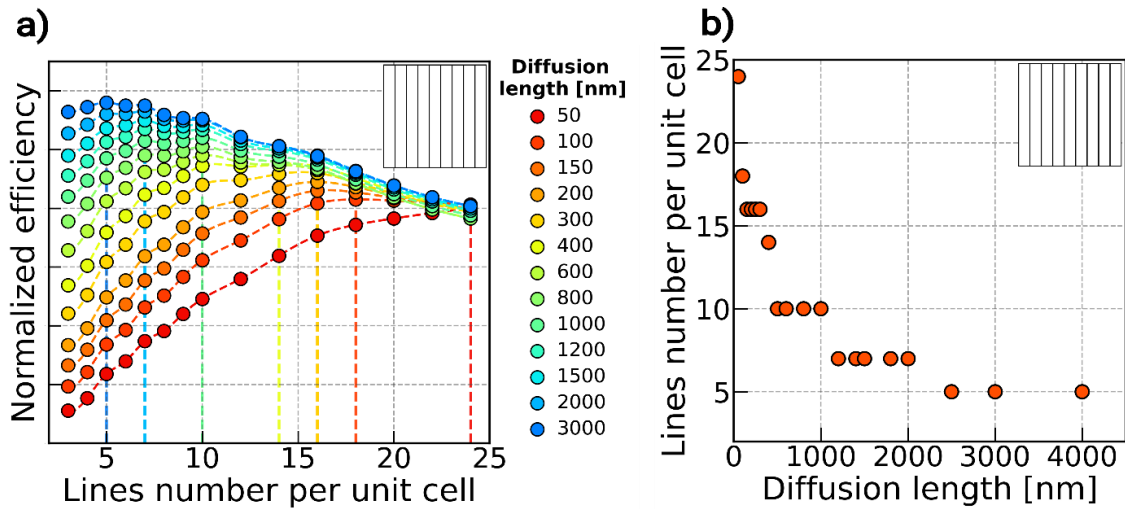


Figure 89. Efficiency results for different diffusion lengths done within a $10\ \mu\text{m}$ unit cell. a) Normalized efficiency (vertically stacked for legibility) of the structure with lines per unit cell for varying diffusion lengths of the active layer. The vertical colourful lines mark the maximum achieved for the given macroscopic parameters. Note the visible shifting toward more complicated structures with a lowering of the diffusion length parameter. **b)** Lines number per unit cell for a given diffusion length that gives the best efficiency values.

In **Figure 89b** the maximum efficiency for the given diffusion length is shown. As seen, the general trend reveals that with increasing diffusion length, the optimum is shifted towards less complicated structures. For instance, for the simple parallel lines, increasing the diffusion length from 50 nm to 4000 nm shifts the optimal periodicity from 24 per unit cell to just 5 lines per unit cell. Right in the middle, the model predicts 7 lines per unit cell for 1500 nm. This prediction also aligns with the expectations, as more complicated structures shade more area, causing more pronounced transmission losses, and affecting the final outcome. On the other hand, samples with higher carrier lifetimes gather photogenerated carriers effectively, irrespective of the nanomesh structure density. Hence, it is crucial in all cases to identify the appropriate complexity factor, which could be either fractal depth or grid period, to adjust it to each pattern and material parameters to determine the optimal position for achieving efficiency. Those results serve as an example of general trends predicted by the 3D model. The main goal of the study is to establish the design rules and predictions on the best-performing geometries.

6.4. Proposed Structures

The primary goal of the geometry design is to minimize the distance that the carrier must traverse to reach the nearest metal line of the nanomesh structure while ensuring low shading ratio losses. Rapidly exploring space structures, i.e. geometric constructions with the property of quickly reaching any point in the surface with the minimum distance required, are preferred for this purpose. Within this chapter, several structure families are proposed and evaluated.

A space-filling fractal refers to a fractal pattern that approaches arbitrarily close to all points in the surface with each iteration of the algorithm, sometimes called the space-filling property. While many structures exhibit this characteristic, some of them, such as the Hilbert curves family[242], fail to meet the minimum surface coverage requirement. In the case of the Hilbert curve, although the distance from the furthest points is reduced by a factor of 2 with each iteration, the curve's length in this process approaches infinity. In other words, such a constructed fractal would shade too much area. The attribute that is primarily sought-after in such geometry, is the simultaneous demonstration of reducing the before-mentioned distance for arbitrarily chosen points on the surface with growing complexity, while keeping at the lowest feasible point the length of the curve. The investigation in this study is focused on identifying and developing the fractals that satisfy both these criteria.

One of such fractals is the space-filling trees family. For the square-shaped surface, the filling tree is constructed as follows. The square unit cell is divided by its two diagonals, resulting in 4 distinct areas. Then, at the midpoint of each of the so obtained 4 sections, the perpendicular line is drawn, scaled down with a ratio of $1/\sqrt{2^n}$ in length where n is the number of the present iteration. The procedure continues for each section added to the geometry. The first three iterations of the algorithm are presented in **Figure 90a**. The geometry with such a constructed algorithm was described by Kuffner [243]. The tree exhibits a property that the maximum distance connecting two arbitrarily selected points of the structure is equal to $\sqrt{2}$ of the unit cell unit length which is the minimum distance possible in case of any square-shaped arrangements, contrary to some randomly distributed nanorods. This property proves to be highly favourable for the designed purpose of transporting free carriers, minimizing resistance losses caused by travelling through the mesh.

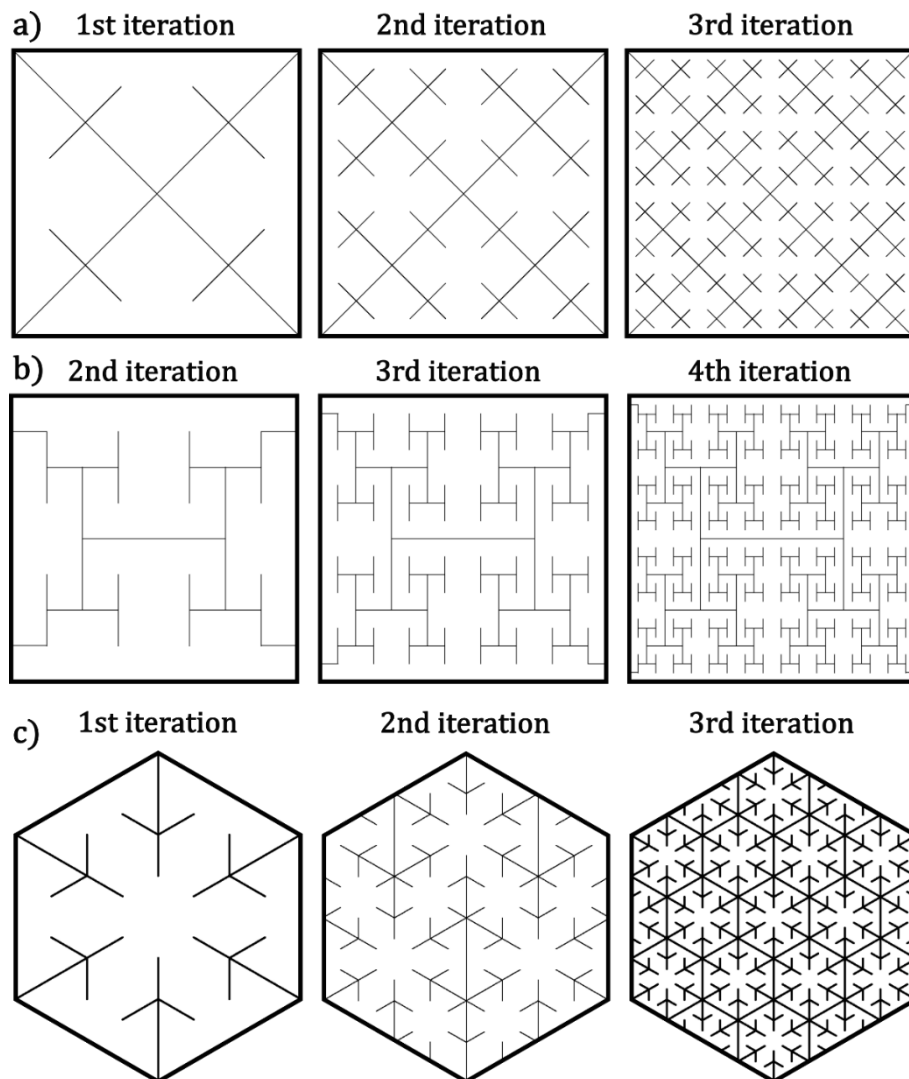


Figure 90. Fractal structures proposed for the geometry of nanomesh electrode design. Three first iterations of: **a)** square space-filling fractal, **b)** H-Tree fractal, **c)** Hexagonal space-filling fractal

Another, a commonly used fractal pattern is the so-called H-Tree fractal, frequently used in the Very Large Scale Integration (VLSI) design approach. This design allows for effective transport of the charge within the system connecting its different parts, and facilitating efficient carrier flow. The H-Tree fractal comprises interconnected lines formed in the shape of the letter 'H'. The self-similar but scaled down by the factor of $\sqrt{2}$ structure is extended from its vertices, further filling the square space. The proper scaling asserts the surface filling and approaching of each point of the system, avoiding overlapping and excess lines not contributing to the transport. The first four iterations of the H-Tree fractal are depicted in **Figure 90b**.

Similarly, the space-filling procedure can also be applied to span a triangular-shaped structure, coming arbitrarily close to a specified point within the surface.

This procedure involves a similar approach as in the case of square space-filling tree fractal, resulting in the structure depicted in **Figure 90c**. In the case of filling hexagonal space, this procedure is repeated six times with successive rotation of the whole pattern to fill the space. The maximum path length between two arbitrarily chosen points within the grid is equal to $\sqrt{3}$.

Across the literature, many tries of defining conductive nanomeshes embedded in the TCO layer have been proposed. The most prominent and commonly seen examples are simple rectangular grid, lines and a close variation of them [114,115,244,245]. These structures serve as a reference point to test the other, more sophisticated structures presented before. **Figure 91** presents the structures along with the modifications that they undergo during the evaluation process.

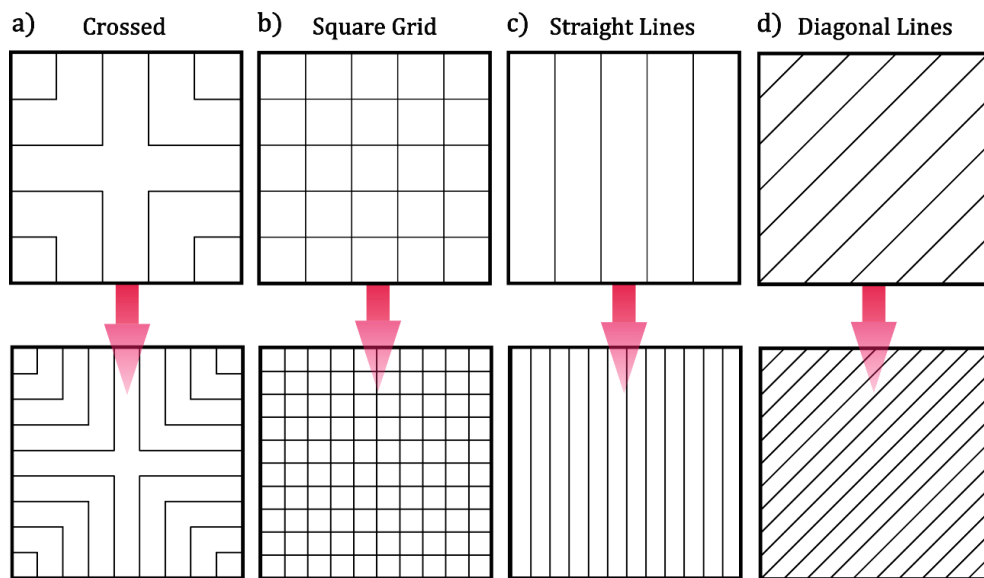


Figure 91. Regular structures employed in the study with increasing complication factor. The complication factor increase usually means the growing number of lines per unit cell, which is visible for the following geometries: **a)** Crossed structure **b)** Square grid **c)** Straight lines and **d)** Diagonal lines

These employed mostly changing the line density of the structure, leading to a decrease in the period. The investigated pattern itself is placed within either a hexagonal or square grid, creating a finely-decorated hierarchical structure. The calculations presented in this chapter take place within a so-defined one-unit cell.

6.5. Efficiency Results

All of the structures presented in **Figure 90** and **Figure 91** have been thoroughly evaluated by varying their fundamental parameters such as line width, period (or fractal iteration) and diffusion length parameter. Note that only a small fraction of the investigated dataset is presented here, as the full amount of the structures exceeds 1000 geometries. The presented results encapsulate the conclusions and trends established through the analysis of this abundant database of structures.

The final efficiency of the proposed structure heavily depends on the line width of the structure since thicker lines give rise to shadow losses without altering the fundamental geometrical properties. All of these parameters exert a profound impact on the final performance of the geometry, therefore the comparison of each structure is conducted under the same macroscopic conditions. The complexity of each structure was also investigated, considering either the spacing (pitch) between the lines used in the structure or the fractal depth in the case of the space-spanning subclass. The model tries to find a delicate equilibrium between the collection performance and shading losses induced by the metallic grid. As the model takes into account the optical response and thickness of the specific active layer, the main goal of the study is to establish the optimal structure for a given active layer parameters. To take into account the difference in the optical response of the cell, namely the different absorption exhibited by the active layer the two architectures of third-generation solar cells are utilized. One of them is the perovskite-silicon (pero-si) tandem cell and the second one is the organic layer. The perovskite-silicon tandem cell is a recently intensively studied architecture [246-248], promising high efficiency at a low cost of production. The optimized perovskite absorber bandgap of the tandem solar cell is equal to 1.65 eV. Another architecture used in the study is the organic fullerene acceptor and polymer donor blend made of PTB7-PC71BM, a commonly employed material in recent studies [249-251].

6.5.1. Diffusion length influence

Efficiency values for all the structures presented in **Figure 90** and **Figure 91** were assigned for varying complexity factors (pattern pitch or fractal depth), For a better comparison between structures with different architecture, the complexity factor was converted to a shaded area assuming constant linewidth. Additionally,

to properly compare the results across distinct active layer materials with the same optical properties (either pero-Si or organic) but different diffusion lengths, simulations for 200, 500 and 1200 nm diffusion lengths within a 10 μm unit cell were performed. Comparison between those two active layers of the third-generation photovoltaics highlights the impact of solar cell optical properties on the predicted parameters. **Figure 92** displays outcomes for tested structures of 15 nm linewidth along with a guide for an eye for improved legibility of the graph.

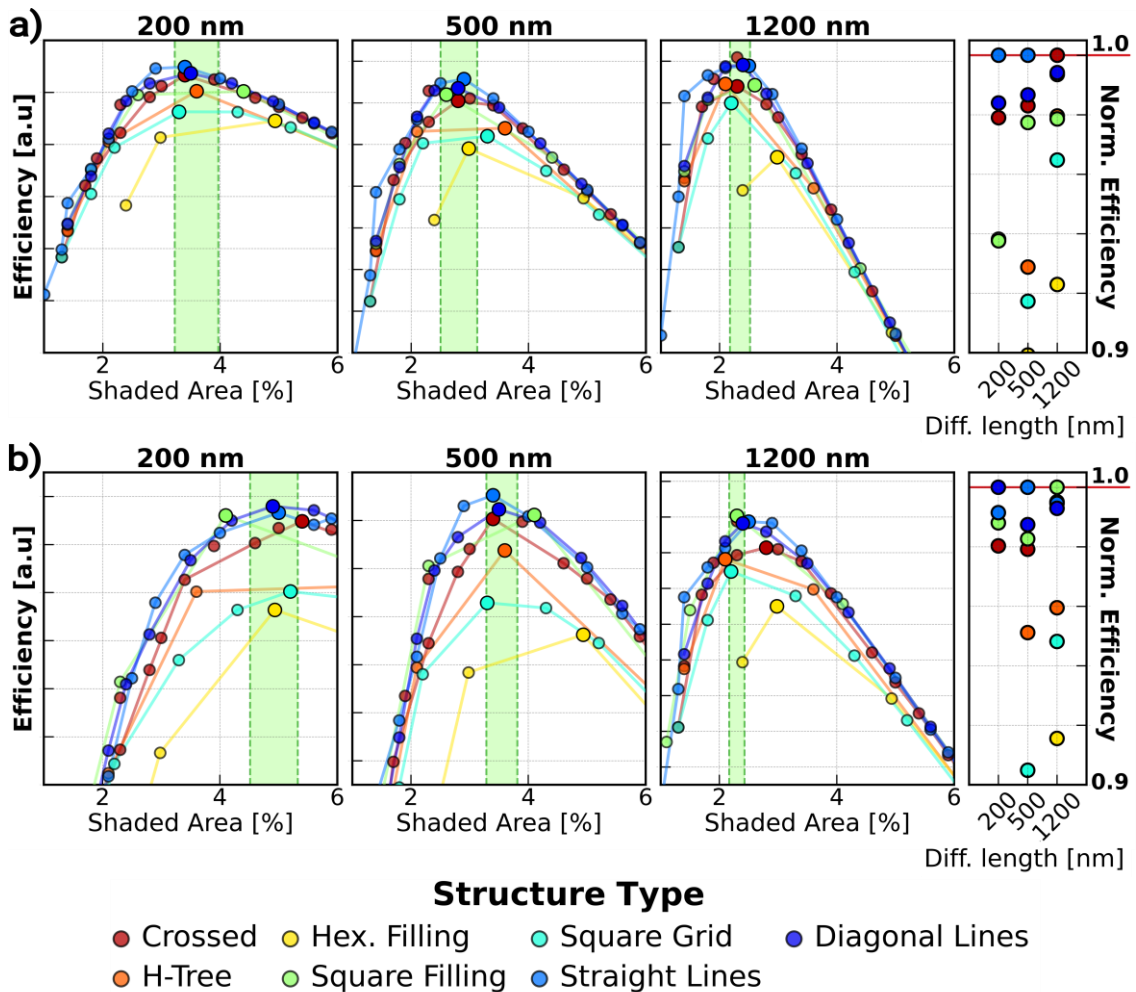


Figure 92. The efficiency results for each of the proposed structures with growing complexity and density per unit vs shaded area for structures with 15 nm linewidth and different active layers. **a)** perovskite-silicon tandem active layer and **b)** organic active layer. Three diffusion lengths are investigated: 200 nm, 500 nm and 1200 nm. In the right column, the maximum normalized efficiency is shown indicating the best-performing structure for the given diffusion length and active layer.

As anticipated, all the structures exhibit a rising trend, reaching a peak before declining as the structural complexity increases. The highlighted green

region marks the optimal shaded area for each diffusion length. It is established as the region within one standard deviation from the mean value of the best three structures efficiency for each subplot. The linewidth of 15 nm was selected to correspond to a thin line replicable through e-beam lithography.

As mentioned previously, the efficiency outcomes are comparable to each other only when stated against the results with the same macroscopic parameters, most notably diffusion length and elementary unit cell. Therefore, the y-axes in **92** display different ranges across the subplots. On the right side of each row, there is a subplot that consolidates the findings, normalized to the best-performing structure in each diffusion length regime. For instance, in the case of the perovskite-silicon tandem cell, the most optimal structures are observed to be straight lines and crossed structures, followed by diagonal lines and crossed structures for shorter diffusion lengths. For the organic active layer, a more diverse range of structures exhibiting the highest efficiencies are observed with diagonal lines, straight lines and square space-filling fractals, closely followed by the crossed structure. For perovskite-silicon solar cells, the optimal shaded areas fluctuate between 2% and 4% at most, whereas for organic absorbers they reach as much as 5% for the 200 nm diffusion length and slightly above 2% for 1200 nm.

Notably, distinctions between different structure types become more prominent in systems featuring thicker lines (around 100 nm), as illustrated in **Figure 93**. In this case, the best performance is nearly always exhibited by straight lines followed by the H-tree fractal, whereas the poorest performance is presented by a hexagonal spanning fractal, unobservable in the figure due to the applied zoom. In this linewidth regime, the crossed and diagonal lines structures yielded significantly worse results. Due to the thick lines' employment, the reached maximum is shifted towards less complicated structures, compared to geometries utilizing 15 nm lines. It's noteworthy that the optimal shaded region is notably shifted, now falling within the 5 - 10% range.

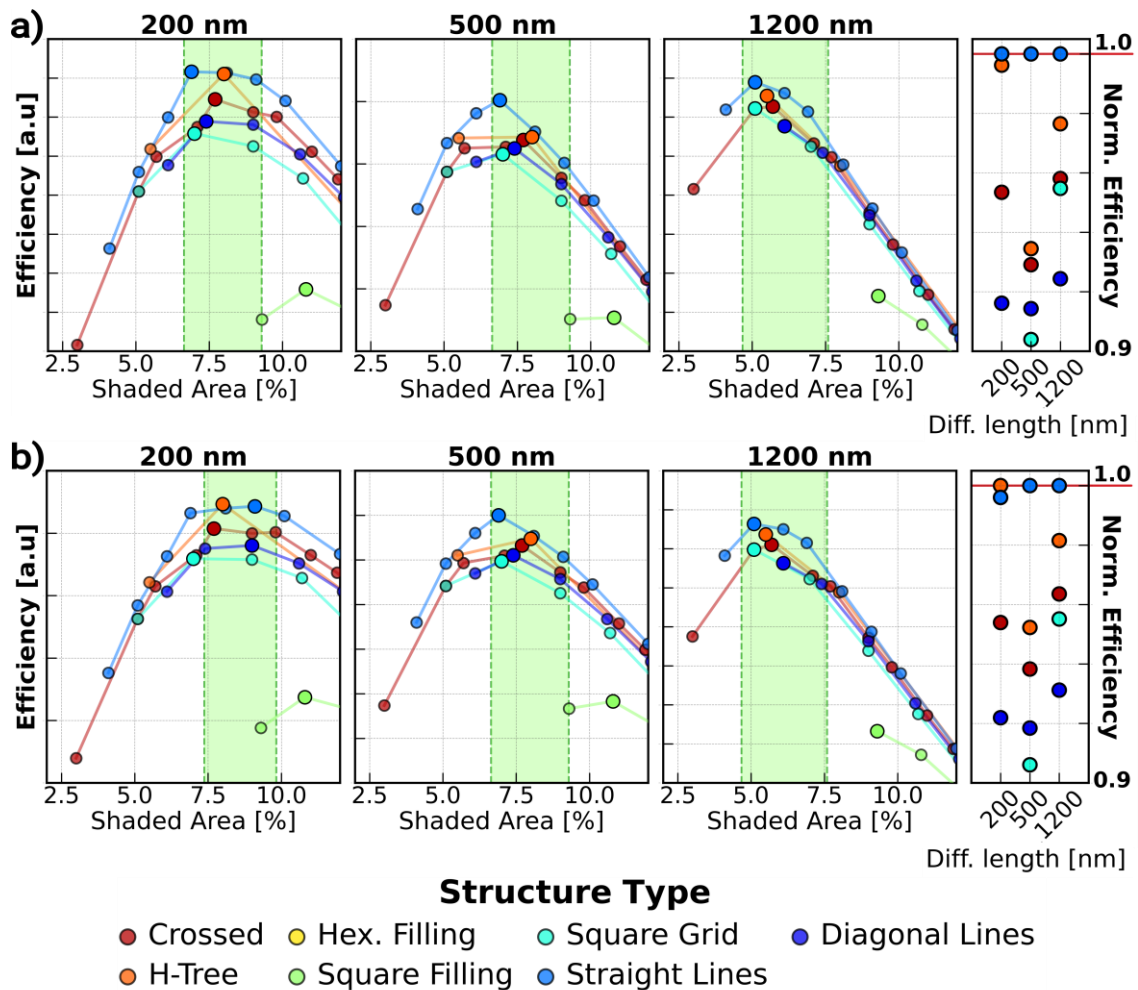


Figure 93. The efficiency results for each of the proposed structures with growing complexity and density per unit vs shaded area for structures with 100 nm linewidth and different active layers. **a)** perovskite-silicon tandem active layer and **b)** organic active layer. Three diffusion lengths are investigated: 200 nm, 500 nm and 1200 nm.

These results raise a question regarding optical losses caused by the metal meshes, even for the best-performing structures, emphasizing the need to lower the thickness of the lines within the system. Once more, fractal-like structures consistently exhibit suboptimal outcomes compared to simple straight lines in most instances, probably due to a very rapid increase in shading losses with successive iteration of the fractal, which is significantly penalized in the final efficiency evaluation.

The differences in the optimal shaded area ratio between perovskite-silicon and organic absorbers are less pronounced for the 100 nm line thickness. It appears that in this case, the geometry itself plays a more fundamental role in the collection efficiency, rather than the outcomes than alterations in the distribution of

photogenerated charges, induced by the different optical responses of the absorbers. Surprisingly, despite their exceptional expansion properties, the space-filling fractal geometries fail to dominate the result, falling short in comparison to much simpler approaches. Traditional rectangular grids, commonly employed, do not exhibit superior performance as well. Instead, it is either straight or diagonally ordered lines that prove to be more effective for the same macroscopic parameters.

6.5.2. Efficiency applied for real cases of third generation photovoltaics

Based upon the results presented in the previous section, three selected structures are examined to compare their applicability varying the line thickness and optimum period for the given linewidths. Within this section, perovskite-silicon and organic active layers are selected and investigated, followed by outcomes derived from a simplistic 2D model. This model's assumptions are significantly constrained, as it excludes the absorber's optical response, as explained in **Section 6.2**. The selected structures for the examination are the following:

- a) Straight lines, chosen for their manufacturing simplicity and consistently high performance across diverse macroscopic parameters.
- b) Rectangular grids, serving as a benchmark for other structures studied, commonly employed in literature as TCE.
- c) Crossed structure, which exhibits reasonable results, particularly notable for thicker lines, which are easier to achieve through photo- and imprint lithography techniques.

The sample with the properties of a pero-Si tandem cell is compared to the 2D model findings in **Figure 94**. The efficiency value is assigned for varying line widths and periods. As expected, the thickening of the line leads to lower efficiency and shifting the curve toward larger periods in all studied cases, showing a preference for less complicated structures. The vertical lines mark the maximum efficiency for the given linewidth parameter.

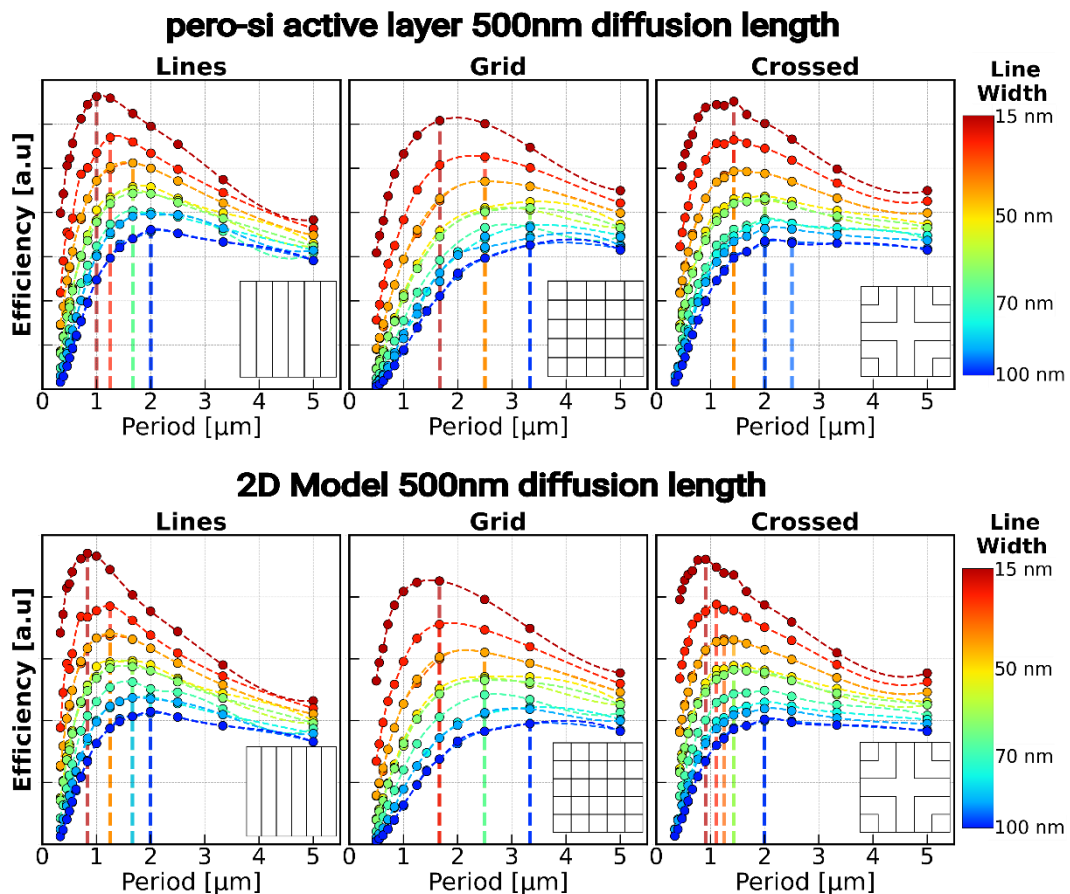


Figure 94. The efficiency of the selected structures evaluated for perovskite-silicon and 2D models. Data presented for different line thicknesses and structure periods within 10 μm unit cell. Vertical lines mark the maximum efficiency for the specific linewidth.

The 3D model consistently predicts less dense structures, resulting in improved light transmission across all investigated structures. Notably, there is a very little disparities between the 2D and 3D models in the case of rectangular grid structures. However, for straight lines exist some discrepancies, especially visible for thinner lines, disappearing beyond 60 nm lines. Furthermore, when comparing the crossed structures, the divergence between the 2D and 3D models becomes more pronounced, as the 3D model consistently indicates the less complicated structures with larger pitch values, exceeding 2 μm for structures with thicker lines. These findings display the importance of accounting for the three-dimensional nature of carrier kinetics in the design of metallic grids, as it has a visible impact on the predicted density and spatial arrangement of the grid elements.

The samples with a very low diffusion length, resembling the organic absorber solar cell and the refractive index of the PTB7-PC71BM are shown in **Figure 95**.

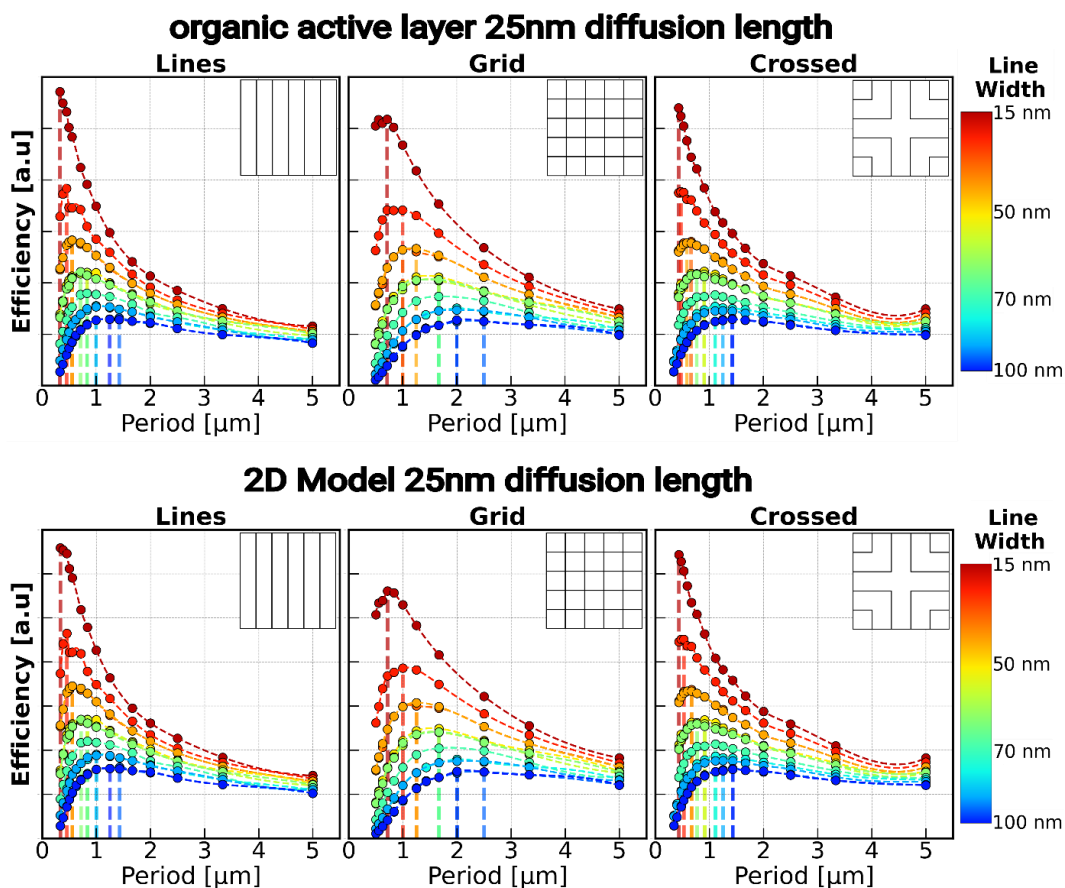


Figure 95. The efficiency of the selected structures evaluated for the organic active layer and 2D models. Data presented for different line thicknesses and structure periods within 10 μm unit cell. Vertical lines mark the maximum efficiency for the specific linewidth.

Interestingly, in the case of the organic active layer, the samples yield very similar optimal period results, regardless of the computational model utilized. For instance, straight lines and rectangular grid structures coherently raise the same optimal periods across those two models. Minor divergences emerge in the case of crossed structure, where again 3D model predicts slightly larger pitches for thinner linewidths. That suggests that the predominant influence on charge transport in such systems stems from the rapid decay and recombination of charges, rather than the optical response of the cell that plays a minor role. This behavior again aligns with the anticipated outcome, since such low diffusion length subordinates every other parameter of the structure and fundamentally dictates the photogenerated charges motion. Both models predict that the geometries made of thin lines reach their maximum efficiency at higher gridline density compared to those made of thicker lines. In this case, the models consistently point out structures with fewer

gridlines traversing the structure, minimizing the efficiency penalty induced by the loss in transmission. The summary of the results is presented in **Figure 96**.

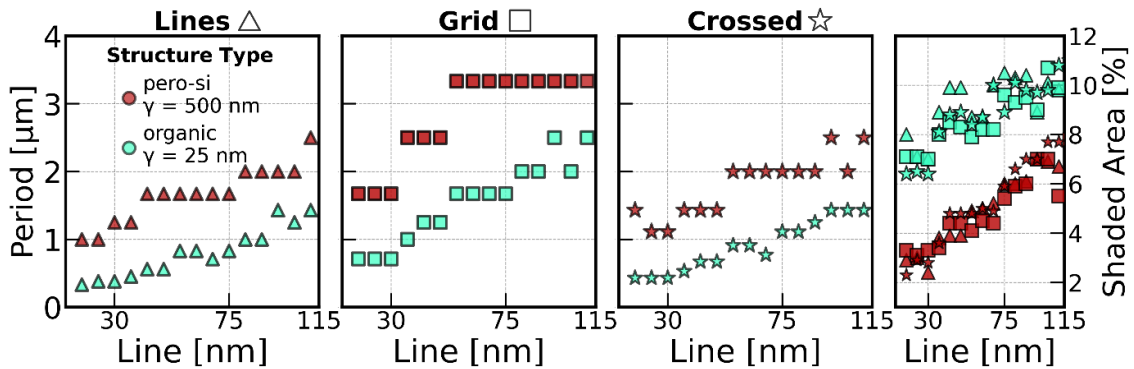


Figure 96. The period of the structure at which the system achieves the maximum efficiency for varying linewidths. On the right, the shaded area associated with the results. Triangles, squares, and stars mark the specific structure layers shown in the subplots. There is a noticeable discrepancy between those two active layers, stemming mostly from the difference in diffusion length.

As visible, the optimal period increases with thicker lines, implying the influence of the shaded area efficiency lowering. Also, as expected the perovskite layer with a longer diffusion length achieves bigger period values as they are less complicated. The periods demonstrate monotonically growing behaviour with increasing line thickness, regardless of used active layer. The optimal period of the perovskite active layer does not fall below 1 μm even for the thinnest lines possible. The organic active layer samples understandably are predicted to perform better with the subwavelength geometries, comprising of the structures with just 200 - 400 nm in period.

The subplot on the far right in **Figure 96** depicts the shading ratio associated with these top-performing structures. Immediately, the striking difference between pero-si and organic absorbers is visible, as the results are separated by around 4 - 5% in the optimal shaded area. This shaded region holds considerable significance in the final efficiency assessment. Optimal geometries with thinner lines at around 15 - 60 nm yield values below 5% and up to 8% for thicker lines in the case of perovskite active layer. As said, the organic active layer with an extremely low diffusion length needs a denser structure and therefore more shading due to the metallic grid, starting at around 6% up to 11%. The results emphasize the need to use thinner lines which allow smaller period possibilities and therefore higher efficiency results with the same shaded area ratio.

The findings presented here, although not experimentally verified in the real devices, align with the literature results where similar concepts were employed. For instance, Knight et al. [113] showed the increase of 2.1 mA/cm² in J_{sc} and a significant sheet resistance drop (15 Ω /sq) for a rectangular grid of 4 μ m period with extremely thin (~22 nm) ITO layer. Also, they showed that the period tuning and controlling shading losses is crucial, since rectangular grid with 1 μ m yielded much worse results.

The model of carrier generation and collection can be further expanded to take into account more transport phenomena to even better reflect the carrier kinetics in the near future. However, this approach would require more input parameters of the employed materials. Nevertheless, the trends depicted by the proposed model are clear and correct: the high mobility absorbers would require less dense structure, leaning toward more transparent grid, whereas materials with low diffusion lengths should be significantly enhanced in terms of the grid. Besides the transport dynamics of the charges, the optical properties after such modification should be considered as well.

6.6. Optical properties

Similar to the case of perovskite with honeycomb structure, the solar cell with modified top layer, was investigated in terms of improved optical properties. To simulate the periodic structures, again RCWA method was employed. In the case of TCE, the transmission and antireflective properties are as important as the electrical properties. Ensuring minimum optical losses is critical for the high-performing systems. As the proposed electrode is meant to be applied to a perovskite or a perovskite-silicon tandem cell, the simulations are performed for the real optical stack of solar cells.

6.6.1. Convergence analysis and RCWA simulation details

Since the main goal was to optimize the reflectivity, three different stacks were compared, illustrated in **Figure 97**: the bare perovskite solar cell, the perovskite cell with periodic nanomesh of the optimized structure and the antireflective texture, known for strong diffractive properties to elongate the

optical length in the sample and prohibit the outcoupling of the light. From the variety of antireflective coatings, the honeycomb texture proposed in the previous studies was employed, as it holds exceptional antireflective properties with proved ease of manufacturing [117,118,156,252]. Also, these studies were conducted to mitigate the unavoidable losses stemming from the metallic nanomesh. The arrangements of the employed nanomesh were chosen based on the previous results, selecting the most promising ones.

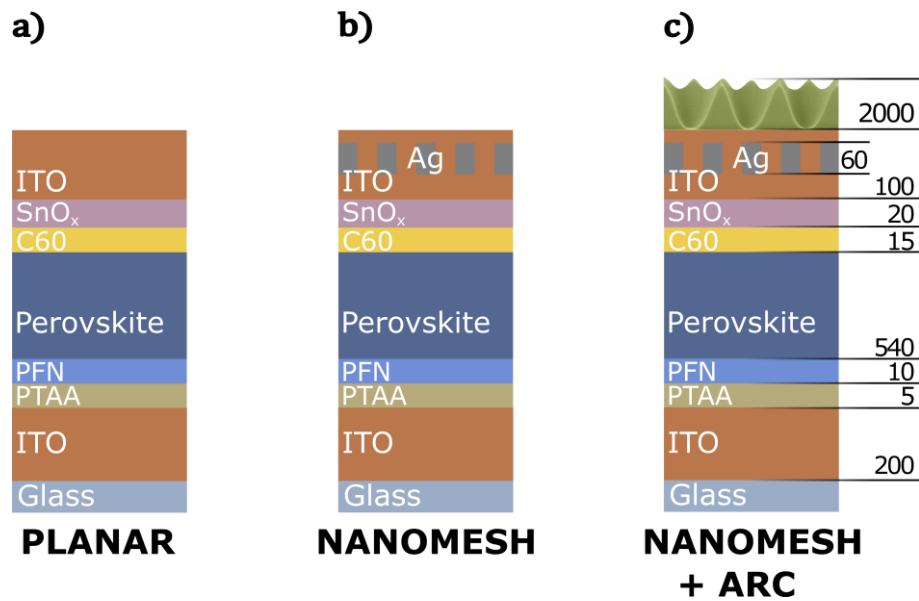


Figure 97. Simulated optical stacks. a) Planar, perovskite solar cell without any ARC coating. **b)** the same stack with nanomesh grid design embodied in the top ITO layer **c)** the stack with applied antireflective texture for maximum reflection loss reduction. On the right, there are exact dimensions utilized in the simulation in nanometers. The position of the nanomesh within the ITO layer does not influence the results obtained from the electrical model described earlier.

First, the convergence studies were conducted to assert the physical meaning of the simulations, similar to the procedure presented in **Section 5.6. Figure 98** presents the preliminary calculations result. The primary goal of this convergence study is to assess whether varying parameters significantly affects the received reflectivity.

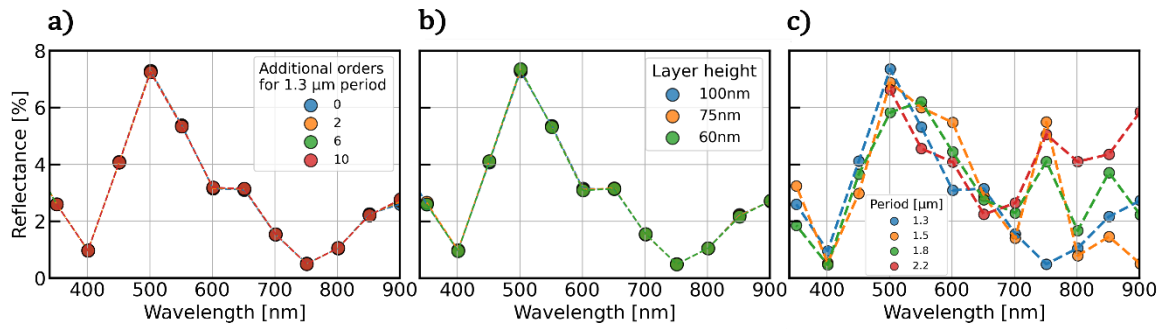


Figure 98. Convergence analysis for RCWA simulation setup for the honeycomb antireflective coating atop of perovskite cell. a) different number of additional plane waves in the calculation **b)** different degrees of discretization of the honeycomb antireflective texture **c)** different periods of the unit cell.

The fundamental setup for these computations involves a honeycomb texture atop the perovskite solar cell, similar to the system presented in **Section 5.3**. Three adjustable parameters were investigated to ensure stable and reproducible outcomes: the number of additional orders incorporated in the simulation for each x and y direction, the layer height to enhance texture discretization, and the period of the simulated unit cell.

Results indicate that the first two parameters yield virtually identical and negligible alterations, ensuring stability in the calculations. Therefore, the final parameters were set at 4 additional orders in each direction and a layer height of 75 nm, respectively. However, modifying the period introduces some discrepancies, particularly in the longer wavelength regime above 700 nm. This behaviour is expected since the structure itself acts like a diffractive structure wherein the period of such optical element is always the fundamental attribute of the system. Since the simulation time – as explained in **Section 3.4.2** – abruptly increases to unfeasible values with increasing period dimensions, the period of the unit cell was selected to facilitate finite simulation time while encompassing all necessary attributes of the physical system. Therefore, the system dimensions used in the simulations were set to $3 \mu\text{m} \times 1.8 \mu\text{m}$. Additionally, the step was chosen to 10 nm for a reliable reflection of the physical properties of the system with a reasonable calculation time for various stacks.

6.6.2. Reflectivity results

The reflection spectra were computed using the RCWA method with the earlier established simulation parameters such as spatial dimensions and additional orders employed, asserting simulations convergence. Various structures were tested to assess their influence on optical losses caused by the introduced gratings, previously identified in **Section 6.5** as the most promising structures. These structures are anticipated to induce not only simple shading losses but also to scatter and diffract the incoming light, being the foremost reason for even more light to be outcoupled.

First, simulations were performed to evaluate the reflectance of straight lines grids with differing periods, ranging from 1 μm down to 500 nm. **Figure 99** showcases the reflectance results with growing lines density, resulting in increasing the shading losses. The simulations confirm this behaviour, where a 500 nm period straight lines structure gives strong reflection around 550 nm wavelengths. As seen, the application of nanomesh leads to detrimental effects on the reflectance, however observed with different intensity, depending on the employed period of the lines.

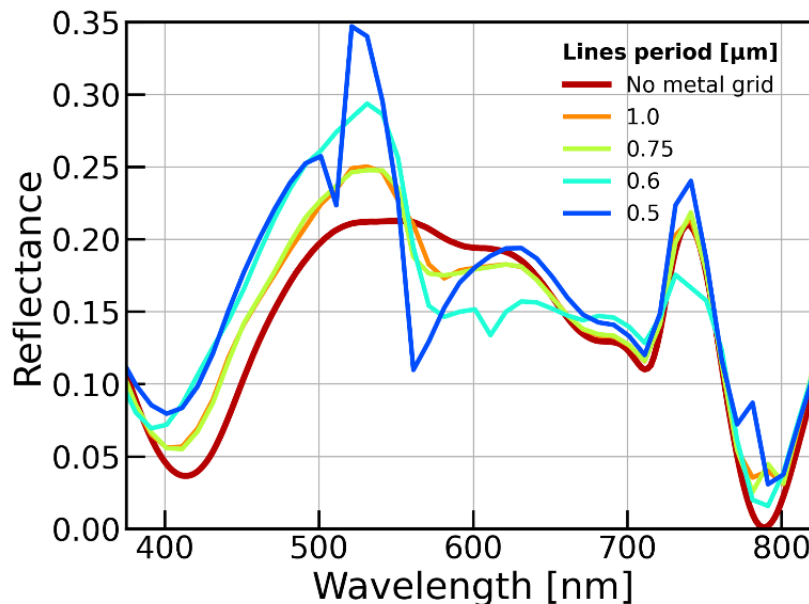


Figure 99. Reflectance spectra of the planar perovskite solar cell along with spectra of the straight lines meshes with varying periods obtained with RCWA method. The smaller period means lower transmittance and thus higher shading ratio. All the simulations with the grids were done with 10 nm step.

The highest reflectance, reaching 35% is obtained for 500 nm period straight lines. However, a slight improvement is noticeable around the 570 – 625 nm range across all investigated structures. Nevertheless, this improvement is outweighed by the increased reflection in other spectral regions, mostly below 550 nm. These findings show the importance of minimizing the shading losses and thus favouring less dense nanomesh arrangements. Despite the limitations of 10 nm step, resulting in a few spikes in reflectance spectra, and some assumptions such as perfectly planar layers, the simulation shows the expected trends of such modified systems.

In the subsequent simulations, the period of the selected structures was set to 1 μm for a more accurate comparison, ensuring similar, but not the same shading losses among the structures. **Figure 100** shows perovskite stack reflectance spectra with two different antireflective coatings applied: a planar thin film of MgF_2 or honeycomb texture applied on top of the ITO layer. As seen in **Figure 100a**, the planar MgF_2 thin film layer application notably reduces the reflectance below 10% across the entire spectral range. However, the introduction of the gratings still results in a significant loss with the exact value of this increase depending on the structure type employed. For instance, rectangular gratings yield up to 20% reflection within the 475 – 500 nm range. A notably low reflectance regardless of the used structure is achieved within the 550 – 750 nm range, highlighting the versatility of this approach when the antireflective coating is properly index-matched. Similar to bare perovskite stack, the lowest weighted reflectance is presented by the structure with the least shading structure, which is straight lines geometry. A highly promising approach involves utilizing not just a planar antireflective coating, but rather a multiscattering texture, akin to that presented in **Section 2.2.2**. Such a structure effectively deals with the reflections coming from different angles. As a result, a wideband antireflective behaviour is exhibited with a noticeable attenuation of the signal up to 750 nm wavelengths. **Figure 100b** presents the results of the honeycomb antireflective structure. After its application, the reflectance is substantially reduced for all of the employed structures. The achieved weighted reflectance spans from 7.7% to 4.9%, raising a very promising outcome, similar to that obtained in **Section 5.4.2** for the real device.

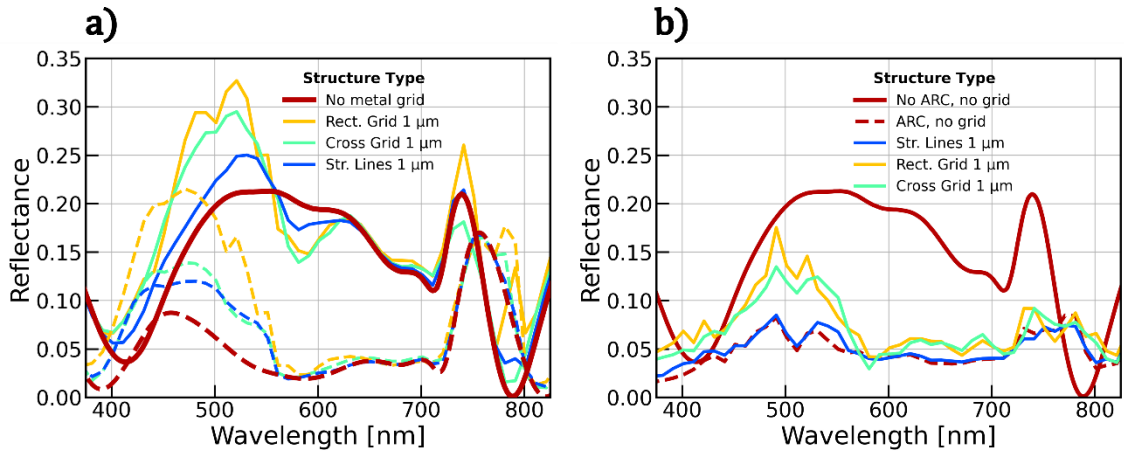


Figure 100. Reflectance spectra for perovskite solar cells of different nanomesh structures with and without antireflective coating application. a) Before and after MgF₂ planar layer application. As seen, the MgF₂ 100 nm thin film very effectively lowers the reflectance losses. **b)** The same structures with honeycomb texture on top along with the bare perovskite layer with the same applied structure.

Similarly, the straight lines geometry applied with a honeycomb texture exerts a subtle modification of the optical properties of the unmodified stack (4.9% vs. 5.2% R_w value). Interestingly, rectangular and cross-grid structures exhibit a slightly worse value, especially visible within the 475 – 550 nm range, resulting in 7.7% and 7.0% R_w , respectively. These findings suggest that the utilization of a multiscattering texture holds promise as a strategy to mitigate reflection losses. **Table 9** summarizes the weighted reflectance results for different investigated structures. It is apparent that while the incorporation of a straight lines conductive grid has a significant and beneficial effect on electrical performance, its optical impact can be effectively mitigated by applying an appropriate antireflective texture.

Table 9. Weighted reflectance results for different grids and antireflective coatings applied on perovskite cell.

Sample	As such	+Planar MgF ₂	+HC
Planar perovskite	14.4%	5.1%	4.9%
Straight lines 1 μm	15.3%	6.4%	5.2%
Rectangular 1 μm	17.5%	8.9%	7.7%
Cross structure 1 μm	16.1%	6.7%	7.0%

The findings suggest a significant potential in the structured grid for solar cells when paired with nanoimprinted ARC for additional antireflection properties enhancement. While the grids seem to have a rather detrimental effect in terms of incoupling the incoming light, these concerns can be addressed by choosing the right light management strategy, proposed and evaluated here.

6.7. Summary

A new model of assessing the applicability of nanogrids for TCO applications was proposed. It relies not only on the geometry of the grid, but also on the optical response of the solar cell – in particular the refractive index, thickness and diffusion length of the photogenerated carriers. Constructing such models is of great importance, since they are much more close-tailored approach to the specific application, in this case, the transparent grids for solar cells. By the assessment used by the model, some of the promising structures with well-defined periods were proposed.

Besides, the optical properties of such modification was analyzed. As expected, these grids introduce some shading losses that yield worse results in terms of transparency, leading to worse performance. This study addressed this issue that needs to be solved by using the two approaches known from **Section 2.2** and **Section 5.4**. which involve planar and texturized anti-reflective coating. The such proposed modification led to a very optimistic change in the simulated reflectivity, indicating that the overall performance of the sample can benefit from it.

CHAPTER 7.

Conclusions and Perspectives

This dissertation was devoted to the investigation and optimization of the operation of the top layer of solar cells. Here, a short summarization of the most important and noteworthy results and concepts presented in the thesis is provided.

CHAPTER 1. CHAPTER 2. and CHAPTER 3. presented a comprehensive introduction of the phenomena observed in the solar cell, industry evolution and relevant literature overview. These chapters meticulously described all the needed information to guide the reader through the next sections and prepare them for the topics presented in the results-filled chapters.

In **CHAPTER 4.** the properties of ALD-grown samples of ZnO thin films with different dopings are presented. Extensive studies were conducted to deeply investigate the optoelectronic properties of these films. Regardless of the cation type, doping induced significant changes in the electrical and optical properties of the samples, notably enhancing conductivity and shifting the optical bandgap towards the shorter wavelengths. Due to its exceptional conductivity and wide range of tunability, the proposed material can be employed in future electronic devices exploiting TCO films, solar cells in particular. Additionally, this chapter introduces another promising concept of transparent electrode, which is a composite oxide-metal-oxide material. Conducted TMM simulations show promising results, surpassing planar, single-layer electrode. However, experimental verification proves to be more challenging. The main reason behind this discrepancy may stem from silver diffusion and agglomeration into larger islands that breaks the continuous metal layer.

In **CHAPTER 5.** one of the earliest successful applications of direct nanoimprinted anti-reflective texture for perovskite solar cells is presented. What is more important, this application did not cause any significant damage to the cell, indicating the potential for future researches utilizing this technique on the perovskite absorber in various research domains beyond photovoltaics. The modified cell yielded highly promising efficiency, surpassing the commonly used planar MgF₂ anti-reflective coating. These results reveal the potential for further exploration, with the possibility of identifying better index-matched photoresists,

promising even lower reflectance losses. The significance of these researches is also indicated by the potential present in perovskite-silicon tandem solar cells. The nanoimprint technique presented here holds the promise to be seamlessly employed into perovskite-silicon solar cells production chain. Such tandem devices would exhibit exceptional antireflective and light-trapping properties combined with the ability of covering the wide range of solar spectrum, paving the way for the development of new record-breaking photovoltaic devices.

CHAPTER 6. combines the concepts described in the two preceding chapters, introducing a new model for transparent conductive electrode assessment as well as proposing the antireflection texture for even better optical performance of such electrode. The findings presented in this chapter are currently at the stage of numerical results, and achieving experimental validation would be a significant step forward in constructing functional, texturized, transparent electrode with embedded nanomeshes. Constructing such models that includes the electrical transport and the optical response of the cell is of great importance, since they are much more close-tailored approach to the specific solar cell active layers. The evaluation yielded by the model offers a roadmap for designing appropriate arrangements of the metallic grid for active layers, such as organic absorbers, perovskite, and tandem configurations. Additionally, the optical properties were examined, focusing on transmission losses due to shading arising from the grids. Application of suitable antireflective coatings can significantly mitigate these losses.

Presenting an abundance of important results that introduce innovative concepts for TCO and antireflective coatings, and combining them in the last chapter, numerically showing the importance of this analysis, this thesis can contribute in the ongoing development of third-generation photovoltaics, particularly perovskite and tandem perovskite-silicon cells. As this technology is currently in its infancy state, these findings paves the way for the new advancements in photovoltaic technology. The aforementioned architecture is expected to secure more industry market share, promising prominent efficiency growth compared to silicon cells and seamless implementation into existing process chains.

This thesis was meant to both explains the physical phenomena present in the solar cells, firmly rooted in the field of solid state physics, while maintain a contemporary perspective with application-oriented approach. It is devoted to exploring the newly discovered topics in the science, specifically to that one that pushes further the boundaries of renewable energy sources.

Appendix: List of scientific articles

Articles and preprints described within the thesis:

1. **Maciej Krajewski**, Adrian Callies, Minasadat Heydarian, Maryamsadat Heydarian, Mario Hanser, Patricia S. C. Schulze, Benedikt Bläsi, Oliver Höhn, Roller Nanoimprinted Honeycomb Texture as an Efficient Antireflective Coating for Perovskite Solar Cells, *Advanced Materials Interfaces*, **2023**, 2300134
[doi: 10.1002/admi.202300134](https://doi.org/10.1002/admi.202300134)
2. **Maciej Krajewski**, Mateusz Tokarczyk, Piotr Świętochowski, Piotr Wróbel, Maria Kaminska, Aneta Drabinska, Structural, Optical, and Electrical Properties of Hafnium–Aluminum–Zinc-Oxide Films Grown by Atomic Layer Deposition for TCO Applications, *ASC Omega*, VSI, **2023**
[doi:10.1021/acsomega.3c04256](https://doi.org/10.1021/acsomega.3c04256)
3. **Maciej Krajewski**, Yorick Bleiji, Piotr Wróbel, Esther Alarcon Llado, Aneta Drabińska, Embedded nanomeshes for improved transparent electrode performance applied on perovskite tandem and organic solar cells - a numerical study – currently under review

Other scientific articles and preprints, not directly linked to and not covered by the thesis:

4. Przemysław Puła, **Maciej Krajewski**, Paulina Chyży, Paweł Majewski, Copolymer-templated gas sensors based on metal oxides nanowires with ALD-made core-shell coatings for enhanced detection – in the final preparation stage
5. **Maciej Krajewski**, Piotr Piotrowski, Wojciech Mech, Krzysztof Korona, Jacek Wojtkiewicz, Marek Pilch, Andrzej Kaim, Aneta Drabińska, Maria Kamińska, Optical Properties and Light-Induced Charge Transfer in Selected Aromatic C60 Fullerene Derivatives and in Their Bulk Heterojunctions with Poly(3-Hexylthiophene), *Materials* 15 (19), **2022**
[doi: 10.3390/ma15196908](https://doi.org/10.3390/ma15196908)

6. Piotr Piotrowski, Wojciech Mech, Kamila Zarębska, **Maciej Krajewski**, Krzysztof P. Korona, Maria Kamińska, Magdalena Skompska, Andrzej Kaim, Mono- and Di-Pyrene [60]Fullerene and [70]Fullerene Derivatives as Potential Components for Photovoltaic Devices, *Molecules* **2021**, 26(6), 1561
[doi:10.3390/molecules26061561](https://doi.org/10.3390/molecules26061561)

7. Jarosław Judek, Arkadiusz Gertych, **Maciej Krajewski**, Karolina Czerniak-Łosiewicz, Anna Łapińska, Jan Sobieski, Mariusz Zdrojek, Statistical analysis of the temperature dependence of the phonon properties in supported CVD graphene, *Carbon*, **2017**, 124, 1 - 8
[doi:10.1016/j.carbon.2017.08.029](https://doi.org/10.1016/j.carbon.2017.08.029)

Figure List

Figure 1. Global electricity market.....	1
Figure 2. CO ₂ concentration and temperature deviation.....	2
Figure 3. Electricity production costs vs. the photovoltaic capacity.	3
Figure 4. Two types of semiconducting material.....	5
Figure 5. p-n junction diagrams in the thermodynamic equilibrium.....	6
Figure 6. Solar cell under illumination operation scheme with photogenerated carriers route.	8
Figure 7. I-V characteristic of p-n junction in both conditions: dark and under illumination.....	9
Figure 8. Solar cell I-V characteristic with commonly adopted convention. .	10
Figure 9. Real solar cell behaviour.	11
Figure 10 Solar spectrum power density measured at different atmospheric conditions.	13
Figure 11. Solar irradiation world map.....	14
Figure 12. Efficiency limits for selected solar cells.	15
Figure 13. Sketch of optical losses inside the solar cell.	16
Figure 14. Current Maximum Efficiencies achieved by different photovoltaic technologies	18
Figure 15. Silicon solar cell.	19
Figure 16. Thin film solar cell.....	20
Figure 17. Perovskite solar cell scheme.....	21
Figure 18 Perovskite cell energy diagram and bandgap tunability.	22
Figure 19. Optical properties of ITO thin film.....	25
Figure 20. Reflectance alteration due to the different plasma frequencies in the selected, highly conductive materials.....	27
Figure 21. Planar layered antireflective coatings.	30
Figure 22. Selected TCO/metal/TCO optical stacks.	31
Figure 23 SEM images of silver nanowires transparent electrodes creating a randomly distributed conducting grid using a wide array of techniques.....	32
Figure 24. SEM images of periodic metallic structures, creating conductive patterns with a variety of shapes and configurations.	33
Figure 25. SEM images of antireflective textures for effective light incoupling.	34
Figure 26. Various deposition techniques characteristics..	35

Figure 27. Selected literature examples of the ALD technique.	36
Figure 28. ALD setup photo.	37
Figure 29. Different modes of adsorbing material in the ALD process, depending on the chemistry of the process.	38
Figure 30. Different growth modes during the deposition.	39
Figure 31. ALD growth characteristics.	41
Figure 32. One cycle of ALD technique growth scheme.	43
Figure 33. Doping through ALD technique scheme.	44
Figure 34. Cross-section of the ALD-grown samples. a) TEM image of	45
Figure 35. Interference lithography setup scheme.	47
Figure 36. Thermally assisted Roller nanoimprint process scheme.	49
Figure 37. Roller nanoimprint system.	50
Figure 38. SEM electron beam scheme.	52
Figure 39. XRD operational principle scheme.	54
Figure 40 UV-Vis-NIR spectroscopy method scheme.	56
Figure 41. Hall effect and van der Pauw measurement setup.	58
Figure 42 Transfer matrix method scheme.	62
Figure 43 Elementary cell of a diffractive texture used in RCWA calculations.	65
Figure 44. ZnO crystal Structure.	67
Figure 45. ZnO valence and conduction bands energy levels along with the most commonly met donors and their positions in the bandgap.	68
Figure 47. Electrical parameters of ZnO and AZO thin films for varying growth temperatures.	71
Figure 48. Electrical parameters of ZnO and AZO thin films for varying diethylzinc precursor pulse duration at 190 – 200 °C growth temperature, 200 nm thickness.	72
Figure 49. Electrical parameters of ZnO and AZO thin films for varying purge duration at 190 – 200 °C growth temperature, 200 nm thickness.	73
Figure 50 The electrical parameters obtained for varying aluminium cation pulse ratio with all the other growth parameters kept constant at the optimum, previously established levels.	75
Figure 51. SEM images of zinc oxide with various aluminum dopant content.	76
Figure 52. Morphology of the AZO thin films with 4% of aluminum content for increasing material thickness.	76
Figure 53. SEM cross-sections of 500 nm aluminum doped zinc oxide (4%) at different angles.	77

Figure 54. Real appearances of the samples with different thicknesses.....	78
Figure 55. Transmission spectra of 4% AZO thin films for varying thickness ranging from 20 to 500 nm grown on a glass substrate.....	78
Figure 56. Sample growth scheme with varying dopant content of a) ZnO:Al (AZO) and b) ZnO:Hf:Al (HAZO).....	81
Figure 57. SEM images of ALD-grown thin film ZnO samples.	82
Figure 58. Granulometry results obtained from SEM images for both types of dopant samples with varying concentrations.....	83
Figure 59. Atomic Force Microscopy images in 3D projection of the samples, showing the surface morphology and roughness of each sample with different dopant concentrations.....	84
Figure 60. X-Ray Diffraction studies.	84
Figure 61. Electrical parameters of the studied materials for varying cation metal content.....	86
Figure 62. Optical transmittance spectra of: a) AZO and b) HAZO thin films ..	88
Figure 63. Tauc plots obtained from transmittance spectra of a) AZO and b) HAZO thin films ..	89
Figure 64. Optical bandgap of the thin film samples determined from Tauc plots.....	90
Figure 65. Complex refractive index extracted from the ellipsometric measurements of a) - b) AZO and c) - d) HAZO.....	92
Figure 66. TMM calculations results.....	95
Figure 67. T_w and R_w based on TMM calculations for different composite, multilayer systems comprising of a) 3-layer stack of AZO-Ag-AZO, b) 5-layer stack and c) 9-layer stack.....	96
Figure 68. T_w and R_w based on TMM calculations for 3-layer stack of AZO-Ag-AZO with antireflective MgF_2 coating.....	97
Figure 69. Real appearance of the multilayer composite electrodes. T.....	98
Figure 70. Transmission spectra of different AZO/Ag/AZO stacks, deposited on the glass substrate.....	99
Figure 71. Schemes and SEM images of different textures with varying spatial periods and features size.	104
Figure 72. Different textures imprinted on top of the glass substrate visible under different angles and magnifications.....	105
Figure 73. Examples of poorly replicated structures.....	106
Figure 74. Reflectivity for the honeycomb structure with different spin-coating speed.....	107

Figure 75. Reflectivity results for the imprinted samples on the glass substrate with black paint on the bottom surface.	108
Figure 76. Perovskite solar cell cross-section.	109
Figure 77. The real appearance of the perovskite solar cells.	110
Figure 78. SEM cross-sections of perovskite solar cells with two different nanoimprinted structures along with their schematical drawing.	110
Figure 79. Reflectance measurements of a perovskite solar cell with two different nanoimprinted textures applied: needle-like and honeycombs. ..	111
Figure 80. Real images of the perovskite solar cells with varying top surfaces.	112
Figure 81. Reflectance results of the perovskite solar cell along with the spectra obtained from the RCWA simulations.	113
Figure 82. Simulated reflectivity results along with the simulated optical stacks schemes.	115
Figure 83. External quantum efficiency spectra normalized to J_{sc} received in J-V measurements of a perovskite cell.	116
Figure 84. J-V curves of the studied solar cells samples under standard AM1.5g solar spectrum illumination conditions.	117
Figure 85. RCWA simulation setup.	120
Figure 86. Reflectance results for three different wavelengths obtained for varying layer heights.	121
Figure 87. Schematic drawing of two proposed models of photogenerated carriers' behaviour.	123
Figure 88. Collection probability heatmaps of the space-filling fractal for varying diffusion lengths.	126
Figure 89. Collection probability of the structure for varying diffusion lengths.	127
Figure 90. Efficiency results for different diffusion lengths done within a 10 μm unit cell.	128
Figure 91. Fractal structures proposed for the geometry of nanomesh electrode design.	130
Figure 92. Regular structures employed in the study with increasing complication factor.	131
Figure 93. The efficiency results for each of the proposed structures with growing complexity and density per unit vs shaded area for structures with 15 nm linewidth and different active layers.	133

Figure 94. The efficiency results for each of the proposed structures with growing complexity and density per unit vs shaded area for structures with 100 nm linewidth and different active layers.	135
Figure 95. The efficiency of the selected structures evaluated for perovskite-silicon and 2D models.	137
Figure 96. The efficiency of the selected structures evaluated for the organic active layer and 2D models.	138
Figure 97. The period of the structure at which the system achieves the maximum efficiency for varying linewidths.	139
Figure 98. Simulated optical stacks.	141
Figure 99. Convergence analysis for RCWA simulation setup for the honeycomb antireflective coating atop of perovskite cell.	142
Figure 100. Reflectance spectra of the planar perovskite solar cell along with spectra of the straight lines meshes with varying periods obtained with RCWA method.	143
Figure 101. Reflectance spectra for perovskite solar cells of different nanomesh structures with and without antireflective coating application.	145

References

- [1] Sippel, S., Meinshausen, N., Fischer, E. M., Székely, E., and Knutti, R., 2020, "Climate Change Now Detectable from Any Single Day of Weather at Global Scale," *Nat Clim Chang*, **10**(1), pp. 35–41.
- [2] Cavicchioli, R., Ripple, W. J., Timmis, K. N., Azam, F., Bakken, L. R., Baylis, M., Behrenfeld, M. J., Boetius, A., Boyd, P. W., Classen, A. T., Crowther, T. W., Danovaro, R., Foreman, C. M., Huisman, J., Hutchins, D. A., Jansson, J. K., Karl, D. M., Koskella, B., Mark Welch, D. B., Martiny, J. B. H., Moran, M. A., Orphan, V. J., Reay, D. S., Remais, J. V., Rich, V. I., Singh, B. K., Stein, L. Y., Stewart, F. J., Sullivan, M. B., van Oppen, M. J. H., Weaver, S. C., Webb, E. A., and Webster, N. S., 2019, "Scientists' Warning to Humanity: Microorganisms and Climate Change," *Nat Rev Microbiol*, **17**(9), pp. 569–586.
- [3] Moritz, C., and Agudo, R., 2013, "The Future of Species under Climate Change: Resilience or Decline?," *Science* (1979), **341**(6145), pp. 504–508.
- [4] Pirani, A., Connors, S., Péan, C., Berger, S., Caud, N., Chen, Y., Goldfarb, L., Gomis, M., Huang, M., Leitzell, K., Lonnoy, E., Matthews, J., Maycock, T., Waterfield, T., Yelekçi, O., Yu, R., Zhou, B., Bellouin, N., Coppola, E., Jones, R., Krinner, G., Marotzke, J., Naik, V., Plattner, G., Rogelj, J., Rojas, M., Sillmann, J., Storelvmo, T., Thorne, P., Trewin, B., Achuta Rao, K., Adhikary, B., Allan, R., Armour, K., Bala, G., Barimalala, R., Canadell, J., Cassou, C., Cherchi, A., Collins, W., Collins, W., Corti, S., Cruz, F., Dentener, F., Dereczynski, C., Di Luca, A., Diongue Niang, A., Doblas-Reyes, F., Dosio, A., Douville, H., Engelbrecht, F., Eyring, V., Fischer, E., Forster, P., Fox-Kemper, B., Fuglestvedt, J., Fyfe, J., Gillett, N., Gorodetskaya, I., Gutierrez, J., Hamdi, R., Hawkins, E., Hewitt, H., Hope, P., Islam, A., Jones, C., Kaufman, D., Kopp, R., Kosaka, Y., Kossin, J., Krakovska, S., Lee, J., Li, J., Mauritsen, T., Meinshausen, M., Min, S., Monteiro, P., Ngo-Duc, T., Otto, F., Pinto, I., Raghavan, K., Ranasinghe, R., Ruane, A., Ruiz, L., Sallée, J., Samset, B., Sathyendranath, S., Seneviratne, S., Sörensson, A., Szopa, S., Takayabu, I., Tréguier, A., van den Hurk, B., Vautard, R., von Schuckmann, K., Zaehle, S., Zhang, X., and Zickfeld, K., 2021, *Citation of the IPCC Working Group I Contribution to the Sixth Assessment Report*, Cambridge University Press, Cambridge, New York.
- [5] Kroepsch, A. C., Maniloff, P. T., Adgate, J. L., McKenzie, L. M., and Dickinson, K. L., 2019, "Environmental Justice in Unconventional Oil and Natural Gas Drilling and Production: A Critical Review and Research Agenda," *Environ Sci Technol*, **53**(12), pp. 6601–6615.
- [6] Moore, C. W., Zielinska, B., Pétron, G., and Jackson, R. B., 2014, "Air Impacts of Increased Natural Gas Acquisition, Processing, and Use: A Critical Review," *Environ Sci Technol*, **48**(15), pp. 8349–8359.
- [7] Liu, L., Ryu, B. J., Sun, Z., Wu, N., Cao, H., Geng, W., Zhang, X., Jia, Y., Xu, C., Guo, L., and Wang, L., 2019, "Monitoring and Research on Environmental Impacts

Related to Marine Natural Gas Hydrates: Review and Future Perspective,” *J Nat Gas Sci Eng*, **65**, pp. 82–107.

[8] IRENA, “Renewable Energy Power by Technology,” **11**(33) [Online]. Available: <https://ourworldindata.org/grapher/installed-global-renewable-energy-capacity-by-technology>. [Accessed: 25-Jun-2023].

[9] “Global Electricity Demand Forecast, IRENA,” **4**(10) [Online]. Available: <https://www.iea.org/data-and-statistics/charts/global-installed-solar-pv-capacity-by-scenario-2010-2030>. [Accessed: 25-Jun-2023].

[10] Harde, H., and Salby, M. L., “What Controls the Atmospheric CO₂ Level? Global Warming View Project Terahertz Spectroscopy View Project What Controls the Atmospheric CO₂ Level?”

[11] Malhi, G. S., Kaur, M., and Kaushik, P., 2021, “Impact of Climate Change on Agriculture and Its Mitigation Strategies: A Review,” *Sustainability (Switzerland)*, **13**(3), pp. 1–21.

[12] Monnin, E., Indermühle, A., Dällenbach, A., Flückiger, J., Stauffer, B., Stocker, T. F., Raynaud, D., and Barnola, J. M., 2001, “Atmospheric CO₂ Concentrations over the Last Glacial Termination,” *Science* (1979), **291**(5501), pp. 112–114.

[13] Wuebbles, D. J., and Jain, A. K., 2001, “Concerns about Climate Change and the Role of Fossil Fuel Use,” *Fuel Processing Technology*, **71**, pp. 99–119.

[14] Höök, M., and Tang, X., 2013, “Depletion of Fossil Fuels and Anthropogenic Climate Change-A Review,” *Energy Policy*, **52**, pp. 797–809.

[15] Zeebe, R. E., and Tyrrell, T., 2019, “History of Carbonate Ion Concentration over the Last 100 Million Years II: Revised Calculations and New Data,” *Geochim Cosmochim Acta*, **257**, pp. 373–392.

[16] Galbraith, E. D., and Eggleston, S., 2017, “A Lower Limit to Atmospheric CO₂ Concentrations over the Past 800,000 Years,” *Nat Geosci*, **10**(4), pp. 295–298.

[17] Khatiwala, S., Primeau, F., and Hall, T., 2009, “Reconstruction of the History of Anthropogenic CO₂ Concentrations in the Ocean,” *Nature*, **462**(7271), pp. 346–349.

[18] Wehner, M., Stone, D., Mitchell, D., Shiogama, H., Fischer, E., Graff, L. S., Kharin, V. V., Lierhammer, L., Sanderson, B., and Krishnan, H., 2018, “Changes in Extremely Hot Days under Stabilized 1.5 and 2.0 °C Global Warming Scenarios as Simulated by the HAPPI Multi-Model Ensemble,” *Earth System Dynamics*, **9**(1), pp. 299–311.

[19] Schleussner, C. F., Lissner, T. K., Fischer, E. M., Wohland, J., Perrette, M., Golly, A., Rogelj, J., Childers, K., Schewe, J., Frieler, K., Mengel, M., Hare, W., and Schaeffer, M., 2016, “Differential Climate Impacts for Policy-Relevant Limits to Global Warming: The Case of 1.5 °C and 2 °C,” *Earth System Dynamics*, **7**(2), pp. 327–351.

[20] Seneviratne, S. I., Rogelj, J., Séférian, R., Wartenburger, R., Allen, M. R., Cain, M., Millar, R. J., Ebi, K. L., Ellis, N., Hoegh-Guldberg, O., Payne, A. J., Schleussner, C. F., Tschakert, P., and Warren, R. F., 2018, “The Many Possible Climates from the Paris Agreement’s Aim of 1.5 °C Warming,” *Nature*, **558**(7708), pp. 41–49.

- [21] Schewe, J., Levermann, A., and Meinshausen, M., 2011, "Climate Change under a Scenario near 1.5°C of Global Warming: Monsoon Intensification, Ocean Warming and Steric Sea Level Rise," *Earth System Dynamics*, **2**(1), pp. 25–35.
- [22] Barcikowska, M. J., Weaver, S. J., Feser, F., Russo, S., Schenk, F., Stone, D. A., Wehner, M. F., and Zahn, M., 2018, "Euro-Atlantic Winter Storminess and Precipitation Extremes under 1.5°C vs. 2°C Warming Scenarios," *Earth System Dynamics*, **9**(2), pp. 679–699.
- [23] Wehner, M. F., Reed, K. A., Loring, B., Stone, D., and Krishnan, H., 2018, "Changes in Tropical Cyclones under Stabilized 1.5 and 2.0°C Global Warming Scenarios as Simulated by the Community Atmospheric Model under the HAPPI Protocols," *Earth System Dynamics*, **9**(1), pp. 187–195.
- [24] UCSD, "Keeling Curve Data" [Online]. Available: <https://keelingcurve.ucsd.edu/permissions-and-data-sources/>. [Accessed: 25-Jun-2023].
- [25] NOAA, "Global Temperature Growth Anomaly" [Online]. Available: <https://www.nci.noaa.gov/access/monitoring/climate-at-a-glance/global/time-series>. [Accessed: 25-Jun-2023].
- [26] Osman, A. I., Chen, L., Yang, M., Msigwa, G., Farghali, M., Fawzy, S., Rooney, D. W., and Yap, P. S., 2023, "Cost, Environmental Impact, and Resilience of Renewable Energy under a Changing Climate: A Review," *Environ Chem Lett*, **21**(2), pp. 741–764.
- [27] Barbato, L., Centi, G., Iaquaniello, G., Mangiapane, A., and Perathoner, S., 2014, "Trading Renewable Energy by Using CO₂: An Effective Option to Mitigate Climate Change and Increase the Use of Renewable Energy Sources," *Energy Technology*, **2**(5), pp. 453–461.
- [28] Owusu, P. A., and Asumadu-Sarkodie, S., 2016, "A Review of Renewable Energy Sources, Sustainability Issues and Climate Change Mitigation," *Cogent Eng*, **3**(1).
- [29] 2011, *Summary for Policy Makers Lead Authors: Special Advisor*, Abu Dhabi.
- [30] Solaun, K., and Cerdá, E., 2019, "Climate Change Impacts on Renewable Energy Generation. A Review of Quantitative Projections," *Renewable and Sustainable Energy Reviews*, **116**.
- [31] "PV Prices vs. Global Capacity" [Online]. Available: <https://ourworldindata.org/grapher/solar-pv-prices-vs-cumulative-capacity>. [Accessed: 30-Jun-2023].
- [32] Solaun, K., and Cerdá, E., 2019, "Climate Change Impacts on Renewable Energy Generation. A Review of Quantitative Projections," *Renewable and Sustainable Energy Reviews*, **116**.
- [33] Rudan, M., 2015, *Physics of Semiconductor Devices*, Springer New York.
- [34] Patterson, J., and Bailey, B., 2007, *Solid-State Physics*, Springer, Berlin.
- [35] Sadowski, M. L., Potemski, M., and Grynberg, M., 1999, *Optical Properties of Semiconductor Nanostructures*.

- [36] Wenham, S. R., Martin A. Green, Muriel E. Watt, Richard Corkish, and Alistair Sproul, 2012, *Applied Photovoltaics*, Earthscan.
- [37] Sze, S. M., and Ng, K. K., 2007, *Physics of Semiconductor Devices*, John Wiley & Sons, Hoboken.
- [38] Shockley, W., 1949, "The Theory of P-n Junctions in Semiconductors and p-n Junction Transistors," *Bell System Technical Journal*, **28**(3).
- [39] Hall, R. N., 1952, "Electron-Hole Recombination in Germanium," *Physical Review*, **87**, p. 387.
- [40] Shockley, W., and Read, W. T., 1952, "Statistics of the Recombinations of Holes and Electrons," *Physical Review*, **87**(5), pp. 835–842.
- [41] Cariou, R., Benick, J., Feldmann, F., Höhn, O., Hauser, H., Beutel, P., Razeq, N., Wimplinger, M., Bläsi, B., Lackner, D., Hermle, M., Siefer, G., Glunz, S. W., Bett, A. W., and Dimroth, F., 2018, "III-V-on-Silicon Solar Cells Reaching 33% Photoconversion Efficiency in Two-Terminal Configuration," *Nat Energy*, **3**(4), pp. 326–333.
- [42] Zhang, X., Li, C., Xu, J., Wang, R., Song, J., Zhang, H., Li, Y., Jing, Y. N., Li, S., Wu, G., Zhou, J., Li, X., Zhang, Y., Li, X., Zhang, J., Zhang, C., Zhou, H., Sun, Y., and Zhang, Y., 2022, "High Fill Factor Organic Solar Cells with Increased Dielectric Constant and Molecular Packing Density," *Joule*, **6**(2), pp. 444–457.
- [43] Wolf, M., and Rauschenbacht, H., 1963, "Series Resistance Effects on Solar Cell Measurements," *Advanced Energy Conversion*, **3**, pp. 455–479.
- [44] Jain, A., and Kapoor, A., 2004, "Exact Analytical Solutions of the Parameters of Real Solar Cells Using Lambert W-Function," *Solar Energy Materials and Solar Cells*, **81**(2), pp. 269–277.
- [45] Leonowicz, Z., Institute of Electrical and Electronics Engineers, IEEE Electromagnetic Compatibility Society, IEEE Power & Energy Society, IEEE Industry Applications Society, and Industrial and Commercial Power Systems Europe (4th : 2020 : Online), *Conference Proceedings : 2020 IEEE International Conference Environment and Electrical Engineering and 2020 IEEE Industrial and Commercial Power Systems Europe (EEEIC / I & CPS Europe) : 9-12 June, 2020, Madrid, Spain*.
- [46] Hansen, C., 2015, *Parameter Estimation for Single Diode Models of Photovoltaic Modules*, Albuquerque.
- [47] Bishop, J. W., 1988, "Computer Simulation of the Effects of Electrical Mismatches in Photovoltaic Cell Interconnection Circuits," *Solar Cells*, **25**, p. 73.
- [48] Gueymard, C. A., Myers, D., and Emery, K., 2002, "Proposed Reference Irradiance Spectra for Solar Energy Systems Testing," *Solar Energy*, **73**(6), pp. 443–467.
- [49] NREL, "Reference Air Mass 1.5 Solar Spectral Irradiance Spectrum" [Online]. Available: <https://www.nrel.gov/grid/solar-resource/spectra-am1.5.html>.
- [50] "World Irradiation Map" [Online]. Available: <https://solargis.com/maps-and-gis-data/download/world>. [Accessed: 28-Jun-2023].
- [51] Shockley, W., and Queisser, H. J., 1961, "Detailed Balance Limit of Efficiency of P-n Junction Solar Cells," *J Appl Phys*, **32**(3), pp. 510–519.

- [52] Queisser, H. J., 2009, "Detailed Balance Limit for Solar Cell Efficiency," *Mater Sci Eng B Solid State Mater Adv Technol*, **159–160**(C), pp. 322–328.
- [53] Marti, A., and Arafijo, G. L., 1996, "Limiting Efficiencies for Photovoltaic Energy Conversion in Multigap Systems," *Solar Energy Materials and Solar Cells*, **43**, pp. 203–222.
- [54] Rühle, S., 2016, "Tabulated Values of the Shockley-Queisser Limit for Single Junction Solar Cells," *Solar Energy*, **130**, pp. 139–147.
- [55] De Vos, A., 1980, "Detailed Balance Limit of the Efficiency of Tandem Cells," *Journal of Physics D: Applied*, **13**, p. 839.
- [56] "Refractive Index Database" [Online]. Available: <https://refractiveindex.info/>. [Accessed: 01-Jul-2023].
- [57] Green, M. A., 2009, "The Path to 25% Silicon Solar Cell Efficiency: History of Silicon Cell Evolution," *Progress in Photovoltaics: Research and Applications*, **17**(3), pp. 183–189.
- [58] "Most Efficient Solar Cell with 47.6 Percent Efficiency" [Online]. Available: <https://www.ise.fraunhofer.de/en/press-media/press-releases/2022/fraunhofer-ise-develops-the-worlds-most-efficient-solar-cell-with-47-comma-6-percent-efficiency.html>. [Accessed: 30-May-2022].
- [59] Futscher, M. H., and Ehrler, B., 2016, "Efficiency Limit of Perovskite/Si Tandem Solar Cells," *ACS Energy Lett*, **1**(4), pp. 863–868.
- [60] Hossain, M. I., Qarony, W., Ma, S., Zeng, L., Knipp, D., and Tsang, Y. H., 2019, "Perovskite/Silicon Tandem Solar Cells: From Detailed Balance Limit Calculations to Photon Management," *Nanomicro Lett*, **11**(1).
- [61] Neder, V., Tabernig, S. W., and Polman, A., 2022, "Detailed-Balance Efficiency Limits of Two-Terminal Perovskite/Silicon Tandem Solar Cells with Planar and Lambertian Spectral Splitters," *J Photonics Energy*, **12**(01), pp. 1–11.
- [62] "Photovoltaics Market Share by Technology" [Online]. Available: <https://www.iea.org/reports/solar-pv-global-supply-chains>. [Accessed: 01-Jul-2023].
- [63] "NREL Best Research-Cell Efficiency Chart" [Online]. Available: <https://www.nrel.gov/pv/cell-efficiency.html>.
- [64] Allen, T. G., Bullock, J., Yang, X., Javey, A., and De Wolf, S., 2019, "Passivating Contacts for Crystalline Silicon Solar Cells," *Nat Energy*, **4**(11), pp. 914–928.
- [65] Ribeyron, P. J., 2017, "Crystalline Silicon Solar Cells: Better than Ever," *Nat Energy*, **2**(5).
- [66] "Silicon Cell Image" [Online]. Available: <https://www.nature.com/articles/am201082/figures/1>. [Accessed: 31-Aug-2023].
- [67] Bouich, A., Hartiti, B., Ullah, S., Ullah, H., Touhami, M. E., Santos, D. M. F., and Mari, B., 2019, "Experimental, Theoretical, and Numerical Simulation of the Performance of $\text{CuIn}_x\text{Ga}_{(1-x)}\text{S}_2$ -Based Solar Cells," *Optik (Stuttg)*, **183**, pp. 137–147.

- [68] Bouanani, B., Joti, A., Bachir Bouiadjra, F. S., and Kadid, A., 2020, "Band Gap and Thickness Optimization for Improvement of CIGS/CIGS Tandem Solar Cells Using Silvaco Software," *Optik (Stuttg)*, **204**.
- [69] Paudel, N. R., Wieland, K. A., and Compaan, A. D., 2012, "Ultrathin CdS/CdTe Solar Cells by Sputtering," *Solar Energy Materials and Solar Cells*, **105**, pp. 109–112.
- [70] Barbato, M., Artegiani, E., Bertoncetto, M., Meneghini, M., Trivellin, N., Mantoan, E., Romeo, A., Mura, G., Ortolani, L., Zanoni, E., and Meneghesso, G., 2021, "CdTe Solar Cells: Technology, Operation and Reliability," *J Phys D Appl Phys*, **54**(33).
- [71] Feurer, T., Reinhard, P., Avancini, E., Bissig, B., Löckinger, J., Fuchs, P., Carron, R., Weiss, T. P., Perrenoud, J., Stutterheim, S., Buecheler, S., and Tiwari, A. N., 2017, "Progress in Thin Film CIGS Photovoltaics – Research and Development, Manufacturing, and Applications," *Progress in Photovoltaics: Research and Applications*, **25**(7), pp. 645–667.
- [72] "CIGS Cell Image" [Online]. Available: <https://www.empa.ch/web/s604/cigs-efficiency-record-2021>. [Accessed: 01-Sep-2023].
- [73] Yamaguchi, M., Dimroth, F., Geisz, J. F., and Ekins-Daukes, N. J., 2021, "Multi-Junction Solar Cells Paving the Way for Super High-Efficiency," *J Appl Phys*, **129**(24).
- [74] Van Riesen, S., Neubauer, M., Boos, A., Rico, M. M., Gourdel, C., Wanka, S., Krause, R., Guernard, P., and Gombert, A., 2015, "New Module Design with 4-Junction Solar Cells for High Efficiencies," *AIP Conference Proceedings*, American Institute of Physics Inc.
- [75] Yoon, H., Granata, J. E., Hebert, P., King, R. R., Fetzer, C. M., Colter, P. C., Edmondson, K. M., Law, D., Kinsey, G. S., Krut, D. D., Ermer, J. H., Gillanders, M. S., and Karam, N. H., 2005, "Recent Advances in High-Efficiency III-V Multi-Junction Solar Cells for Space Applications: Ultra Triple Junction Qualification," *Progress in Photovoltaics: Research and Applications*, pp. 133–139.
- [76] Pérez-Higueras, P., and Fernández Editors, E. F., *Green Energy and Technology High Concentrator Photovoltaics Fundamentals, Engineering and Power Plants*.
- [77] Alves, M., Pérez-Rodríguez, A., Dale, P. J., Domínguez, C., and Sadewasser, S., 2020, "Thin-Film Micro-Concentrator Solar Cells," *JPhys Energy*, **2**(1).
- [78] Wang, X., Zhi, L., and Müllen, K., 2008, "Transparent, Conductive Graphene Electrodes for Dye-Sensitized Solar Cells," *Nano Lett*, **8**(1), pp. 323–327.
- [79] Zhang, W., Zhu, R., Li, F., Wang, Q., and Liu, B., 2011, "High-Performance Solid-State Organic Dye Sensitized Solar Cells with P3HT as Hole Transporter," *Journal of Physical Chemistry C*, **115**(14), pp. 7038–7043.
- [80] de la Mora, M. B., Amelines-Sarria, O., Monroy, B. M., Hernández-Pérez, C. D., and Lugo, J. E., 2017, "Materials for Downconversion in Solar Cells: Perspectives and Challenges," *Solar Energy Materials and Solar Cells*, **165**, pp. 59–71.

- [81] Lim, M. J., Ko, Y. N., Chan Kang, Y., and Jung, K. Y., 2014, "Enhancement of Light-Harvesting Efficiency of Dye-Sensitized Solar Cells via Forming TiO₂ Composite Double Layers with down/up Converting Phosphor Dispersion," *RSC Adv*, **4**(20), pp. 10039–10042.
- [82] Eperon, G. E., Stranks, S. D., Menelaou, C., Johnston, M. B., Herz, L. M., and Snaith, H. J., 2014, "Formamidinium Lead Trihalide: A Broadly Tunable Perovskite for Efficient Planar Heterojunction Solar Cells," *Energy Environ Sci*, **7**(3), pp. 982–988.
- [83] Masharin, M. A., Shahnazaryan, V. A., Benimetskiy, F. A., Krizhanovskii, D. N., Shelykh, I. A., Iorsh, I. V., Makarov, S. V., and Samusev, A. K., 2022, "Polaron-Enhanced Polariton Nonlinearity in Lead Halide Perovskites," *Nano Lett*, **22**(22), pp. 9092–9099.
- [84] Kojima, A., Teshima, K., Shirai, Y., and Miyasaka, T., 2009, "Organometal Halide Perovskites as Visible-Light Sensitizers for Photovoltaic Cells," *J Am Chem Soc*, **131**(17), pp. 6050–6051.
- [85] Ogomi, Y., Morita, A., Tsukamoto, S., Saitho, T., Fujikawa, N., Shen, Q., Toyoda, T., Yoshino, K., Pandey, S. S., Ma, T., and Hayase, S., 2014, "CH₃NH₃S_nxPb(1-x)I₃ Perovskite Solar Cells Covering up to 1060 Nm," *Journal of Physical Chemistry Letters*, **5**(6), pp. 1004–1011.
- [86] Sutherland, B. R., and Sargent, E. H., 2016, "Perovskite Photonic Sources," *Nat Photonics*, **10**(5), pp. 295–302.
- [87] Minami, T., 2013, "Transparent Conductive Oxides for Transparent Electrode Applications," *Semiconductors and Semimetals*, Academic Press Inc., pp. 159–200.
- [88] Lokanc, M., Eggert, R., and Redlinger, M., 2015, *The Availability of Indium: The Present, Medium Term, and Long Term*.
- [89] Haacke, G., 1976, "New Figure of Merit for Transparent Conductors," *J Appl Phys*, **47**(9), pp. 4086–4089.
- [90] Mendez-Gamboa, J. A., Castro-Rodriguez, R., Perez-Quintana, I. V., Medina-Esquivel, R. A., and Martel-Arbelo, A., 2016, "A Figure of Merit to Evaluate Transparent Conductor Oxides for Solar Cells Using Photonic Flux Density," *Thin Solid Films*, **599**, pp. 14–18.
- [91] Sepulveda-Mora, S. B., and Cloutier, S. G., 2012, "Figures of Merit for High-Performance Transparent Electrodes Using Dip-Coated Silver Nanowire Networks," *J Nanomater*, **2012**.
- [92] Shanmugam, N., Pugazhendhi, R., Elavarasan, R. M., Kasiviswanathan, P., and Das, N., 2020, "Anti-Reflective Coating Materials: A Holistic Review from PV Perspective," *Energies (Basel)*, **13**(10), pp. 1–93.
- [93] Girtan, M., 2012, "Comparison of ITO/Metal/ITO and ZnO/Metal/ZnO Characteristics as Transparent Electrodes for Third Generation Solar Cells," *Solar Energy Materials and Solar Cells*, **100**, pp. 153–161.
- [94] Kim, Y. S., Lee, Y. J., Heo, S. B., Lee, H. M., Kim, J. H., Kim, S. K., Chae, J. H., Choi, J. I., and Kim, D., 2011, "Fabrication and Characterization of Ag Intermediate

Transparent and Conducting TiON/Ag/TiON Multilayer Films,” *Opt Commun*, **284**(9), pp. 2303–2306.

[95] Dang, T. Van, Pammi, S. V. N., Choi, J., and Yoon, S. G., 2017, “Utilization of AZO/Au/AZO Multilayer Electrodes Instead of FTO for Perovskite Solar Cells,” *Solar Energy Materials and Solar Cells*, **163**(January), pp. 58–65.

[96] Liu, L., Ma, S., Wu, H., Zhu, B., Yang, H., Tang, J., and Zhao, X., 2015, “Effect of the Annealing Process on Electrical and Optical Properties of SnO₂/Ag/SnO₂ Nanometric Multilayer Film,” *Mater Lett*, **149**, pp. 43–46.

[97] Yu, S., Liu, Y., Zheng, H., Li, L., and Sun, Y., 2017, “Improved Performance of Transparent-Conducting AZO/Cu/AZO Multilayer Thin Films by Inserting a Metal Ti Layer for Flexible Electronics,” *Opt Lett*, **42**(15), p. 3020.

[98] Jeong, J. A., Park, Y. S., and Kim, H. K., 2010, “Comparison of Electrical, Optical, Structural, and Interface Properties of IZO-Ag-IZO and IZO-Au-IZO Multilayer Electrodes for Organic Photovoltaics,” *J Appl Phys*, **107**(2).

[99] Park, Y.-S., Park, H.-K., Jeong, J.-A., Kim, H.-K., Choi, K.-H., Na, S.-I., and Kim, D.-Y., 2009, “Comparative Investigation of Transparent ITO/Ag/ITO and ITO/Cu/ITO Electrodes Grown by Dual-Target DC Sputtering for Organic Photovoltaics,” *J Electrochem Soc*, **156**(7), p. H588.

[100] Kim, D., 2010, “Low Temperature Deposition of Transparent Conducting ITO/Au/ITO Films by Reactive Magnetron Sputtering,” *Appl Surf Sci*, **256**(6), pp. 1774–1777.

[101] Sahu, D. R., and Huang, J. L., 2007, “The Properties of ZnO/Cu/ZnO Multilayer Films before and after Annealing in the Different Atmosphere,” *Thin Solid Films*, **516**(2–4), pp. 208–211.

[102] Chakaroun, M., Lucas, B., Ratier, B., Defranoux, C., Piel, J. P., and Aldissi, M., 2009, “High Quality Transparent Conductive Electrodes in Organic Photovoltaic Devices,” *Thin Solid Films*, **518**(4), pp. 1250–1253.

[103] Guillén, C., and Herrero, J., 2011, “TCO/Metal/TCO Structures for Energy and Flexible Electronics,” *Thin Solid Films*, **520**(1), pp. 1–17.

[104] Zhang, C., Ji, C., Park, Y. B., and Guo, L. J., 2021, “Thin-Metal-Film-Based Transparent Conductors: Material Preparation, Optical Design, and Device Applications,” *Adv Opt Mater*, **9**(3).

[105] Sawada, M., Higuchi, M., Kondo, S., and Saka, H., 2001, *Characteristics of Indium-Tin-Oxide/Silver/Indium-Tin-Oxide Sandwich Films and Their Application to Simple-Matrix Liquid-Crystal Displays*.

[106] Han, B., Huang, Y., Li, R., Peng, Q., Luo, J., Pei, K., Herczynski, A., Kempa, K., Ren, Z., and Gao, J., 2014, “Bio-Inspired Networks for Optoelectronic Applications,” *Nat Commun*, **5**.

[107] Peng, Q., Li, S., Han, B., Rong, Q., Lu, X., Wang, Q., Zeng, M., Zhou, G., Liu, J. M., Kempa, K., and Gao, J., 2016, “Colossal Figure of Merit in Transparent-Conducting Metallic Ribbon Networks,” *Adv Mater Technol*, **1**(6), pp. 1–4.

[108] Basarir, F., Irani, F. S., Kosemen, A., Camic, B. T., Oytun, F., Tunaboylu, B., Shin, H. J., Nam, K. Y., and Choi, H., 2017, “Recent Progresses on Solution-Processed Silver

Nanowire Based Transparent Conducting Electrodes for Organic Solar Cells,” *Mater Today Chem*, **3**, pp. 60–72.

[109] Yu, Z., Li, L., Zhang, Q., Hu, W., and Pei, Q., 2011, “Silver Nanowire-Polymer Composite Electrodes for Efficient Polymer Solar Cells,” *Advanced Materials*, **23**(38), pp. 4453–4457.

[110] José Andrés, L., Fe Menéndez, M., Gómez, D., Luisa Martínez, A., Bristow, N., Paul Kettle, J., Menéndez, A., and Ruiz, B., 2015, “Rapid Synthesis of Ultra-Long Silver Nanowires for Tailor-Made Transparent Conductive Electrodes: Proof of Concept in Organic Solar Cells,” *Nanotechnology*, **26**(26), pp. 1–9.

[111] Leem, D. S., Edwards, A., Faist, M., Nelson, J., Bradley, D. D. C., and De Mello, J. C., 2011, “Efficient Organic Solar Cells with Solution-Processed Silver Nanowire Electrodes,” *Advanced Materials*, **23**(38), pp. 4371–4375.

[112] Yang, K., Rahman, M. A., Jeong, K., Nam, H. S., Kim, J., and Lee, J., 2014, “Semitransparent, Thin Metal Grid-Based Hybrid Electrodes for Polymer Solar Cells,” *Mater Sci Semicond Process*, **23**(1), pp. 104–109.

[113] Knight, M. W., van de Groep, J., Bronsveld, P. C. P., Sinke, W. C., and Polman, A., 2016, “Soft Imprinted Ag Nanowire Hybrid Electrodes on Silicon Heterojunction Solar Cells,” *Nano Energy*, **30**(July), pp. 398–406.

[114] Li, L., Zhang, B., Zou, B., Xie, R., Zhang, T., Li, S., Zheng, B., Wu, J., Weng, J., Zhang, W., Huang, W., and Huo, F., 2017, “Fabrication of Flexible Transparent Electrode with Enhanced Conductivity from Hierarchical Metal Grids,” *ACS Appl Mater Interfaces*, **9**(45), pp. 39110–39115.

[115] Gao, T., Huang, P. S., Lee, J. K., and Leu, P. W., 2015, “Hierarchical Metal Nanomesh/Microgrid Structures for High Performance Transparent Electrodes,” *RSC Adv*, **5**(87), pp. 70713–70717.

[116] Hong, S., Yeo, J., Kim, G., Kim, D., Lee, H., Kwon, J., Lee, H., Lee, P., and Ko, S. H., 2013, “Nonvacuum, Maskless Fabrication of a Flexible Metal Grid Transparent Conductor by Low-Temperature Selective Laser Sintering of Nanoparticle Ink,” *ACS Nano*, **7**(6), pp. 5024–5031.

[117] Bläsi, B., Hauser, H., Höhn, O., Kübler, V., Peters, M., and Wolf, A. J., 2011, “Photon Management Structures Originated by Interference Lithography,” *Energy Procedia*, **8**, pp. 712–718.

[118] Hauser, H., 2013, “Nanoimprint Lithography for Solar Cell Texturization,” Dissertation, Albert-Ludwigs-Universität Freiburg.

[119] Yoo, G. Y., Nurrosyid, N., Lee, S., Jeong, Y., Yoon, I., Kim, C., Kim, W., Jang, S. Y., and Do, Y. R., 2020, “Newly Developed Broadband Antireflective Nanostructures by Coating a Low-Index MgF₂ Film onto a SiO₂ Moth-Eye Nanopattern,” *ACS Appl Mater Interfaces*, **12**(9), pp. 10626–10636.

[120] Arto Pakkala, and Matti Putkonen, 2010, *Handbook of Deposition Technologies for Films and Coatings, Third Edition: Science, Applications and Technology, Chapter 8*, Elsevier, Amsterdam, Boston USA, Heidelberg, London.

- [121] Yeh, Y. W., Lin, S. H., Hsu, T. C., Lai, S., Lee, P. T., Lien, S. Y., Wu, D. S., Li, G., Chen, Z., Wu, T., and Kuo, H. C., 2021, "Advanced Atomic Layer Deposition Technologies for Micro-LEDs and VCSELs," *Nanoscale Res Lett*, **16**(1).
- [122] Cheng, H.-T., Qiu, J., Peng, C.-Y., Kuo, H.-C., Feng, M., and Wu, C.-H., 2022, "29 GHz Single-Mode Vertical-Cavity Surface-Emitting Lasers Passivated by Atomic Layer Deposition," *Opt Express*, **30**(26), p. 47553.
- [123] Chu, C. L., Wu, K., Luo, G. L., Chen, B. Y., Chen, S. H., Wu, W. F., and Yeh, W. K., 2018, "Stacked Ge-Nanosheet GAAFETs Fabricated by Ge/Si Multilayer Epitaxy," *IEEE Electron Device Letters*, **39**(8), pp. 1133–1136.
- [124] Chen, M. L., Sun, X., Liu, H., Wang, H., Zhu, Q., Wang, S., Du, H., Dong, B., Zhang, J., Sun, Y., Qiu, S., Alava, T., Liu, S., Sun, D. M., and Han, Z., 2020, "A FinFET with One Atomic Layer Channel," *Nat Commun*, **11**(1).
- [125] Fei, Y., 2023, "Optimization of ULED Electrical Properties with AlGaIn/GaN Tunnel Junction Layer," University of California.
- [126] Agarwal, L., Priya, G. L., Papnassam, E., Kumar, B. P., and Venkatesh, M., 2023, "A Novel Metal Dielectric Metal Based GAA-Junction-Less TFET Structure for Low Loss SRAM Design," *Silicon*, **15**(7), pp. 2989–3001.
- [127] Lühn, O., Van Hoof, C., Ruythooren, W., and Celis, J. P., 2008, "Barrier and Seed Layer Coverage in 3D Structures with Different Aspect Ratios Using Sputtering and ALD Processes," *Microelectron Eng*, **85**(10), pp. 1947–1951.
- [128] Elam, J. W., Routkevitch, D., Mardilovich, P. P., and George, S. M., 2003, "Conformal Coating on Ultrahigh-Aspect-Ratio Nanopores of Anodic Alumina by Atomic Layer Deposition," *Chemistry of Materials*, **15**(18), pp. 3507–3517.
- [129] Johnson, R. W., Hultqvist, A., and Bent, S. F., 2014, "A Brief Review of Atomic Layer Deposition: From Fundamentals to Applications," *Materials Today*, **17**(5), pp. 236–246.
- [130] Wu, Y., Giddings, A. D., Verheijen, M. A., Macco, B., Prosa, T. J., Larson, D. J., Roozeboom, F., and Kessels, W. M. M., 2018, "Dopant Distribution in Atomic Layer Deposited ZnO:Al Films Visualized by Transmission Electron Microscopy and Atom Probe Tomography," *Chemistry of Materials*, **30**(4), pp. 1209–1217.
- [131] Swerts, J., Peys, N., Nyns, L., Delabie, A., Franquet, A., Maes, J. W., Van Elshocht, S., and De Gendt, S., 2010, "Impact of Precursor Chemistry and Process Conditions on the Scalability of ALD HfO₂ Gate Dielectrics," *J Electrochem Soc*, **157**(1), p. G26.
- [132] Yuan, G. J., Xie, J. F., Li, H. H., Lu, H. L., and Tian, Y. Z., 2019, "Atomic Layer Deposition of Inorganic Films for the Synthesis of Vertically Aligned Carbon Nanotube Arrays and Their Hybrids," *Coatings*, **9**(12).
- [133] Szindler, M., Szindler, M. M., Dobrzański, L. A., Szindler, M., and Szindler, M. M., 2015, *Surface Morphology and Optical Properties of Al₂O₃ Thin Films Deposited by ALD Method* *Surface Morphology and Optical Properties of Al₂O₃ Thin Films Deposited by ALD Method*.

- [134] Puurunen, R. L., 2014, "A Short History of Atomic Layer Deposition: Tuomo Suntola's Atomic Layer Epitaxy," *Chemical Vapor Deposition*, **20**(10–12), pp. 332–344.
- [135] Ylilammi, M., Ylivaara, O. M. E., and Puurunen, R. L., 2018, "Modeling Growth Kinetics of Thin Films Made by Atomic Layer Deposition in Lateral High-Aspect-Ratio Structures," *J Appl Phys*, **123**(20).
- [136] Puurunen, R. L., 2005, "Surface Chemistry of Atomic Layer Deposition: A Case Study for the Trimethylaluminum/Water Process," *J Appl Phys*, **97**(12).
- [137] Muneshwar, T., and Cadien, K., 2016, "AxB₂AxB ... Pulsed Atomic Layer Deposition: Numerical Growth Model and Experiments," *J Appl Phys*, **119**(8).
- [138] Ponraj, J. S., Attolini, G., and Bosi, M., 2013, "Review on Atomic Layer Deposition and Applications of Oxide Thin Films," *Critical Reviews in Solid State and Materials Sciences*, **38**(3), pp. 203–233.
- [139] Puurunen, R. L., 2003, "Growth per Cycle in Atomic Layer Deposition: Real Application Examples of a Theoretical Model," *Chemical Vapor Deposition*, **9**(6), pp. 327–332.
- [140] Wang, H., Wang, J. J., Gordon, R., Lehn, J. S. M., Li, H., Hong, D., and Shenai, D. V., 2009, "Atomic Layer Deposition of Lanthanum-Based Ternary Oxides," *Electrochemical and Solid-State Letters*, **12**(4).
- [141] Elliott, S. D., and Nilsen, O., 2011, "(Invited) Reaction Mechanisms in ALD of Ternary Oxides," *ECS Trans*, **41**(2), pp. 175–183.
- [142] Wu, Y., Giddings, A. D., Verheijen, M. A., Macco, B., Prosa, T. J., Larson, D. J., Roozeboom, F., and Kessels, W. M. M., 2018, "Dopant Distribution in Atomic Layer Deposited ZnO:Al Films Visualized by Transmission Electron Microscopy and Atom Probe Tomography," *Chemistry of Materials*, **30**(4), pp. 1209–1217.
- [143] Łuka, G., 2011, *Warstwy ZnO i ZnO:Al Otrzymane Metodą Osadzania Warstw Atomowych Do Zastosowań w Organicznej Elektronice*, Warszawa.
- [144] Guo, L. J., 2007, "Nanoimprint Lithography: Methods and Material Requirements," *Advanced Materials*, **19**(4), pp. 495–513.
- [145] Chou, S. Y., Krauss, P. R., and Renstrom, P. J., 1995, "Imprint of Sub-25 Nm Vias and Trenches in Polymers," *Appl Phys Lett*, **67**, p. 3114.
- [146] Schiff, H., 2008, "Nanoimprint Lithography: An Old Story in Modern Times? A Review," *Journal of Vacuum Science & Technology B: Microelectronics and Nanometer Structures Processing, Measurement, and Phenomena*, **26**(2), pp. 458–480.
- [147] Hauser, H., Berger, P., Michl, B., Müller, C., Schwarzkopf, S., Hermle, M., and Bläsi, B., 2010, "Nanoimprint Lithography for Solar Cell Texturisation," *Micro-Optics 2010*, **7716**, p. 77160X.
- [148] Hauser, H., Michl, B., Schwarzkopf, S., Kübler, V., Müller, C., Hermle, M., and Bläsi, B., 2012, "Honeycomb Texturing of Silicon via Nanoimprint Lithography for Solar Cell Applications," *IEEE J Photovolt*, **2**(2), pp. 114–122.
- [149] Eisenlohr, J., Tucher, N., Hauser, H., Graf, M., Benick, J., Bläsi, B., Goldschmidt, J. C., and Hermle, M., 2016, "Efficiency Increase of Crystalline Silicon Solar Cells with

Nanoimprinted Rear Side Gratings for Enhanced Light Trapping,” *Solar Energy Materials and Solar Cells*, **155**, pp. 288–293.

[150] Bragg, W. H., and Cavendish, M. A., 1913, “The Reflection of X-Rays by Crystals.”

[151] Look, D. C., and Leach, J. H., 2016, “On the Accurate Determination of Absorption Coefficient from Reflectance and Transmittance Measurements: Application to Fe-Doped GaN,” *Journal of Vacuum Science & Technology B, Nanotechnology and Microelectronics: Materials, Processing, Measurement, and Phenomena*, **34**(4), p. 04J105.

[152] van der Pauw L. J., 1958, “A Method of Measuring Specific Resistivity and Hall Effect of Discs of Arbitrary Shape,” *Philips Research Reports*, **13**(1).

[153] Geng, Y., 2022, “Mathematical Analysis of Van Der Pauw’s Method for Measuring Resistivity,” *Journal of Physics: Conference Series*, Institute of Physics.

[154] Koon, D. W., Bahl, A. A., and Duncan, E. O., 1989, “Measurement of Contact Placement Errors in the van Der Pauw Technique,” *Review of Scientific Instruments*, **60**(2), pp. 275–276.

[155] Jošt, M., Köhnen, E., Morales-Vilches, A. B., Lipovšek, B., Jäger, K., Macco, B., Al-Ashouri, A., Krč, J., Korte, L., Rech, B., Schlatmann, R., Topič, M., Stannowski, B., and Albrecht, S., 2018, “Textured Interfaces in Monolithic Perovskite/Silicon Tandem Solar Cells: Advanced Light Management for Improved Efficiency and Energy Yield,” *Energy Environ Sci*, **11**(12), pp. 3511–3523.

[156] Peters, I. M., Hauser, H., Tucher, N., and Bläsi, B., 2016, “Optical Modeling of Honeycomb Textures for Multicrystalline Silicon Solar Cells,” *IEEE J Photovolt*, **6**(6), pp. 1480–1487.

[157] Hugonin, A. J. P., and Lalanne, P., 2012, “RETICOLO CODE 1D for the Diffraction by Stacks of Lamellar 1D Gratings,” pp. 1–16.

[158] Lalanne, P., and Morris, G. M., 1996, “Highly Improved Convergence of the Coupled-Wave Method for TM Polarization,” *Optics Letters*, **21**(4), pp. 779–784.

[159] Grann, E. B., Pommet, D. a., Moharam, M. G., and Gaylord, T. K., 1995, “Formulation for Stable and Efficient Implementation of the Rigorous Coupled-Wave Analysis of Binary Gratings,” *Journal of the Optical Society of America A*, **12**(5), pp. 1068–1076.

[160] Krajewski, M., Tokarczyk, M., Świętochowski, P., Wróbel, P., Kamińska, M., and Drabińska, A., 2023, “Structural, Optical, and Electrical Properties of Hafnium-Aluminum-Zinc-Oxide Films Grown by Atomic Layer Deposition for TCO Applications,” *ACS Omega*, **8**(33), pp. 30621–30629.

[161] Tomlins, G. W., Routbort, J. L., and Mason, T. O., 2000, “Zinc Self-Diffusion, Electrical Properties, and Defect Structure of Undoped, Single Crystal Zinc Oxide,” *J Appl Phys*, **87**(1), pp. 117–123.

[162] Hagemark, K. I., and Chacka, L. C., 1975, “Electrical Transport Properties of Zn Doped ZnO,” *J Solid State Chem*, pp. 261–270.

[163] Von Wenckstern, H., Weinhold, S., Biehne, G., Pickenhain, R., Schmidt, H., Hochmuth, H., and Grundmann, M., *ASSP 45 - Donor Levels in ZnO*.

- [164] Guziewicz, E., Krajewski, T. A., Przedziecka, E., Korona, K. P., Czechowski, N., Kłopotowski, L., and Terziyska, P., 2020, "Zinc Oxide Grown by Atomic Layer Deposition: From Heavily n-Type to p-Type Material," *Phys Status Solidi B Basic Res*, **257**(2).
- [165] Erhart, P., Albe, K., and Klein, A., 2006, "First-Principles Study of Intrinsic Point Defects in ZnO: Role of Band Structure, Volume Relaxation, and Finite-Size Effects," *Phys Rev B Condens Matter Mater Phys*, **73**(20).
- [166] Schmidt-Mende, L., and MacManus-Driscoll, J. L., 2007, "ZnO - Nanostructures, Defects, and Devices," *Materials Today*, **10**(5), pp. 40–48.
- [167] Gurylev, V., and Perng, T. P., 2021, "Defect Engineering of ZnO: Review on Oxygen and Zinc Vacancies," *J Eur Ceram Soc*, **41**(10), pp. 4977–4996.
- [168] Nakrela, A., Benramdane, N., Bouzidi, A., Kebbab, Z., Medles, M., and Mathieu, C., 2016, "Site Location of Al-Dopant in ZnO Lattice by Exploiting the Structural and Optical Characterisation of ZnO: Al Thin Films," *Results Phys*, **6**, pp. 133–138.
- [169] Van De Walle, C. G., 2000, *Hydrogen as a Cause of Doping in Zinc Oxide*.
- [170] Chen, S. bu, Lu, Z., Zhong, Z. you, Long, H., Gu, J. hua, and Long, L., 2016, "Microstructure and Optoelectronic Properties of Galliumtitanium-Zinc Oxide Thin Films Deposited by Magnetron Sputtering," *Optoelectron Lett*, **12**(4), pp. 280–284.
- [171] Illiberi, A., Scherpenborg, R., Roozeboom, F., and Poodt, P., 2014, "Atmospheric Spatial Atomic Layer Deposition of In-Doped ZnO," *ECS Journal of Solid State Science and Technology*, **3**(5), pp. P111–P114.
- [172] Lee, D. J., Kwon, J. Y., Kim, J., Kim, K. J., Cho, Y. H., Cho, S. Y., Kim, S. H., Xu, J., and Kim, K. B., 2014, "Ultrasoother, High Electron Mobility Amorphous In-Zn-O Films Grown by Atomic Layer Deposition," *Journal of Physical Chemistry C*, **118**(1), pp. 408–415.
- [173] Wang, G. G., Zeng, J., Han, J. C., and Wang, L. Y., 2014, "Highly Transparent and Conductive Ga-Doped ZnO Films with Good Thermal Stability Prepared by Dual-Target Reactive Sputtering," *Mater Lett*, **137**, pp. 307–310.
- [174] Luka, G., Wachnicki, L., Witkowski, B. S., Krajewski, T. A., Jakiela, R., Guziewicz, E., and Godlewski, M., 2011, "The Uniformity of Al Distribution in Aluminum-Doped Zinc Oxide Films Grown by Atomic Layer Deposition," *Mater Sci Eng B Solid State Mater Adv Technol*, **176**(3), pp. 237–241.
- [175] Elam, J. W., and George, S. M., 2003, "Growth of ZnO/Al₂O₃ Alloy Films Using Atomic Layer Deposition Techniques," *Chemistry of Materials*, **15**(4), pp. 1020–1028.
- [176] Tao, Y. M., Ma, S. Y., Chen, H. X., Meng, J. X., Hou, L. L., Jia, Y. F., and Shang, X. R., 2011, "Effect of the Oxygen Partial Pressure on the Microstructure and Optical Properties of ZnO:Cu Films," *Vacuum*, **85**(7), pp. 744–748.
- [177] Rekha, K., Nirmala, M., Nair, M. G., and Anukaliani, A., 2010, "Structural, Optical, Photocatalytic and Antibacterial Activity of Zinco Xide and Manganese Doped Zinc Oxide Nanoparticles," *Physica B Condens Matter*, **405**(15), pp. 3180–3185.

- [178] Ahn, B. Du, Kang, H. S., Kim, J. H., Kim, G. H., Chang, H. W., and Lee, S. Y., 2006, "Synthesis and Analysis of Ag-Doped ZnO," *J Appl Phys*, **100**(9).
- [179] Cerrato, E., Gionco, C., Berruti, I., Sordello, F., Calza, P., and Paganini, M. C., 2018, "Rare Earth Ions Doped ZnO: Synthesis, Characterization and Preliminary Photoactivity Assessment," *J Solid State Chem*, **264**, pp. 42–47.
- [180] Shukla, S., and Sharma, D. K., 2019, "A Review on Rare Earth (Ce and Er)-Doped Zinc Oxide Nanostructures," *Materials Today: Proceedings*, Elsevier Ltd, pp. 793–801.
- [181] Sernelius, B. E., Berggren, K.-F., Jin, Z.-C., Hamberg, I., and Granqvist, C. G., "Band-Gap Tailoring of ZnO by Means of Heavy Al Doping," *Phys Rev B*, **37**, pp. 15–1988.
- [182] Gao, Z., and Banerjee, P., 2019, "Review Article: Atomic Layer Deposition of Doped ZnO Films," *Journal of Vacuum Science & Technology A*, **37**(5), p. 050802.
- [183] Kang, K. M., Wang, Y., Kim, M., Lee, C., and Park, H. H., 2021, "Al/F Codoping Effect on the Structural, Electrical, and Optical Properties of ZnO Films Grown via Atomic Layer Deposition," *Appl Surf Sci*, **535**.
- [184] Zamani Meymian, M. R., Mousavi, M. A., Rabbani, M., and Fallah, M., 2021, "Effects of Thallium–Aluminum-Codoped Zinc Oxide Thin Film as a New Transparent Conducting Oxide," *Physica Status Solidi (A) Applications and Materials Science*, **218**(9).
- [185] Cao, H. T., Pei, Z. L., Gong, J., Sun, C., Huang, R. F., and Wen, L. S., 2004, "Preparation and Characterization of Al and Mn Doped ZnO (ZnO: (Al, Mn)) Transparent Conducting Oxide Films," *J Solid State Chem*, **177**(4–5), pp. 1480–1487.
- [186] Bocchese, F., Cornil, D., Haye, E., Cornil, J., and Lucas, S., 2022, "Three-Zone Model for Ti, Al Co-Doped ZnO Films Deposited by Magnetron Sputtering," *Surfaces and Interfaces*, **28**.
- [187] Srinatha, N., Raghu, P., Mahesh, H. M., Madhu, A., Hussain, S., Dam, S., Kumar M R, S., and Angadi, B., 2021, "Study on the Effect of Ni Co-Doping on Structural, Micro-Structural and Optical Properties of Transparent AZO Thin Films," *Opt Mater (Amst)*, **113**.
- [188] Hsi, C. S., Hsiung, B., Hou, B. Y., Chen, G. J., and Fu, S. L., 2008, "Effect of Ru Addition on the Properties of Al-Doped ZnO Thin Films Prepared by Radio Frequency Magnetron Sputtering on Polyethylene Terephthalate Substrate," *J Alloys Compd*, **464**(1–2), pp. 89–94.
- [189] Choi, B. G., Kim, I. H., Kim, D. H., Lee, K. S., Lee, T. S., Cheong, B., Baik, Y. J., and Kim, W. M., 2005, "Electrical, Optical and Structural Properties of Transparent and Conducting ZnO Thin Films Doped with Al and F by Rf Magnetron Sputter," *J Eur Ceram Soc*, **25**(12 SPEC. ISS.), pp. 2161–2165.
- [190] El Ghouli, J., Bouguila, N., Gómez-Lopera, S. A., and El Mir, L., 2013, "Structural and Optical Properties of Nanoparticles (V, Al) Co-Doped ZnO Synthesized by Sol-Gel Processes," *Superlattices Microstruct*, **64**, pp. 451–459.

- [191] Geng, Y., Xie, Z. Y., Yang, W., Xu, S. S., Sun, Q. Q., Ding, S. J., Lu, H. L., and Zhang, D. W., 2013, "Structural, Optical, and Electrical Properties of Hf-Doped ZnO Films Deposited by Atomic Layer Deposition," *Surf Coat Technol*, **232**, pp. 41–45.
- [192] Bergum, K., Hansen, P. A., Fjellvåg, H., and Nilsen, O., 2014, "Structural, Electrical and Optical Characterization of Ti-Doped ZnO Films Grown by Atomic Layer Deposition," *J Alloys Compd*, **616**, pp. 618–624.
- [193] Shukla, R. K., Srivastava, A., Srivastava, A., and Dubey, K. C., 2006, "Growth of Transparent Conducting Nanocrystalline Al Doped ZnO Thin Films by Pulsed Laser Deposition," *J Cryst Growth*, **294**(2), pp. 427–431.
- [194] Bergum, K., Hansen, P. A., Fjellvåg, H., and Nilsen, O., 2014, "Structural, Electrical and Optical Characterization of Ti-Doped ZnO Films Grown by Atomic Layer Deposition," *J Alloys Compd*, **616**, pp. 618–624.
- [195] Krajewski, T. A., Dybko, K., Luka, G., Wachnicki, L., Kopalko, K., Paszkowicz, W., Godlewski, M., and Guziewicz, E., 2015, "Analysis of Scattering Mechanisms in Zinc Oxide Films Grown by the Atomic Layer Deposition Technique," *J Appl Phys*, **118**(3).
- [196] Shokhovets, S., Gobsch, G., and Ambacher, O., 2006, "Conduction Band Parameters of ZnO," *Superlattices Microstruct*, **39**(1–4), pp. 299–305.
- [197] Viezbicke, B. D., Patel, S., Davis, B. E., and Birnie, D. P., 2015, "Evaluation of the Tauc Method for Optical Absorption Edge Determination: ZnO Thin Films as a Model System," *Phys Status Solidi B Basic Res*, **252**(8), pp. 1700–1710.
- [198] Tauc, J., 1974, *Amorphous and Liquid Semiconductors*, Springer, London and New York.
- [199] Klein, J., Kampermann, L., Mockenhaupt, B., Behrens, M., Strunk, J., and Bacher, G., 2023, "Limitations of the Tauc Plot Method," *Adv Funct Mater*.
- [200] Ye, J. D., Gu, S. L., Zhu, S. M., Liu, S. M., Zheng, Y. D., Zhang, R., and Shi, Y., 2005, "Fermi-Level Band Filling and Band-Gap Renormalization in Ga-Doped ZnO," *Appl Phys Lett*, **86**(19), pp. 1–3.
- [201] Banerjee, P., Lee, W. J., Bae, K. R., Lee, S. B., and Rubloff, G. W., 2010, "Structural, Electrical, and Optical Properties of Atomic Layer Deposition Al-Doped ZnO Films," *Journal of Applied Physics*.
- [202] Ajimsha, R. S., Das, A. K., Singh, B. N., Misra, P., and Kukreja, L. M., 2010, "Structural, Electrical and Optical Properties of Dy Doped ZnO Thin Films Grown by Buffer Assisted Pulsed Laser Deposition," *Physica E Low Dimens Syst Nanostruct*, **42**(6), pp. 1838–1843.
- [203] Pisarkiewicz, T., Zakrzewska, K., and Leja, E., 1989, "Scattering of Charge Carriers in Transparent and Conducting Thin Oxide Films with a Non-Parabolic Conduction Band," *Thin Solid Films*, **174**(1), pp. 217–223.
- [204] Avadhut, Y. S., Weber, J., Hammarberg, E., Feldmann, C., and Schmedtaufder Günne, J., 2012, "Structural Investigation of Aluminium Doped ZnO Nanoparticles by Solid-State NMR Spectroscopy," *Physical Chemistry Chemical Physics*, **14**(33), pp. 11610–11625.

- [205] Ahn, C. H., Kim, J. H., and Cho, H. K., 2012, "Tunable Electrical and Optical Properties in Composition Controlled Hf:ZnO Thin Films Grown by Atomic Layer Deposition," *J Electrochem Soc*, **159**(4), pp. H384–H387.
- [206] Zhou, X., Jiang, D., Lin, F., Ma, X., and Shi, W., 2008, "Influence of Hf Doping Concentration on Microstructure and Optical Properties of HfxZn1-xO Thin Films," *Physica B Condens Matter*, **403**(1), pp. 115–119.
- [207] Kim, Y. H., Jeong, J., Lee, K. S., Park, J. K., Baik, Y. J., Seong, T. Y., and Kim, W. M., 2010, "Characteristics of ZnO:Al Thin Films Co-Doped with Hydrogen and Fluorine," *Appl Surf Sci*, **256**(16), pp. 5102–5107.
- [208] Wang, F. H., and Yang, T. H., 2016, "Effect of Hydrogen Doping on the Properties of Al and F Co-Doped ZnO Films for Thin Film Silicon Solar Cell Applications," *Thin Solid Films*, **605**, pp. 64–72.
- [209] Zhu, B. L., Wang, J., Zhu, S. J., Wu, J., Wu, R., Zeng, D. W., and Xie, C. S., 2011, "Influence of Hydrogen Introduction on Structure and Properties of ZnO Thin Films during Sputtering and Post-Annealing," *Thin Solid Films*, **519**(11), pp. 3809–3815.
- [210] Wang, F., and Melosh, N. A., 2011, "Plasmonic Energy Collection through Hot Carrier Extraction," *Nano Lett*, **11**(12), pp. 5426–5430.
- [211] Schirato, A., Maiuri, M., Cerullo, G., and Della Valle, G., 2023, "Ultrafast Hot Electron Dynamics in Plasmonic Nanostructures: Experiments, Modelling, Design," *Nanophotonics*, **12**(1), pp. 1–28.
- [212] Takahashi, Y., and Tatsuma, T., 2011, "Solid State Photovoltaic Cells Based on Localized Surface Plasmon-Induced Charge Separation," *Appl Phys Lett*, **99**(18).
- [213] Èppel, A. K., Kriegseis, W., Meyer, B. K., Scharmann, A., Daube, C., Stollenwerk, J., and Trube, J., *Dependence of the Electrical and Optical Behaviour of ITO±silver±ITO Multilayers on the Silver Properties*.
- [214] Sik Jung, Y., Won Choi, Y., Chul Lee, H., and Wook Lee, D., 2003, "Effects of Thermal Treatment on the Electrical and Optical Properties of Silver-Based Indium Tin Oxide/metal/indium Tin Oxide Structures," *Thin Solid Films*, **440**, pp. 278–284.
- [215] Sahu, D. R., Chen, C. Y., Lin, S. Y., and Huang, J. L., 2006, "Effect of Substrate Temperature and Annealing Treatment on the Electrical and Optical Properties of Silver-Based Multilayer Coating Electrodes," *Thin Solid Films*, **515**(3), pp. 932–935.
- [216] Chen, J. Y., and Sun, K. W., 2010, "Growth of Vertically Aligned ZnO Nanorod Arrays as Antireflection Layer on Silicon Solar Cells," *Solar Energy Materials and Solar Cells*, **94**(5), pp. 930–934.
- [217] Lai, F. I., Hsieh, M. Y., Yang, J. F., Hsu, Y. C., and Kuo, S. Y., 2021, "Antireflection Layer of ZnO Nanorod Embedded in PDMS Film for Enhancing Omnidirectional Photovoltaic Performance of CIGS Photovoltaic Cell," *Int J Energy Res*, **45**(1), pp. 1142–1149.
- [218] Chen, J. De, Zhou, L., Ou, Q. D., Li, Y. Q., Shen, S., Lee, S. T., and Tang, J. X., 2014, "Enhanced Light Harvesting in Organic Solar Cells Featuring a Biomimetic Active Layer and a Self-Cleaning Antireflective Coating," *Adv Energy Mater*, **4**(9), pp. 1–8.
- [219] Gombert, A., and Bläsi, B., 2009, "The Moth-Eye Effect - From Fundamentals to Commercial Exploitation," *Functional Properties of Bio-Inspired Surfaces:*

Characterization and Technological Applications, A. Favret, Eduardo, and O. Fuentes, Nestor, eds., World Scientific, pp. 79–102.

[220] Peer, A., Biswas, R., Park, J.-M., Shinar, R., and Shinar, J., 2017, “Light Management in Perovskite Solar Cells and Organic LEDs with Microlens Arrays,” *Opt Express*, **25**(9), p. 10704.

[221] Tockhorn, P., Sutter, J., Colom, R., Kegelmann, L., Al-Ashouri, A., Roß, M., Jäger, K., Unold, T., Burger, S., Albrecht, S., and Becker, C., 2020, “Improved Quantum Efficiency by Advanced Light Management in Nanotextured Solution-Processed Perovskite Solar Cells,” *ACS Photonics*, **7**(9), pp. 2589–2600.

[222] Schmager, R., Hossain, I. M., Schackmar, F., Richards, B. S., Gomard, G., and Paetzold, U. W., 2019, “Light Coupling to Quasi-Guided Modes in Nanoimprinted Perovskite Solar Cells,” *Solar Energy Materials and Solar Cells*, **201**(July), p. 110080.

[223] Deng, K., Liu, Z., Wang, M., and Li, L., 2019, “Nanoimprinted Grating-Embedded Perovskite Solar Cells with Improved Light Management,” *Adv Funct Mater*, **29**(19).

[224] Hossain, M. I., Qarony, W., Jovanov, V., Tsang, Y. H., and Knipp, D., 2018, “Nanophotonic Design of Perovskite/Silicon Tandem Solar Cells,” *J Mater Chem A Mater*, **6**(8), pp. 3625–3633.

[225] Min, H., Lee, D. Y., Kim, J., Kim, G., Lee, K. S., Kim, J., Paik, M. J., Kim, Y. K., Kim, K. S., Kim, M. G., Shin, T. J., and Il Seok, S., 2021, “Perovskite Solar Cells with Atomically Coherent Interlayers on SnO₂ Electrodes,” *Nature*, **598**(7881), pp. 444–450.

[226] Cho, H., Jeong, S. H., Park, M. H., Kim, Y. H., Wolf, C., Lee, C. L., Heo, J. H., Sadhanala, A., Myoung, N. S., Yoo, S., Im, S. H., Friend, R. H., and Lee, T. W., 2015, “Overcoming the Electroluminescence Efficiency Limitations of Perovskite Light-Emitting Diodes,” *Science* (1979), **350**(6265), pp. 1222–1225.

[227] Wang, L., Yuan, G. D., Duan, R. F., Huang, F., Wei, T. B., Liu, Z. Q., Wang, J. X., and Li, J. M., 2016, “Tunable Bandgap in Hybrid Perovskite CH₃NH₃Pb(Br₃-YXy) Single Crystals and Photodetector Applications,” *AIP Adv*, **6**(4).

[228] Krajewski, M., Callies, A., Heydarian, M., Heydarian, M., Hanser, M., Schulze, P. S. C., Bläsi, B., and Höhn, O., 2023, “Roller Nanoimprinted Honeycomb Texture as an Efficient Antireflective Coating for Perovskite Solar Cells,” *Adv Mater Interfaces*, **10**(26).

[229] *SU-8 2000 Permanent Epoxy Negative Photoresist Processing Guidelines*.

[230] Battaglia, C., Escarré, J., Söderström, K., Erni, L., Ding, L., Bugnon, G., Billet, A., Boccard, M., Barraud, L., De Wolf, S., Haug, F. J., Despeisse, M., and Ballif, C., 2011, “Nanoimprint Lithography for High-Efficiency Thin-Film Silicon Solar Cells,” *Nano Lett*, **11**(2), pp. 661–665.

[231] Carlberg, P., Montelius, L., and Tegenfeldt, J., 2008, “Nanoimprint in PDMS on Glass with Two-Level Hybrid Stamp,” *Microelectron Eng*, **85**(1), pp. 210–213.

- [232] Kim, S. C., 2014, "Simulation of Rough Surface of CIGS (CuInGaSe) Solar Cell by RCWA (Rigorous Coupled Wave Analysis) Considering the Incoherency of Light," *J Opt Soc Korea*, **18**(2), pp. 180–183.
- [233] Jeong, J., Kim, M., Seo, J., Lu, H., Ahlawat, P., Mishra, A., Yang, Y., Hope, M. A., Eickemeyer, F. T., Kim, M., Yoon, Y. J., Choi, I. W., Darwich, B. P., Choi, S. J., Jo, Y., Lee, J. H., Walker, B., Zakeeruddin, S. M., Emsley, L., Rothlisberger, U., Hagfeldt, A., Kim, D. S., Grätzel, M., and Kim, J. Y., 2021, "Pseudo-Halide Anion Engineering for α -FAPbI₃ Perovskite Solar Cells," *Nature*, **592**(7854), pp. 381–385.
- [234] Song, Z., Chen, C., Li, C., Awni, R. A., Zhao, D., and Yan, Y., 2019, "Wide-Bandgap, Low-Bandgap, and Tandem Perovskite Solar Cells," *Semicond Sci Technol*, **34**(9), p. 093001.
- [235] Jäger, K., Sutter, J., Hammerschmidt, M., Schneider, P. I., and Becker, C., 2021, "Prospects of Light Management in Perovskite/Silicon Tandem Solar Cells," *Nanophotonics*, **10**(8), pp. 1991–2000.
- [236] Al-Ashouri, A., Köhnen, E., Li, B., Magomedov, A., Hempel, H., Caprioglio, P., Márquez, J. A., Vilches, A. B. M., Kasparavicius, E., Smith, J. A., Phung, N., Menzel, D., Grischek, M., Kegelmann, L., Skroblin, D., Gollwitzer, C., Malinauskas, T., Jošt, M., Matič, G., Rech, B., Schlatmann, R., Topič, M., Korte, L., Abate, A., Stannowski, B., Neher, D., Stolterfoht, M., Unold, T., Getautis, V., and Albrecht, S., 2020, "Monolithic Perovskite/Silicon Tandem Solar Cell with >29% Efficiency by Enhanced Hole Extraction," *Science (1979)*, **370**(6522), pp. 1300–1309.
- [237] Ghosh, D. S., Chen, T. L., and Pruneri, V., 2010, "High Figure-of-Merit Ultrathin Metal Transparent Electrodes Incorporating a Conductive Grid," *Appl Phys Lett*, **96**(4).
- [238] Tvingstedt, K., and Inganäs, O., 2007, "Electrode Grids for ITO-Free Organic Photovoltaic Devices," *Advanced Materials*, **19**(19), pp. 2893–2897.
- [239] Liang, C., Zhao, D., Li, P., Wu, B., Gu, H., Zhang, J., Goh, T. W., Chen, S., Chen, Y., Sha, Z., Shao, G., Sum, T. C., and Xing, G., 2019, "Simultaneously Boost Diffusion Length and Stability of Perovskite for High Performance Solar Cells," *Nano Energy*, **59**, pp. 721–729.
- [240] Sajjad, M. T., Ruseckas, A., and Samuel, I. D. W., 2020, "Enhancing Exciton Diffusion Length Provides New Opportunities for Organic Photovoltaics," *Matter*, **3**(2), pp. 341–354.
- [241] Sun, Q., Yin, Z., Wang, S., Zhao, C., Leng, J., Tian, W., and Jin, S., 2020, "Long-Range Exciton Transport in Perovskite-Metal Organic Framework Solid Composites," *Journal of Physical Chemistry Letters*, pp. 9045–9050.
- [242] Jagdish, H. V., 1997, *Information Processing Letters Information Processing Analysis of the Hilbert Curve for Representing Two-Dimensional Space*.
- [243] Kuffner, J. J., and Lavalley, S. M., 2009, "Space-Filling Trees," Tech Report, Carnegie Mellon University.
- [244] Jang, S., Jung, W. Bin, Kim, C., Won, P., Lee, S. G., Cho, K. M., Jin, M. L., An, C. J., Jeon, H. J., Ko, S. H., Kim, T. S., and Jung, H. T., 2016, "A Three-Dimensional Metal Grid Mesh as a Practical Alternative to ITO," *Nanoscale*, **8**(29), pp. 14257–14263.

- [245] Van De Groep, J., Spinelli, P., and Polman, A., 2012, "Transparent Conducting Silver Nanowire Networks," *Nano Lett*, **12**(6), pp. 3138–3144.
- [246] Chen, D., and Manley, P., 2018, "Nanophotonic Light Management for Perovskite–Silicon Tandem Solar Cells," *J Photonics Energy*, **8**(02), p. 1.
- [247] Al-Ashouri, A., Köhnen, E., Li, B., Magomedov, A., Hempel, H., Caprioglio, P., Márquez, J. A., Vilches, A. B. M., Kasparavicius, E., Smith, J. A., Phung, N., Menzel, D., Grischek, M., Kegelmann, L., Skroblin, D., Gollwitzer, C., Malinauskas, T., Jošt, M., Matič, G., Rech, B., Schlatmann, R., Topič, M., Korte, L., Abate, A., Stannowski, B., Neher, D., Stolterfoht, M., Unold, T., Getautis, V., and Albrecht, S., 2020, "Monolithic Perovskite/Silicon Tandem Solar Cell with >29% Efficiency by Enhanced Hole Extraction," *Science (1979)*, **370**(6522), pp. 1300–1309.
- [248] Bett, A. J., Schulze, P. S. C., Winkler, K. M., Kabakli, Ö. S., Ketterer, I., Mundt, L. E., Reichmuth, S. K., Siefer, G., Cojocar, L., Tutsch, L., Bivour, M., Hermle, M., Glunz, S. W., and Goldschmidt, J. C., 2020, "Two-Terminal Perovskite Silicon Tandem Solar Cells with a High-Bandgap Perovskite Absorber Enabling Voltages over 1.8 V," *Progress in Photovoltaics: Research and Applications*, **28**(2), pp. 99–110.
- [249] Yaffe, O., Chernikov, A., Norman, Z. M., Zhong, Y., Velauthapillai, A., Van Der Zande, A., Owen, J. S., and Heinz, T. F., 2015, "Excitons in Ultrathin Organic-Inorganic Perovskite Crystals," *Phys Rev B Condens Matter Mater Phys*, **92**(4), pp. 1–7.
- [250] Laquai, F., Andrienko, D., Mauer, R., and Blom, P. W. M., 2015, "Charge Carrier Transport and Photogeneration in P3HT : PCBM Photovoltaic Blends," *Macromol Rapid Commun*, **36**, pp. 1001–1025.
- [251] Piotrowski, P., Mech, W., Zarębska, K., Krajewski, M., Korona, K. P., Kamińska, M., Skompska, M., and Kaim, A., 2021, "Mono- and Di-Pyrene [60]Fullerene and [70]Fullerene Derivatives as Potential Components for Photovoltaic Devices," *Molecules*, **26**(1561).
- [252] Tucher, N., Höhn, O., Hauser, H., Müller, C., and Bläsi, B., 2017, "Characterizing the Degradation of PDMS Stamps in Nanoimprint Lithography," *Microelectron Eng*, **180**, pp. 40–44.